EXPANDED POLYSTYRENE GEOFOAM EMBANKMENT FOR SUPPORT OF RAILWAYS AND BRIDGES

by

Ramesh Neupane

A dissertation submitted to the faculty of
The University of Utah
in partial fulfillment of the requirements for the degree of

Doctor of Philosophy

Department of Civil and Environmental Engineering

The University of Utah

August 2015

The University of Utah Graduate School

STATEMENT OF DISSERTATION APPROVAL

The dissertation of **Ramesh Neupane**

has been approved by the following supervisory committee members:

Steven Bartlett	, Chair	**4/03/2015** Date Approved
Evert Lawton	, Member	**4/03/2015** Date Approved
Amanda Bordelon	, Member	**4/06/2015** Date Approved
Eunhye Kim	, Member	**4/03/2015** Date Approved
Clifton Farnsworth	, Member	**4/03/2015** Date Approved

and by **Michael Barber** ,Chair of

the Department of **Civil and Environmental Engineering**

and by David B. Kieda, Dean of The Graduate School.

ABSTRACT

Expanded Polystyrene (EPS) geofoam is a superlight weight material used in various geotechnical engineering applications. The goal of this study was to explore the use of EPS embankment to support railways and bridges without being overstressed during extreme events like earthquakes. Static and dynamic deflections that occur on an embankment along a rail line were measured by using numerical, laboratory and field techniques. A numerical method was used to measure static deflection whereas accelerometers were used in case of dynamic deflection. In the laboratory, large scale triaxial and large chamber tests were conducted to determine the resilient modulus of ballast. In the field, accelerometers were placed on sleepers of commuter and light rail line to collect the data for vertical deflection. Monotonic and cyclic triaxial tests, analytical and numerical methods were used to study bridge support embankments. The dynamics of EPS embankment for support of bridge system was studied and possible lateral restrained systems were developed for moderate to higher seismic excitations.

Large chamber test is more suitable for the calculation of cyclic nonlinear secant modulus. EPS embankment performed well while considering vertical deflection. The combination of dead and earthquake load can be considered as the stress corresponding to 2 percent axial strain. The critical accelerations for sliding, sway and rocking were 0.6 g, 0.2 g and 0.3 g, respectively. Shear keys, embedment of embankment and cables are required for higher excitations.

To my wife, Anju, and daughters, Charu and Samata,
who constantly inspire me to
drive on.

TABLE OF CONTENTS

ACKNOWLEDGEMENTS

I would like to extend my gratitude to my advisor Dr. Steven Bartlett for his continuous support and guidance throughout my graduate studies. I wish to thank Professor Evert Lawton for his encouragement and valuable suggestions. I want to thank my other committee members Dr. Amanda Bordelon, Dr. Eunhye Kim and Dr. Clifton Farsnworth, for providing suggestions in this study.

I would like to thank ACH Foam Technologies and Geneva Rock, Salt Lake City, Utah for providing the EPS geofoam specimens and ballast material for experimental studies. I wish to say thanks for the help provided by Mark Bryant and Trevor Nye during the cyclic triaxial experiments set up for ballast and EPS material.

I thank my wife, Anju, who encouraged me and put her career on hold while I completed my graduate studies. I would like to thank my brother Umesh Neupane for his help.

CHAPTER 1

INTRODUCTION

1.1 Background

Expanded polystyrene (EPS) geofoam is a super-lightweight, closed-cell, and rigid plastic foam-like material used in many civil engineering applications. The predominant shape of EPS product used in most cases is prismatic block, which can vary in size based on the size of the mold. Block molders, or manufacturers of EPS block, use a process where beads of EPS are expanded to form relatively rigid blocks. EPS beads consist of closed-cell polystyrene plastic containing pentane gas. The EPS blocks are created from these beads in a two-stage process, namely, pre-expansion and molding. In the pre-expansion stage, beads are placed within a container and heated with steam to temperatures between 80 and 110^0C. During pre-expansion heating, the pentane vaporizes within the closed cell softening the polystyrene and causing an expansion of the bead to around 50 times its original volume. The expanded beads (called prepuffs) are then allowed to cool for several hours. Following this, the prepuff beads are placed in an enclosed, fixed-wall, stainless steel mold where the spherical beads are continuously resoftened and further expanded using injected, pressurized steam. In this molding stage, further expansion of beads forms a closed-cell relatively rigid block with no significant void space between the spheres. The blocks are then released from the mold and allowed to cure an environmentally-controlled

space for several days (Horvath, 1994).

The application of block-molded EPS geofoam in embankment applications has been reported by many researchers and practitioners. However, only a few studies are currently available regarding the use of block-molded EPS embankment to support railway systems and highway bridges. These topics are a focus of relatively recent and evolving research.

This study focuses on the application and performance of EPS blocks as an ultralight-weight fill material for embankment construction that supports railway and bridge systems associated with soft soil site conditions. For the latter application, the EPS is used for direct support of the bridge system with the aid of deep foundations systems.

The funding for this research is associated with two projects entitled: (1) "Evaluation of Geofoam for Support of Freight Rail Tracks" and (2) "Highway Structures Supported on EPS Embankment without Deep Foundations." The first project is funded by CFIRE (Center for Freight and Research Education) from its University of Memphis affiliate. The second is funded by the Mountain Plains Consortium (MPC) with funding coming from its affiliate at the Utah Transportation Center at the University of Utah. Other research participation for the second topic is also being provided by the Norwegian Public Roads Administration (NPRA). These research projects will be briefly discussed consecutively.

1.2 Problem Statement

Recently, EPS has been used in embankments to support the railway system in Salt Lake City, Utah, in the United States. Large deflections of rail embankment are potentially a major concern in terms of safety. Large deflections can lead to the need to reduce operating speed over problematic zones, or in the worst case possible derailment. There is

no design guidance regarding the permissible amount of vertical deflection on EPS embankment that support railway systems. Therefore, it is important to monitor the amount of dynamic deflection for this type of embankment system. Field methods can be used to measure such deflection, and in combination with numerical evaluations, these measurements and evaluation tools can provide a basis for future design.

Regarding supporting highway bridges on EPS embankment, the Norwegian Public Roads Administration (NPRA) pioneered the technique where the bridge structures rest solely on EPS blocks without deep foundations. However, their design considered only static loading. During extreme events, like earthquake, the bridge and EPS embankment system will be exposed to additional dynamic loadings. For this, the possible modes of movements for rectangular prismatic embankments are interblock and basal sliding, sway and rocking. Therefore, a dynamic evaluation is required to calculate the critical acceleration for these modes. In addition, a lateral restraint system will be developed to resist the associated dead and earthquake forces without overstressing the system members, including the EPS block component.

1.3 Objectives of Study

This research focuses on two applications of EPS block in embankment systems. The first area of focus is support of a railway system. The objectives regarding the use of EPS in the embankment to support railway systems is: (1) to evaluate static and dynamic material properties of ballast, (2) to develop low cost techniques to measure the dynamic rail deflection in the field (i.e., deflection originating from a passing train), and (3) to measure dynamic rail deflection using these techniques.

The second area of focus is the support of a bridge system. The objectives regarding the use of EPS embankment to support bridge systems are (1) to estimate the amount of post-seismic creep and total strain with seismic considerations, (2) to conduct a dynamic study of EPS geofoam embankment for support of a bridge system and (3) to develop and evaluate a seismic lateral restraint system to resist dynamic forces associated with interblock and basal sliding, sway, rocking and uplift using analytical/numerical techniques.

1.4 Research Approach

The research approaches are discussed in two parts. The first part is the use of EPS in the embankment to support railway and the second part is the use of EPS in the embankment to support highway bridges.

1.4.1 EPS Embankments for Support of Railway Systems

The overall objectives for the CFIRE funded project are to develop the preliminary design guidelines for the use of EPS geofoam embankment to support freight rail systems and to provide preliminary information that will eventually lead to the potential development and construction of a full-scale test embankment facility for rail systems. The research developed and reported herein supports, in part, the accomplishment of these overall project objectives. However, some of the research activities are planned for the future and will be done outside the scope of this dissertation.

Part of this research focuses on obtaining and evaluating the rail deflection performance of light rail (i.e., TRAX) and commuter rail (i.e., FrontRunner) systems constructed atop

EPS embankments in the Salt Lake Valley, Utah. EPS geofoam blocks have been recently installed under limited segments of these systems in Salt Lake City, Utah. The locomotive loads from commuter rail and light rail are less than that of freight rail; however the commuter rail locomotive loads are approximately 80 percent of those experienced by freight rail; hence an evaluation of the deflection performance of this latter system would be useful. The FrontRunner commuter rail system is located in Corner Canyon, Draper City, Utah and has both EPS geofoam and earthen embankment that has been evaluated herein. Similarly, the light rail system along the West Valley Line near Roper Yard in South Salt Lake City, Utah, has an EPS geofoam embankment and was used for deflection monitoring.

The substructure of embankment materials used in commuter rail systems are ballast, sub-ballast, EPS geofoam and granular soil. The static deflection of EPS embankment has been studied by Li (2014) using the finite difference numerical technique as incorporated in the commercial version of Fast Lagrangian Analysis of Continua (FLAC). This study made an a priori estimation of the static deflection of the FrontRunner System at the Corner Canyon location prior to the obtaining and publishing of the deflection information obtained for this dissertation.

In addition, results of monotonic and cyclic laboratory tests conducted on EPS and ballast were performed in the Civil Engineering Laboratory at the University of Utah. The results from this testing were incorporated into the numerical evaluations of Li (2014). The material properties of ballast were unknown and were explored using bench-scale and large-diameter cylinder tests. These series of monotonic and cyclic triaxial tests were conducted at relatively low axial strain using strain-controlled testing. The results of these

tests were used to determine the low-strain moduli of elasticity and rigidity (i.e., Young's modulus and cyclic nonlinear modulus).

Subsequently, as additional work was completed for this dissertation, confirmatory field measurements of the rail deflections were carried out during the passage of trains on the FrontRunner system in Corner Canyon using an accelerometer array placed on the rail ties. Three component accelerometers were glued on these concrete ties (i.e., sleepers) and a high-speed data logger was attached to these instruments to record the acceleration time history of the passing trains. Deflections of the accelerometers were obtained using a double integration process of the acceleration time histories. The commercially available software SeismoSignal™ (SeismoSoft, 2015) was used to filter the noise and process the data. Also, an optical technique was developed as a direct measurement method, but was not deployed in the field due to poor site conditions (i.e., strong wind) that occurred during the testing window. The optical method was evaluated in the laboratory using vertical displacements generated from a cyclic test. Displacement time histories for this test obtained from a linear variable differential transformer (LVDT) were compared with those obtained from the optical technique and were found to be in good agreement.

1.4.2 EPS Embankments for Support of Bridge Systems

There are three main objectives associated with the second research project funded by the MPC and NPRA: (1) conceptualize and develop an EPS block foundation support system for single-span bridge structures and pedestrian overpasses using cases obtained from the Norwegian Public Roads Administration (NPRA) and additional calculations and testing, (2) evaluate the potential performance of such system(s) under static and seismic

loadings, and (3) make recommendations for future research/testing/development required for implementation of this technology in the United States and elsewhere.

This dissertation directly addresses these objectives with the goal of making recommendations for the design and construction of bridge structures supported directly by EPS geofoam without the need of deep foundations or soil improvement at sites located on soft ground conditions. If not designed and constructed properly, the EPS bridge support system could be subjected to a large amount of creep settlement of the EPS block and foundation soils resulting from the structural dead loads, from the live traffic loadings, or from loadings associated with a large seismic event. The stress-strain behavior of EPS geofoam under monotonic and cyclic loadings is time dependent for both short-term and long-term loading conditions. The short-term loadings for the EPS support system may originate from locomotive, rail car, vehicular traffic, etc., and the long-term loading is produced by gravity (i.e., self-weight of the materials and components with the system). Long-term loadings can produce deformation of the EPS block under a constant applied stress condition, which is commonly referred to as creep.

Excessive creep in EPS bridge support systems can lead to reaching a serviceability limit state in terms of unacceptable settlement of the bridge and its components. This in turn may reduce the performance of the bridge system or shorten its operational lifespan. Both the potential for pre - and postearthquake creep settlement are addressed by this study. These were explored by performing monotonic, cyclic triaxial and long-term creep tests in the soil mechanics laboratory of the Civil Engineering Department of the University of Utah and by evaluating these results using analytical and numerical techniques.

For seismic events, the EPS lateral restraint system must be sufficient to resist seismic

forces associated with basal and interlayer sliding, and with sway and rocking. In short, the lateral restraint system should be capable of resisting the associated dead and live forces without overstressing the system members, including the EPS block components. A laboratory test program was used to define and evaluate the permissible (i.e., allowable) normal and shear stresses that could potentially develop in the EPS during seismic loading. Postcyclic creep tests were subsequently performed to measure the postearthquake creep in the EPS specimens caused by the earthquake cycling. The results of the testing program were used to check for potential overstressing of the EPS blocks by a seismic event when a lateral restraint system(s) was introduced to the bridge support system. The laboratory test program described below was conducted as part of this development and evaluation.

1.4.2.1 Creep Settlement Associated with Cyclic and Extreme Loading

The potential for additional postearthquake creep strain induced in the EPS was explored by laboratory testing which included monotonic, cyclic and postcyclic loadings performed in a triaxial test apparatus. Routine monotonic uniaxial compression tests were done to obtain the properties of the EPS specimens. Higher density EPS are generally required for bridge support systems. In this study EPS 25, EPS 29 and EPS 39 were used for monotonic and cyclic testing.

The cyclic uniaxial strain-controlled tests were performed using 5, 15 and 30 cycles. After testing, postcyclic creep strain was also measured with dead load applied. These numbers of cycles were selected to represent typical numbers of significant stress cycles induced by a range of earthquake conditions based on the work of Seed and Idriss (1982). These authors developed a relationship for the number of equivalent stress cycles, and

earthquake magnitude at which 5, 15 and 30 cycles were taken to be representative of the significant number of stress cycles cause by low, moderate and high seismic excitations, respectively. The amount of permanent cyclic strain was calculated from the results of cyclic uniaxial tests. Also, EPS embankment constructed for bridge support systems will have negligible confinement, and thus the laboratory tests were conducted without confinement.

The dead load was applied continuously after the cyclic loading and postcyclic creep strain was measured. This is the creep associated with dead load after the application of cyclic load that simulated the seismic excitation. In the test, a sample was subjected to constant dead load corresponding to the stress level of 1 percent axial strain. Postcyclic creep strain for design period was calculated as the ratio of total compression to the original height of the specimen. The total creep strain was then calculated as the sum of the cyclic plastic axial strain and postcyclic creep strain.

1.4.2.2 Lateral Restraint System to Support Bridge During Earthquake

This study focused on bridge structures supported directly by EPS geofoam placed atop soft ground conditions without the aid of support from deep foundation systems or from soil improvement. Lateral restraint strategies were introduced and evaluated to prevent the potential for excessive movement of the bridge support system and to decrease the possibility of overstressing of the EPS blocks from seismic events.

In these evaluations, the major focus was on analyzing the static and dynamic behavior of the EPS support embankment located directly below the spread footings of the bridge. Two general geometries were considered for the supporting embankment: (1) rectangular

prismatic, and (2) trapezoidal prismatic embankments.

In the first geometrical configuration, relatively stiff (i.e., high density) EPS was proposed to be placed underneath the spread footings of bridge in the zone most affected by the bridge loads. Accordingly, in the adjacent bridge approach embankment areas, where significant bridge loading is not anticipated, a less stiff (i.e., lower density) EPS was proposed. A protective concrete load distribution slab and road pavement were proposed in the approach areas to protect the EPS embankment from overstressing due to traffic loadings.

For the second geometrical configuration, trapezoidal prismatic embankment was proposed to support the bridge and footings with higher density EPS used in the trapezoidal section and lower density EPS used in the approach areas. The side slope of embankment was made 2H:1V similar to the embankments described in Aaboe and Frydenlund (2011).

Both geometries were evaluated for load bearing and seismic stability. Because of its relatively slender nature, the rectangular prismatic embankment was also evaluated for potential sway and rocking modes during seismic excitation. For this, the fundamental period of the support embankment was calculated and evaluated for various modes of excitations in terms of the critical acceleration.

In the end, if an ultimate limit state was reached for the seismic case, shear keys and embedment of the embankment were proposed for excitation above the critical acceleration. In addition, cabling and/or thread bars were proposed to increase the resistance and stability against excessive sway and rocking without internally overstressing the EPS blocks. The combination of the dead load, live traffic load, and seismically induced stresses in the EPS embankment were ultimately compared with the recommended

allowable shear and normal stresses developed from the laboratory test program to guard against the potential for excessive postseismic creep.

In addition, a joint was recommended at the interface between the bridge support and bridge approach systems to reduce the potential for stress transfer at this location. Due to the difference in the loading conditions, a floating slab was also recommended to be placed between the footing of bridge and load distribution slab of pavement. This was done to overcome the effects of possible differential settlement between these systems.

1.5 References

Aaboe, R., and Frydenlund, T. E. (2011). "40 years of experience with the use of EPS geofoam blocks in road construction." *Proc., 4th Intl. Conf on Geofoam Blocks in Construction Applications,* Lillestrom, Norway.

Horvath, J. (1994). "Expanded polystyrene (EPS) geofoam: an introduction to material behavior." *Geotextiles and Geomembranes*, 13(4), 263-280.

Li, S. (2014). "Evaluation and numerical modeling of deflection and vertical displacement of rail systems supported by EPS geofoam embankments." MS thesis, The University of Utah, Utah, USA.

Seed, H. B., and Idriss, I. (1982). *Ground motions and soil liquefaction during earthquakes*, Earthquake Engineering Research Institute, Oakland, California, USA.

SeismoSoft (2015). "SeismoSignal 5.1.0." <http//www.seismosoft.com/en/Download.aspx>. (February 17, 2015).

CHAPTER 2

STATIC AND CYCLIC TEST ON RAILWAY BALLAST

2.1 Introduction

The amount of deflection of the rail caused by the passing of a locomotive or rail car is a significant safety issue for rail system operations. Large deflections could pose the risk of possible derailment, especially at higher speeds of operation. Dynamic rail deflection can occur on all types of embankment support systems. Most rail embankments have been made using compacted, conventional fill materials like soil and rock. However, recently EPS geofoam has been used as an embankment material to support rail systems for limited cases in northern Europe and in the United States

Several studies have been carried out to monitor railway track deflections occurring in conventional embankment materials using various measurement techniques (Ho et al., 2006; Bowness et al., 2007; Lu, 2008; Pinto et al., 2009; Psimoulis and Stiros, 2013). However, very little has been done to measure static and dynamic rail deflection of systems constructed atop EPS embankments. Fortunately, the Utah Transit Authority (UTA) FrontRunner commuter rail system crosses a relatively large EPS embankment in Corner Canyon located in Draper City, Utah. This innovative embankment system offers an excellent opportunity to measure and evaluate the deflections of such a system.

The EPS embankment consists (from top to bottom) of EPS geofoam block, a reinforced concrete load distribution slab, structural fill, sub-ballast, ballast, ties (sleepers) and steel rail. The amount of deflection in an embankment system mainly depends on EPS geofoam and ballast materials. The deflection of the system can be determined by using numerical evaluation. Numerical techniques require the material properties of embankment. Since the material properties of EPS are known, laboratory testing was required to determine the properties of ballast. The material testing and evaluation in this chapter supports subsequent numerical evaluations by describing the small and large strain stiffness of the ballast material used at the Corner Canyon EPS embankment site (Li, 2014).

There are many field and laboratory methods for obtaining the stiffness properties of fill and ballast materials. Deflectometer and plate bearing load tests are the most common field methods, whereas the triaxial test is a common laboratory method for evaluating the modulus of elasticity (Ping et al., 2002). In field applications, the ballast material will be subjected to both long-term dead loads (i.e., static) and cyclic (i.e., repetitive) train loads.

There are several laboratory studies for the determination of material stiffness and behavior of ballast material under static and cyclic loads (Suiker et al., 2005; Anderson and Fair, 2008; Sevi and Ge, 2011). Suiker et al. (2005) conducted both static and cyclic triaxial testing of ballast and sub-ballast materials in the laboratory. The cyclic loading revealed that the material was compacted during cycling, and the strength and stiffness of material was increased. The resilient modulus of the specimen was increased with increase in number of cycles when a cyclic load was applied on railroad ballast (Anderson and Fair, 2008). The cyclic triaxial test results on ballast materials showed that resilient modulus of ballast was higher for larger grain sizes and higher level of stresses (Sevi and Ge, 2011).

The modulus of elasticity is often called "Young's" modulus and represents the ratio of deviatoric stress to axial strain in the elastic range. This modulus is most appropriately used for evaluating the effects of dead loads placed on the system for axial strains that do not exceed the elastic range of the material. The resilient modulus represents a very low-strain elastic modulus for recoverable strains induced by repetitive cyclic loading. This is the appropriate modulus for evaluating rail deflection caused by train loadings.

The main objective of this part of the study was to determine the value of Young's modulus and the resilient modulus for the ballast material used at the Corner Canyon embankment using two different laboratory techniques. These results are compared and recommendations are made based on the strengths and limitations and cost effectiveness of the test methods.

Both monotonic and cyclic triaxial tests were carried out to bracket the potential range of field behavior of the ballast material. The monotonic and cyclic testing was conducted using large-scale triaxial and large chamber test equipment. The ballast samples for the large-scale triaxial testing were supplied by the UTA. Samples for large chamber testing were obtained from the Staker-Parson Pit located south of Herriman, Utah. The pit materials were the same as those used by UTA for the Corner Canyon site.

Drained monotonic and cyclic triaxial tests were first conducted in a large-scale triaxial setup. Subsequently, large-scale chamber tests were also performed using one-dimensional (i.e., constrained) compression, which produced estimates of the constrained modulus. This was subsequently converted to Young's and cyclic loading moduli using elastic theory.

2.2 Material Description

The particle size of the ballast material ranged from 25.4 mm to 76.2 mm. The ballast consisted of angular to subangular quartzite gravel. The large steel chamber available in the laboratory was approximately 1.064 m in diameter and 0.914 m in height. The large-scale triaxial setup had a capacity to accommodate a sample of 152 mm in diameter and 330 mm in height. Because of the large size of the steel chamber, the obtained pit material was directly used for the large chamber testing. However for the triaxial testing, the sample material had to be crushed into a particle size less than 25.4 mm. This was done because the triaxial testing procedure from ASTM (2004) requires that the largest particle size of the specimen should be smaller than 1/6 of the test chamber diameter.

2.3 Experimental Setup and Procedure

2.3.1 Large-Scale Triaxial Test

The large-scale triaxial test equipment consisted of a triaxial cell, a console, a FlowTrac^{TM} pump, a de-aired water tank and a MTS^{TM} system. The triaxial cell consisted of a triaxial base, vertical metal bars, plexiglass chamber and top cap. The console supplied pressure to the triaxial cell. The FlowTrac^{TM} pump manufactured by GeoComp Corporation of Foxborough, Massachusetts was used to supply the pressure on the sample. The triaxial cylinder was made by Research Engineering Incorporation, California. The de-aired water tank provided de-aired water to the sample. The MTS^{TM} system measured the load and displacement according to the loading protocol. The test was divided into three stages: sample preparation, sample saturation and shearing. The sample preparation and sample saturation procedure were the same for both monotonic and cyclic triaxial tests.

2.3.1.1 Sample Preparation

The test equipment was thoroughly cleaned, and the ballast material was prepared and compacted in the triaxial cell. The density of the ballast material was measured by using the volume of the specimen mold which had a diameter of 152 mm and a height of 330 mm. The specimen mold was placed on the triaxial base plate which contained attachments for three vertical metal bars. A vacuum pump was attached to the middle of the mold as shown in Figure 2.1. Two O-rings were placed on each side of the mold holding in place two sample membranes. Double membranes were used to reduce the potential for puncture. Two porous stones were boiled in water and one of them was placed onto the triaxial base plate.

Figure 2.1. Mold attached to the vacuum

The material was weighed and compacted using a tamping rod in four equal layers each with a height of 82.5 mm. Special care was taken during compaction so that the membrane was not punctured. The bulk density of the compacted specimen was calculated to be 1410 kg/m^3.

Upon compacting all the layers, at the top, saturated porous stone was placed over the sample. The metal top cap was then placed above the porous stone and leveled and adjusted. The vacuum line was then disconnected from the middle of the mold and connected to the bottom outlet valve. At this point, the metal mold was removed from the specimen and the O-rings were rearranged as shown in Figure 2.2.

Figure 2.2. Specimen after removing the mold

Silicon vacuum grease was applied on the top of all three metal rods coming out of the triaxial bottom plate. Then the O-rings were removed from both the triaxial base and top cap. Vacuum grease was also applied over the parts where O-rings had been previously placed. Then the O-rings were moved back in place. Vacuum grease was also applied to the top of the plexiglass chamber wall, and the chamber wall placed over the sample. Once the chamber wall was seated on the base, it was pushed down and slightly twisted back and forth until a good seal was obtained. The middle valve on the triaxial base was connected with a de-aired water tank and the cell was filled with de-aired water. Once the water reached the top of the specimen, it was allowed to spill out from the top port, and the cell was tipped in various directions to remove all air bubbles. The completed sample setup is shown in Figure 2.3.

Figure 2.3. Specimen setup completed and chamber fully flooded with de-aired water

2.3.1.2 Sample Saturation

The middle valve of the triaxial base was connected with the test control console to apply the cell pressure. A confining cell pressure of 34.5 kPa was selected and applied to the sample to replicate the state of stress for a shallow field burial condition of about 600 mm. The bottom valve of the triaxial base was connected to the de-aired water reservoir. Once the sample was saturated, the bottom valve was detached from the de-aired water line and was connected with the output line of the FlowTrac™ pump. The cell pressure was increased to 41.4 kPa and a back pressure of 6.9 kPa was applied from the FlowTrac™ pump. The FlowTrac™ pump and fully assembled triaxial setup placed in the MTS™ load frame for uniaxial compression testing are shown in Figure 2.4.

Figure 2.4. Triaxial setup with console and FlowTrac in MTS Machine

2.3.1.3 Uniaxial Monotonic Loading

The vertical stress was applied in a strain-controlled manner using a drained condition for the specimen chamber. The loading protocol was set with the strain rate of 1.65 mm/minute (0.5 % per minute) in the MTS™ system (Figure 2.5). Once the load was applied, this system provided output measurements of elapsed time, displacement and force. Subsequently, this information was evaluated using the area and membrane corrections discussed in ASTM (2004). The area and membrane correction equations are given in Eqs (2.1) and (2.2), respectively. The correction for area is:

$$A = A_c/(1 - \epsilon_1) \tag{2.1}$$

where A_c = average cross-sectional area and ϵ_1= axial strain for the given axial load

Figure 2.5. System to control and measure load and displacement

The correction for the rubber membrane is:

$$\Delta(\sigma_1 - \sigma_3)_m = (4E_m t_m \epsilon)/D_c \quad (2.2)$$

where $\Delta(\sigma_1 - \sigma_3)_m$ is the membrane correction to be subtracted from the measured principal stress difference, D_c is the diameter of the specimen after consolidation, E_m is Young's modulus for the membrane material, t_m is thickness of the membrane, and ϵ is the axial strain

2.3.1.4 Cyclic Triaxial Loading

Like the monotonic loading, the cyclic loading was applied under strain-controlled and drained conditions. The loading protocol was set to an amplitude of 5 mm, a frequency of 0.5 Hz and to 10000 stress cycles. The area and membrane corrections were also applied to the results of this testing.

2.3.2 Large Chamber Test

The large chamber test equipment consisted of a steel chamber, a loading actuator and an MTS system. The test procedure was divided into two stages: sample preparation and loading.

2.3.2.1 Sample Preparation

For compaction purposes, the inner sides of the large chamber were divided into five equal markings, each having a height 152.4 mm. The ballast material was shoveled into

the large chamber and compaction was made on each layer to acquire a height of 152.4 mm until all five layers had been placed and compacted. This compaction was done by using a large hand tamper to obtain a compaction state similar to that of field conditions. In compacting each layer, 75 blows were applied by the hand tamper. A head space of 152.4 mm was left at the top of the compacted specimen for seating and moving the loading ram. The process of compaction using the hand tamper is shown in Figure 2.6. The prepared specimen with the loading ram positioned for testing are shown in Figure 2.7 and Figure 2.8, respectively. The specimen bulk density was calculated from the weight of the specimen and the volume of ballast in the chamber. The initial bulk density of the compacted sample before testing was 1450 kg/m^3.

Figure 2.6. Compaction with tamper

Figure 2.7. Specimen with actuator, stress cell and LVDT

Figure 2.8. Specimen ready for testing

2.3.2.2 Loading

The chamber was connected to the MTS system and subjected to cyclic loading by an actuator with a total capacity of 267 kN. The strain or displacement controlled loading was done in two stages in order to measure the behavior at lower and higher levels of axial strain. In the first stage, cyclic testing was conducted at a maximum amplitude of 5 mm. In the second stage, a maximum amplitude of 30 mm was used during cycling. For the cyclic tests, a frequency of 0.5 Hz, 1000 number of cycles and 20 data points for each cycle were used for loading protocol. The test results around the 800^{th} cycle was considered for comparison with the results of cyclic triaxial test. The protocol was set so that it yielded time, displacement and force as output. At the end of each stage, the distance from the top of the specimen cover was measured in reference to the chamber top in order to calculate the change in volume of the specimen during testing. The bulk density at the end of each stage of test was then determined from these measurements and the initial weight of the specimen.

2.4 Monotonic and Cyclic Triaxial Test Results

The data from both the monotonic and cyclic tests were obtained in the form of time, displacement and force. The evaluation of these tests was done by plotting axial stress versus axial strain to calculate Young's modulus of elasticity and cyclic loading modulus. The axial strain was calculated from the ratio of the measured displacement to the original height of the specimen. In addition, the cross-sectional area used for the stress calculation was corrected accordingly using Eq. (2.1). The deviatoric stress was then calculated by dividing the measured force by the corrected cross-sectional area of the specimen. In addition, the membrane correction for the latex membrane was made using the relation

given in Eq. (2.2). For this, Young's modulus of elasticity of latex membrane was considered to be 1400 kPa (ASTM, 2004). Ultimately, the corrected deviatoric stress was calculated by subtracting the stress obtained from Eq. (2.2) from the uncorrected value.

2.4.1 Monotonic Triaxial Test Results

The obtained data were reduced, evaluated and plotted. In order to evaluate the elastic modulus, values of the deviatoric stress were plotted versus the corresponding axial strain. An initial seating condition was observed in the beginning of the test. A seating correction was made and the data were replotted using the adjusted deviatoric stress (Figure 2.9). The slope of initial linear portion of this curve was used to estimate Young's modulus of elasticity which was found to be 52000 kPa. This value is within the upper range of values reported by Anderson and Fair (2008) of 30000 to 60000 kPa for stone-ballast materials.

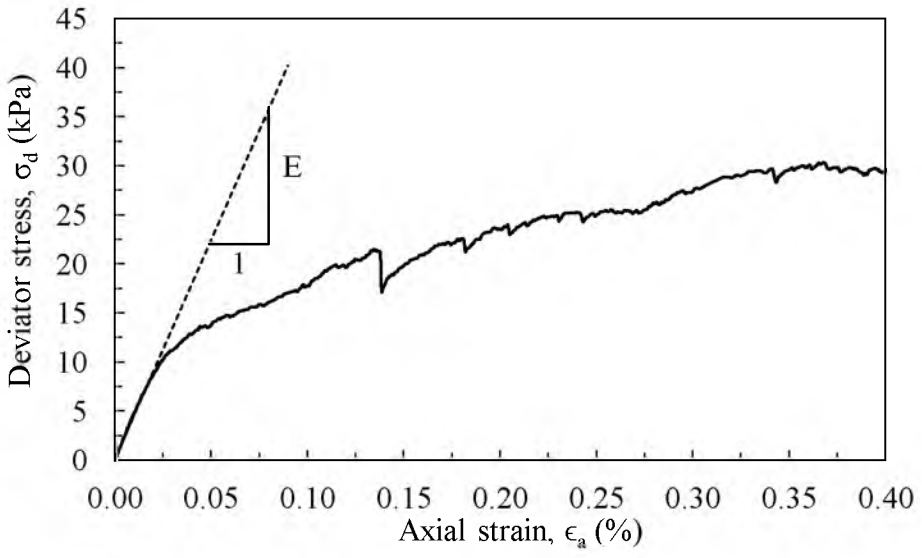

Figure 2.9. Stress-strain behavior of ballast under the monotonic loading in triaxial test

2.4.2 Cyclic Triaxial Test Results

Similarly, the cyclic deviatoric stress and cyclic axial strain were calculated from the displacement and force data. The triaxial test result for 10000 numbers of cycles is shown in Figure 2.10. The test was conducted at low level of amplitude and low level of confinement because average dynamic deflection was found in the range of 1 mm to 5 mm in most of the cases under the traffic load (Bowness et al., 2007) and the ballast in the field was at shallow depth. The test results showed the behavior of stress-strain relation during loading and unloading to be nonlinear. The shape of the curve for loading and unloading was found to be different.

The deviatoric stress versus cyclic axial strain at third cycle and eight hundredth cycle is shown in Figure 2.11. The stress-strain relation of third cycle and eight hundredth cycle were polynomial of third order and fifth order, respectively. The nonlinear behavior during loading might be due to the very low level of confinement. The modulus obtained during loading was named as cyclic nonlinear modulus hereafter. The cyclic nonlinear modulus is strain dependent. The tangent modulus varied throughout a cycle of loading along the hysteresis loop. In most of the cases it is possible to calculate the average modulus over the entire loop which is defined by secant modulus. However, it is difficult to calculate the secant modulus for this cyclic triaxial test due to the large variation of axial strain.

2.5 Large Chamber Test Results

One dimension consolidation test under cyclic testing in large chamber provides data related to time, displacement and force. The result of cyclic loading in a large chamber test is shown in Figure 2.12.

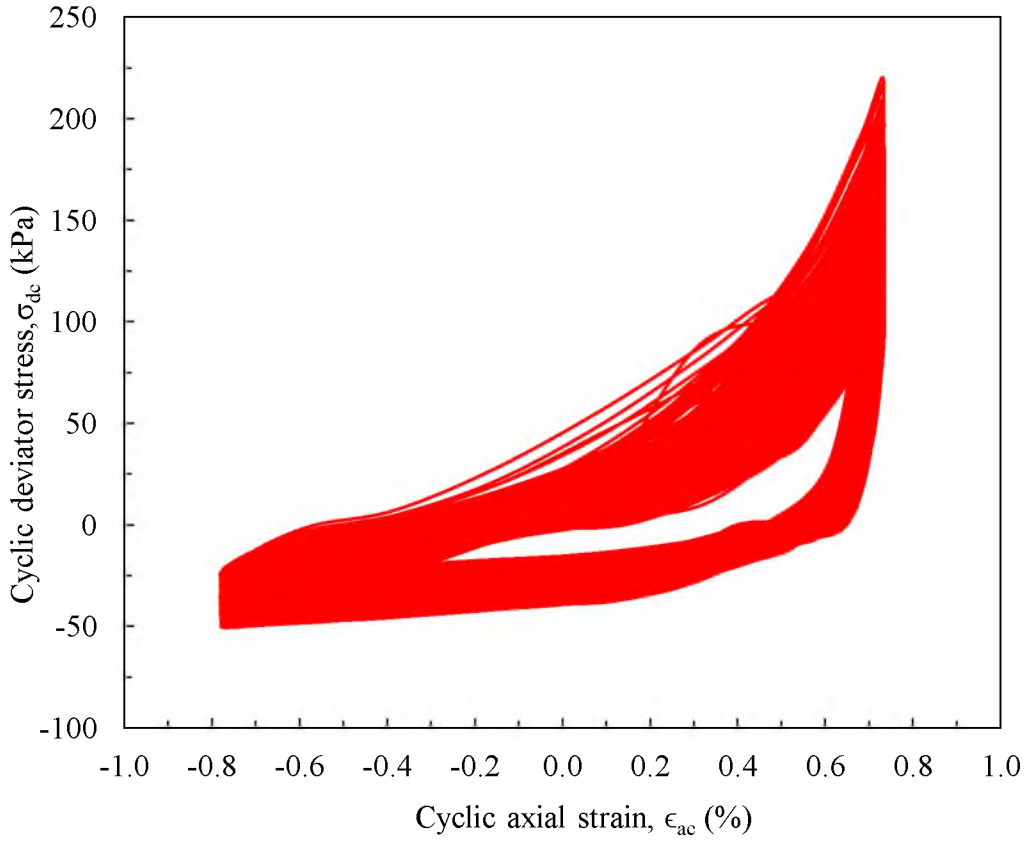

Figure 2.10. Cyclic triaxial test results on ballast at 10000 cycles

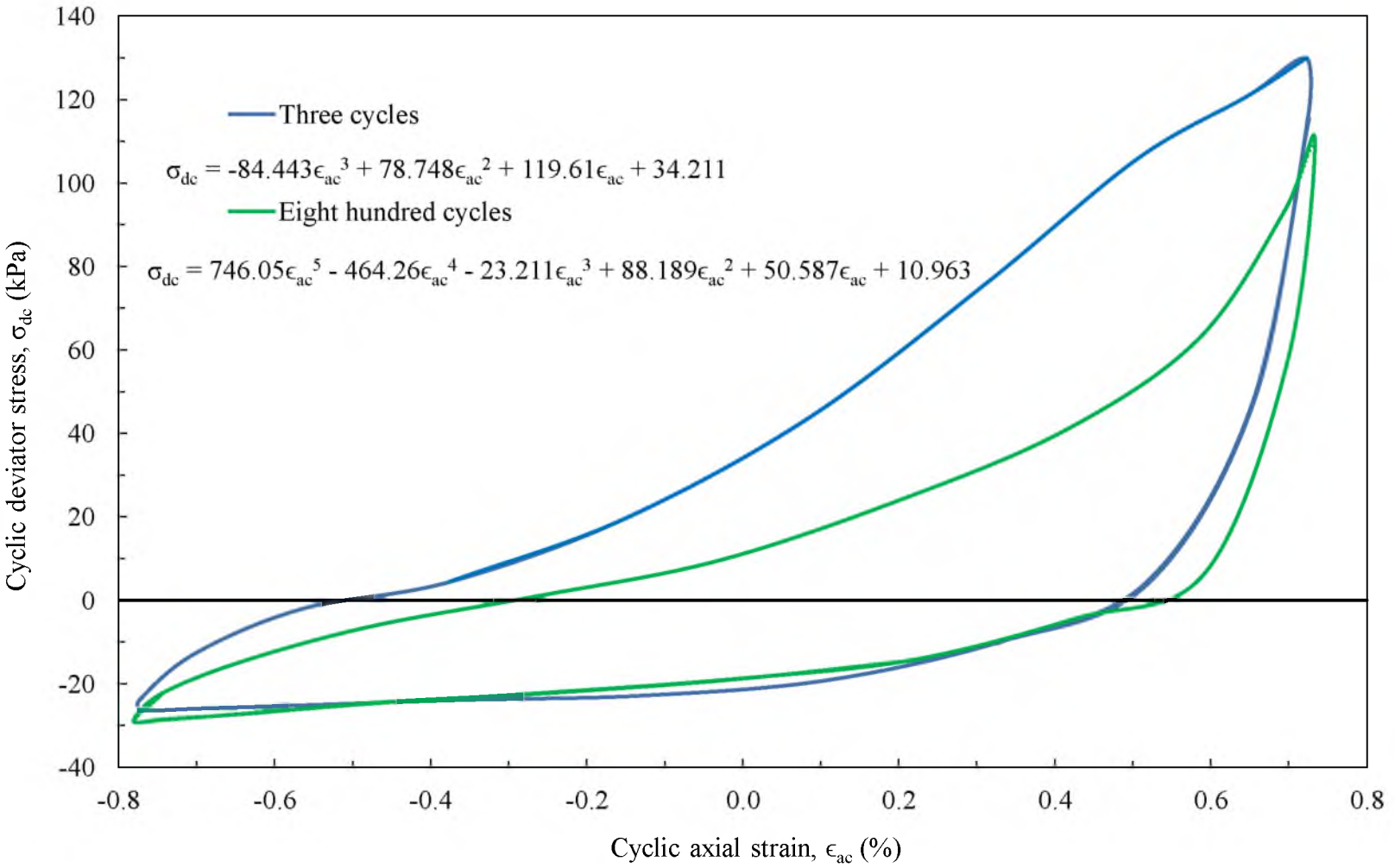

Figure 2.11. Cyclic nonlinear modulus in large triaxial test

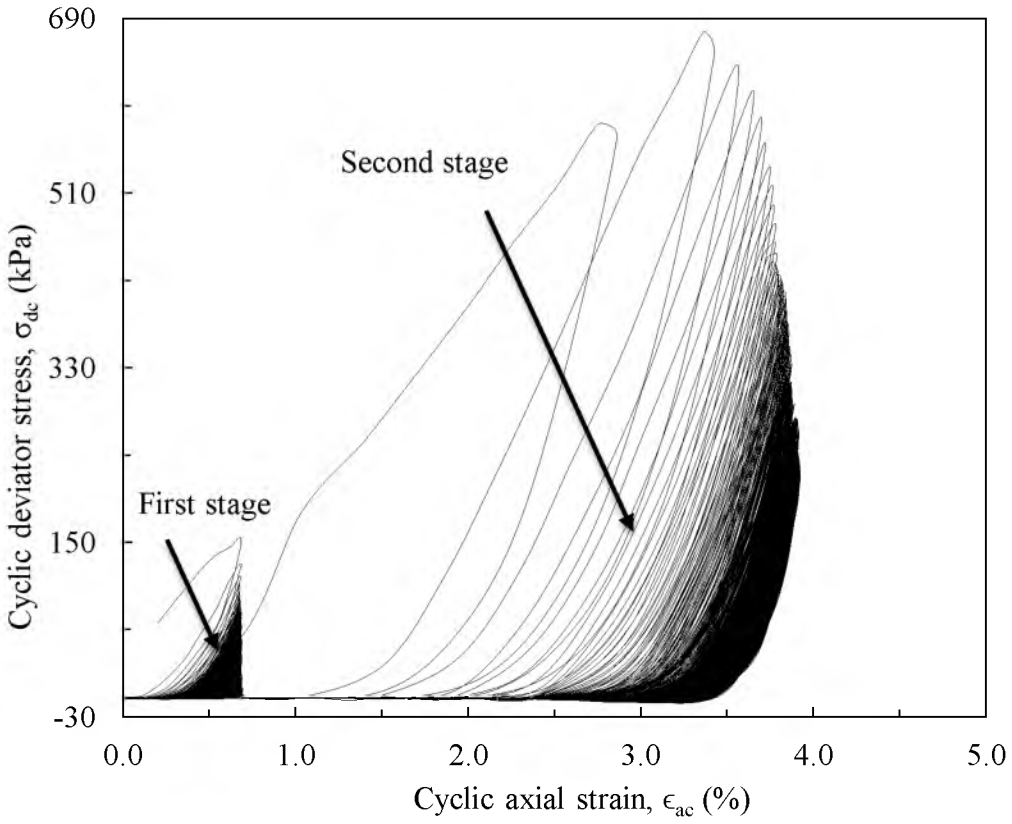

Figure 2.12. Cyclic tests on ballast in large chamber tests at two amplitudes

In Figure 2.12, the stress-strain behavior of the first and second stage of cyclic loading is shown. The cyclic tests results were included to measure the Young's modulus but the monotonic test results from the large chamber were not included because the modulus at low amplitude cyclic test is more representative of Young's modulus.

The large chamber cyclic test results showed the stress-strain behavior is still nonlinear at low amplitude and stress-strain curves for loading and unloading are close to symmetrical. The average cyclic nonlinear secant modulus of loading and unloading can be determined from the stress-strain relationship at small range of strain. The average modulus is similar to the constrained modulus. This modulus was not at a very low level of strain and therefore cannot represent the true resilient modulus. The cyclic nonlinear

modulus was then determined using Eq.(2.3) (Fang, 1990).

$$M = \frac{E(1-\nu)}{(1+\nu)(1-2\nu)} \tag{2.3}$$

where M = Constrained modulus, E = Young's modulus and ν = Poisson's ratio.

The results from the large chamber test for first stage at the start and at the end of test are shown in Figure 2.13 and Figure 2.14. The results of large chamber tests for the second stages are shown in Figure 2.15 and Figure 2.16, respectively. An average value of 32000 kPa and 65000 kPa of constrained modulus were obtained from the cyclic test on the large chamber at low and high amplitude, respectively, during loading and unloading.

The Poisson's ratio of ballast material can be determined from the recorded data in Flow Trac™ during large scale triaxial test. But in this test, the recorded volume data in the Flow Trac were not consistent during the test and therefore were not considered for the calculation of Poisson's ratio. So, the Poisson's ratio of ballast material was assumed to be 0.3 based on Li et al. (2008). The average value of cyclic nonlinear moduli during loading and unloading were 24000 kPa and 48000 kPa, respectively. The densities for first and second stages were found to be 1500 kg/m^3 and 1600 kg/m^3. The cyclic modulus in the second stage was higher due to the compaction of material. Similar findings were observed in Suiker et al. (2005). In the second stage, the amplitude (y) was almost six times larger than the first stage that might have produced such large compaction. Table 2.1 and Figure 2.17 provide the density and cyclic nonlinear modulus at different levels of amplitudes. It revealed that density and modulus both increased with increase in amplitudes.

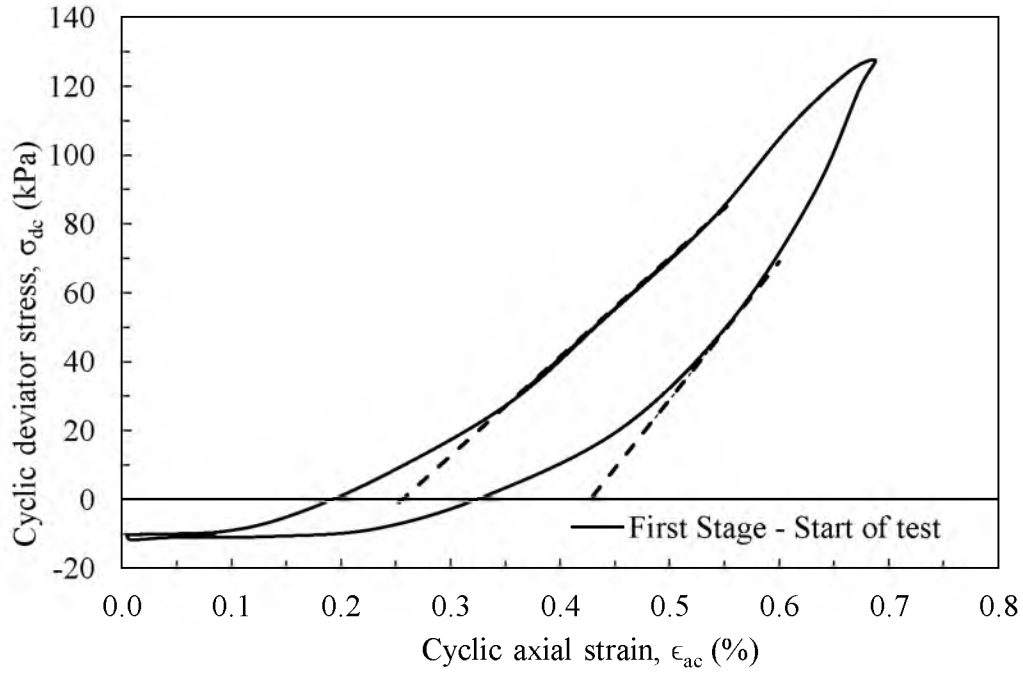

Figure 2.13. Cyclic nonlinear secant modulus at beginning of test for first stage

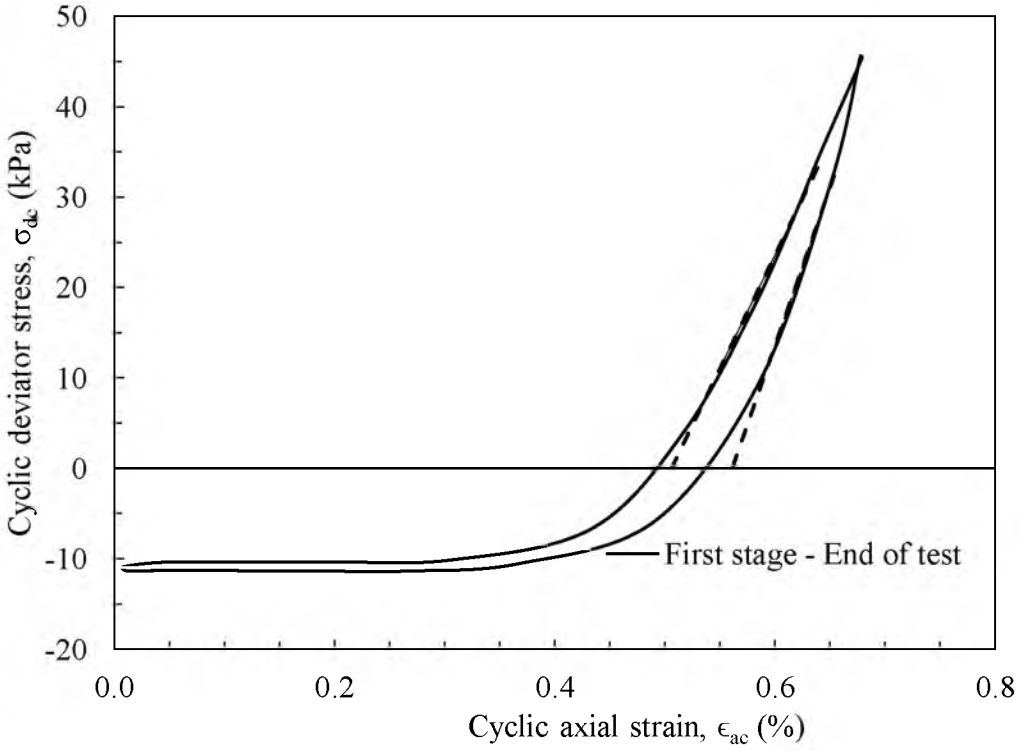

Figure 2.14. Cyclic nonlinear secant modulus at the end of test for first stage

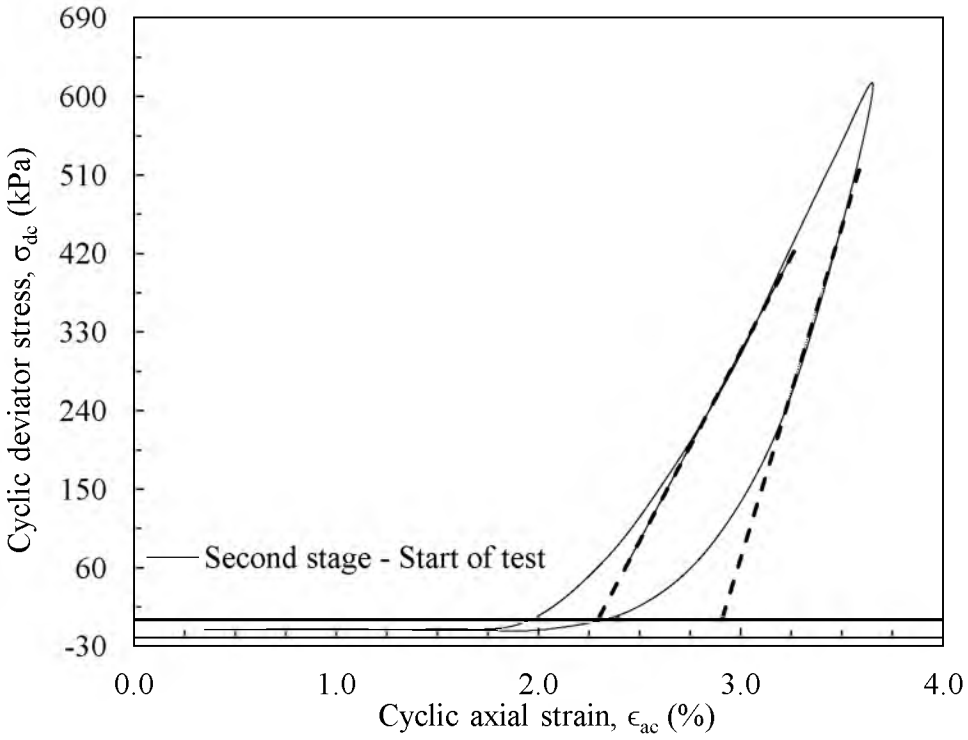

Figure 2.15. Cyclic nonlinear secant modulus at beginning of test for second stage

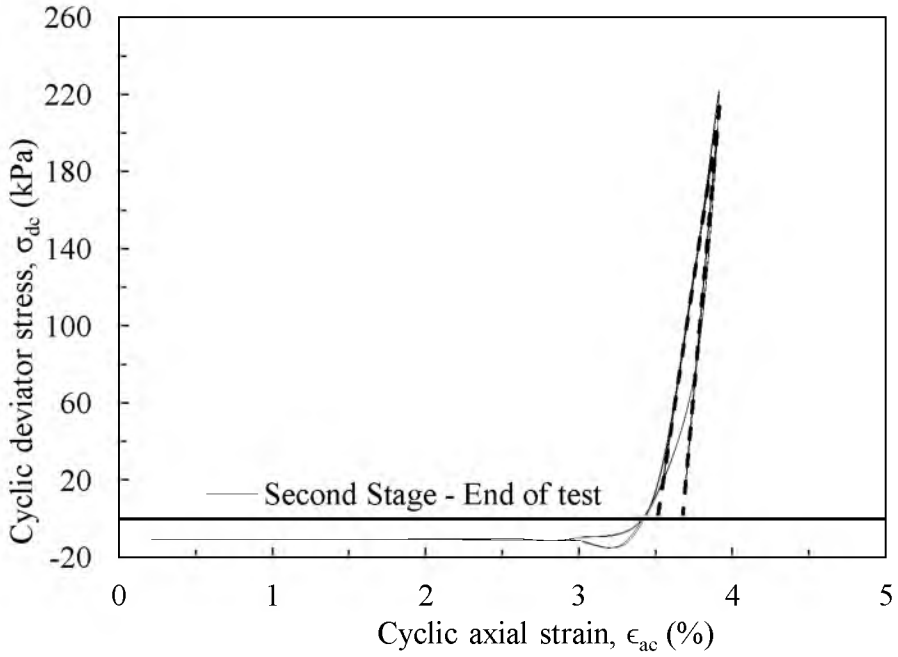

Figure 2.16. Cyclic nonlinear secant modulus at end of test for second stage

Table 2.1. Density and cyclic nonlinear secant modulus at different stages of loading

Stages ----------	Amplitude *(mm)*	Density *(Kg/m^3)*	Cyclic nonlinear secant modulus *(kPa)*
First	5	1500	24000
Second	30	1600	48000

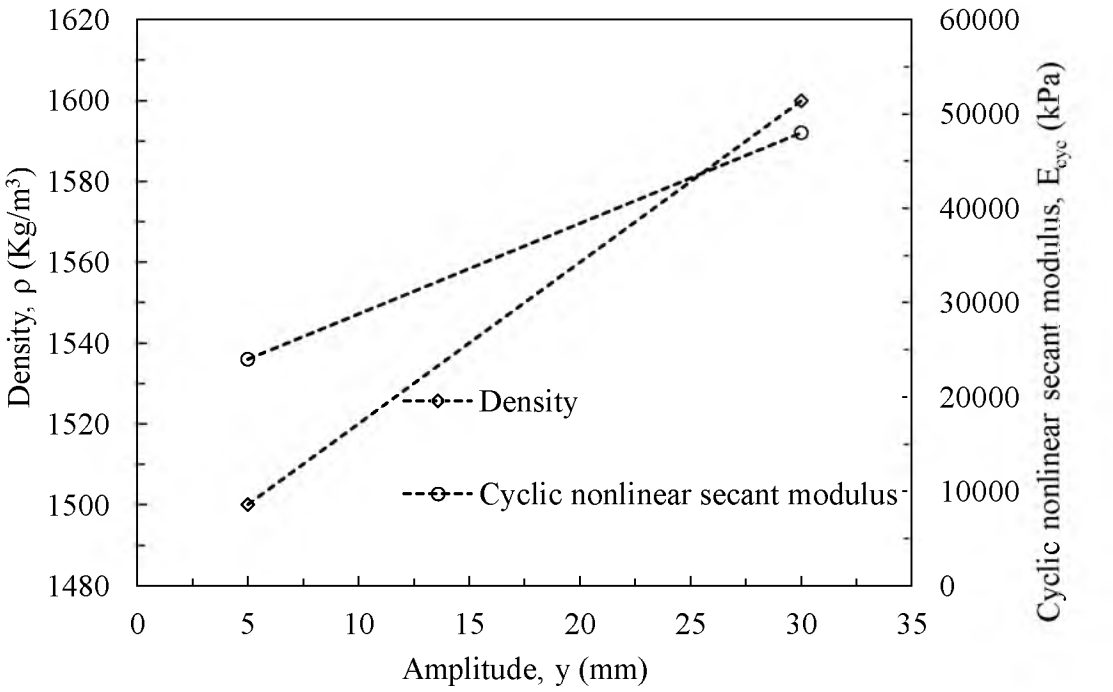

Figure 2.17. Density and cyclic nonlinear modulus at two levels of amplitude

2.6 Comparison of Moduli

Cyclic triaxial test is a more representative test in most of the cases but requires lot of effort for sample preparation. However, during this study the stress-strain behavior for loading and unloading was found to be quite different and therefore moduli within the small strain could not be calculated. In this test, the compaction was done by tamping which was different from the vibro-compaction in the field. The compaction by tamping was difficult due to flexible boundary condition. The cyclic loading was applied at a very low level of confinement. The compaction and confinement may have yielded highly nonlinear stress-strain behavior during loading.

In case of low confinement, a large chamber test could be a good alternative to large scale triaxial tests as it can be conducted with relatively less effort and would yield better stress-strain behavior. In this study, the cyclic nonlinear secant modulus at low level of amplitude was found to be 24000 kPa in large chamber tests. This value cannot represent true resilient modulus because the amplitude during cyclic loading was not small enough to produce low strain moduli. The ballast material is usually compacted in the field by using vibro-compaction while in case of laboratory tests, a different method of compaction (tamping) was used. Even if the test did not produce true resilient moduli, the modulus obtained from the large chamber test was more representative than that obtained from large scale cyclic triaxial tests for cyclic loading produced by passing trains.

2.7 Conclusions

Monotonic and cyclic triaxial tests on large scale triaxial and cyclic tests at low and high amplitudes on large chamber were conducted in the laboratory to determine the

Young's modulus of elasticity and cyclic nonlinear secant modulus of ballast material that has been used in railway track of FrontRunner commuter rail system in Draper City of Utah. The monotonic triaxial test results revealed that the Young's modulus of elasticity was 52000 kPa at very low confining pressure.

The cyclic nonlinear secant modulus at low amplitude (5 mm) was found to be 24000 kPa in large chamber tests. The stress-strain relation for loading and unloading in a large chamber test is more symmetrical in comparison to the large scale cyclic triaxial test. The modulus obtained from the large chamber test was referred to as cyclic nonlinear secant modulus. The cyclic nonlinear secant modulus doubled when the amplitude was increased by 6 times in the large chamber test. In the test, the material could have been compacted due to the higher amplitude of loadings. The increased in stiffness of material was also reported by Suiker et al. (2005) during cyclic loading. The compaction might have increased the density of material. The increased in density implies the increase in cyclic nonlinear modulus of material. The Young's modulus and cyclic nonlinear secant modulus obtained from these tests can be used for determining the static and dynamic deflection by using numerical technique. The modulus obtained from the large chamber test was more representative of cyclic loading produced by passing trains. The large chamber test itself is less time consuming and cost effective in comparison to triaxial test.

2.8 References

Anderson, W. F., and Fair, P. (2008). "Behavior of railroad ballast under monotonic and cyclic loading." *Journal of Geotechnical and Geoenvironmental Engineering*, 134(3), 316-327.

ASTM D4767 (2004). *Standard test method for consolidated undrained triaxial compression test for cohesive soils*, American Society for Testing and Materials, West Conshohocken, PA, USA.

Bowness, D., Lock, A., Powrie, W., Priest, J., and Richards, D. "Monitoring the dynamic displacements of railway track." *Proc., Institution of Mechanical Engineers, Part F: Journal of Rail and Rapid Transit*, 13-22.

Fang, H. Y. (1990). *Foundation engineering handbook*, Springer, New York, USA.

Ho, S., Tsang, W., Lee, K., Lee, K., Lai, W., Tam, H., and Ho, T. "Monitoring of the vertical movements of rail sleepers with the passage of trains." *Proc., Institution of Engineering and Technology International Conference on Railway Condition Monitoring, 2006*, IEEE, 108-114.

Li, G.-X., Chen, Y.-M., and Tang, X.-W. "Geosynthetics in civil and environmental engineering." *Proc., Geosynthetics Asia 2008 Proceedings of the 4th Asian Regional Conference on Geosynthetics in Shanghai, China, Zhejiang University Press, Hangzhou and Springer-Verlag GmbH Berlin*.

Li, S. (2014). "Evaluation and numerical modeling of deflection and vertical displacement of rail systems supported by EPS geofoam embankments." MS thesis, The University of Utah, Utah, USA.

Lu, S. (2008). "Real-time vertical track deflection measurement system." Ph.D. thesis, University of Nebraska, Lincoln, Nebraska, USA.

Ping, W. V., Yang, Z., and Gao, Z. (2002). "Field and laboratory determination of granular subgrade moduli." *Journal of Performance of Constructed Facilities*, 16(4), 149-159.

Pinto, N., Ribeiro, C., Mendes, J., and Calçada, R. (2009). "An optical system for monitoring the vertical displacements of the track in high speed railways." *Proc., 3rd International Integrity Reliability and Failure,* Portugal, 1-9.

Psimoulis, P. A., and Stiros, S. C. (2013). "Measuring deflections of a short-span railway bridge using a robotic total station." *Journal of Bridge Engineering*, 18(2), 182-185.

Sevi, A., and Ge, L. (2011). "Cyclic behaviors of railroad ballast within the parallel gradation scaling framework." *Journal of Materials in Civil Engineering*, 24(7), 797-804.

Suiker, A. S., Selig, E. T., and Frenkel, R. (2005). "Static and cyclic triaxial testing of ballast and subballast." *Journal of Geotechnical and Geoenvironmental Engineering*, 131(6), 771-782.

CHAPTER 3

DYNAMIC DEFLECTION MONITORING OF EPS EMBANKMENT TO SUPPORT RAILWAY SYSTEM

3.1 Introduction

The amount of deflection of the rail caused by the passing of a locomotive or rail car is a significant safety issue for rail system operations. Large deflections could pose the risk of possible derailment, especially at higher speeds of operation. Dynamic rail deflections can occur on all types of embankment support systems.

The amount of deflection can be measured by using direct or indirect methods. For direct methods, measurement is usually done by via survey equipment, lasers, or other optical equipment (e.g., high-speed cameras) deployed in the field. When optical techniques are used, optical equipment is used to obtain images, and those images are subsequently processed to determine relative displacement. For indirect methods, the amount deflection is measured either by instrumentation and numerical interpretation. The most common indirect method involves the installation of accelerometers or geophones at the site. These sensors can provide time history data of acceleration or velocity. This information can be integrated to provide estimates of displacement of the rail versus time.

The use of optical techniques to measure the dynamic deflection on rails and rail ties (i.e., sleepers) that sit atop the embankment made from conventional materials has been carried out by several researchers (Ho et al., 2006; Bowness et al., 2007; Lu, 2008; Pinto et al., 2009; Psimoulis and Stiros, 2013). The videography and image processing techniques were used to monitor the vertical displacements of rail sleepers with the passage of trains by Ho et al. (2006). Bowness et al. (2007) monitored the dynamic displacement of railway track using remote video monitoring system. Lu (2008) developed a system to measure track deflection from a moving railcar. The system was comprised of a loaded hopper car fitted with a camera/lesser sensor system which detected the vertical deflection of the rail relative to the wheel/rail contact point. Pinto et al. (2009) used an optical system for monitoring the vertical displacements of the track in high speed railways. The system was based on a diode laser module mounted away from the track. Psimoulis and Stiros (2013) measured the deflection of a short-span railway bridge using a robotic total station (RTS).

The use of indirect methods to measure the dynamic deflection in the field has been carried out by several researchers (Madshus and Kaynia, 2000; Bowness et al., 2007; Chebli et al., 2008; Priest and Powrie, 2009; Ling et al., 2010). Madshus and Kaynia (2000) studied the motions of the track and embankment by installing the accelerometers in the field. In this study the displacement was calculated and the results were compared with numerical simulation. Bowness et al. (2007) monitored the dynamic deflection of railway tracks by placing the geophones on the sleepers. The field test results were then compared with the results obtained from an optical target method. Chebli et al. (2008) studied the dynamic response of high-speed ballasted railway tracks using a three-

dimensional (3D) periodic model and in-situ measurement. As an in-situ measurement, accelerometers were installed at various locations to measure the vertical acceleration and displacement. In this method, the accelerometers were placed on the sleepers. The in-situ measurement results were then compared with the results obtained from a 3D periodic model. Priest and Powrie (2009) evaluated the dynamic track modulus by measuring track velocity during train passage. In this method, geophones were attached to the sleeper outside the rail. Dynamic displacement was calculated from the measured velocity. Ling et al. (2010) studied train induced vibration response characteristics and dynamic stability of track structures by installing accelerometers on sleepers, rail and embankment slopes.

The use of EPS geofoam for railway embankments has not been studied to any great extent. Frydenlund et al. (1987) reported the use of EPS block in the abutment to support a railway bridge in Norway. The deflection was measured on the sleepers. The maximum deflection was found to be around 7 mm. O'Brien (2001) described the innovative solution for the replacement of an old railway bridge by using EPS geofoam embankment in the United Kingdom (UK). From this study, one can understand the potential of using EPS geofoam as a lightweight fill material for railway embankments for short term and long term purposes. So far, there are very few studies focusing exclusively on vertical deflection monitoring of EPS embankment to support a railway system.

In the United States, EPS geofoam was recently incorporated into portions of the commuter and light rail systems in Salt Lake City, Utah by the Utah Transit Authority (UTA). The FrontRunner commuter rail south line extends from Salt Lake City to Provo, Utah. Along this line at Corner Canyon in Draper City, EPS has been used in the

embankment in order to minimize the stress over a reinforced concrete box culvert. This location has both EPS geofoam and adjacent earthen embankment. Similarly, the light rail line (Green Line) extends from West Valley Central to Salt Lake City International Airport. In this line, EPS has been used in the embankment near Roper Yard, which is operated by the Union Pacific Railroad. These two sites were selected to monitor the dynamic deflections of EPS geofoam embankment.

The monitoring of the amount of vertical dynamic deflection of the rail (i.e., deflection due to passage of a train) is necessary in order to find the amount of deflection. The monitoring of deflection is important because more than acceptable deflection could pose potential safety issues. There are no guidelines regarding the acceptable level of deflection occurring in EPS embankment to support railway system. This study would yield data on deflection occurring in both EPS and earthen embankment. The comparison of amount of deflection could give an idea of how much deflection would occur in EPS embankment in comparison to the earthen embankment. This study could provide a basis for understanding the typical levels of vertical deflection that develop in these somewhat unique systems.

The main objectives of the study were to: (1) develop an optical technique to measure the dynamic vertical deflection, (2) evaluate the performance of the developed optical technique, (3) measure the vertical deflection during passage of trains using accelerometers and (4) compare the results of vertical deflection of EPS embankment with those of the earthen embankment.

In order to measure dynamic vertical deflection in field setting, accelerometers were glued onto sleepers. The data obtained from the accelerometers were converted into

displacement time history and the amount of vertical deflection was determined by using the commercially available software SeismoSignal.

3.2 Field Description

The FrontRunner commuter rail system in the Corner Canyon area in Draper City, Utah has rail embankment constructed of both EPS geofoam and conventional fill materials. The site is shown in Figure 3.1. This system consists of (from top to bottom): steel rail, ballast, sub-ballast, concrete reinforcing slab, EPS geofoam and sand. The slope of an embankment is 2H:1V. The cross-section of an embankment is shown in Figure 3.2. Similarly, a photo of the EPS embankment used to support light rail along the Green Line near Roper Yard is shown in Figure 3.3.

Figure 3.1. Embankment with EPS geofoam and conventional fill materials in Draper city of Utah along the FrontRunner line

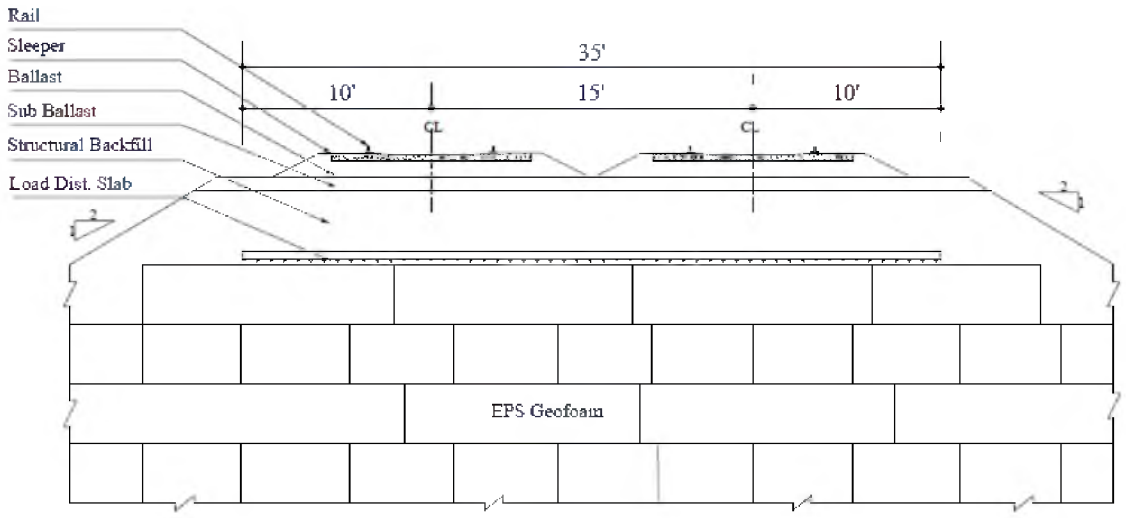

Figure 3.2. Cross-section of an EPS geofoam embankment at corner canyon of Draper City of Utah

Figure 3.3. EPS embankment to support light rail along the Green Line near Roper Yard of Utah

3.3 Equipment and Methods

3.3.1 Dynamic Deflection Monitoring

In the study, an optical target technique was developed for measuring the dynamic deflection of the rail, but this techniques was not deployed in the field due to poor weather conditions (high winds). However, an accelerometer array was installed in the field and the data from these were interpreted to provide estimates of rail deflections.

3.3.1.1 Development of Optical Technique

In this method, a paper target (Figure 3.4) was developed and used for laboratory testing of the system and optical interpretation. The target was attached to a wooden frame and kept on the MTS machine as shown.

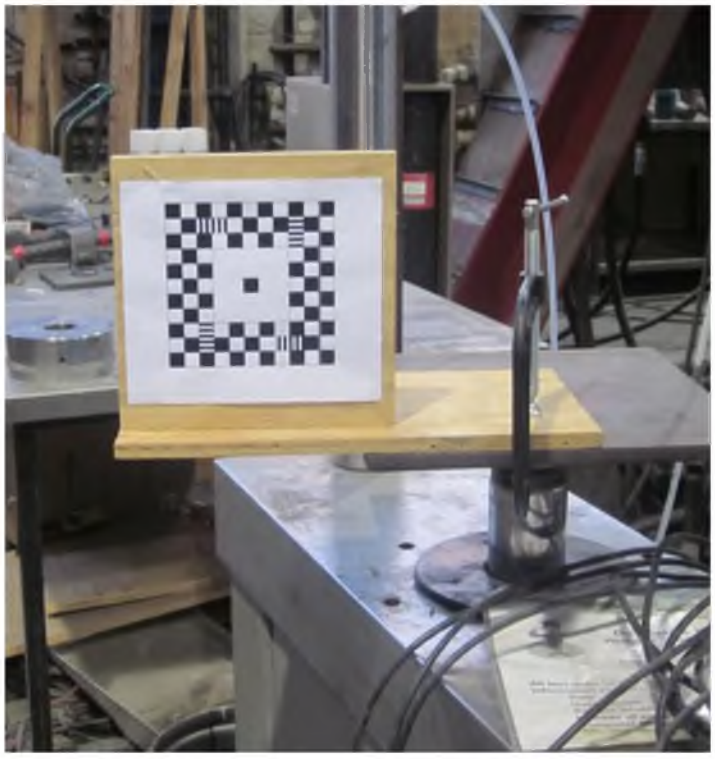

Figure 3.4. Target setup on MTS machine

The MTS machine has an actuator that can be controlled to produce a systematic and controlled vertical displacement. A LVDT was used to measure the linear displacement versus time. A loading protocol was set up in the MTS machine for cyclic loading of a frequency 0.5 Hz and peak to peak amplitude of 7 mm. The protocol was written to yield time and displacement as output.

Bowness et al. (2007) considered the minimum distance between target and camera to be 10 m in order to minimize the effects of train vibration on the camera. This recommendation was used for this study, where video was recorded by setting a Go-Pro^{TM} camera and telescope at a 10 m distance from the target as shown in Figure 3.5. The Go-Pro^{TM} camera was able to take pictures and videos at a rate of 120 frames per second, and had a Wi-Fi system which could be connected to another electronic device to display the target. The target was made with black and white squares in order to make analysis easier. After recording the video, an image processing technique was employed to find the vertical deflection.

Figure 3.5. Camera-telescope setup for video recording

In the method, the video recordings were converted into several still frames. The first frame was taken as the base image. The center of the target was determined in terms of pixel number for each frames. The displaced position of center of the target in the vertical direction was determined in terms of pixels and was converted into linear distance.

For the analysis, an algorithm was developed in MATLAB. The algorithm is given in Appendix A. In this process, all images were uploaded initially. The central black square box of the target was chosen as the region of interest. The region was selected to make sure that the total displacement of the square still remains within the peripheral white region. A matrix was created with zeros in all rows and columns. The region of interest was then replaced by the matrix with zero values. Therefore, this region became completely different from the peripheral zones. A histogram was made for the linearly spaced vectors, which were prepared from a one-dimensional (1D) matrix. The 1D matrix was obtained from the rows and columns of the selected region. The threshold value of the pixels in the region was then determined. Values smaller than threshold were made zero. Similarly, values greater than threshold were set equal to one.

The total number of rows where the values were nonzero represented the length of the square. Thus, the total number of pixels along the length of one small square was determined. The identity of the center region was then determined in terms of its pixel number. The pixel numbers for the center region of subsequent images were determined in similar manner. Once the minimum pixel numbers were determined, then each pixel number was subtracted from this. (The pixel numbers represented the distance in terms of the number of pixels from the minimum value.) A linear scale was used to measure the side of the big square. The total number of pixels at one side of the big square were also

calculated. A conversion factor was determined for converting pixels into corresponding linear displacement. The time was calculated by dividing the frames to the number of frames in one second. For example, if there were 200 frames in 10 seconds then the 20 frames were obtained in 1 second. From this, a plot was made between displacement and time. The total displacement was then determined from the plot. The displacement versus time from both optical techniques and data extracted from MTS machine was plotted on the same graph for comparison (Figure 3.6).

After laboratory verification, a similar instrument was developed for field implementation. At the Corner Canyon embankment site, there is no level ground around for a distance of 10 m from the target on the rail to where the embankment slope begins. The embankment slopes away from the rail on a 2H:1V side slope.

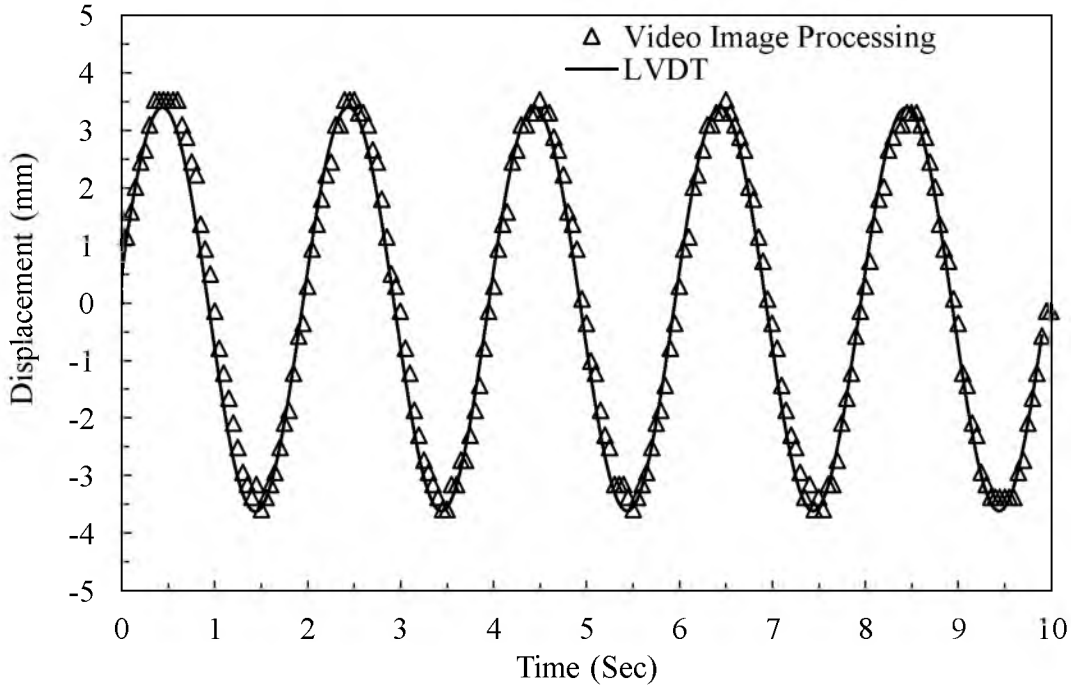

Figure 3.6. Comparison of displacement obtained from image processing in optical technique and LVDT measurement in MTS machine

Therefore in order to measure the deflection on sloped ground, a modification of the setup was introduced. A telescoping rod was fixed on a survey tripod, and the telescope with a Go-Pro™ camera was mounted at the top of the rod. The rod and camera attached were able to rotate (Figure 3.7). The target could be seen using a Wi-Fi device such as smart phone or tablet using the Wi-Fi system of the Go-Pro™ camera. Unfortunately, however, this technique proved to be very sensitive to vibration for wind and other ambient sources.

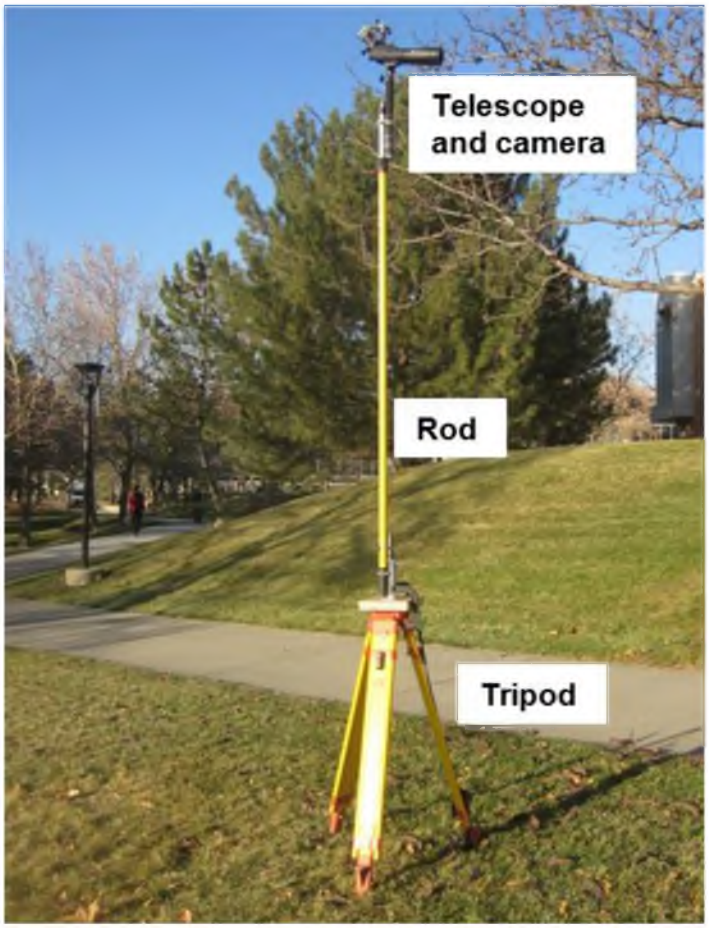

Figure 3.7. Optical technique instrument setup for field measurement of vertical deflection

3.3.1.2 Accelerometers for Dynamic Deflection Monitoring

Five accelerometers of model 4630A manufactured by Measurement Specialties Inc., California (Figure 3.8) were used in the sites for deflection monitoring. The triaxial accelerometers were cubical in shape with dimension of 25.4 mm. The dynamic range of the accelerometers was $\pm 2g$ to $\pm 100g$ with an operating temperature of -55^{0}c to 125^{0}c (Measurement-Specialities, 2015). Data from the accelerometers were collected at a sampling interval of 1 x 10^{-3} sec (1000 Hz). The accelerometers were glued on the concrete tie (i.e., sleeper) to measure the deflection. Figure 3.9 shows the orientation of the accelerometer on the sleeper. As shown in Figure 3.9, the Z axis was oriented along the vertical direction, the Y axis was parallel to the rail and the X axis was perpendicular to the rail. The spacing between the accelerometers were installed using the live load configuration provided by American Railway Engineering and Maintenance-of-Way Association (AREMA) manual (AREMA, 2007) for the train locomotive (Figure 3.10).

Figure 3.8. Model 4630A accelerometer

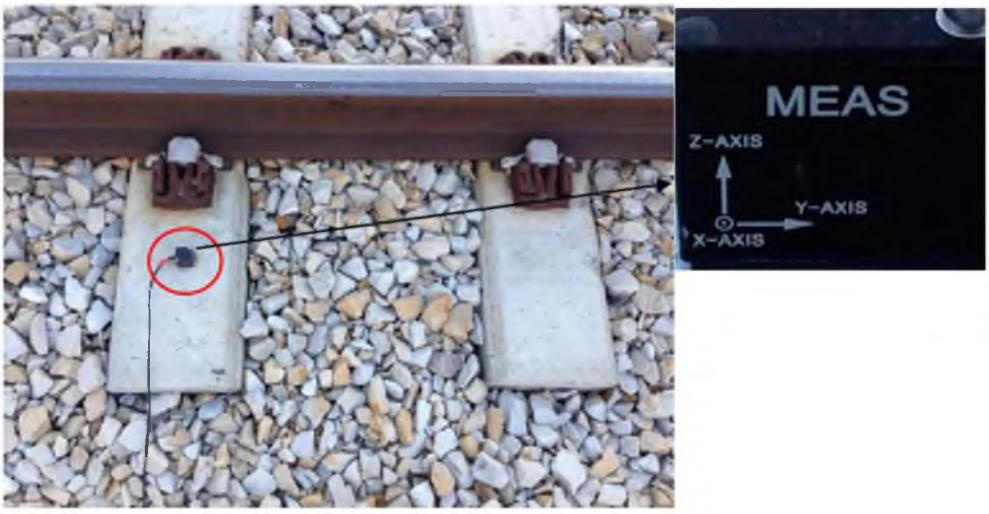

Figure 3.9. Accelerometer glued on sleeper with its orientation

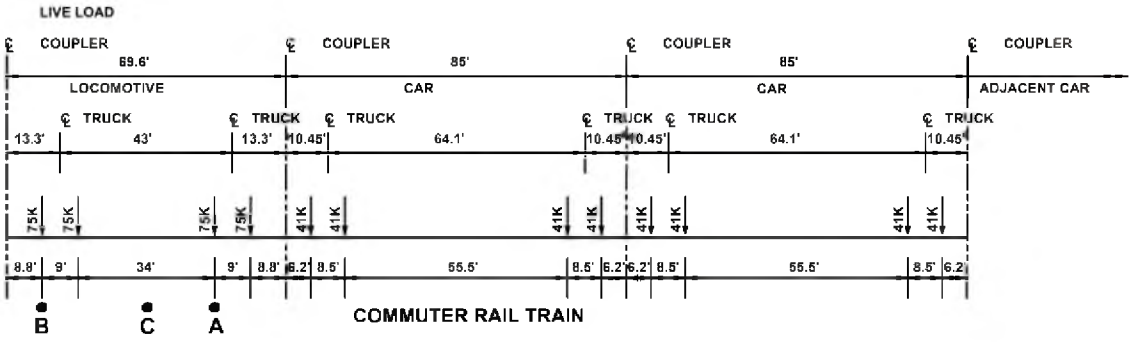

Figure 3.10. Axial load configurations for locomotive and cars with position of accelerometers at A, B and C (AREMA, 2007) for FrontRunner

In Figure 3.10, the letters A, B and C denote the position of the accelerometers. The maximum axle load was exerted by a locomotive is 75 K (kips). The configuration of accelerometers was chosen in such a way that the maximum load could be recorded by the sensors. Similarly, Figure 3.11 shows the positioning of accelerometers at A, B and C in the sleepers along the light rail line. A similar orientation and positioning was used for the light rail measurements.

Figure 3.11. Accelerometers positions at A, B and C along the light rail line

The FrontRunner train had three double decker passenger cars, one single decker car and a locomotive as shown in Figure 3.12 (locomotive is shown at far left of photo). The train is southbound in this case and is enroute to Provo, Utah. The light train had two cars as shown in Figure 3.13.

Two accelerometers were glued at positions A and B where the maximum axle load would be exerted on the sleeper. A third accelerometer was glued at position C which lied in between A and B. The accelerometers were then connected to the data logger to extract data. The data logger to be used in the instrumentation was CR9000X is shown in Figure 3.14. The basic CR9000X system consists of CR9011 power supply module, a CR9032 CPU module and CR9052DC Anti-Alias Filter Module with DC Excitation. The filter module connector has a number of channels. Each input channel consists of both regulated constant voltage excitation (VEX) and regulated constant current excitation (IEX) channels.

Figure 3.12. Front runner heading south on the route with three double deck cars, one single deck car and a locomotive

Figure 3.13. Light rail heading towards the West Valley Central with two passenger cars

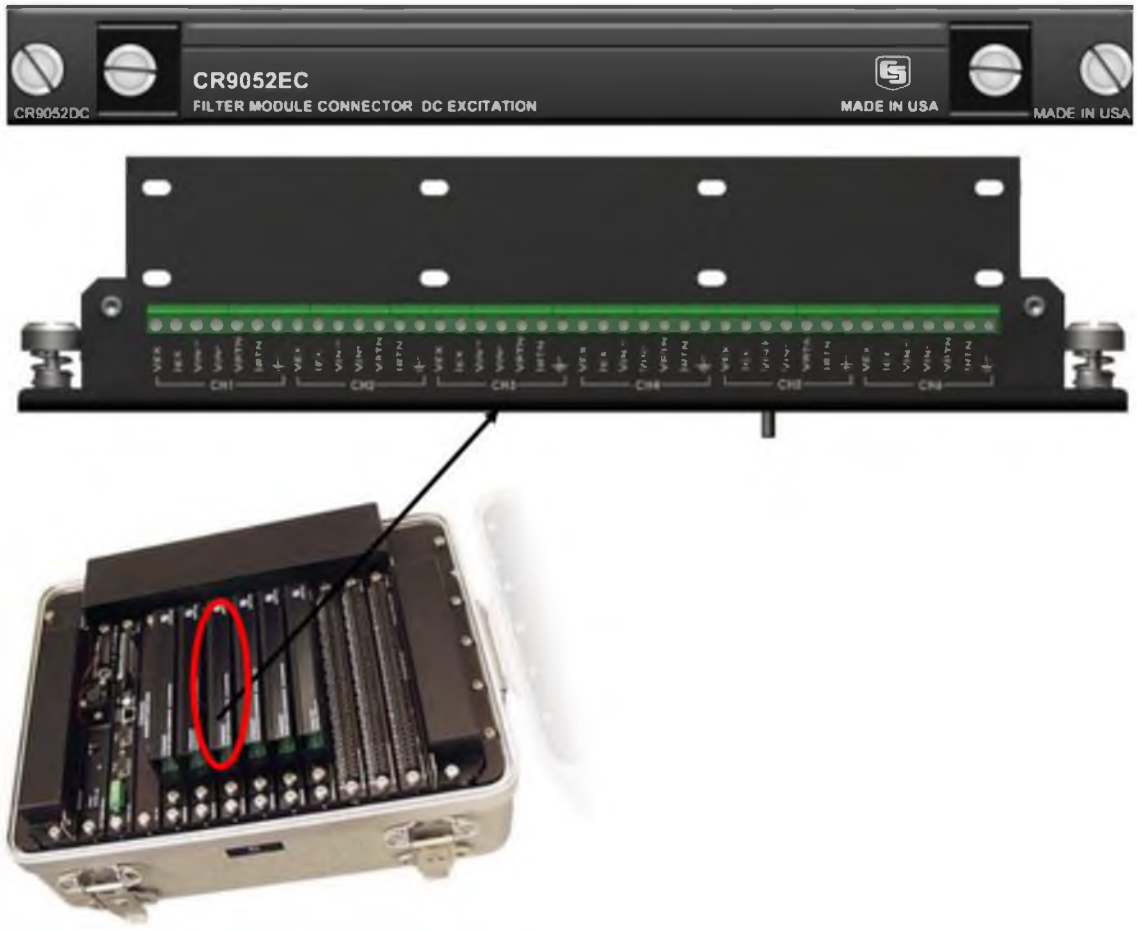

Figure 3.14. CR9000X measurement and control system with CR9052DC Anti-Alias filter modulus and DC excitation

There are five ports for excitation with high voltage input, low voltage input, return and ground. Each accelerometer has five colored wires, namely, red, green, white, black and silver which were connected to the five ports on data loggers: excitation (VEX or IEX), high side of the differential voltage input (VIN+), low side of the differential voltage input (VIN-), return (VRTN or IRTN) and ground, respectively.

The Real-time Data Acquisition, RTDAQ™ (RTDAQ, 2011) software was used for the collection of data and was connected to the USB serial port. In RTDAQ, there are three tabs for operation: clock/program, monitor data and collect data. The recorded time

in the data logger and pc was synchronized by using the update and check button. The monitor data tab is important for the collection of data. It consists of a ports and flags window. In this window, the flag should be turned on during collection of data. The green light on the flag denotes the flag is turned on. Once the train approached the embankment, the flag was turned on. Shortly after the train passed through the embankment array, this flag was turned off.

The data between time of flag being turned on and being turned off were recorded. The collection data tab was used for data collection. In this tab, there are three collection options: collect mode, file mode and file format. All the data options were used in the collect mode. In the file mode and file format, append to end of file and ASCII table data were selected. The start collection tab was used for the collection of data.

After data collection, the next step consisted of the analysis of the field accelerometer data. This was done using the commercially available software SeismoSignal™ (SeismoSoft, 2015). This software has filtering and baseline correction routines which can be used to convert the input acceleration time history to velocity and displacement time histories.

The collected data were impacted by high frequency noise (i.e., vibration) which created spurious baseline errors. Therefore, the baseline correction and frequency filtering features of this software were employed to re-baseline the measurements and to remove unwanted high frequency signal. The available baseline corrections methods were: constant, linear, quadratic and cubic. For this study, the linear baseline correction function was chosen because it provided the most reasonable adjustment to the trend in the data. After completing the base line correction, Fourier and power spectra were

plotted for each of the train events. The Fourier amplitude spectrum shows the distribution of amplitude of motion with frequency and the power spectrum reveals the power spectral density with respect to frequency. The frequency band for filtering was determined based on plots of the Fourier and power spectrum (Figures 3.15, 3.16 and 3.17). These plots suggest that much of the signal above about 70 Hz is high frequency noise from vibration, which is not of interest for estimating the deflection of the rail from the moving train.

In addition, the SeismoSignal^{TM} software has four types of filter configurations: lowpass, highpass, bandpass and bandstop. For the creation of the filter configurations, three filter types are available: Butterworth, Chebyshev and Bessel filters. In this study, a Butterworth filter type was used which featured a flat response in the pass band. The bandpass filtering configuration was applied in the study which allows signals to pass through the given frequency range. The lower frequency in the bandpass was chosen to be large (10 seconds) based on the time required during the passage of the train and the high frequency was selected based on the frequency and power spectrum plots (Figures 3.15, 3.16 and 3.17). The baseline corrected and filtered time series provides records of the acceleration, velocity and displacement time history of the rail ties. The vertical displacement of the tie was used to estimate the vertical deflection of the rail because there was little opportunity for relative vertical movement between the rail and the rail ties.

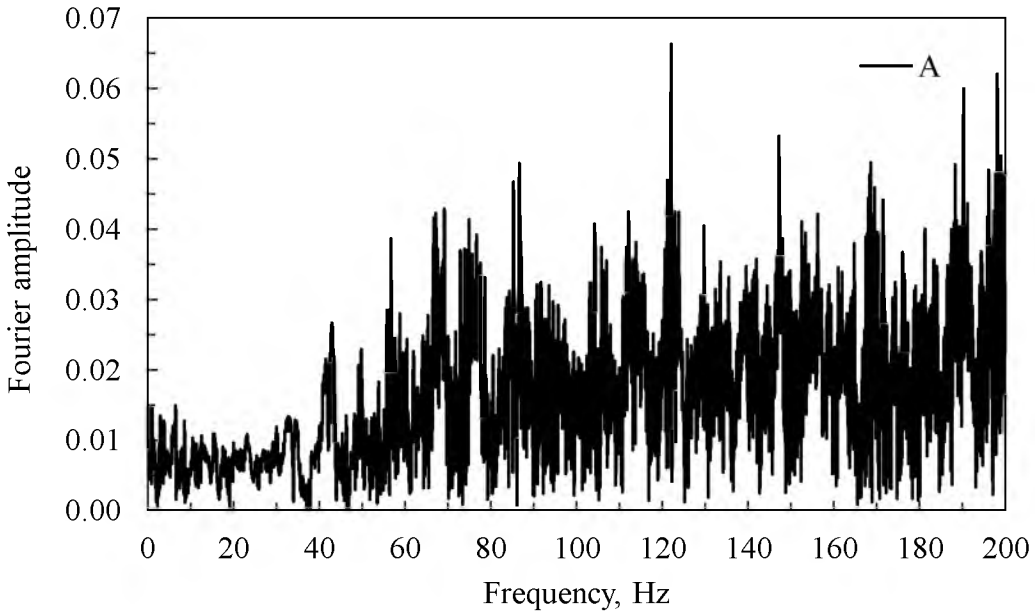

(a)

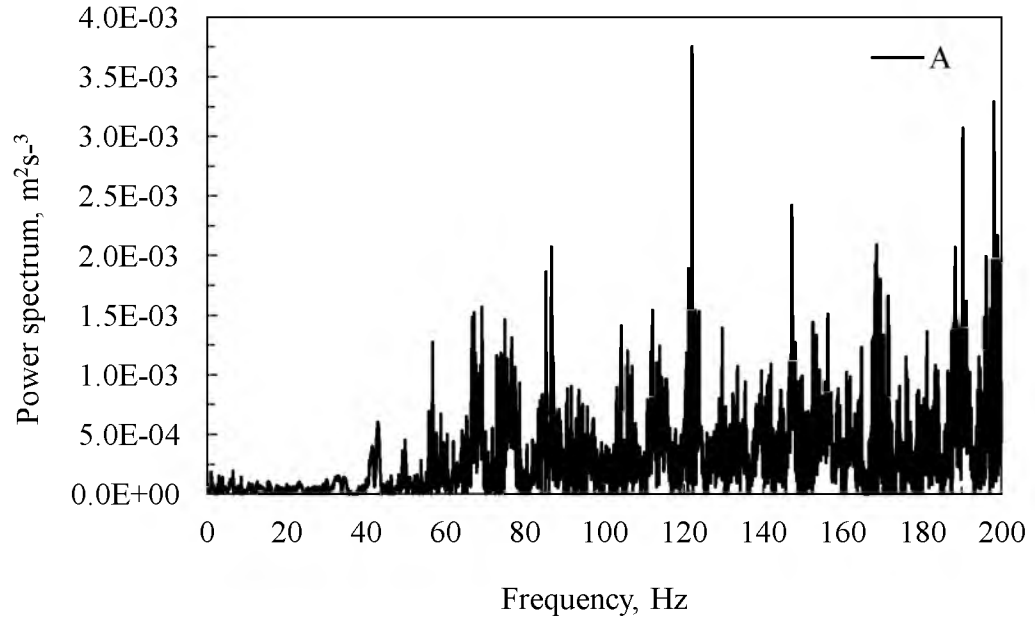

(b)

Figure 3.15. The record of accelerometer at position A along the commuter rail line (a) Fourier amplitude and (b) Power spectrum

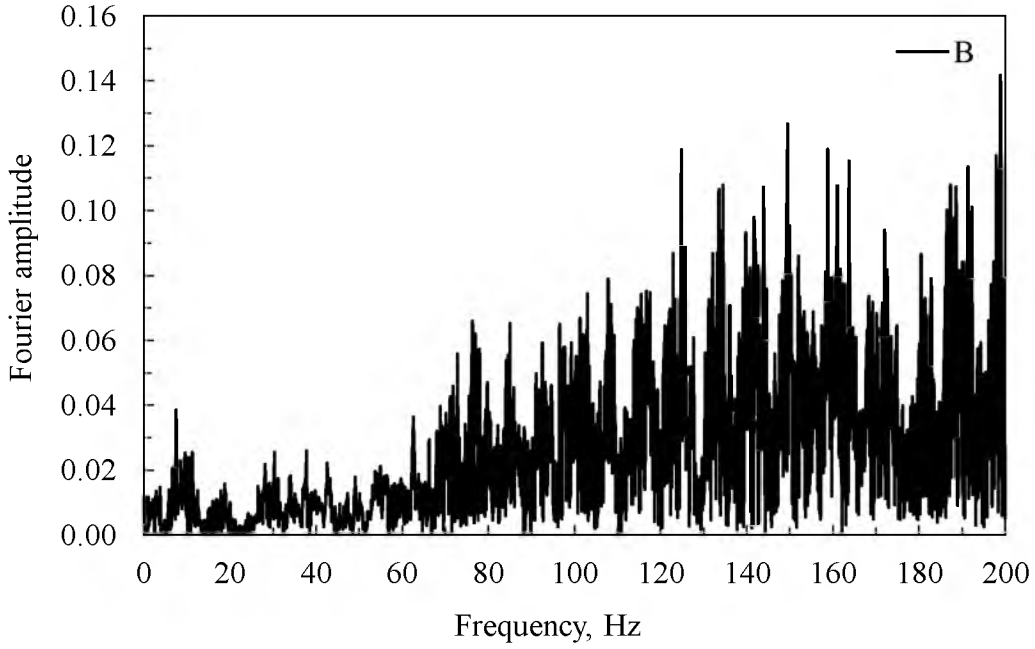

(a)

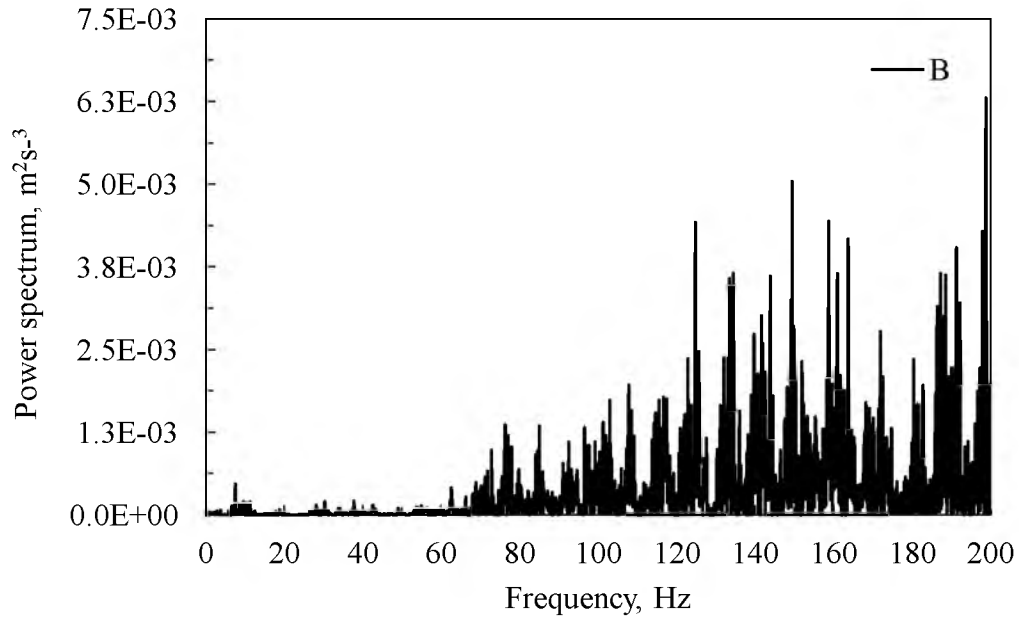

(b)

Figure 3.16. The record of accelerometer at position B along the commuter rail line (a) Fourier amplitude and (b) Power spectrum

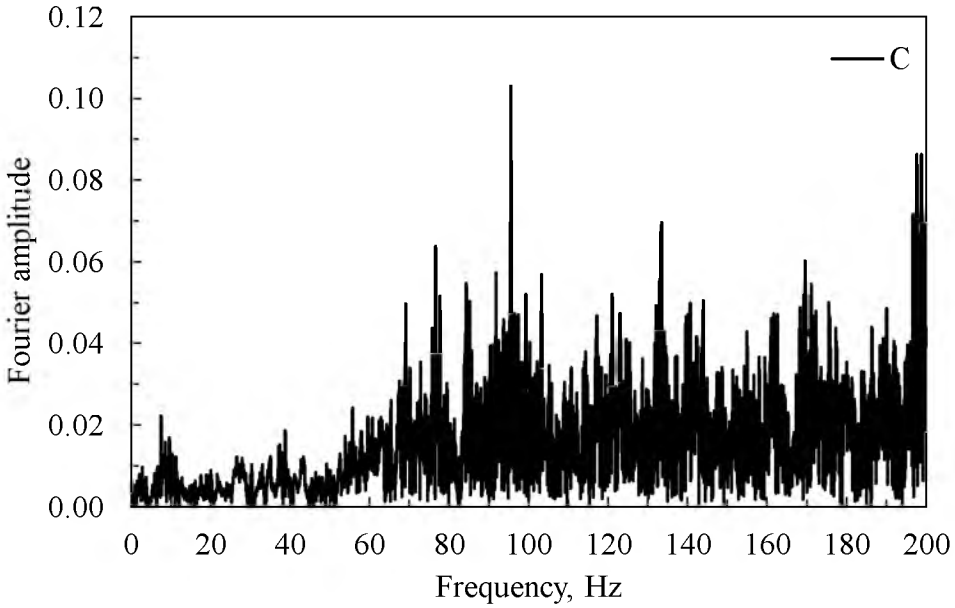

(a)

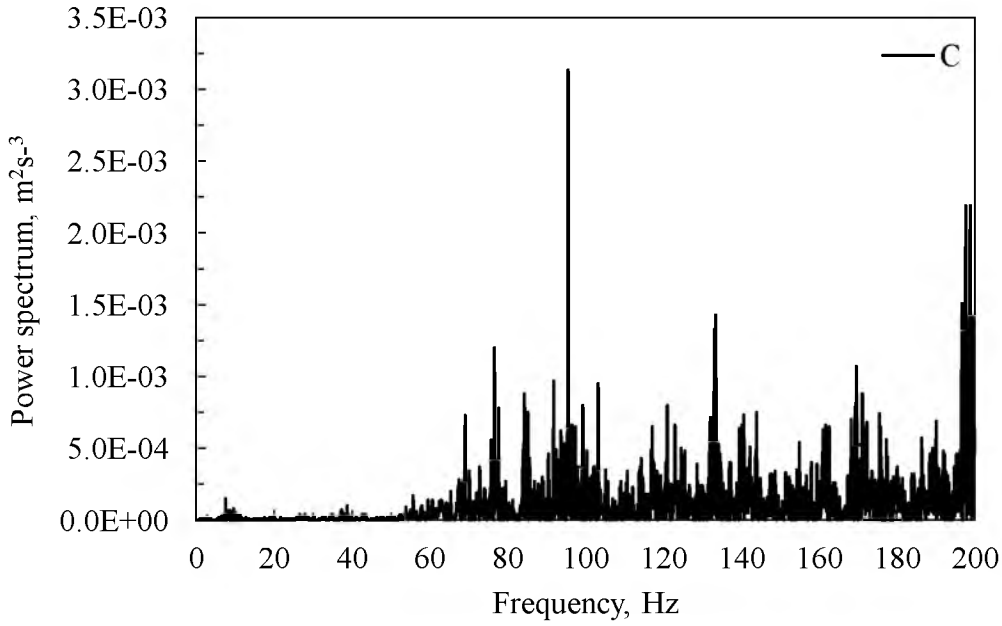

(b)

Figure 3.17. The record of accelerometer at position C along the commuter rail line (a) Fourier amplitude and (b) Power spectrum

3.4 Results from Field Measurements

3.4.1 Optical Technique

The results from the test of the laboratory optical technique matched well with the MTS results. This proved that the optical technique, as developed, was able to give reliable results in controlled conditions. However, subsequently this technique was not deployed in the field due to field geometrical constraints and weather conditions. The technique so developed for the field did not perform to its fullest capacity because the study site was windy during the field testing. In addition, it was not possible to gain additional access to the site at a later date when more favorable weather conditions might have prevailed due to the time limits placed on the deflection monitoring by the UTA track access permit. Therefore, the technique was not used for field measurements at the Corner Canyon site.

Nonetheless, the developed technique and algorithm may be useful for future projects or for laboratory measurements for cases where the ambient conditions are more favorable. In short, the optical technique presents a very low cost alternative when compared with the expense required to deploy an accelerometer array and its corresponding high-speed data acquisition system; hence because of this, the optical technique merits further consideration and development.

3.4.2 Accelerometer Array

The orientation of the accelerometers and their locations are shown in Figures 3.9 and 3.11. The possible influence that filtering might have on the vertical displacement results was studied by using various values for the upper frequency of the band pass filter. The

estimated displacement time history corresponding to an upper band pass frequency of 30, 60 and 90 Hz are shown in Figure 3.18. This parametric change revealed that the selected displacement record was not significantly altered by the selection of the high frequency for the band pass filter.

The displacement results from the accelerometers positioned at points A, B and C in the EPS embankments along the commuter rail line and light rail lines are described separately in the following sections.

3.4.2.1 Commuter Rail Line

The Fourier amplitude and power spectra of the recorded data from accelerometers positioned at A, B and C were analyzed in order to finalize the filtering process and to select the upper frequency in the bandpass filtering. The Fourier amplitude and power spectrum of A, B and C positions are shown in Figures 3.15, 3.16 and 3.17, respectively.

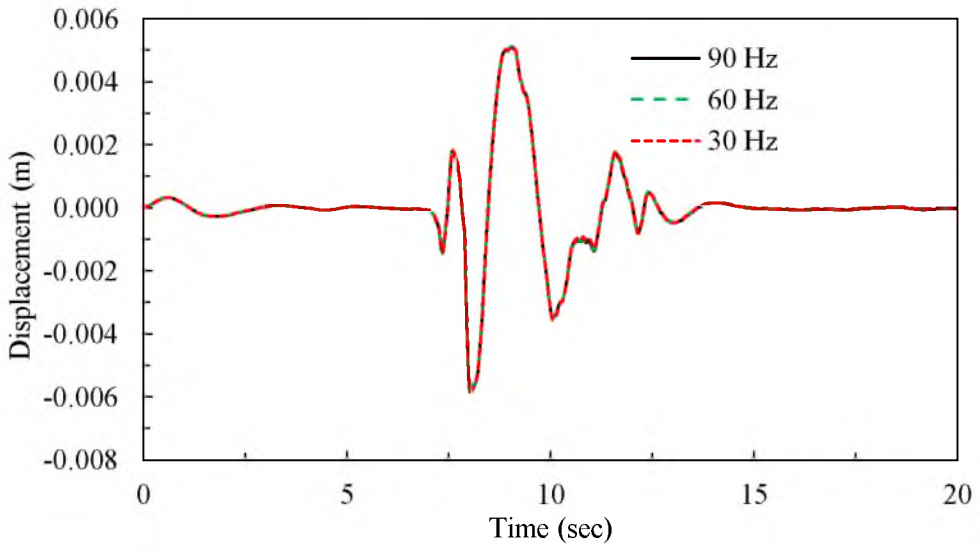

Figure 3.18. Vertical displacement record using different levels for the upper frequency in the bandpass filter

Based on these plots, it was concluded that the average value of frequency beyond which significant noise started was about 70 Hz and the lowest level of frequency to be considered was 0.1 Hz.

The train bound to Salt Lake City from Provo will be referred to as the north bound (NB) train, and that bound from Salt Lake to Provo will be referred to as the south bound (SB) train hereafter. The train shown in Figure 3.10 was an SB train. In the study, three NB trains named 1, 2 and 3 were monitored for estimating the vertical deflection of rail atop EPS embankment. Three NB trains were named 4, 5 and 6 were monitored for the determination of vertical deflection of rail atop earthen embankment. The accelerometers were placed on the sleepers adjacent to the NB train track, whereas the SB train track was located 1.5 m distance from the position of the accelerometers. The NB trains were used for measuring vertical deflection because the vertical stress on embankments was assumed to be higher under the NB train track due to the placement of the accelerometers directly on this track. However, one NB and one SB train were monitored to compare the results in terms of the vertical deflections.

The input acceleration and the vertical displacement of three trains on the EPS embankment are shown in Figures 3.19, 3.20 and 3.21. Figure 3.19 reveals the input acceleration and the vertical displacement measured by the accelerometer at position A due to trains 1, 2 and 3. In Figure 3.19, a somewhat higher peak displacement occurred at the beginning of the record when the train had just entered over the EPS embankment at about 8 seconds of elapsed time. The maximum displacement for this spike was found to be 6 mm. However, a typical average displacement of about 2 mm was observed for many of the deflection events (Figure 3.20 and 3.21).

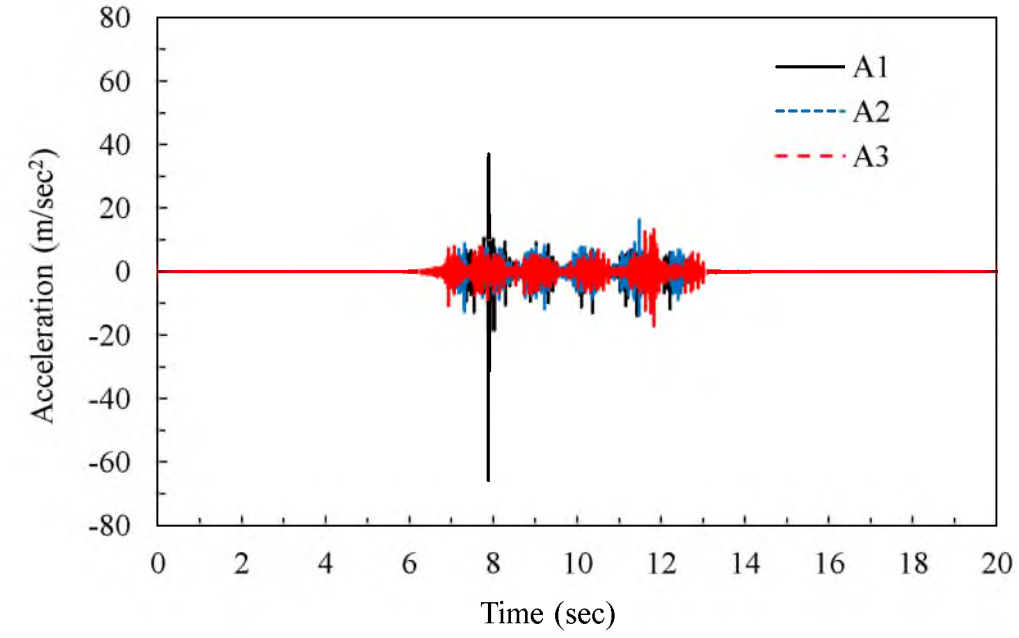

(a)

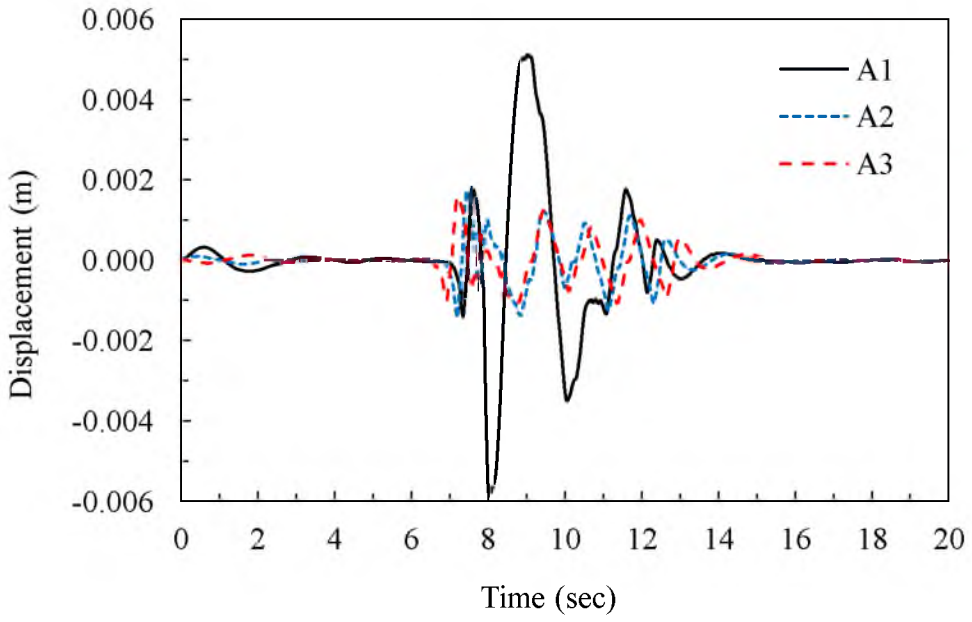

(b)

Figure 3.19. The record of accelerometer position at A of EPS embankment along the commuter rail line (a) Input acceleration and (b) Vertical displacement

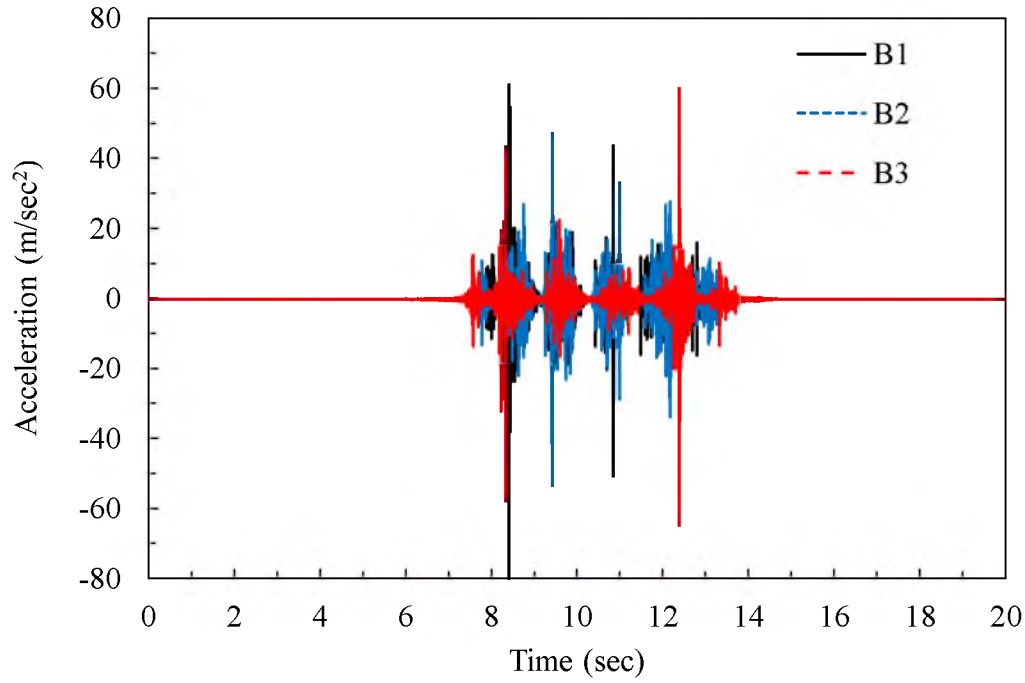

(a)

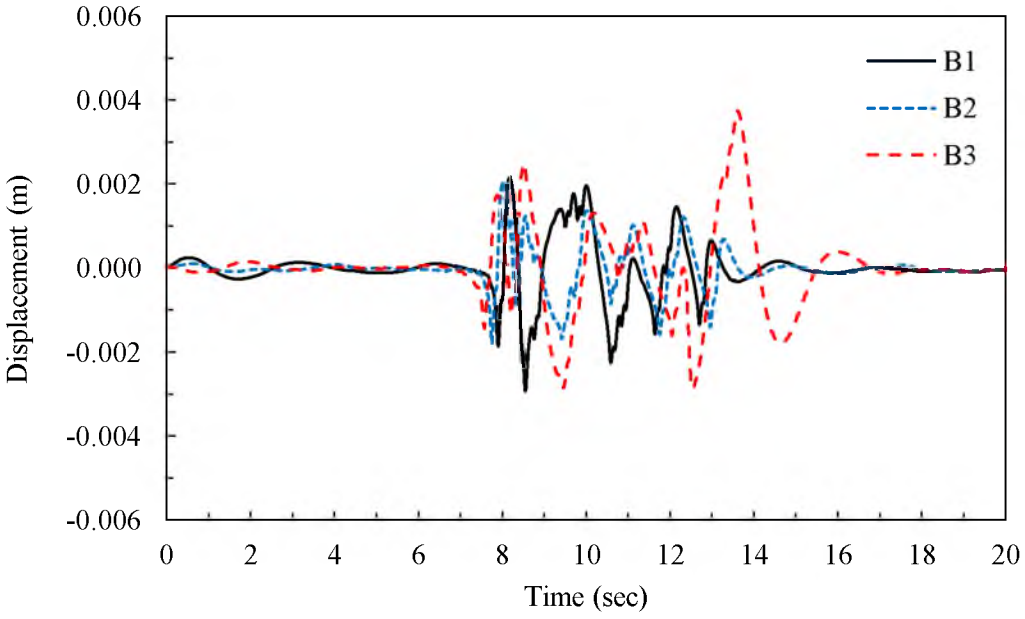

(b)

Figure 3.20. The record of accelerometer position at B of EPS embankment along the commuter rail line (a) Input acceleration and (b) Vertical displacement

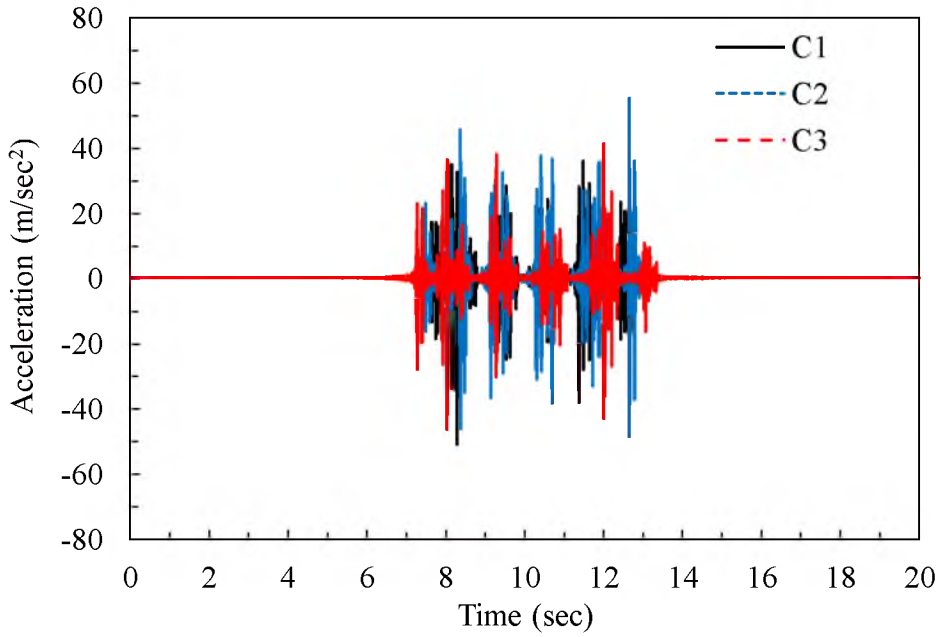

(a)

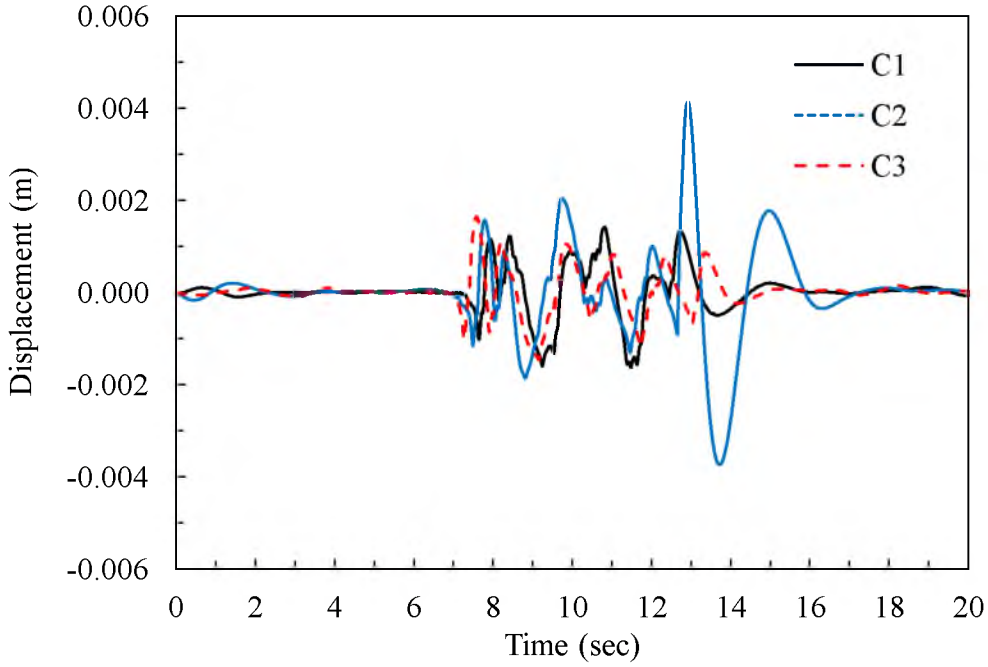

(b)

Figure 3.21. The record of accelerometer position at C of EPS embankment along the commuter rail line (a) Input acceleration and (b) Vertical displacement

Figure 3.20 shows the input acceleration and vertical displacement of the EPS embankment recorded at position B for trains 1, 2 and 3. The third train produced acceleration spike once it had left the EPS portion of the embankment. The maximum and average displacement were found to be around 4 mm and 2 mm, respectively.

Figure 3.21 shows the input acceleration and vertical displacement of EPS embankment measured by an accelerometer at position C for trains 1, 2 and 3. Figure 3.21 shows the maximum and maximum average vertical displacement of EPS were around 4 mm and 2 mm, respectively. The second train produced a spike at the end when it crossed the embankment. The combined accelerometer records for positions A, B and C for trains 1, 2 and 3 are shown in Figure 3.22. These records show that the maximum and average vertical displacement were around 6 mm and 2 mm, respectively. These vertical displacement results are similar to those measured on sleepers for an earthen embankment railway track using geophones by Bowness et al. (2007). These authors report a maximum and average displacement of around 6 mm and 3.5 mm.

For one event, two trains (NB direction and SB direction) passed over the EPS embankment array within short time span. The displacement was monitored for this event. In this analysis, the record of NB train and SB train was denoted by AN and AS for the accelerometer position at location A. Similar notations were used for accelerometers positioned at B and C. The input acceleration of both trains while passing the array is shown in Figure 3.23. The analysis was done separately for each of the accelerometers and trains. Comparative plots of the input acceleration and vertical displacements of the EPS embankment recorded by accelerometers A, B and C are shown in Figures 3.24, 3.25 and 3.26, respectively.

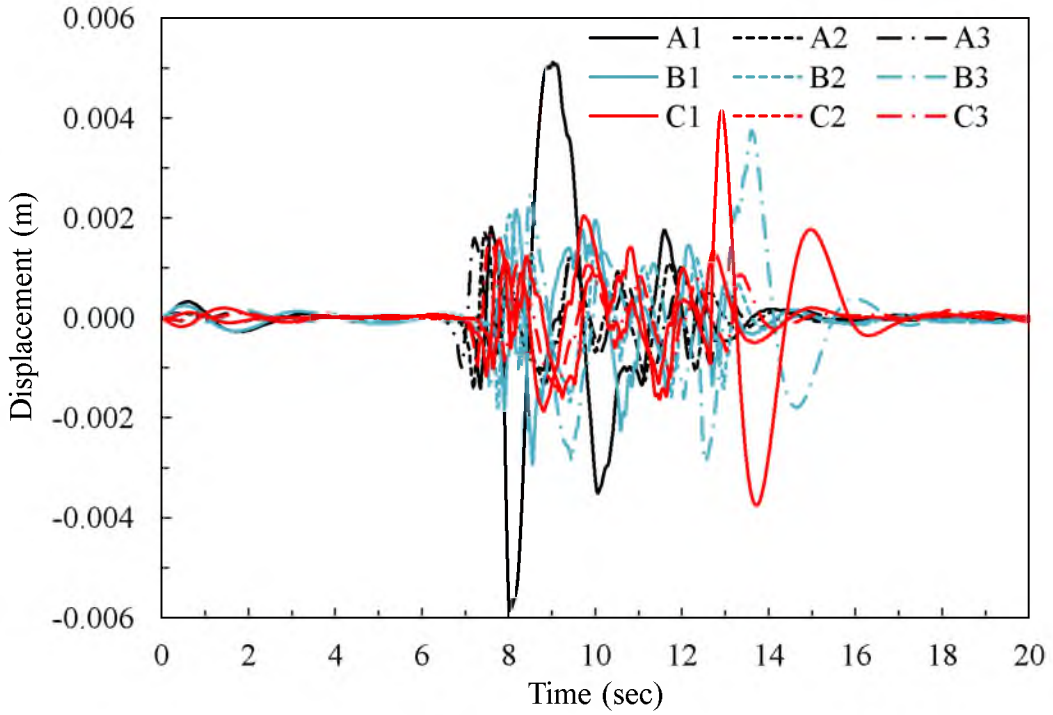

Figure 3.22. Vertical displacement recorded by accelerometers at positions A, B and C for trains 1, 2 and 3 in the EPS embankment along the commuter rail line

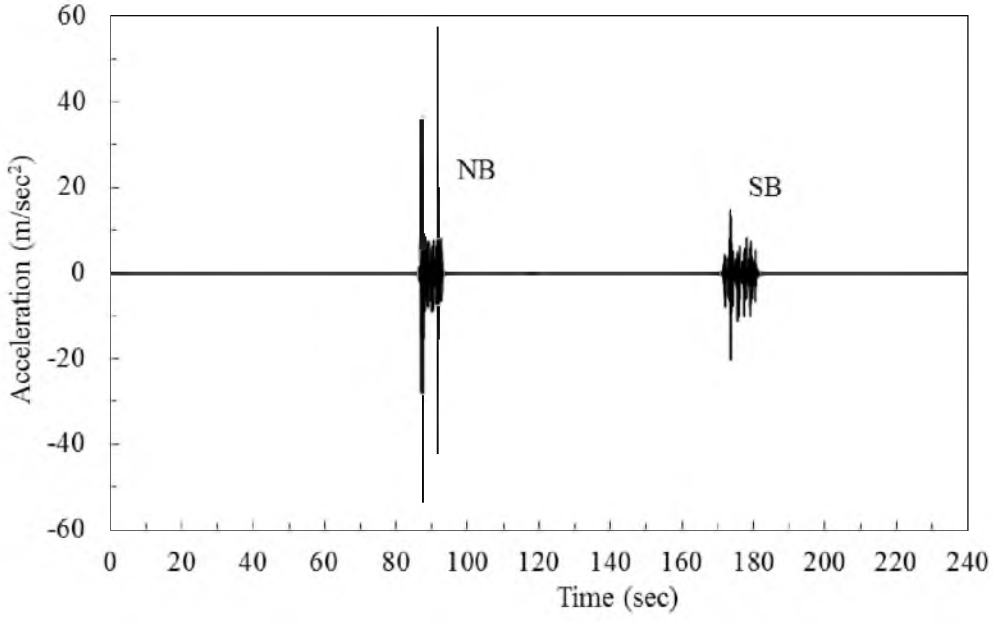

Figure 3.23. The input acceleration of NB and SB train while crossing the EPS embankment along the commuter rail line

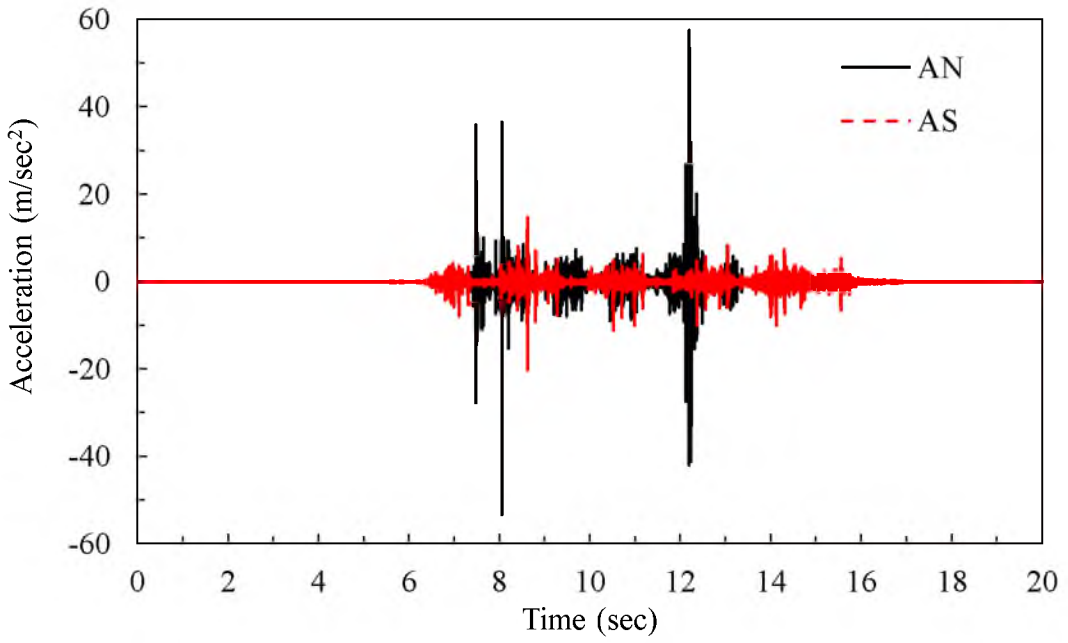

(a)

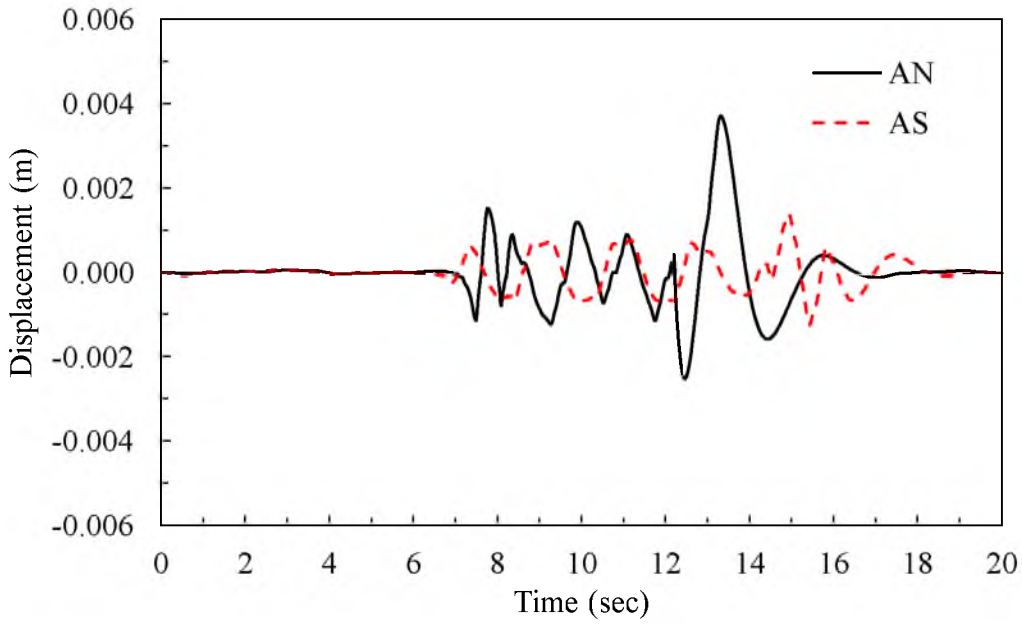

(b)

Figure 3.24. The comparative plot of record on EPS embankment by accelerometer at position A (a) Input acceleration and (b) Vertical displacement

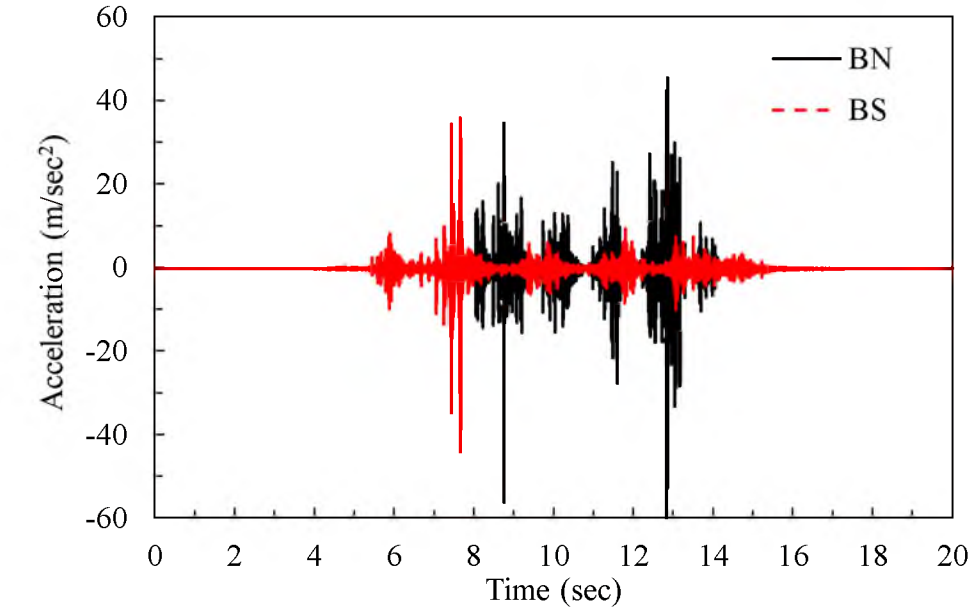

(a)

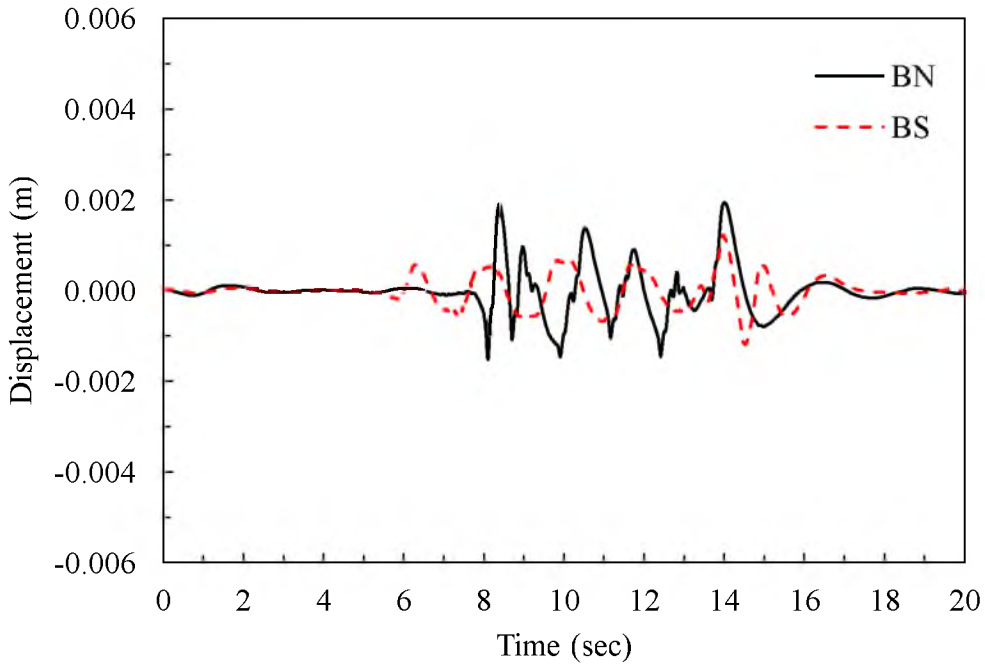

(b)

Figure 3.25. The comparative plot of record on EPS embankment by accelerometer at position B (a) Input acceleration and (b) Vertical displacement

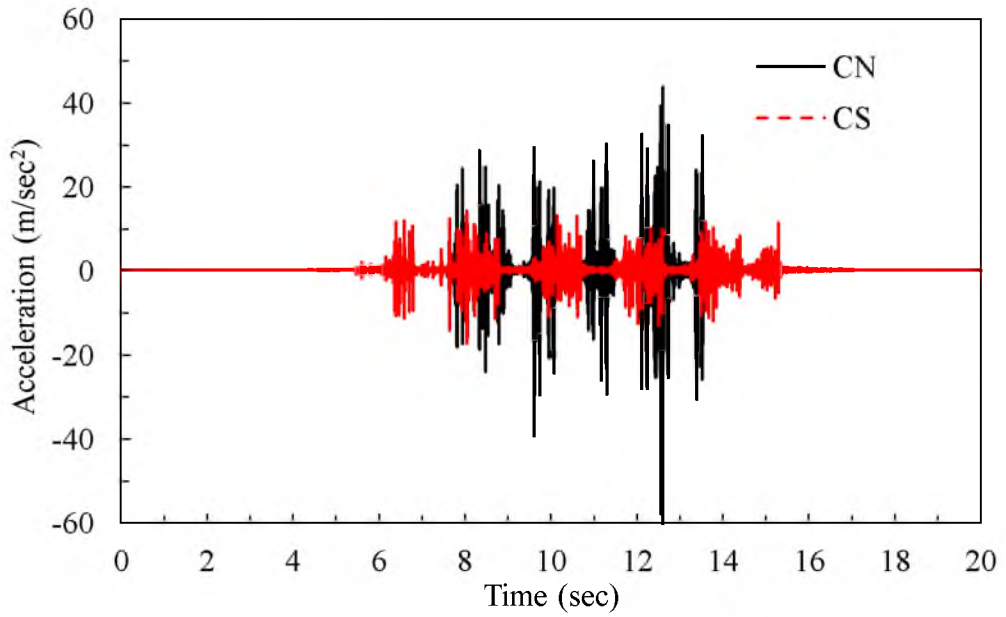

(a)

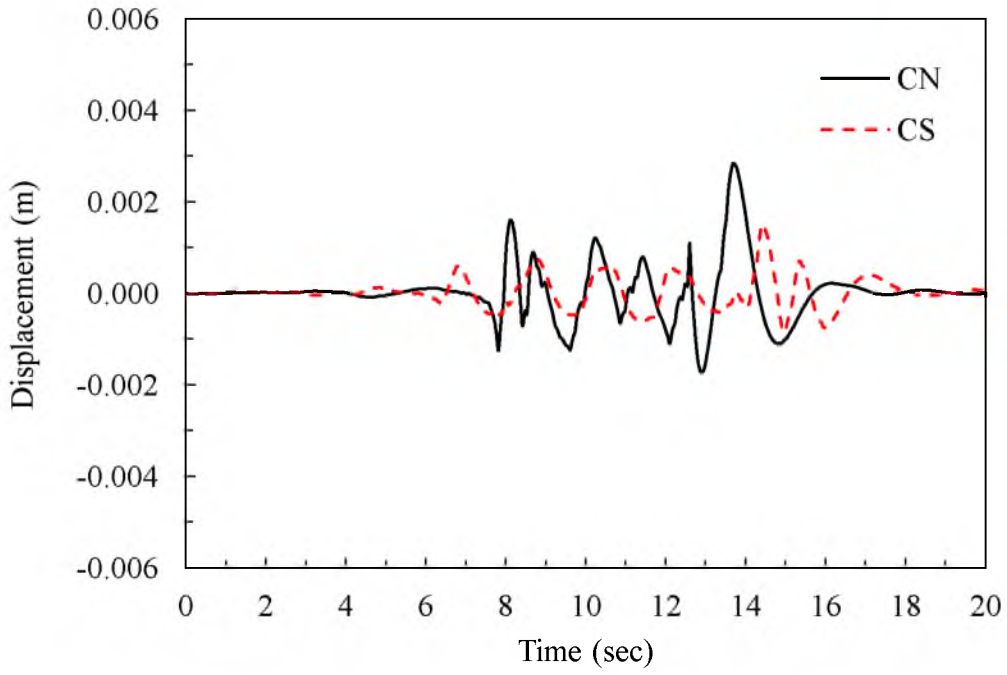

(b)

Figure 3.26. The comparative plot of record on EPS embankment by accelerometer at position C (a) Input acceleration and (b) Vertical displacement

These figures show that the maximum and average vertical displacements for the NB train were about 4 mm and 1.5 mm, respectively, whereas about 1 mm and 0.75 mm were recorded for the SB train, respectively. The lower values for the SB train were due to its greater distance from the position of the accelerometer array placed on the NB rail.

The input acceleration and vertical displacements for three train events named as 4, 5 and 6 on the adjacent earthen embankments are shown in Figures 3.27, 3.28 and 3.29, respectively. Figure 3.27 shows the maximum displacement occurred when train 4 just entered this portion of the embankment. There was an initial displacement spike at the beginning of this passing, followed by lower displacements a few seconds afterward. The maximum and maximum average displacements were about 12 mm and 3 mm, respectively, for the earthen embankment.

Figure 3.28 shows the maximum displacement occurred when trains 5 and 6 just arrived on the earthen portion of the embankment. The maximum and average displacements were around 13 mm and 5 mm, respectively.

A high displacement event occurred when train 6 entered onto the earthen embankment. Figure 3.29 shows a maximum and average displacement of around 22 mm and 5 mm, respectively. The combined displacement results for records at positions A, B and C for trains 4, 5 and 6 are shown in Figure 3.30. This combined plot shows a maximum vertical displacement and maximum average vertical displacement of about 22 mm and 7.5 mm, respectively. These results are higher than those reported by Bowness et al. (2007) for earthen embankment. The difference in results might be due to differences in the embankment materials, construction, geometry, train loads, and from experimental error.

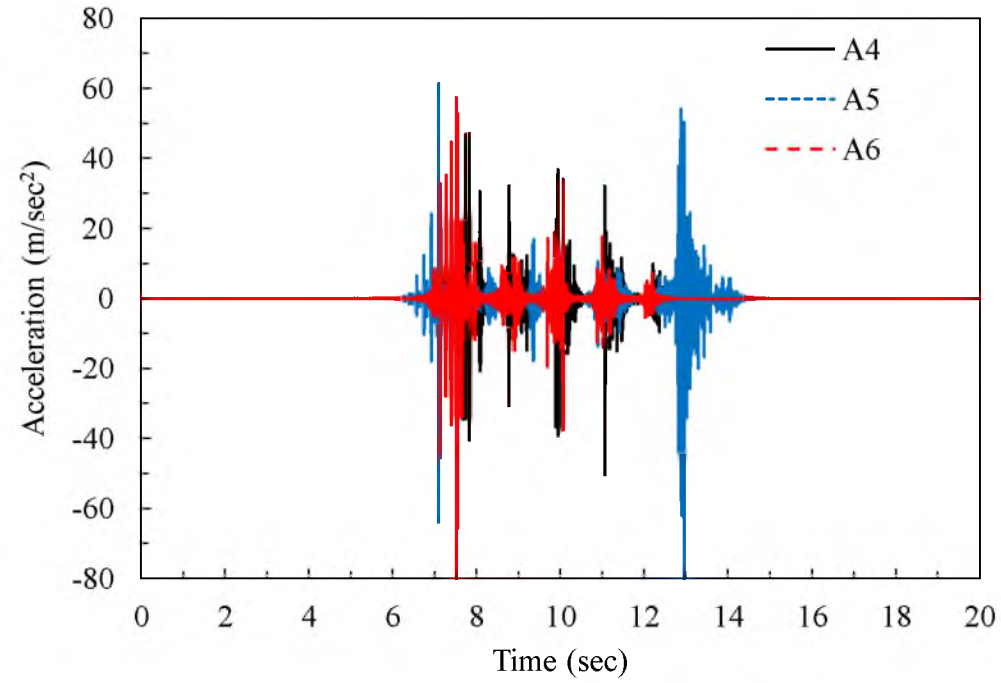

(a)

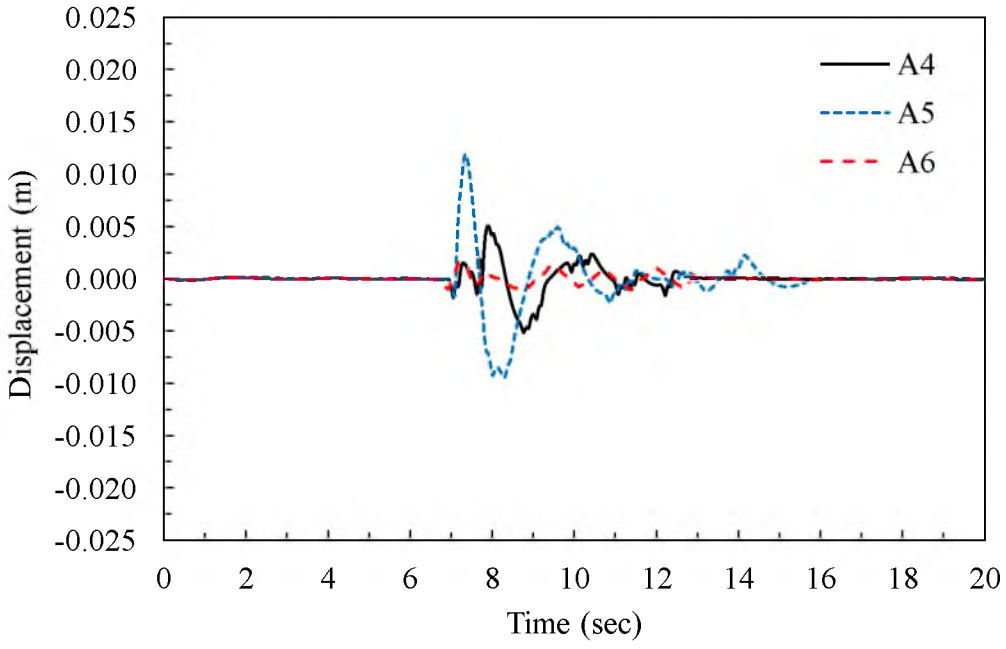

(b)

Figure 3.27. The record of accelerometer position at A of earthen embankment along the commuter rail line (a) Input acceleration and (b) Vertical displacement

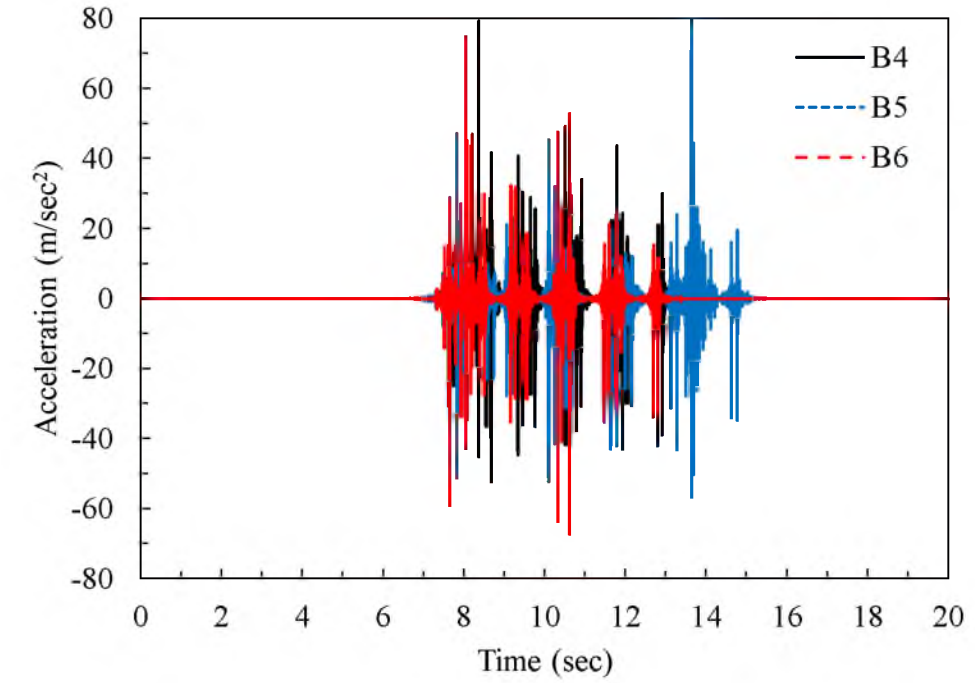

(a)

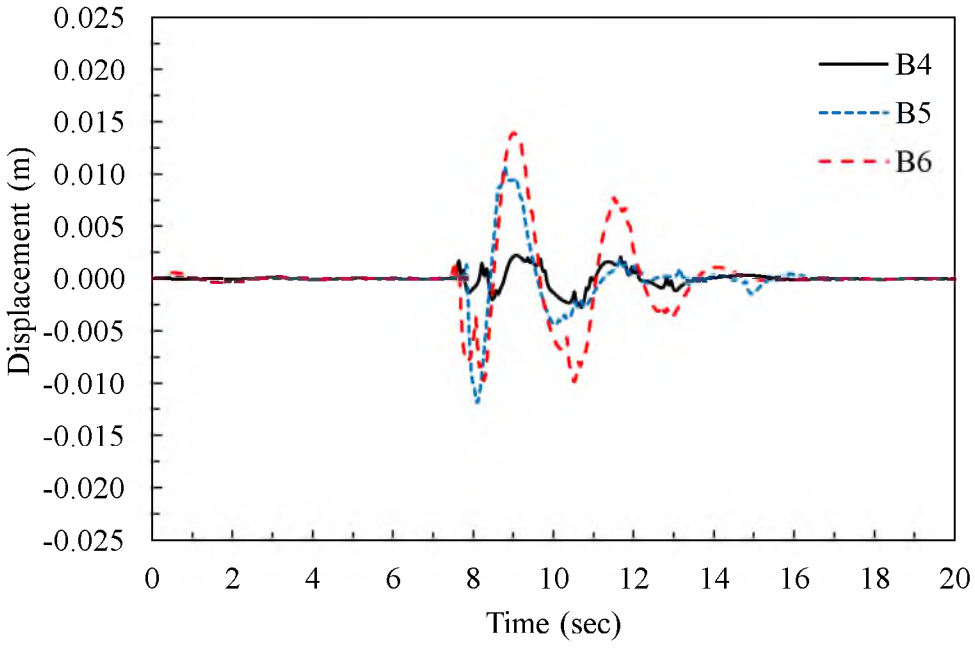

(b)

Figure 3.28. The record of accelerometer position at B of earthen embankment along the commuter rail line (a) Input acceleration and (b) Vertical displacement

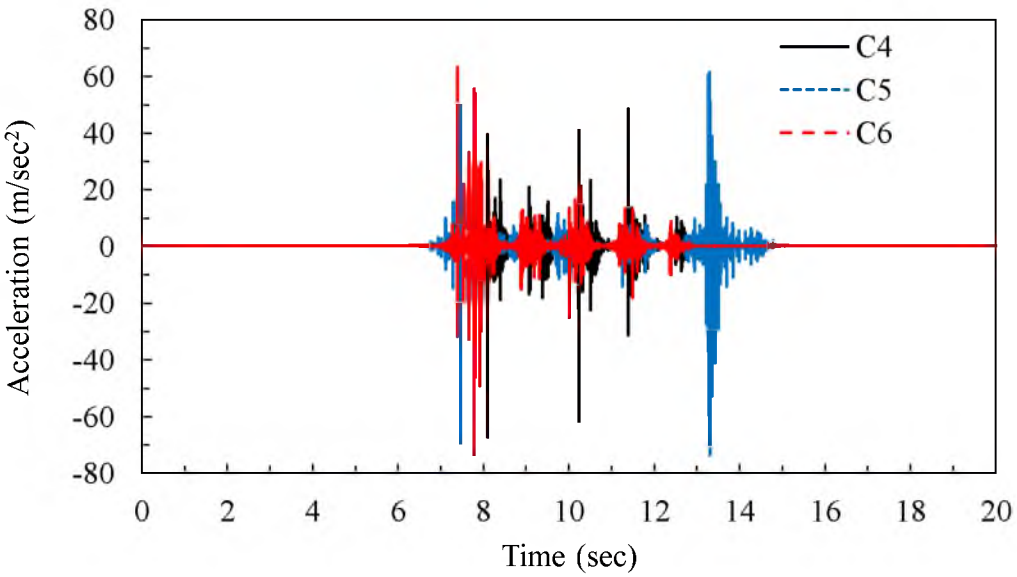

(a)

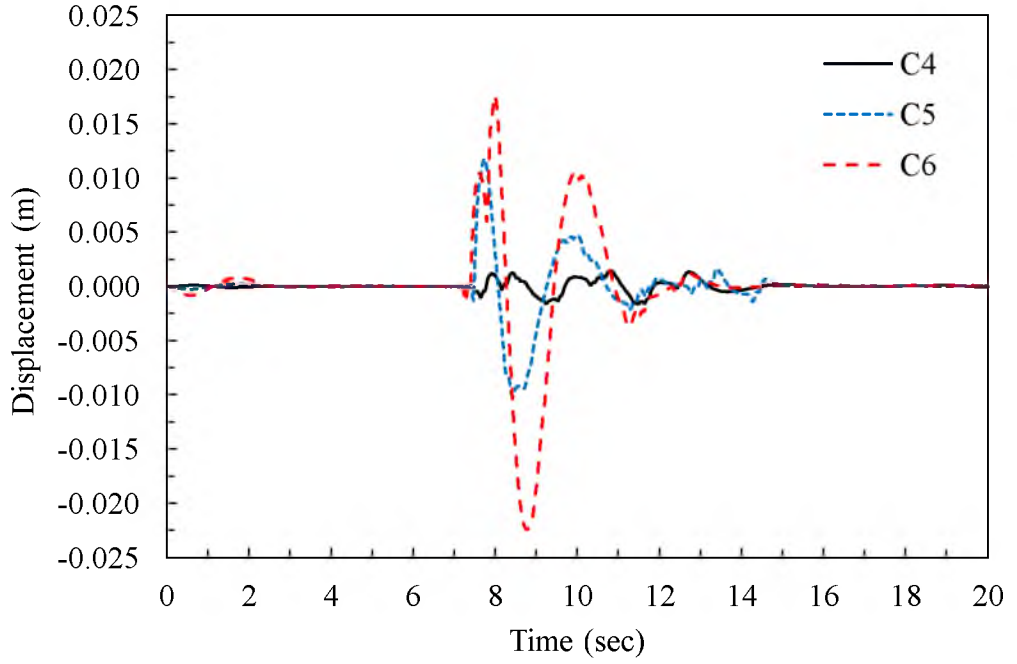

(b)

Figure 3.29. The record of accelerometer position at C of earthen embankment along the commuter rail line (a) Input acceleration and (b) Vertical displacement

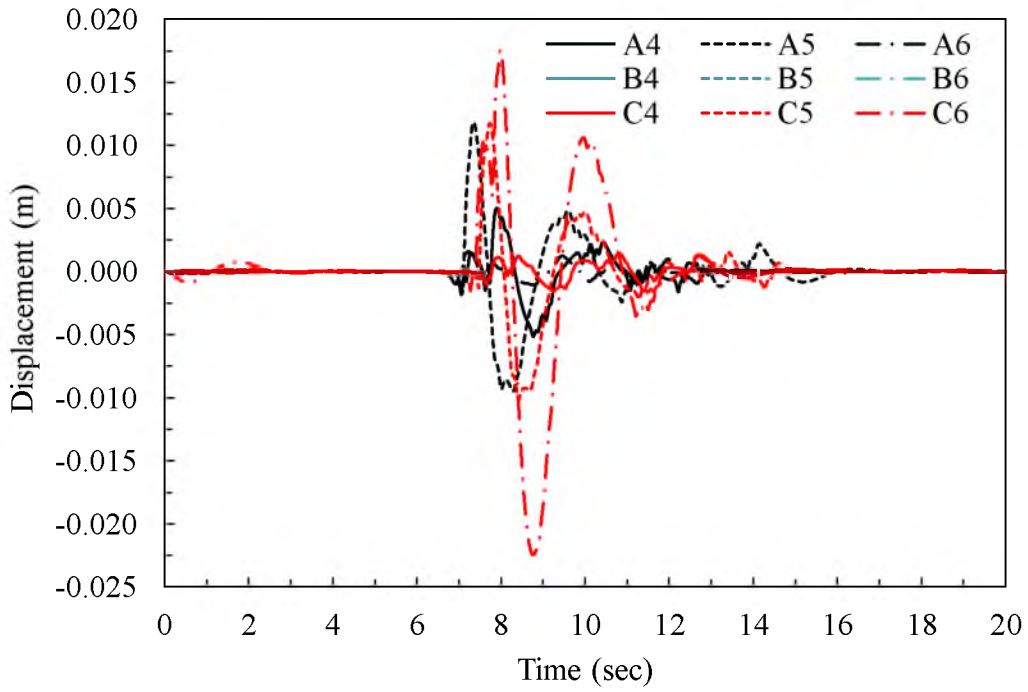

Figure 3.30. Vertical displacement recorded by accelerometers at positions A, B and C for trains 4, 5 and 6 in the earthen embankment along the commuter rail line

In summary, the maximum and average vertical displacements for the earthen embankment were found to be higher than those of the EPS embankment. This could be due to the fact that the soil in earthen embankment could have lateral compression due to combined dead and live loads. However, in case of EPS embankment due to inherent properties of EPS material the lateral compression is less likely to occur. Therefore the minimum vertical displacement might occur in the EPS embankment. The measurements suggest that the EPS embankment, as constructed at this site, is performing as well as, or slightly better than the earthen embankment in terms of rail deflections. The EPS material is desired over conventional fill material for new and reconstruction in soft soil condition.

3.4.2.2 Light Rail Line Array

The Fourier amplitude and power spectrum for the A, B and C positions are shown in Figures 3.31, 3.32 and 3.33, respectively, for the UTA light rail system (i.e., TRAX). The average frequency beyond which significant noise started was about 80 Hz for both Fourier amplitude and power spectrum. Thus, the highest frequency considered in the data interpretation was 80 Hz. The time taken for trains to pass the sensors was less than 10 sec and the lowest level of frequency to be considered was 0.1 Hz.

The westbound (WB) train bound to West Valley Central Station from Salt Lake City International Airport was monitored for this study. The train from the West Valley Central Station to Airport will be referred to as the east bound (EB) train hereafter. The train shown in Figure 3.13 is the WB train. In this study, five WB trains named 1, 2, 3, 4 and 5 were monitored for the determination of the vertical deflection of concrete rail sleepers constructed atop a large EPS embankment. The WB trains were selected for the monitoring, and the accelerometers were placed on the sleepers for the WB rail. At this location, the EB track was about 1.5 m distance from the position of the accelerometers on the WB rail.

The acceleration time histories and the vertical displacement of five trains traveling on the EPS embankment are shown in Figures 3.34, 3.35 and 3.36. Figure 3.34 shows the input acceleration and the vertical displacements estimated by the accelerometer at position A due to trains 1, 2 3, 4 and 5. The process of converting the acceleration time history to displacement was the same as that used for the FrontRunner system, discussed previously, except the upper frequency for the band pass filter was set to 80 Hz.

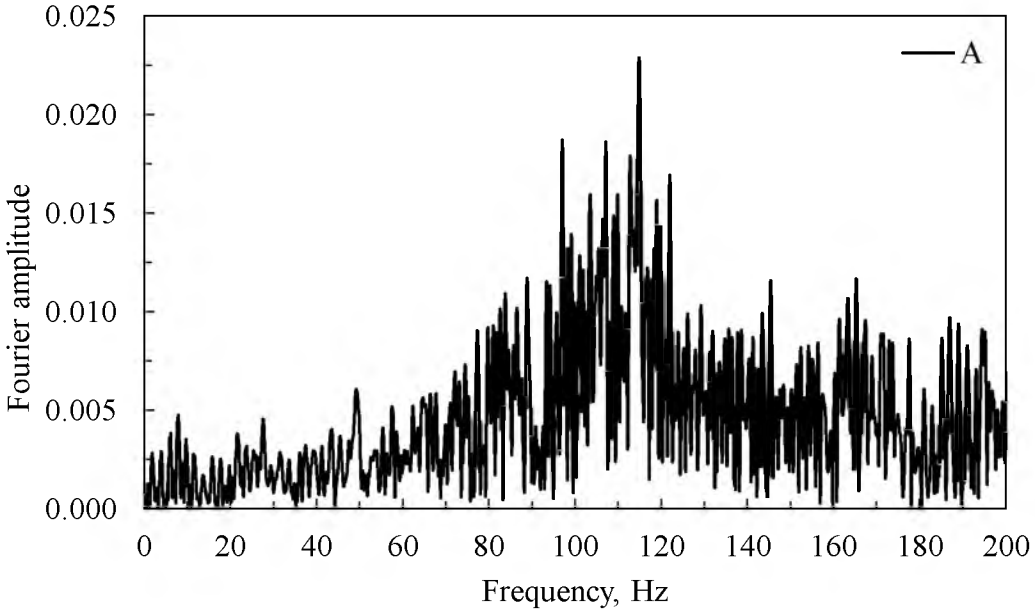

(a)

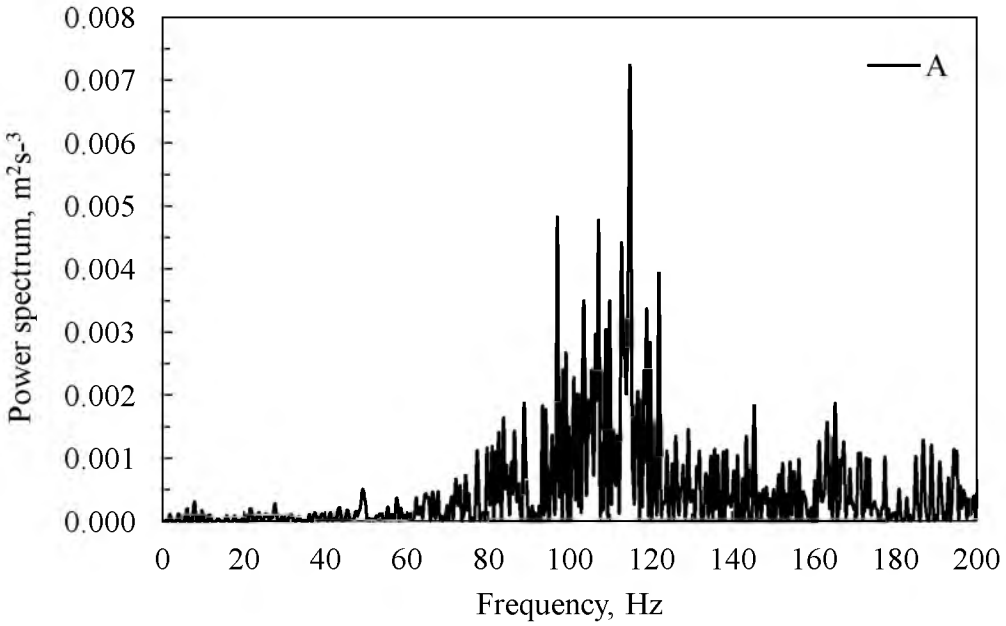

(b)

Figure 3.31. The record of accelerometer at position A along the light rail line (a) Fourier amplitude and (b) Power spectrum

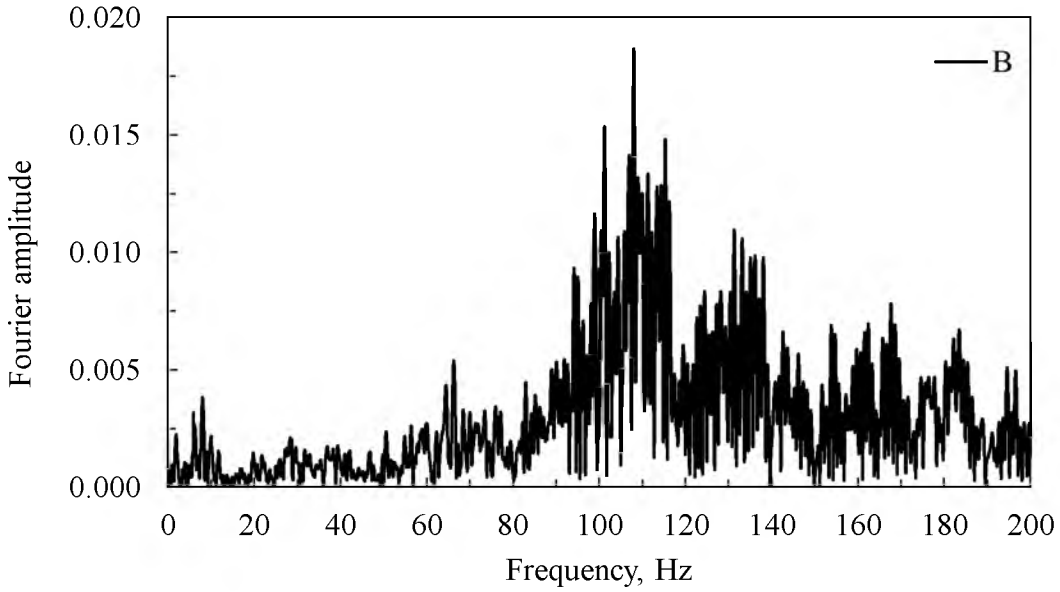

(a)

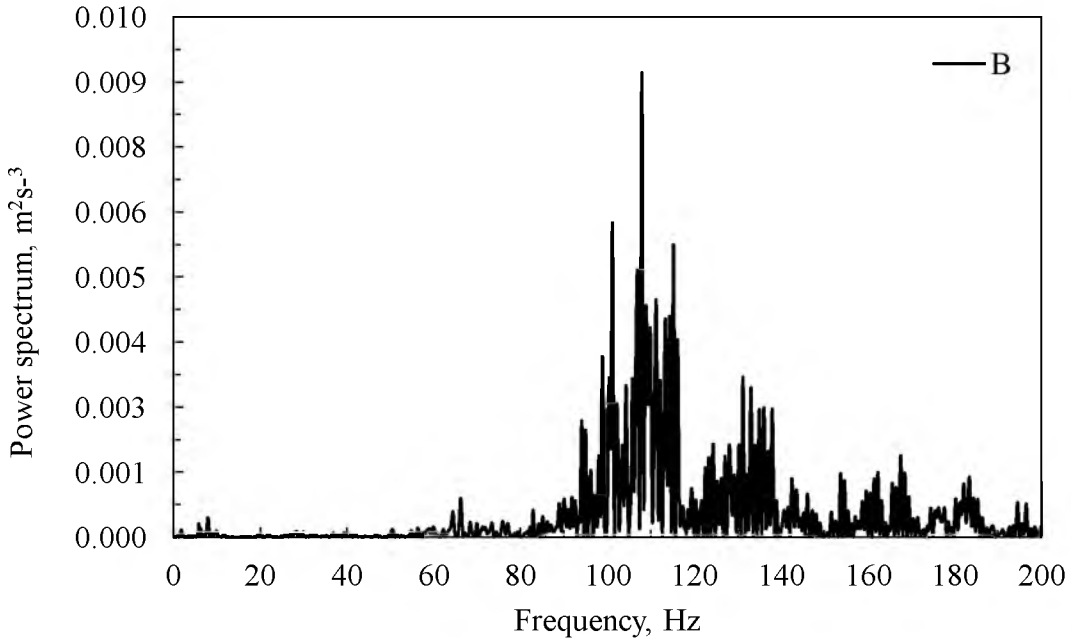

(b)

Figure 3.32. The record of accelerometer at position B along the light rail line
(a) Fourier amplitude and (b) Power spectrum

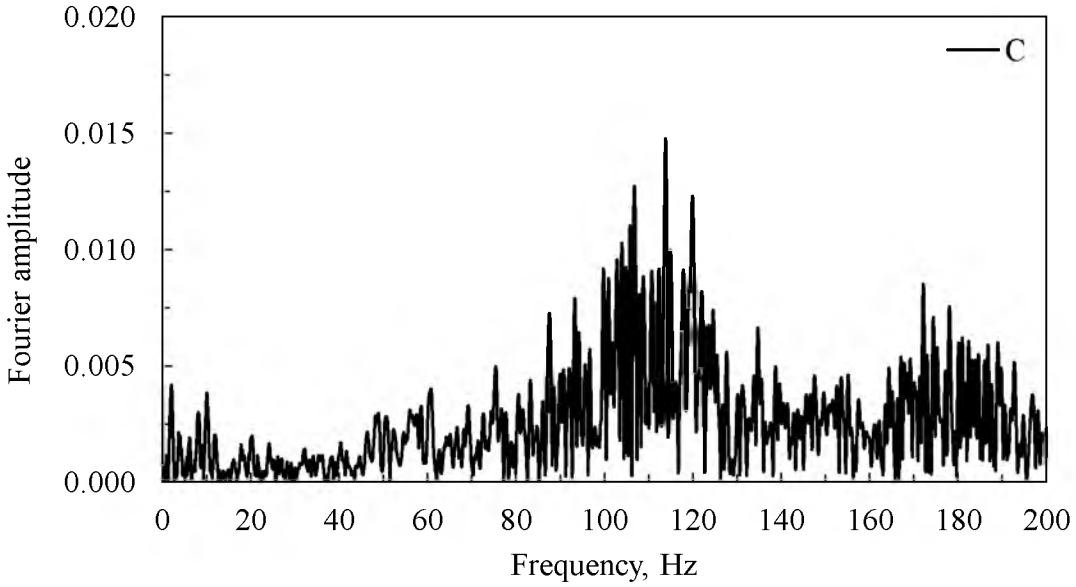

(a)

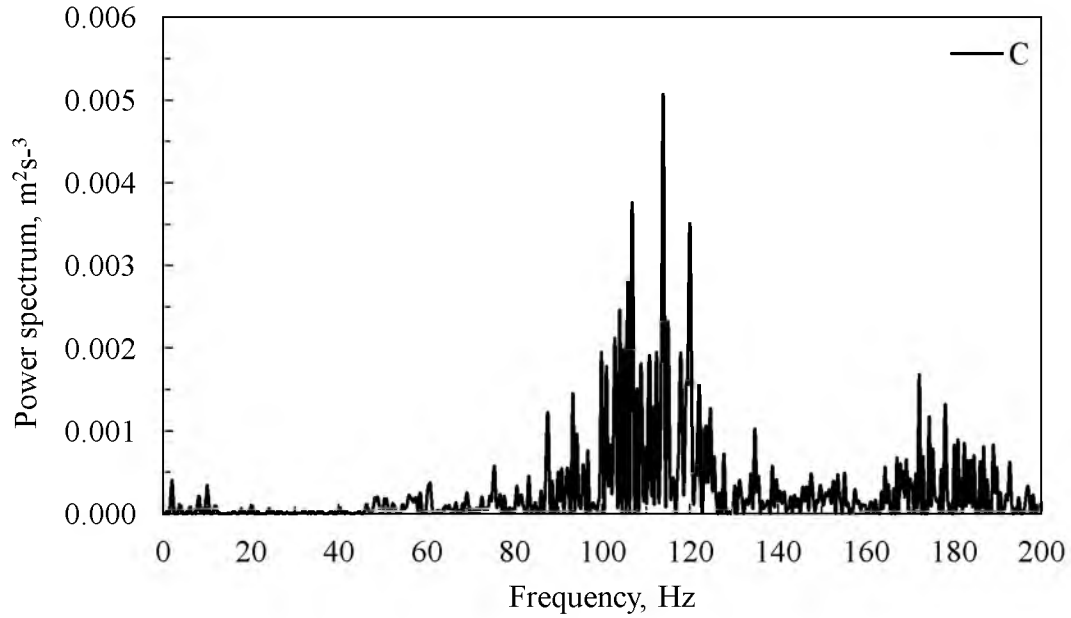

(b)

Figure 3.33. The record of accelerometer at position C along the light rail line
(a) Fourier amplitude and (b) Power spectrum

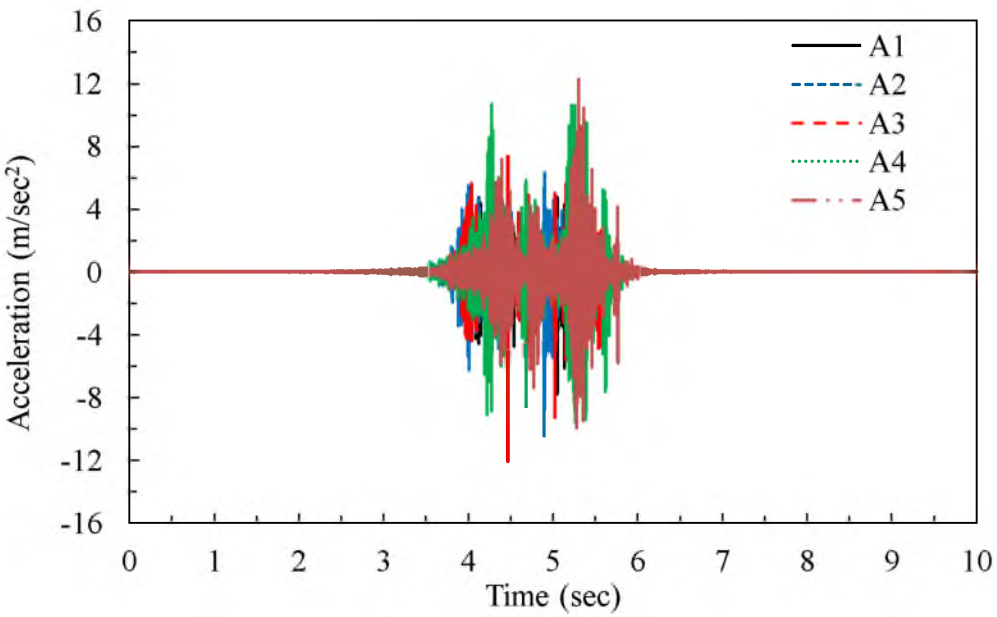

(a)

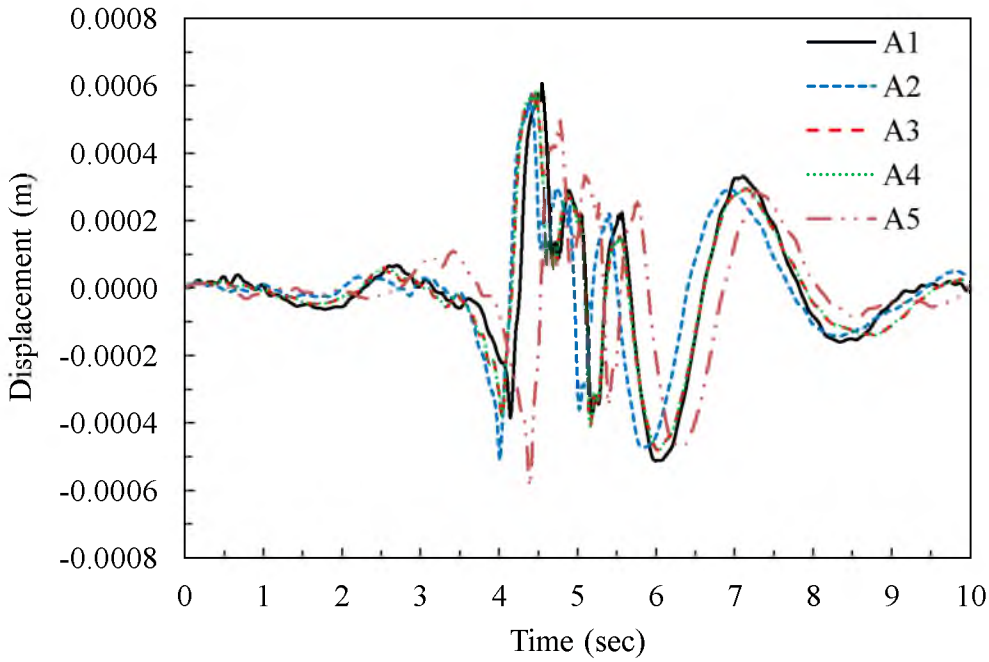

(b)

Figure 3.34. The record of accelerometer position at A of EPS embankment along the light rail line (a) Input acceleration and (b) Vertical displacement

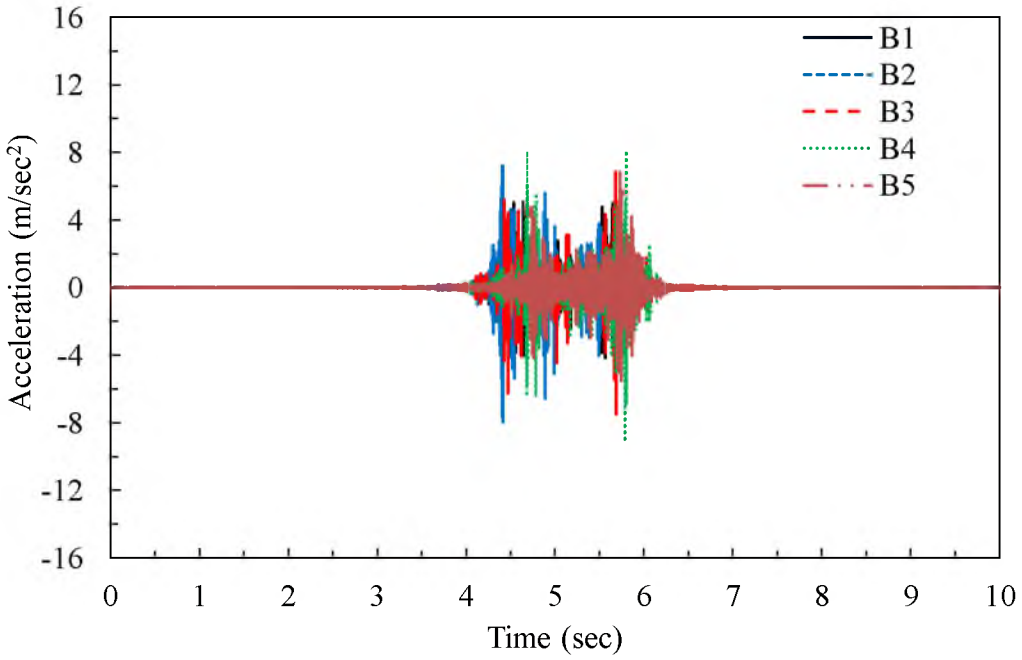

(a)

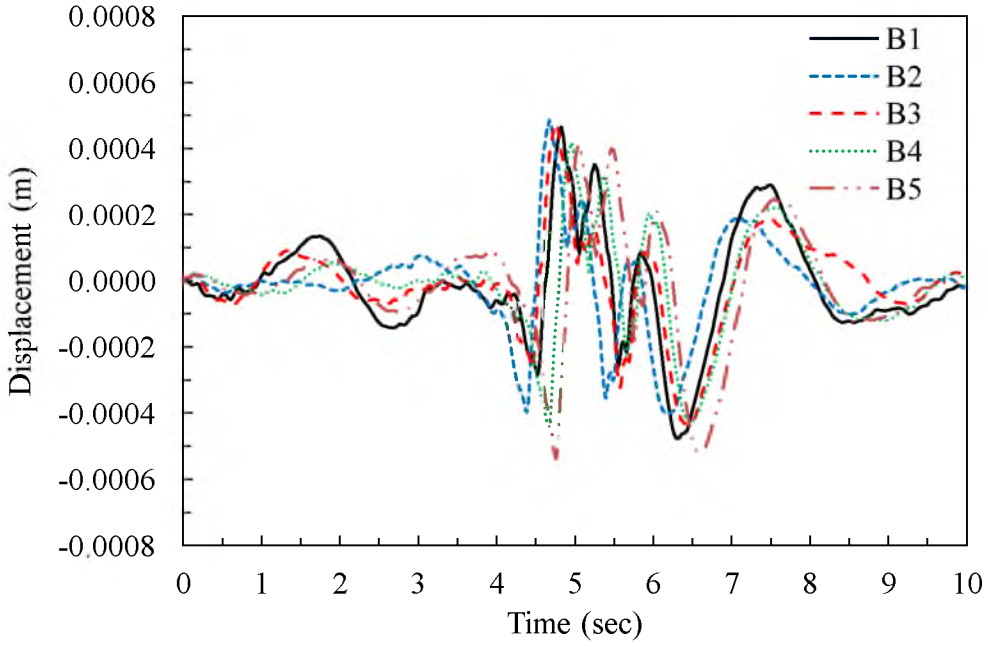

(b)

Figure 3.35. The record of accelerometer position at B of EPS embankment along the light rail line (a) Input acceleration and (b) Vertical displacement

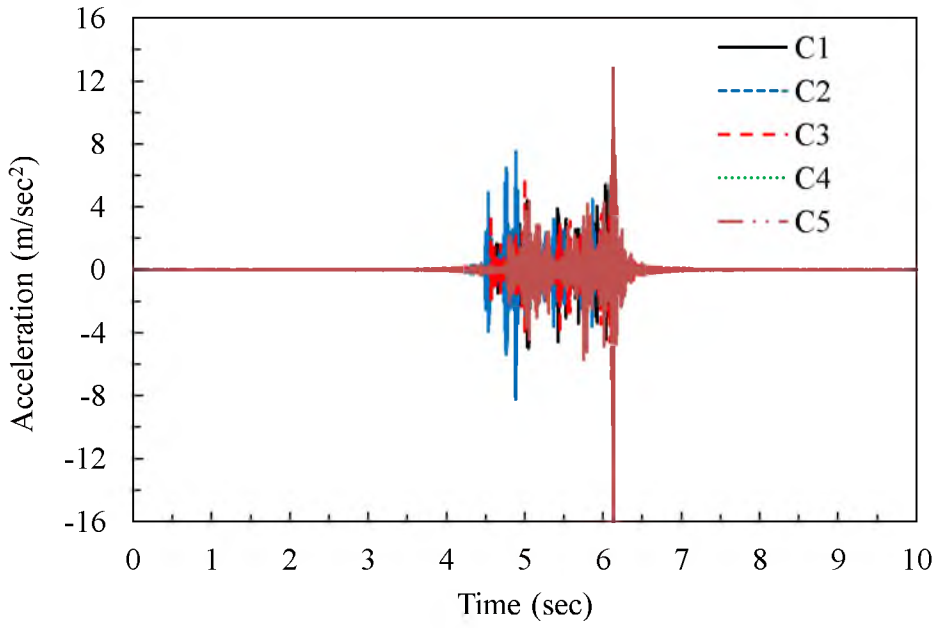

(a)

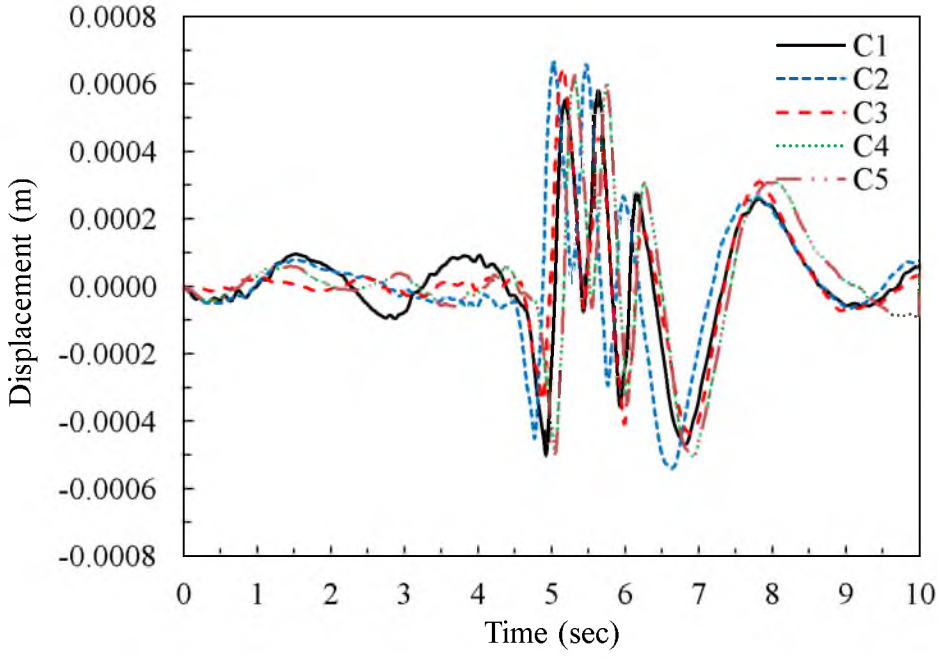

(b)

Figure 3.36. The record of accelerometer position at C of EPS embankment along the light rail line (a) Input acceleration and (b) Vertical displacement

In Figure 3.34, the maximum displacement was estimated to be about 0.6 mm. Figure 3.35 shows the input acceleration and vertical displacement of the EPS embankment recorded for the position of accelerometer at B for trains 1, 2, 3, 4 and 5. The maximum displacement was about 0.5 mm. Figure 3.36 shows the input acceleration and vertical displacement of the EPS embankment measured by accelerometer at position C for trains 1, 2, 3, 4 and 5. Figure 3.34 shows the maximum vertical displacement of EPS was about 0.7 mm.

The records on accelerometers at positions A, B and C for trains 1, 2, 3, 4 and 5 show the average vertical displacements were about 0.6 mm. This value is approximately 4 times smaller than the maximum average vertical displacements that occurred in the EPS embankment along the FrontRunner commuter rail line. This is due to the small dead and live load in the case of the light rail line.

3.5 Conclusions

The FrontRunner commuter rail south line extends from Salt Lake City to Provo, Utah. UTA used EPS in the embankments along this line at Corner Canyon in Draper, Utah in order to minimize the vertical stress and subsequent consolidation settlement of the foundation soils underlying a concrete box culvert. This site was selected in this study to monitor the dynamic rail deflection because the site has both EPS geofoam and earthen embankments. Similarly, the light rail green line at River Trail was selected to monitor dynamic deflection. Accelerometer arrays were deployed to measure the acceleration time histories of several trains passing through this area. Subsequently, these time histories were baseline corrected and filtered to produce estimates of the displacement

time history.

In addition, a low cost optical technique for vertical deflection measurement was developed. The method was used to measure the deflection in the laboratory and the deflection was compared with LVDT results. The percentage difference of results from these two methods was around 2 percent. However, this method had some limitations in the field. Wind, elevation of site and vibration from trains were major constraints for obtaining accurate results; hence the optical technique was not successfully used to obtain field estimates of deflection. However, this method may still prove to be applicable for laboratory use, or for situations where the conditions for field deployment are more favorable.

Results from the accelerometer array show the maximum and average displacements for the sleepers positioned on the EPS embankment were about 6 mm and 2 mm, respectively, for the FrontRunner system. The same system constructed on earthen embankment underwent a maximum and average displacement of 22 mm and 7.5 mm, respectively. Therefore, the average displacement occurring on the EPS embankment was about 25 percent of that incurred by the earthen embankment.

The average value of the vertical displacements occurring atop the EPS embankment for the light rail (i.e., TRAX) line were about 0.6 mm. This average value is almost four times smaller than the average displacement value measured for the FrontRunner system. This suggests that deflections of rail systems on EPS embankments are relatively small and therefore have a similar or better performance than that of earthen embankments. A larger amount of deflection in case of the earthen embankment could have been because of lateral compression of soil due to combined dead and live loads, whereas in the case of

EPS embankment, lateral compression is less likely to occur due to the inherent property of EPS material.

3.6 References

AREMA (2007). "Manual for Railway Engineering." American Railway Engineering and Maintenance-of Way Association, Lanham, Maryland, USA.

Bowness, D., Lock, A., Powrie, W., Priest, J., and Richards, D. "Monitoring the dynamic displacements of railway track." *Proc., Institution of Mechanical Engineers, Part F: Journal of Rail and Rapid Transit*, 13-22.

Chebli, H., Clouteau, D., and Schmitt, L. (2008). "Dynamic response of high-speed ballasted railway tracks: 3D periodic model and in situ measurements." *Soil Dynamics and Earthquake Engineering*, 28(2), 118-131.

Frydenlund, T. E., Myhre, O., Refsdal, G., and Aaboe, R. (1987). "Plastic foam in road embankments."Norwegian Road Research Laboratory, Norwegian Edition 61 (in English).

Ho, S., Tsang, W., Lee, K., Lee, K., Lai, W., Tam, H., and Ho, T. "Monitoring of the vertical movements of rail sleepers with the passage of trains." *Proc., Institution of Engineering and Technology International Conference on Railway Condition Monitoring, 2006*, IEEE, 108-114.

Ling, X.-Z., Chen, S.-J., Zhu, Z.-Y., Zhang, F., Wang, L.-N., and Zou, Z.-Y. (2010). "Field monitoring on the train-induced vibration response of track structure in the Beiluhe permafrost region along Qinghai–Tibet railway in China." *Cold Regions Science and Technology*, 60(1), 75-83.

Lu, S. (2008). "Real-time vertical track deflection measurement system." Ph.D. thesis, University of Nebraska, Lincoln, Nebraska, USA.

Madshus, C., and Kaynia, A. (2000). "High-speed railway lines on soft ground: dynamic behaviour at critical train speed." *Journal of Sound and Vibration*, 231(3), 689-701.

Measurement-Specialities (2015). "Model 4630 Accelerometer." <http//www.meas-spec.com/downloads/4630.pdf>. (March 4, 2015).

O'Brien, A. (2001). "Design and construction of the UK's first polysterene embankment for railway use." *Proc., 3rd International EPS Geofoam Conference,* Salt Lake City, Utah, USA.

Pinto, N., Ribeiro, C., Mendes, J., and Calçada, R. (2009). "An optical system for monitoring the vertical displacements of the track in high speed railways." *Proc., 3rd International Integrity Reliability and Failure,* Portugal, 1-9.

Priest, J., and Powrie, W. (2009). "Determination of dynamic track modulus from measurement of track velocity during train passage." *Journal of Geotechnical and Geoenvironmental Engineering*, 135(11), 1732-1740.

Psimoulis, P. A., and Stiros, S. C. (2013). "Measuring deflections of a short-span railway bridge using a robotic total station." *Journal of Bridge Engineering*, 18(2), 182-185.

RTDAQ (2011). "Campbell Scientific, Inc.", Logan, Utah.

SeismoSoft (2015). "SeismoSignal 5.1.0." <http//www.seismosoft.com/en/Download.aspx>. (February 17, 2015).

CHAPTER 4

LABORATORY INVESTIGATION OF POSTCYCLIC CREEP STRAIN BEHAVIOR OF EPS GEOFOAM FOR CYCLIC LOADINGS CAUSED BY EXTREME EVENTS

4.1 Introduction

The use of block-molded EPS geofoam in the field of geotechnical engineering is not new. The Norwegians used geofoam blocks as lightweight fill materials to build road embankments over soft soils in the early 1970s (Refsdal, 1985; Aaboe, 1987). It has been used in embankments (Elragi, 2000; Zou et al., 2000; Newman et al., 2009), earth retaining structures (Elragi, 2000; Trandafir et al., 2010), pavements (Beinbrech and Hillmann, 1997; Duškov, 1997), buried pipes (Elragi, 2000; Lingwall, 2011) and backfill for bridge abutments (Elragi, 2000; Snow and Nickerson, 2004; Stuedlein and Negussey, 2013).

In the past, embankments with conventional fill materials like soil and rock have been used as bridge support systems. Similar to using a geosynthetical reinforced soil (GRS) for bridge abutments, EPS geofoam can be used as the bridge support system without the need for installation of a deep foundation system. The Norwegian Public Roads Administration (NPRA) has pioneered this technology for applications at quick clay sites to support relatively light-weight, steel, concrete and wooden bridge structures having relatively short spans (i.e., about 100 m). These embankments have demonstrated acceptable levels of

performance in terms of the bearing capacity and creep settlement of the EPS and underlying foundation soils (Aaboe and Frydenlund, 2011).

One of the primary design issues regarding an EPS bridge support system is that of the acceptable or allowable stress to be used in the design of the EPS embankment. If the stresses from the dead and live loads are too high, then unacceptable construction settlement and creep may occur. To address this issue, the National Cooperative Highway Research Program (NCHRP 529) recommends limiting the vertical stress in the EPS block resulting from the combination of dead and live loads to a value corresponding to the unconfined compressive resistance of the EPS block measured at 1 percent axial strain.

However, the primary focus of the guidance found in NCHRP 529 is to provide design criteria for EPS embankment systems, and not EPS bridge support systems. The former system has relatively modest requirements in terms of vertical support, whereas the latter system must directly support the weight of the bridge. Unfortunately there are no guidelines developed for EPS bridge support systems focusing on the "acceptable" or allowable stress under the combination of dead loads (bridge and pavement section weight) and live loads (e.g., traffic, earthquake, impact, etc.).

At first, it seems reasonable to adopt the recommended 1 percent elastic limit stress of NCHRP 529. However, EPS bridge support systems must also be designed to resist the design dead load and extreme loads such as those from earthquakes. Because of the relatively large magnitude of potential stresses from these loadings, the combination of the stresses induced by such loads may temporarily exceed the "1 percent elastic limit stress" guideline of NCHRP 529. The consequences of the temporary exceedance may result in additional creep deformation of the block within the EPS embankment. Therefore, the

purpose of this study is to explore the long-term settlement associated with the combination of dead and cyclic loading conditions.

There has been previous work focusing on the behavior of EPS under cyclic loadings (Duškov, 1997; Athanasopoulos et al., 1999; Trandafir et al., 2010); however, these studies varied considerably regarding their objectives, methods and the conditions for cyclic loading (i.e., amplitude, rate, method of application, etc.). None of these tests explores effects of cycling on the postcyclic creep behavior. Duškov (1997) conducted uniaxial strain-controlled, cyclic loading tests on EPS geofoam to study the impact of traffic loading on pavement/geofoam systems. Permanent vertical deformations ranging from 0.4 to 0.7 percent were observed for the applied range of cyclic axial stresses. Athanasopoulos et al. (1999) conducted resonant column and cyclic uniaxial tests under strain-controlled conditions on specimens with average densities of 12.4 and 17.1 kg/m^3 to develop the dynamic properties of EPS for dynamic response modeling. These test results indicated the geofoam density significantly affected the dynamic shear modulus, whereas no substantial effect of density on the damping ratio was noticed. Trandafir et al. (2010) conducted stress-controlled cyclic uniaxial tests on EPS geofoam specimens with densities of 15, 25 and 32 kg/m^3 in both the elastic and plastic strain ranges. From these test results, cyclic strain amplitudes of up to 0.87 to 1.0 percent were considered as threshold amplitudes for viscoelastic and visco-elasto-plastic behavior, respectively. Trandafir et al. (2010) found that EPS geofoam showed yielding and elasto-plastic-visco-plastic behavior at strains greater than about 1 percent.

For the bridge support applications, it is expected that the dynamic strain levels will approach or exceed 1 percent strain for a limited time interval(s) during moderate to major

earthquakes. However, if the linear range temporarily exceeds, it becomes necessary to quantify the seismic and postseismic deformation behavior of the EPS blocks in terms of permanent cyclic and postcyclic creep deformation. Ultimately from a design perspective, it is important that the total permanent deformation from these two sources remain within tolerable limits so that the serviceability or function of the bridge support system is not compromised. As a preliminary design goal, it is desirable that the total permanent strain incurred from cyclic and creep be limited to about 2 percent in a 50-year post-construction period.

To explore this concept further, it became necessary to conduct laboratory cyclic and postcyclic creep testing to determine the total permanent strain (cyclic + postcyclic creep) that may occur under the combination of static (i.e., dead) and earthquake (cyclic) loads. The main objectives of this study are to: (1) quantify the total permanent strain considering both postcyclic creep strain and permanent cyclic strain induced in the EPS support system by an earthquake loading, (2) quantify these strains for various densities of EPS specimens.

These issues were explored by performing a series of strain-controlled monotonic and stress-controlled uniaxial cyclic tests where the associated postcyclic creep measurements were made on EPS geofoam specimens of varying density. The testing was done on the cyclic uniaxial device housed in the Soil Mechanics Laboratory of the University of Utah. Because EPS embankments, as typically constructed, have negligible confinement, all tests were done without confinement. In addition because higher densities of EPS may be required for bridge support systems, this study used densities of EPS 25, EPS 29 and EPS 39 (i.e., kg/m^3) for the cyclic uniaxial testing; however specimens of EPS 15 and EPS 19 were also evaluated in monotonic uniaxial tests. It is hoped that the obtained and interpreted

test results will be valuable to designers who consider the effects of cyclic loading on EPS systems.

4.2 Experimental Setup

The uniaxial equipment for testing is shown in Figure 4.1 and was manufactured by GeoComp Corp. of Foxborough, Massachusetts. It consists of the LoadTrac, FlowTrac, and a hydraulic power unit. The LoadTrac consists of a load frame, load cell, displacement transducer and uniaxial cell. Two FlowTrac pumps, one for the sample pressure and the other for the cell pressure are available but were not used. The hydraulic power unit was connected with the servo controller. The power unit in conjunction with servo provides the cyclic loading on the specimen.

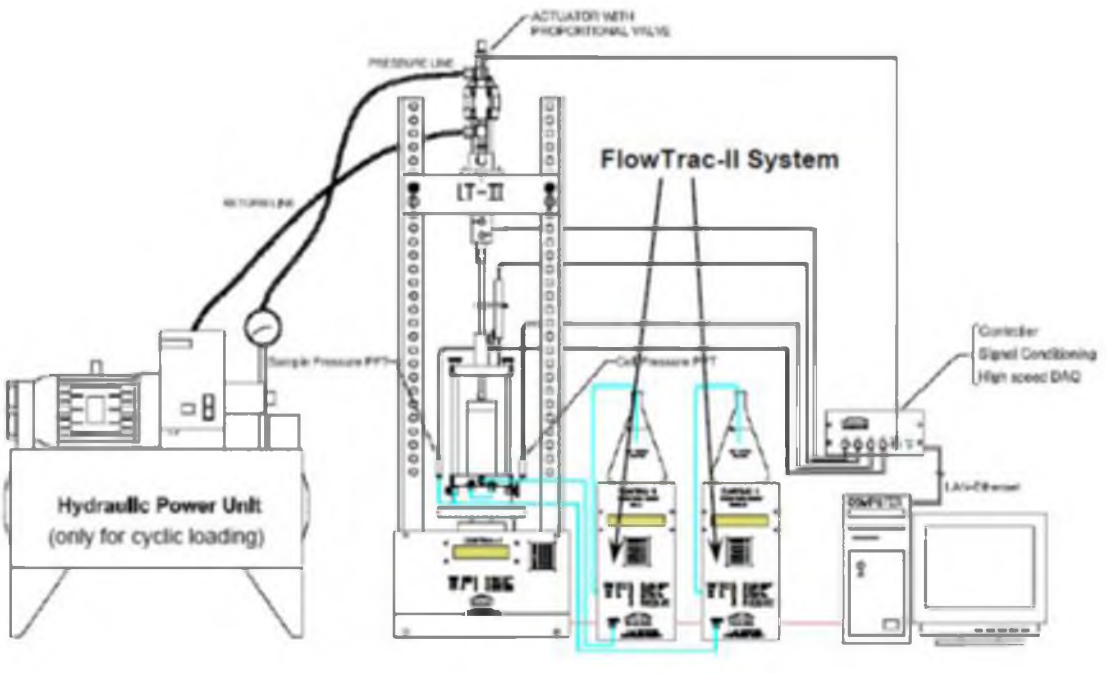

Figure 4.1. Uniaxial equipment available at the University of Utah, after Geocomp (2006)

A series of monotonic uniaxial testing, cyclic uniaxial testing and the associated post-cyclic creep measurements were done on EPS geofoam specimens using the above system. The testing system utilized a state of the art microprocessor with controlled and fully-automated test equipment. The system is a complete, self-contained unit with all of the capabilities required to perform fully automated cyclic tests and to automatically record and store experimental data. The system had the capability for applying both monotonic and cyclic loadings. The specimen selected for this study were of sizes 50 mm, 71 mm and 100 mm diameter, which can be accommodated in the plexiglass cell. For this study, a 100 mm diameter cell was used.

4.3 Experimental Procedure

The experimental laboratory test program was divided into three series of tests: monotonic uniaxial testing, cyclic uniaxial testing and postcyclic creep measurement.

4.3.1 Monotonic Uniaxial Tests

In these tests, EPS 15, EPS 19, EPS 25, EPS 29 and EPS 39 were used. The monotonic uniaxial test was done into two steps. The first was preparation of sample and the second was monotonic loading.

4.3.1.1 Sample Preparation

Cylindrical specimens of 100 mm diameter by 100 mm height was used for testing. An example specimen is shown in Figure 4.2. The dimension and weight of the sample was obtained to calculate the bulk density of each specimen. A porous stone was placed at the lower platen of the LoadTrac to ensure a flat and even surface.

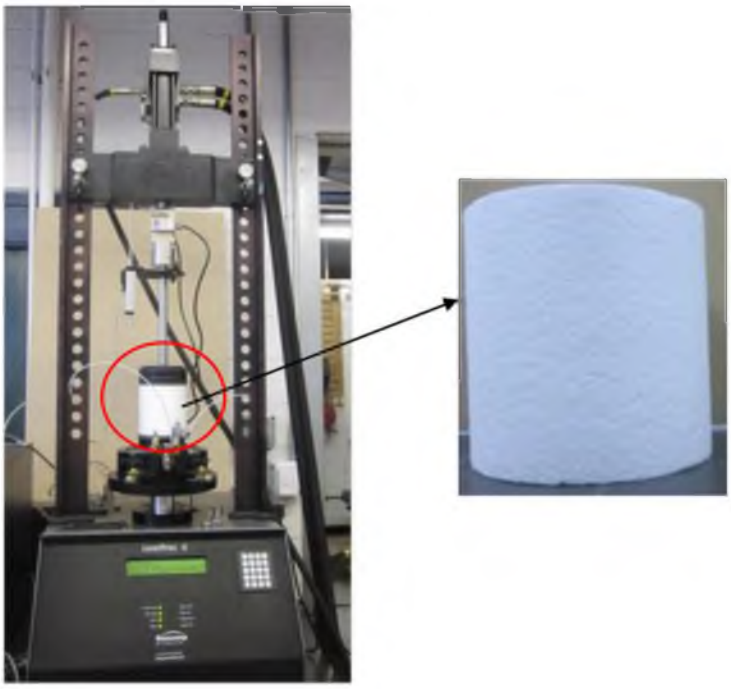

Figure 4.2. A complete setup EPS sample for monotonic and cyclic uniaxial test

The sample was then placed above the porous stone and another porous stone was placed at the top of the sample. The completed setup of the sample ready for testing is shown in Figure 4.2.

4.3.1.2 Monotonic Loading

The sample was then loaded under a strain-controlled condition at a rate of 10 percent per minute. Once the loading had been completed, the data were collected and plotted to produce the relation between deviatoric stress versus axial strain. From plots of this type, the compressive resistance of the EPS corresponding to uniaxial stress values of 1 percent, 1.5 percent, 1.75 percent, 2 percent, 5 percent and 10 percent axial strain levels were determined.

4.3.2 Cyclic Uniaxial Tests

The cyclic uniaxial test was done in three steps: sample preparation, consolidation and cyclic loading. For these tests, specimens of EPS 25, EPS 29 and EPS 39 were used.

4.3.2.1 Sample Preparation

The same specimen dimensions used for these monotonic test were used in the cyclic tests. The density of each specimen was calculated and recorded. The distribution of specimen density for the monotonic and cyclic uniaxial tests is shown in Figure 4.3.

4.3.2.2 Consolidation

In this step, a constant static deviatoric stress (σ_{ds}) was applied on the sample until the elastic and creep strain were essentially completed. The applied stress corresponded to the stress level obtained at 1 percent axial strain based on the results of the monotonic uniaxial tests. The duration at which the elastic plus creep strain ceased was previously determined from several trials for EPS of all densities. The duration of the consolidation phase was determined by plotting the percentage of vertical strain against time and logarithmic of time. The strain plots for EPS 25 at an applied deviatoric stress of 1.5 percent compressive resistance are shown in Figures 4.4 and 4.5. From the data in these figures, it is clear that creep strain dominated the behavior after about one minute of application of deviatoric stress and was more or less occurring at a constant rate. Similar trends were observed for other EPS densities. Thus, the time for precyclic consolidation was set to 30 minutes for all EPS specimens for the various densities tested by this research.

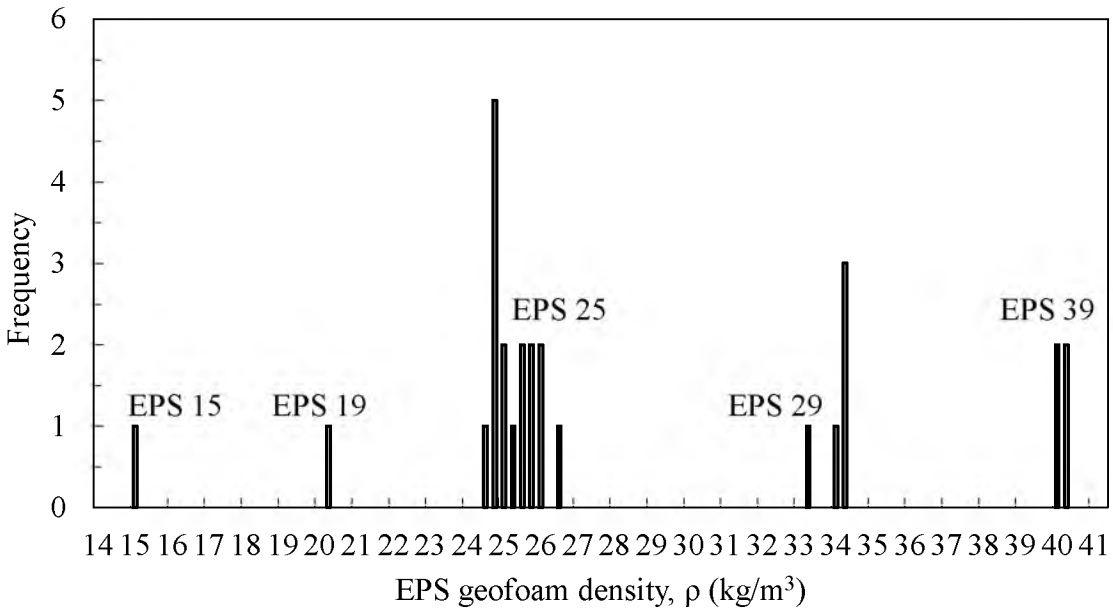

Figure 4.3. Density distribution of tested EPS geofoam specimens

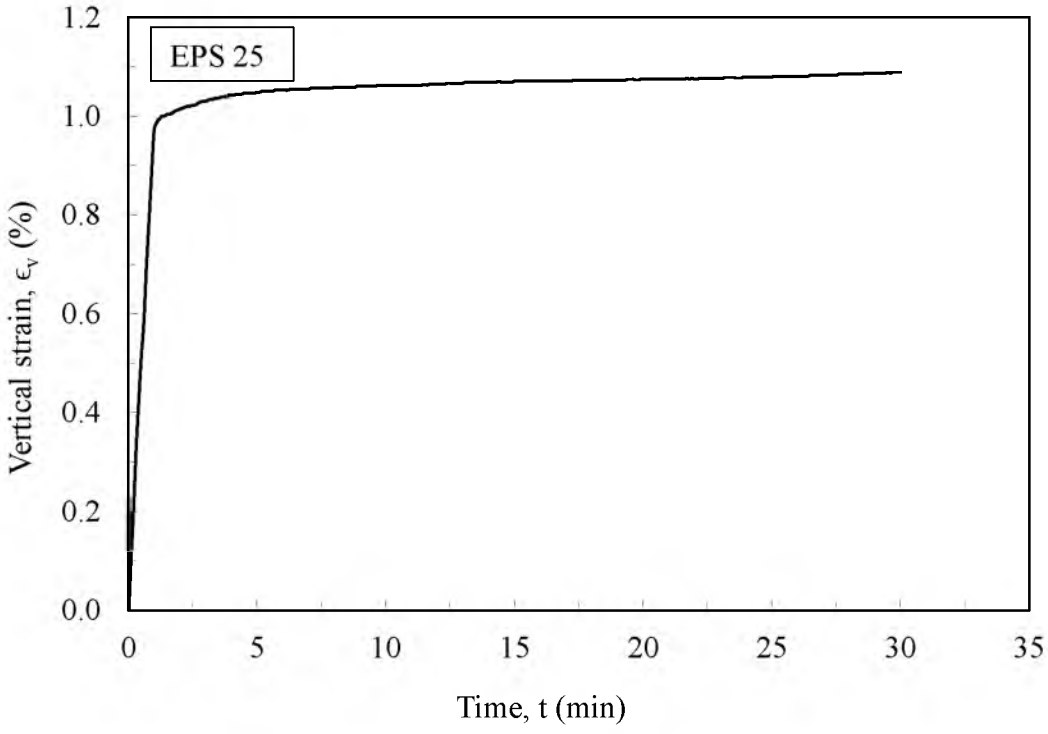

Figure 4.4. Vertical strain versus time for precyclic test

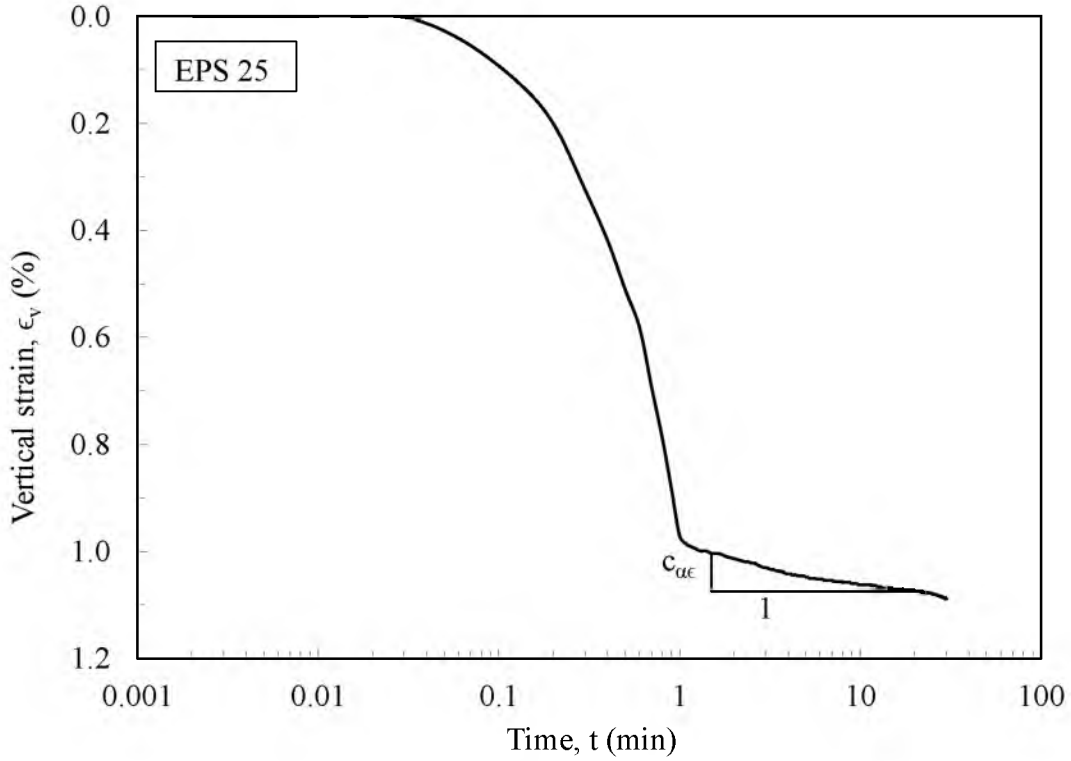

Figure 4.5. Vertical strain versus logarithmic of time for precyclic test

4.3.2.3 Cyclic Loading

The relationship between number of equivalent stress cycles and earthquake magnitude was developed by Seed and Idriss (1982). On the basis of this study, 5, 15 and 30 cycles were selected in this study to represent short, moderate and long durations of seismic excitation, respectively. The frequency (*f*) of cycling was set to 1 Hz and the sampling rate for the data points was set to 20 Hz.

After the consolidation phase, a cyclic deviatoric stress ($\Delta\sigma_{dc}$) was applied to the samples using stress levels corresponding to 1.5 percent, 1.75 percent, 2 percent and 5 percent total axial strain obtained from the monotonic tests. For example, if the goal was to reach a stress level associated with 1.5 percent total strain, then the cyclic deviatoric

produced an additional 0.5 percent strain in addition to the 1.0 percent strain that was obtained during the consolidation phase. Hence, the magnitude of the cyclic deviatoric stress was calculated by subtracting the stress level corresponding to 1 percent axial strain (obtained from the monotonic tests results) from the stress level corresponding to 1.5 percent, 1.75 percent, 2 percent and 5 percent total axial strain (i.e., total strain produced by monotonic and cyclic loading). For EPS 25, cyclic uniaxial tests were conducted at stress levels corresponding to 1.5 percent, 1.75 percent, 2 percent total axial strain using 5, 15 and 30 cycles. Hence, the additional cyclic deviatoric strain components corresponding to these total strain values are 0.5, 0.75 and 1.0 percent, respectively. The cyclic triaxial test result of EPS 25 at cyclic deviatoric stress corresponding to 0.5 percent strain under 15 cycles is shown in Figure 4.6.

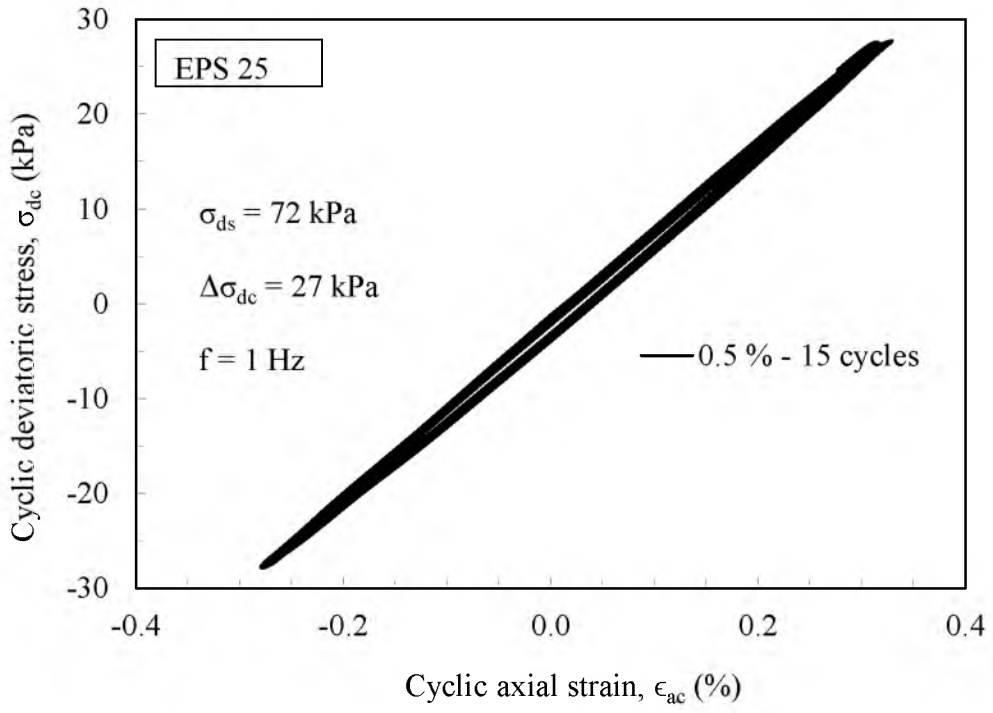

Figure 4.6. Cyclic deviatoric stress versus cyclic axial strain

4.3.3 Postcyclic Creep Tests

The postcyclic creep tests were conducted using the same cyclic equipment. The post-cyclic creep strain is the vertical strain associated with the vertical load applied after cycling, which for the field condition represents the long-term dead load of the EPS bridge support system. In these tests, the samples were subjected to a postcyclic constant uniaxial vertical stress corresponding to the stress level at 1 percent axial strain obtained from the monotonic tests. In the cyclic testing equipment, there was no provision of reapplying the vertical load on the specimen immediately after the cyclic loading without unloading the sample. The system is programed to automatically unload after cycling. Therefore the sample was reloaded back to the appropriate stress level and allowed to undergo postcyclic creep strain. The sample was reloaded back to a vertical stress level equivalent to 1 percent axial strain obtained from the monotonic tests. In addition, a few tests were conducted at higher postcyclic stress levels to explore the influence of higher stress levels on the post-cyclic creep behavior.

The duration of application of the load for the postcyclic creep measurements was determined from several trials. In order to establish the postcyclic duration, plots were made of the percentage of total axial vertical strain versus arithmetic time and logarithm of time plots. (The total axial strain represents 1 percent precycling monotonic axial strain and an additional 0.5 percent single amplitude cyclic strain). The plot of vertical total strain against time and logarithm of time for EPS 25 at a stress level corresponding to 1.5 percent total strain and for 15 stress cycles is shown in Figures 4.7 and 4.8.

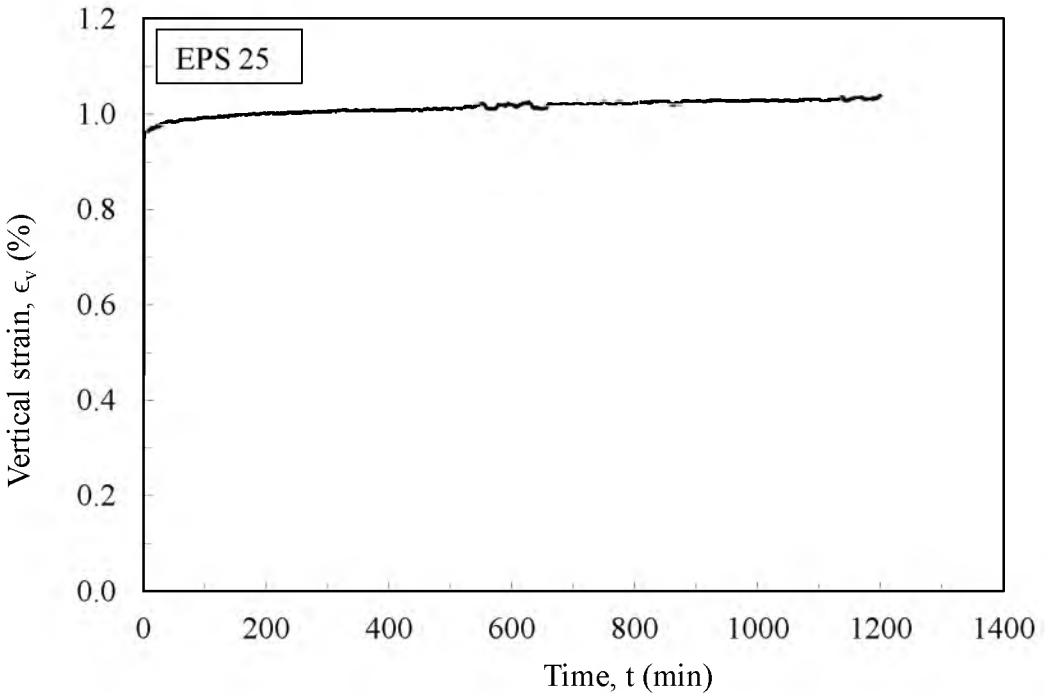

Figure 4.7. Vertical strain versus time for postcyclic test

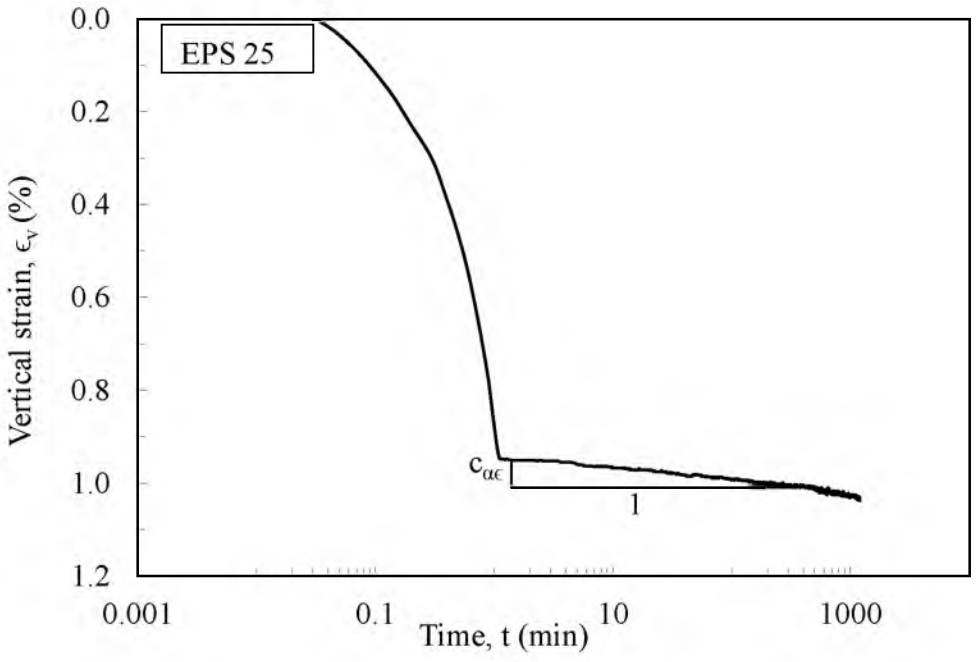

Figure 4.8. Vertical strain versus logarithm of time for postcyclic test

Based on the data in these figures, it is clear that the creep started after about one minute of postcyclic load and more or less reached a constant rate at about 20 hours. Therefore, all postcyclic creep tests were conducted for 20 hours.

4.4 Test Results

4.4.1 Monotonic Uniaxial Tests

The data from these tests were analyzed to find the relation of the deviatoric stress versus axial strain. The deviatoric stress is the ratio of the applied load per cross-sectional unit area for the specimen and the vertical strain is the ratio of displacement to the original height of the specimen. For these tests, a seating correction was made on the results. Subsequently, data plots were made for the adjusted values of deviatoric stress and vertical strain. The combined plots of EPS 15, EPS 19, EPS 25, EPS 29 and EPS 39 are shown in Figure 4.9. The combined plots of normalized vertical stress against vertical strain are given in Figure 4.10. The normalized vertical stress was calculated as the ratio of the recorded deviatoric stress to the deviatoric stress measured at 10 percent axial strain, normalized for the results from each individual test. The stress level at which nonlinearity began can also be seen in these figures. It is clear that the upper bound value of linear range was different for different densities of EPS. In addition, these figures show higher linear ranges for higher stiffness of EPS. The nonlinearity of EPS began at vertical strains equal to or greater than 1.5 percent for EPS 25, or greater, and increased for higher densities of EPS.

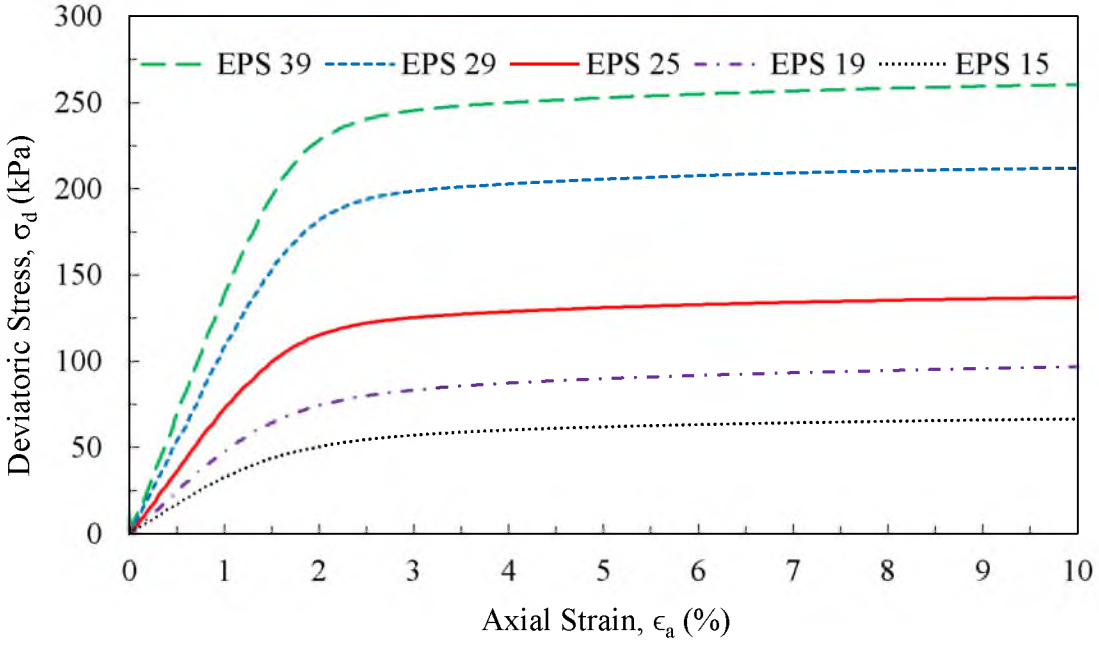

Figure 4.9. Deviatoric stress versus axial strain

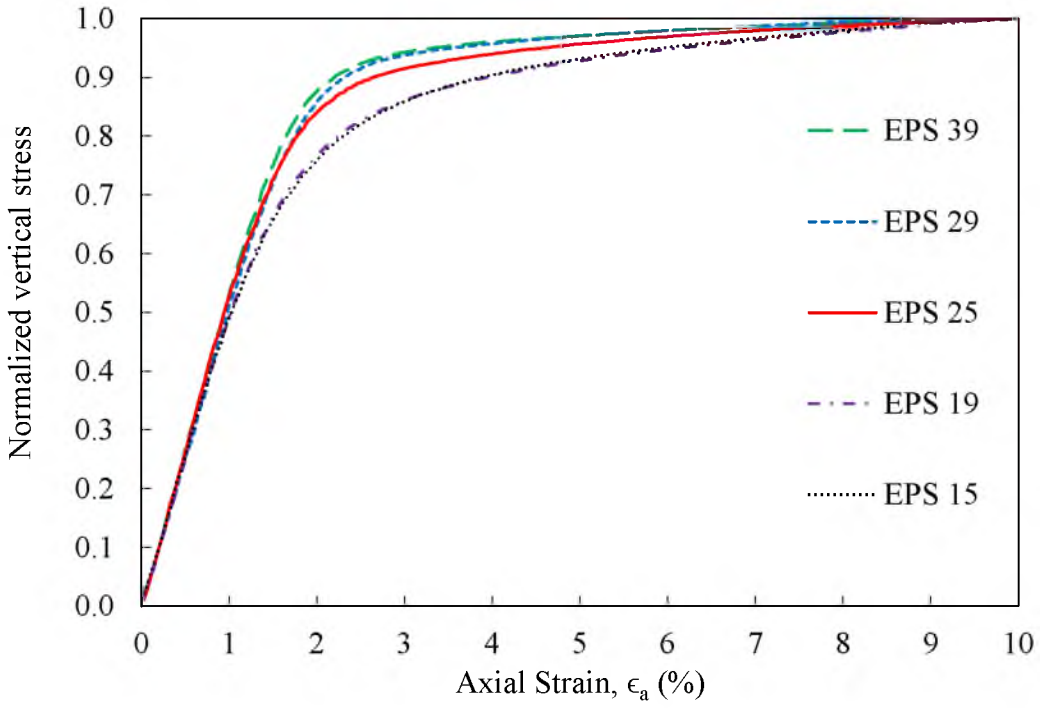

Figure 4.10. Normalized vertical stress versus axial strain

The plots of deviatoric stress versus axial strain were used to determine the stresses at 1 percent, 1.5 percent, 1.75 percent, 2 percent, 5 percent and 10 percent axial strain. The Young's modulus (E) is the slope of the linear elastic portion of stress-strain curve. The moduli for the various densities of EPS was determined from Figure 4.9 and tabulated in Table 4.1.

The relationship between Young's modulus and EPS density is obtained from the plot shown in Figure 4.11. The relationship given in Eq. (4.1) is a second order polynomial. A similar type of relationship was used by Horvath (1995).

$$E = 4.8719\rho^2 + 150.69\rho \tag{4.1}$$

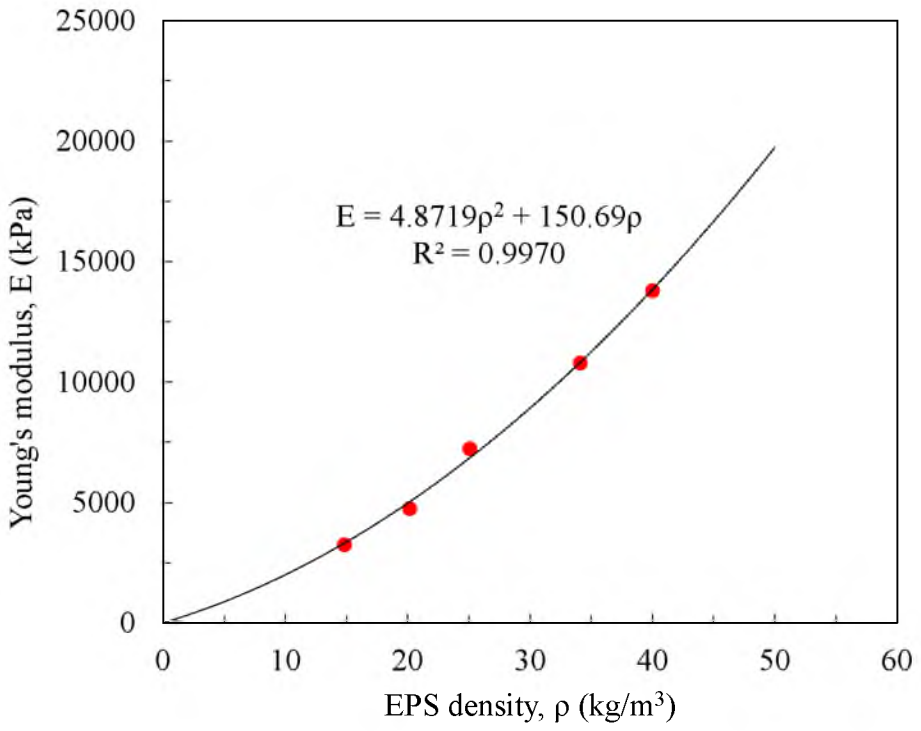

Figure 4.11. Correlation of Young's modulus and EPS density

Table 4.1. Summary of monotonic uniaxial test results

EPS type ----------	Density *(kg/m^3)*	Axial strain *(%)*	Young's modulus *(kPa)*	Static deviatoric stress *(kPa)*
EPS 15	14.8	1	3242	32
		1.5		43
		1.75		47
		2		50
		5		62
		10		66
EPS 19	20.2	1	4747	47
		1.5		64
		1.75		70
		2		74
		5		90
		10		97
EPS 25	25.1	1	7223	72
		1.5		99
		1.75		109
		2		115
		5		131
		10		137
EPS 29	34.1	1	10778	108
		1.5		152
		1.75		169
		2		182
		5		205
		10		212
EPS 39	40.1	1	13779	138
		1.5		196
		1.75		215
		2		228
		5		253
		10		260

4.4.2 Cyclic Uniaxial Tests

During the consolidation phase, measurements of the vertical displacement and elapsed time were collected. From this, the axial vertical strain versus elapsed time was calculated and plotted (Figures 4.4 and 4.5). The precyclic creep strain was determined from the ratio of vertical compression during loading once creep had initiated to the original height of the sample. This compression was similar to the secondary settlement as described in Holtz et al. (2010). The equation for secondary settlement (S_s) is,

$$S_s = C_{\alpha\epsilon} H_0 log \frac{t}{t_p} \tag{4.2}$$

In Eq. (4.2), $C_{\alpha\epsilon}$ is the secondary compression strain index, H_0 is the original height of the sample, t is the design time and t_p is the time required to complete the primary consolidation. In these tests, the dead load was applied for 30 minutes and the rate of creep strain measured. In order to calculate the potential creep strain for a 50-year service life period of a bridge support system, a linear extrapolation was done. The precyclic creep strain for various cases is tabulated in Table 4.2.

The cyclic uniaxial test results provided the vertical stresses and cyclic axial strain. The cyclic uniaxial deviatoric stress was then determined from the shear stresses. It was calculated as two times the shear stress minus the average static deviatoric stress. Following this, a plot was made between the cyclic uniaxial deviatoric stress and cyclic axial strain. The plot of cyclic uniaxial deviatoric stress versus cyclic axial strain for EPS 25 is shown in Figure 4.12. For these cases, the total vertical strain (1 percent static and 0.5 percent single amplitude cyclic strain) was 1.5 percent (Figure 4.12).

Table 4.2. Summary of precyclic creep tests

EPS type ----------	Density *(kg/m^3)*	Axial strain *(%)*	Static deviator stress *(kPa)*	Precyclic creep strain in 50 years *(%)*
EPS 25	25.0	1	72	0.311
	25.4	1	72	0.356
	25.5	1	72	0.351
	24.7	1	72	0.226
	25.6	1	72	0.267
	24.6	1	72	0.372
	24.9	1	72	0.389
	24.5	1	72	0.393
	25.8	1	72	0.250
	26.3	1	72	0.364
	24.5	1	72	0.436
	24.6	1	72	0.267
	24.8	1	72	0.286
EPS 29	33.8	1	108	0.441
	34.0	1	108	0.541
	33.2	1	108	0.352
	34.2	1	108	0.205
EPS 39	40.0	1	138	0.697
	41.1	1	138	0.243
	39.8	1	138	0.391

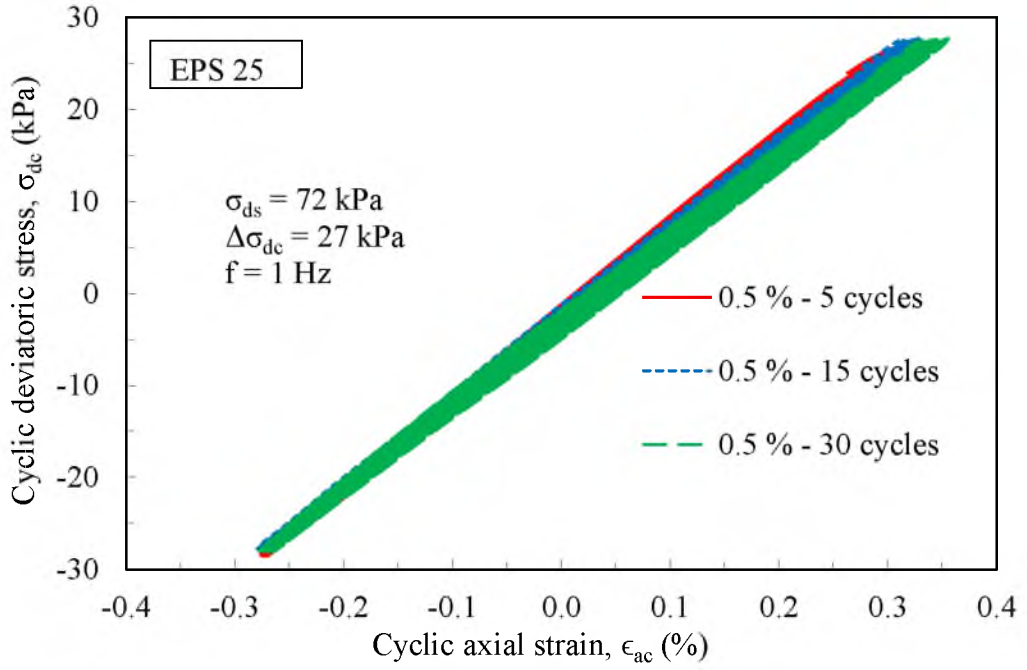

Figure 4.12. Results of cyclic uniaxial test at same level of cyclic deviatoric stresses but at different number of cycles (5, 15 and 30 number of cycles) on EPS 25

In this plot, the three samples were subjected to the same static and cyclic deviatoric stresses using three different numbers of total cycles (5, 15 and 30 cycles). Figure 4.13 shows the results of the cyclic uniaxial tests with three different levels of cyclic deviatoric stress and 5 different numbers of cycles. Figure 4.14 shows the results of the same deviatoric stresses but with three different numbers of applied cycles (5, 15 and 30 cycles). Figures 4.15 and 4.16 show the results of cyclic uniaxial test for four different levels of cyclic deviatoric stresses at 15 cycles and the same cyclic deviatoric stresses (corresponding to 2 percent total strain) at three different numbers of cycles on EPS 25, respectively.

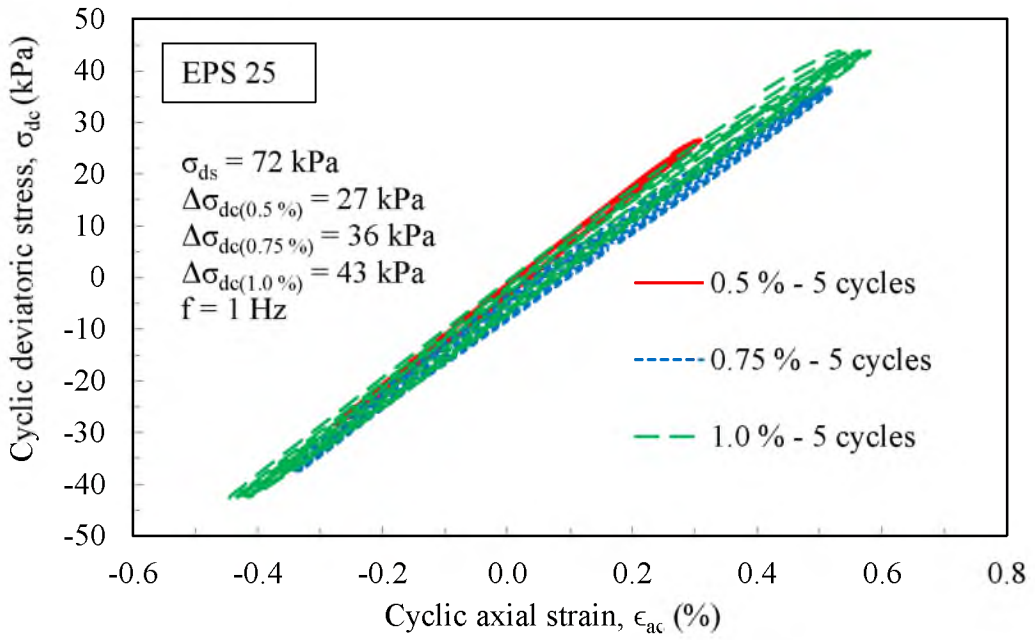

Figure 4.13. Results of cyclic uniaxial tests on three samples at three different cyclic deviatoric stresses with same number of cycles on EPS 25

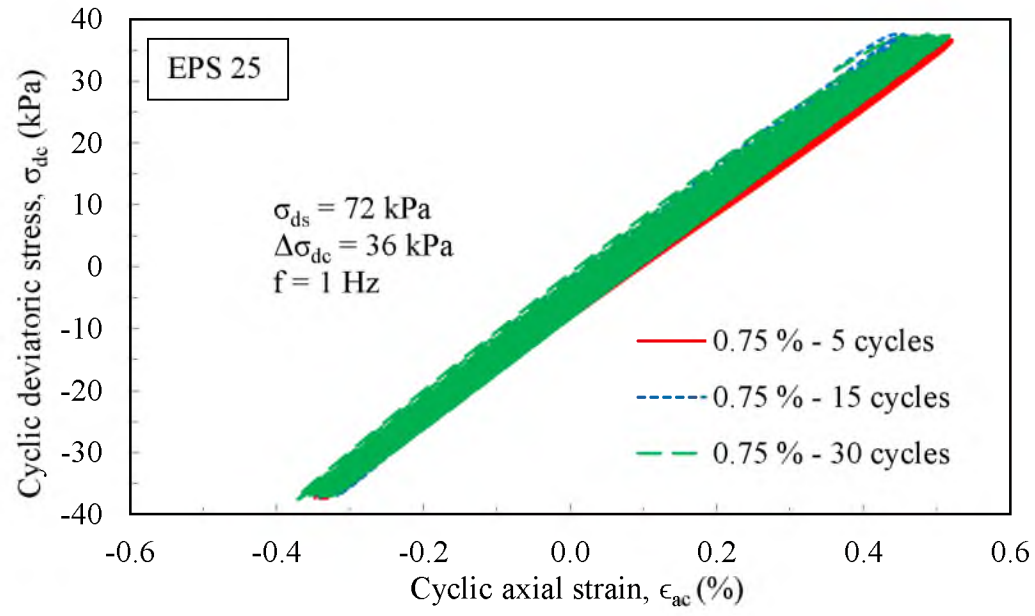

Figure 4.14. Results of cyclic uniaxial tests on three samples at same cyclic deviatoric stresses with three different numbers of cycles on EPS 25

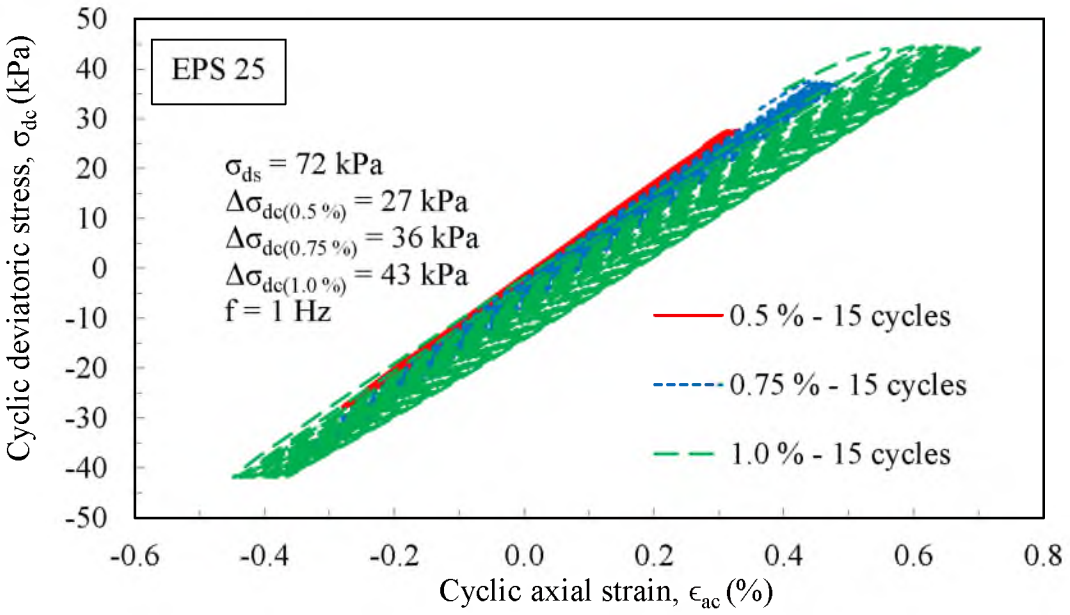

Figure 4.15. Results of cyclic uniaxial tests on four samples at 15 numbers of cycles with four different cyclic deviatoric stresses on EPS 25

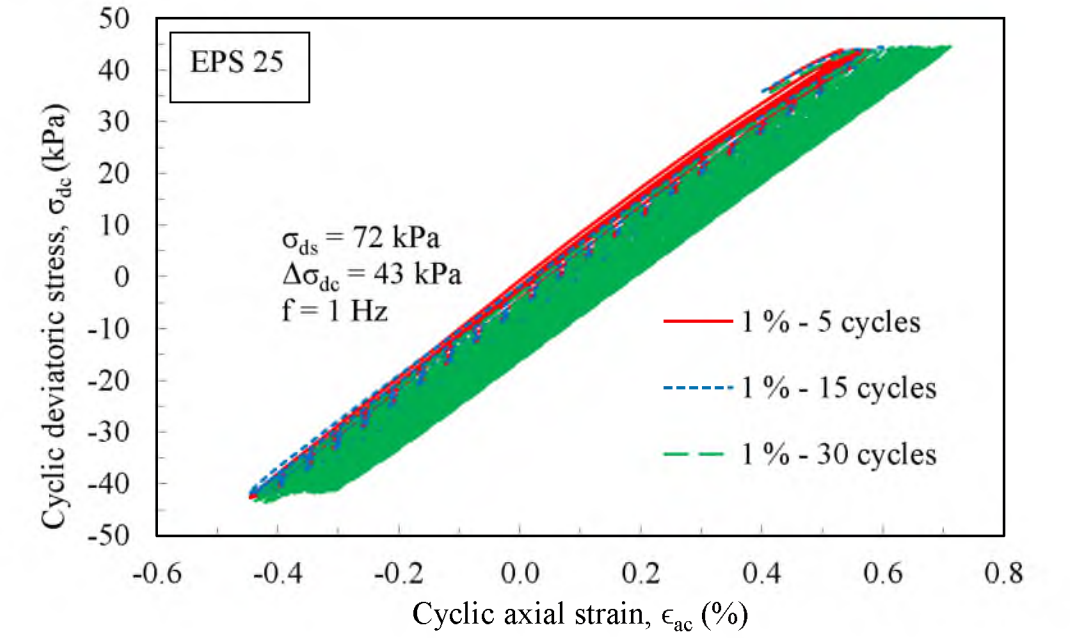

Figure 4.16. Results of cyclic uniaxial tests on three samples at same level of cyclic deviatoric stresses with three different numbers of cycles on EPS 25

Figure 4.17 shows the test results of cyclic uniaxial tests for three different levels of cyclic deviatoric stress at 30 cycles. Figure 4.18 shows the test results for three different levels of cyclic deviatoric stresses at 15 cycles for EPS 25. In the series of tests shown in Figure 4.18, the postcyclic deviatoric stress was set equal to the cyclic + monotonic deviatoric stresses which produced postcyclic loading equal to the peak loading obtained during cycling. Figures 4.19 and 4.20 show the cyclic uniaxial test results for two different levels of cyclic deviatoric stresses for three different numbers of cycles, and the same level of cyclic deviatoric stress at three different numbers of cycles performed on EPS 29 and EPS 39, respectively.

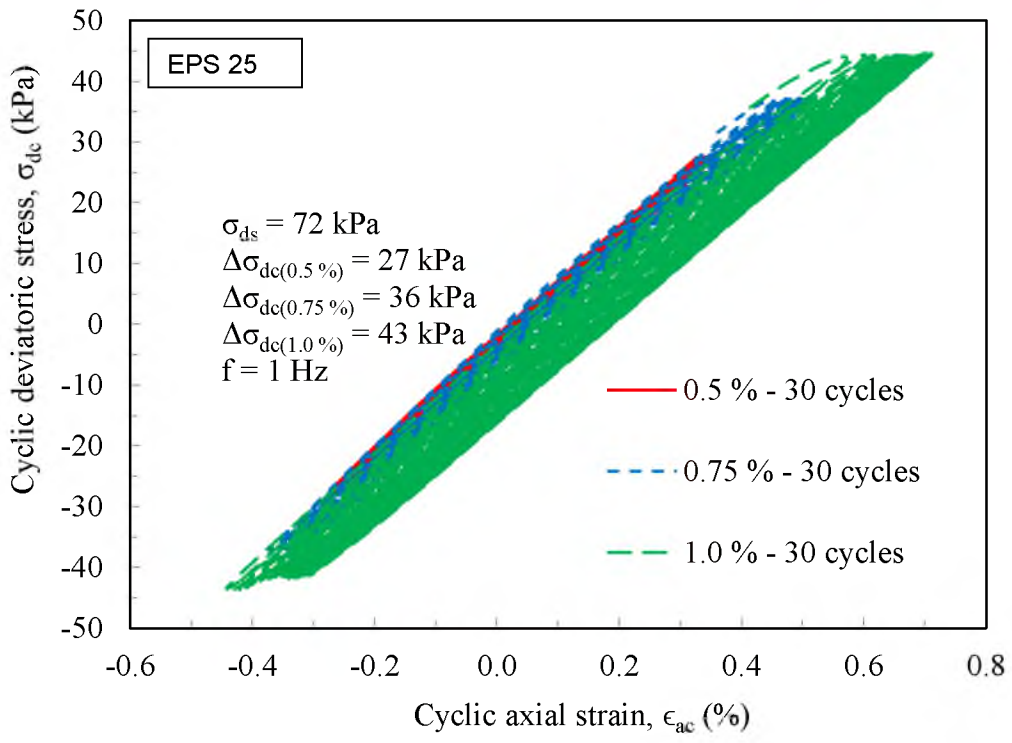

Figure 4.17. Results of cyclic uniaxial tests on three samples at three different levels of cyclic deviatoric stresses with 30 numbers of cycles on EPS 25

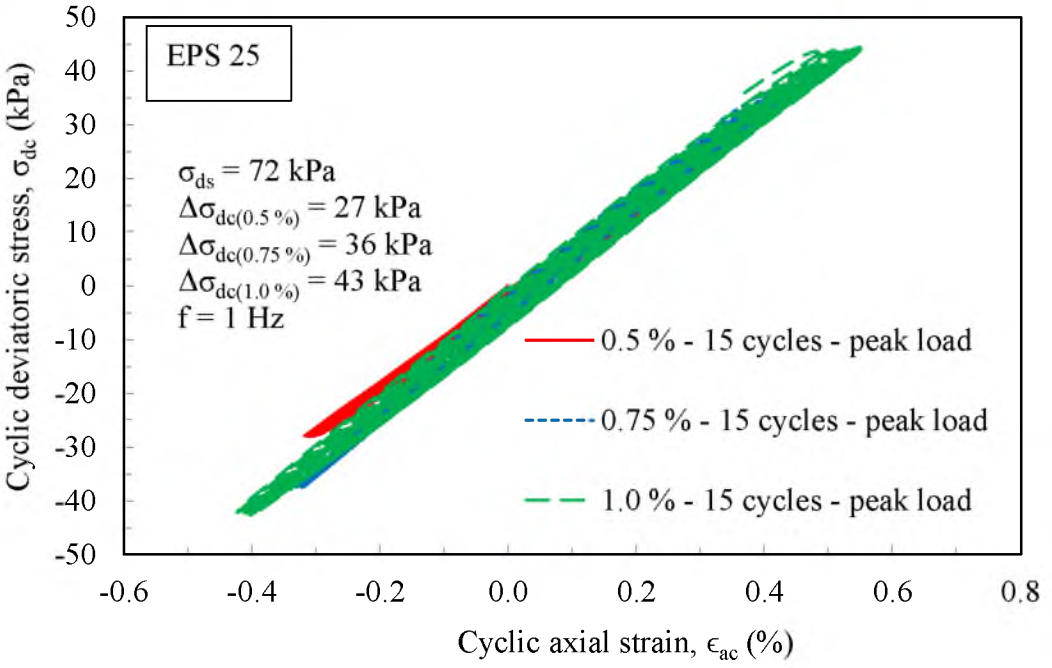

Figure 4.18. Results of cyclic uniaxial tests on three samples at three different levels of cyclic deviatoric stresses under peak load with 15 numbers of cycles on EPS 25

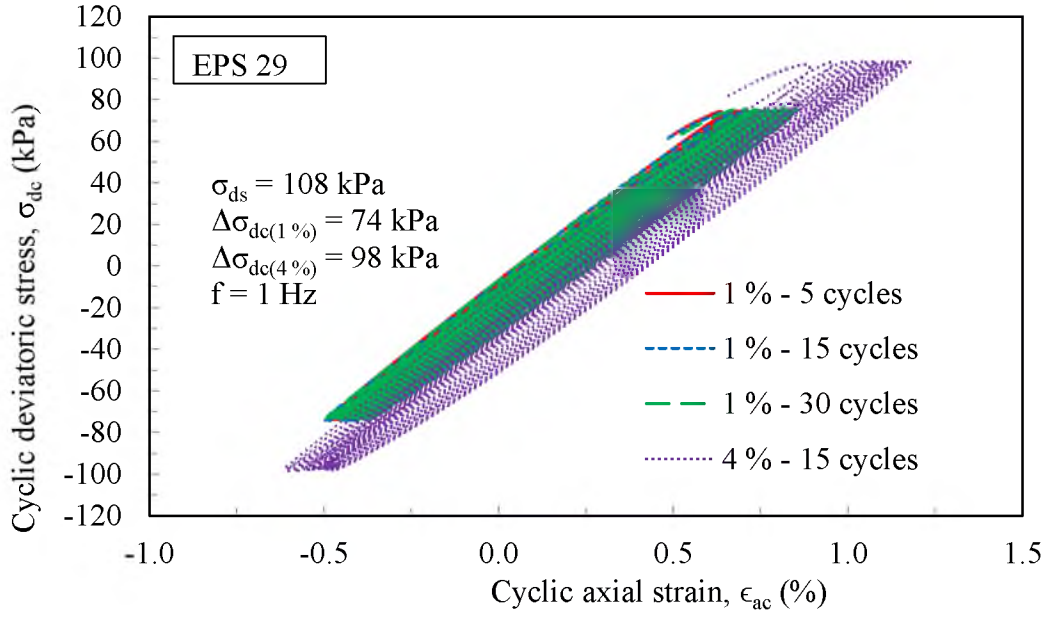

Figure 4.19. Results of cyclic uniaxial tests on four samples at two different levels of cyclic deviatoric stresses with three different numbers of cycles on EPS 29

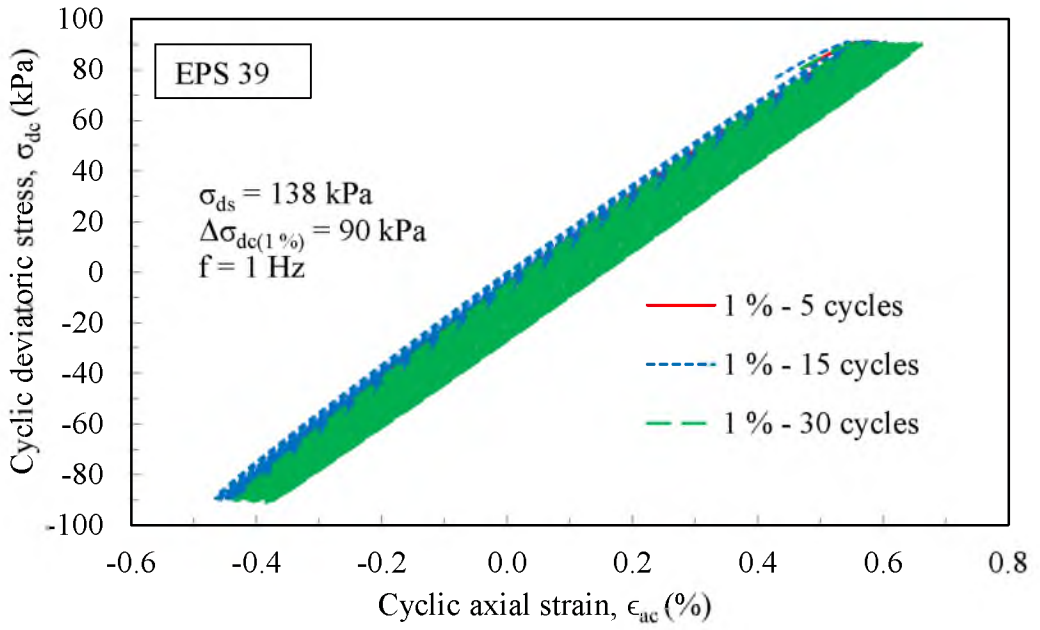

Figure 4.20. Results of cyclic uniaxial tests on three samples at same level of cyclic deviatoric stresses with three different numbers of cycles on EPS 39

Based on the results of the cyclic uniaxial tests, the EPS material showed larger amounts of permanent plastic strain for higher levels of cyclic deviatoric stress. This was also true for the tests where the deviatoric stress was kept constant but the number of cycles increased. Thus, the amount of permanent cyclic strain (i.e., walking distance of the hysteresis loop) increased with increasing applied cyclic deviatoric stress and with the number of applied stress cycles. These results were expected and consistent with the known cyclic behavior of EPS.

The degraded Young's modulus (E_c) for the cyclic testing was calculated as the secant modulus that represents the slope of the line drawn through the middle of the hysteresis loop (Figure 4.21). The load reversal point is the highest point of stress-strain loop, and the origin is the center of hysteresis loop. The mean value of the modulus was calculated by taking the average value of E_c using the average of E for the first and last cycles of test.

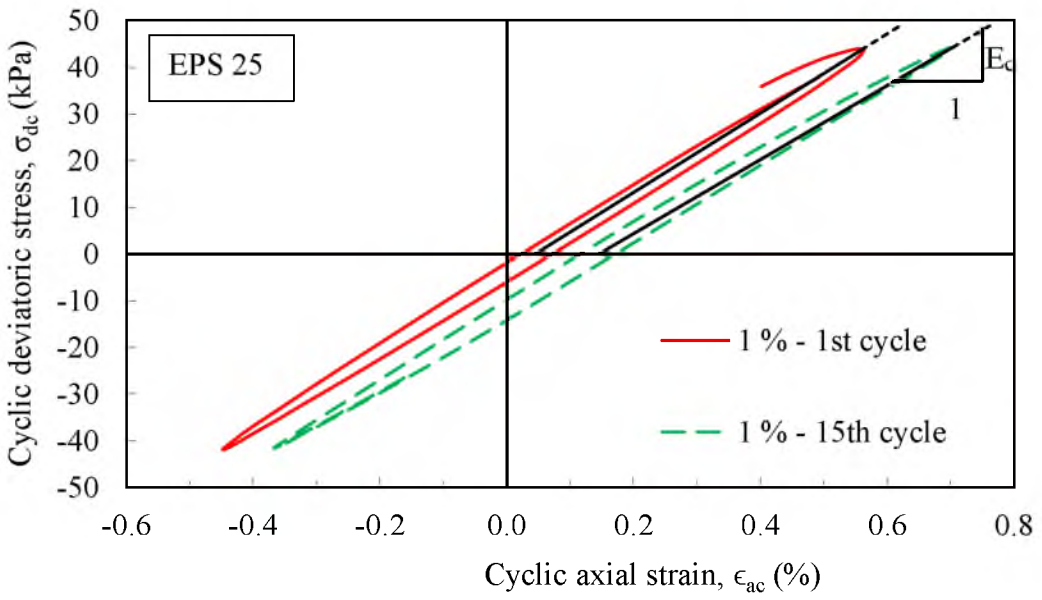

(a)

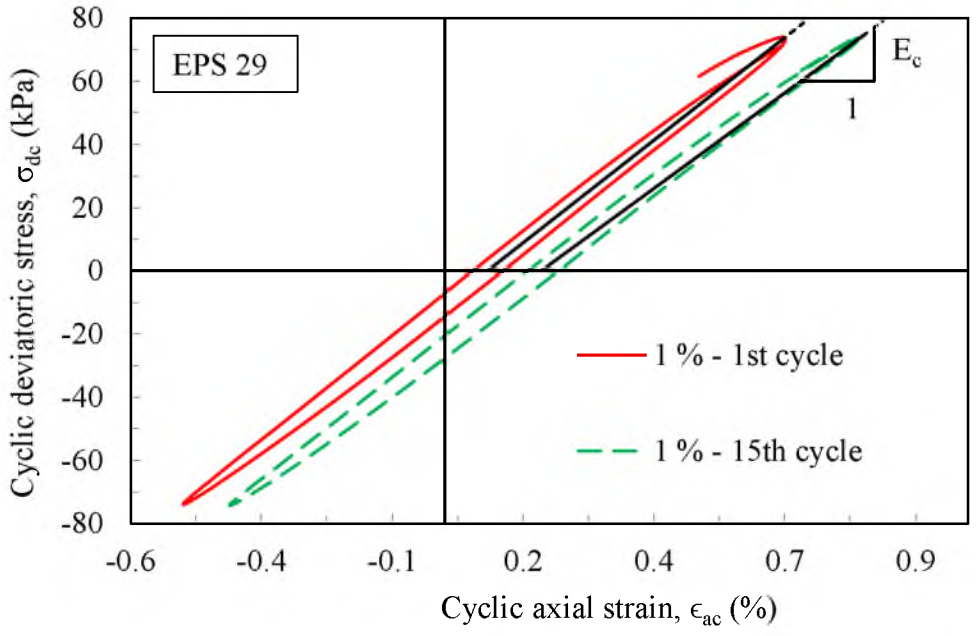

(b)

Figure 4.21. Cyclic stress-strain hysteresis loop and corresponding Young's modulus (E_c) (a) EPS 25 (b) EPS 29 and (c) EPS 39

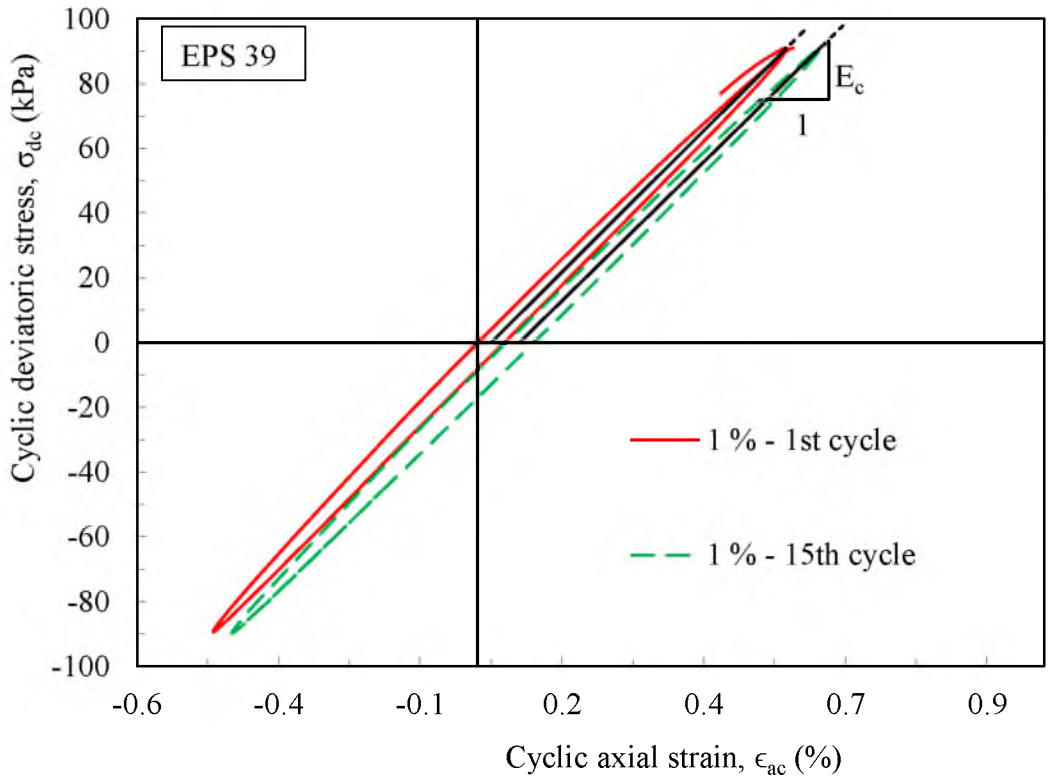

(c)

Figure 4.21. Continued

The plots of cyclic deviatoric stress versus cyclic axial strain to determine E_c for EPS 25, EPS 29 and EPS 39 at stress levels corresponding to 2 percent at 15 cycles are shown in Figure 4.21.

Since the material is within the linear range, or near the linear range for strain levels of about 2 percent or less, the mean shear modulus (G) was calculated from the relationship of G and E given in Eq. (4.2).

$$G = \frac{E}{2(1+\nu)} \tag{4.3}$$

In Eq. (4.3), v is the Poisson's ratio. The relation of v as a function of EPS density was given in Horvath (1995) is presented in Eq.(4.4).

$$v = 0.0056\rho + 0.0024 \tag{4.4}$$

The calculated values of v and G are given in Table 4.3. The plots of G and ρ are also shown in Figure 4.22, which provides the relationship of G and ρ. The shear modulus versus ρ relation was fitted with a second order polynomial equation, Eq. (4.5). This equation is similar to the relation between E and ρ given in Horvath (1995).

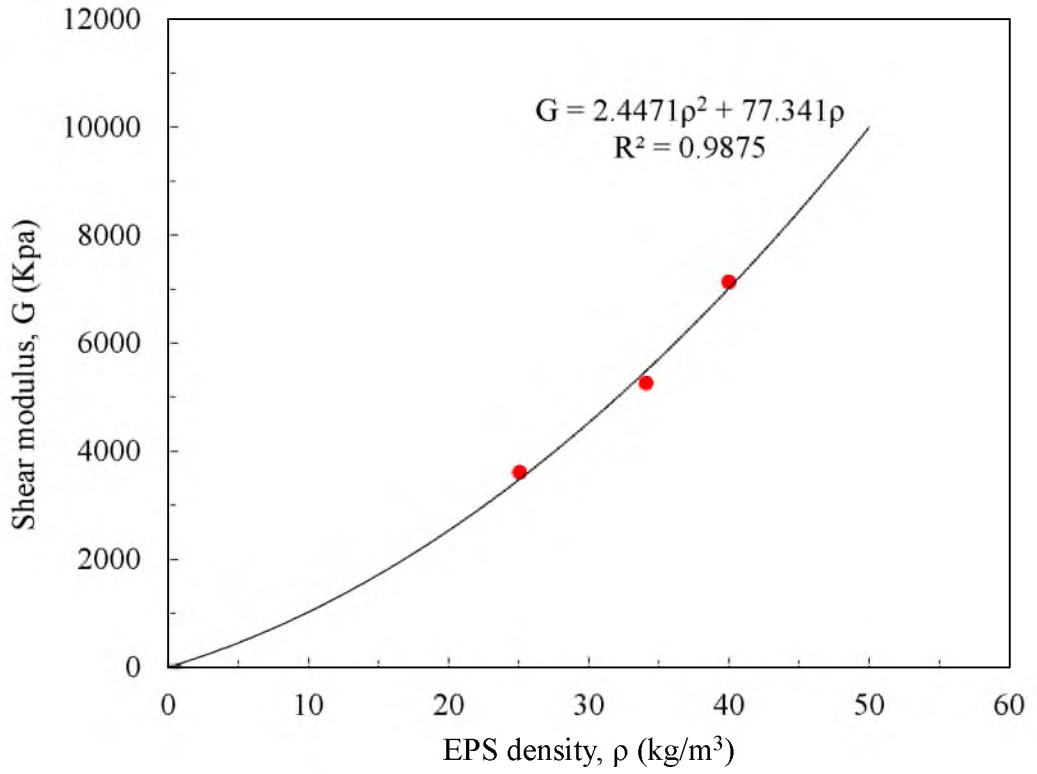

Figure 4.22. Correlation of shear modulus and EPS density

Table 4.3. Summary of cyclic uniaxial test results

EPS type	ρ	ϵ_a	N	σ_{ds}	$\Delta\sigma_{dc}$	σ_t	$E_{c\,(mean)}$	ν	$G_{c\,(mean)}$	ϵ_{ap}
----------	*(kg/m^3)*	*(%)*	----------	*(kPa)*	*(kPa)*	*(kPa)*	*(kPa)*	----------	*(kPa)*	*(%)*
	25.0	1.5	5	72	27	99	9796	0.142	4288	0.008
	25.4	1.5	15	72	27	99	9544	0.145	4168	0.014
	25.5	1.5	30	72	27	99	9234	0.145	4033	0.028
	24.7	1.75	5	72	36	109	8499	0.141	3725	0.030
	25.6	1.75	15	72	36	109	9284	0.146	4051	0.045
	24.6	1.75	30	72	36	109	8739	0.140	3833	0.065
EPS 25	24.9	2	5	72	43	115	8678	0.142	3800	0.048
	24.5	2	15	72	43	115	8209	0.140	3602	0.139
	25.8	2	30	72	43	115	8548	0.147	3727	0.140
	26.3	5	15	72	59	131	8455	0.150	3677	0.239
	24.5	1.5	5	72	27	99	8823	0.139	3872	0.029
	24.6	1.75	15	72	36	109	9428	0.140	4134	0.036
	24.8	2	30	72	43	115	9466	0.141	4148	0.067
	33.8	2	5	108	74	182	13457	0.192	5646	0.070
EPS 29	34.0	2	15	108	74	182	12547	0.193	5259	0.147
	33.2	2	30	108	74	182	12409	0.188	5222	0.179
	34.2	5	15	108	98	205	12606	0.194	5278	0.288
	40.0	2	5	138	90	228	17482	0.226	7127	0.032
EPS 39	41.1	2	15	138	90	228	17298	0.232	7018	0.060
	39.8	2	30	138	90	228	17548	0.225	7161	0.110

$$G = 1.1126\rho^2 + 127.31\rho \quad (4.5)$$

The axial strain under cyclic loading was calculated for all densities from the cyclic uniaxial test data and is depicted in Table 4.3. Figure 4.23 shows the repeated cyclic tests at which a cyclic deviatoric stress corresponding to 2 percent strain was applied in the first phase and a cyclic deviatoric stress corresponding to 1.5 percent strain was applied in the second phase. Similarly, Figure 4.24 reveals the repeated cyclic tests in which cyclic deviatoric stresses corresponded to 5 percent and 1.5 percent were applied in the first and second phases respectively.

In the repeated cyclic tests, the changes of Young's modulus between the two cyclic loads were measured. The values of E_c were determined from Figures 4.23 and 4.24 are shown in Table 4.4.

From Table 4.4, the value of E_c increased during second cyclic load of first repeated cyclic load test (cyclic loading at 2 percent and 1.5 percent axial strain). A similar pattern was observed during the second repeated cyclic load test (cyclic loading at 5 percent and 1.5 percent axial strain). This means that material becomes stiffened after the seismic excitation. These results imply that the earthquake load is advantageous to EPS geofoam in terms of strength.

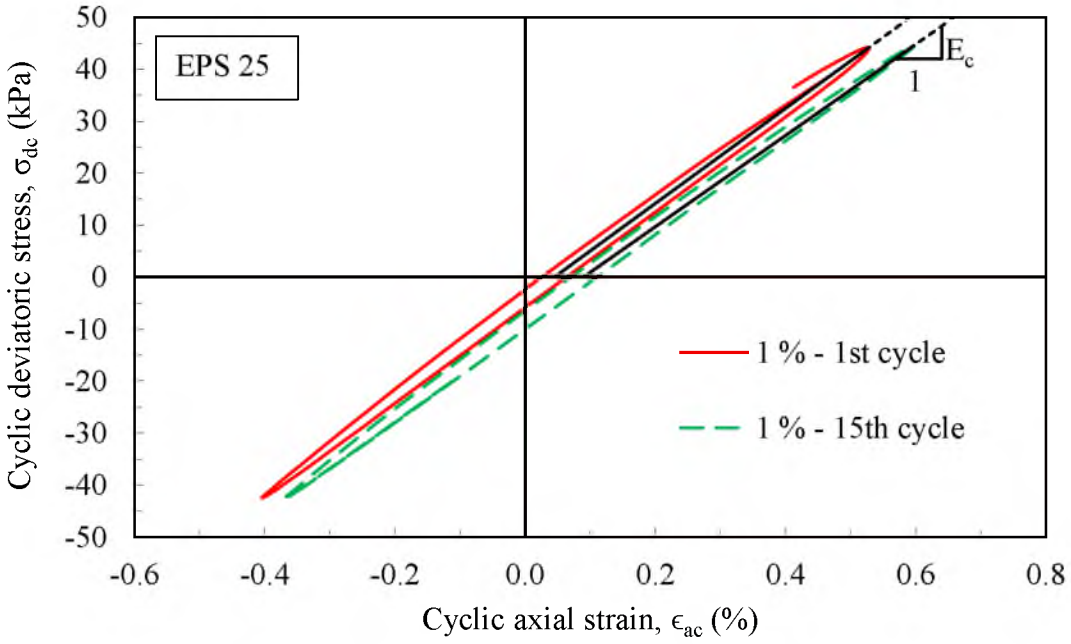

(a)

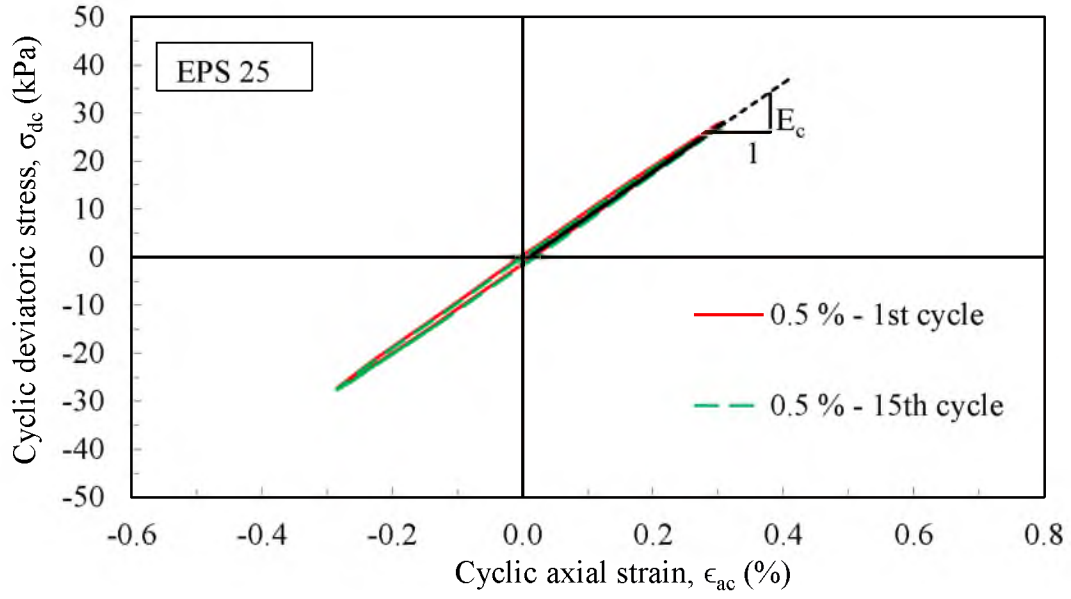

(b)

Figure 4.23. Repeated cyclic uniaxial tests at two different cyclic deviatoric stresses (a) Stress corresponds to 1 % strain (b) Stress corresponds to 0.5 % strain

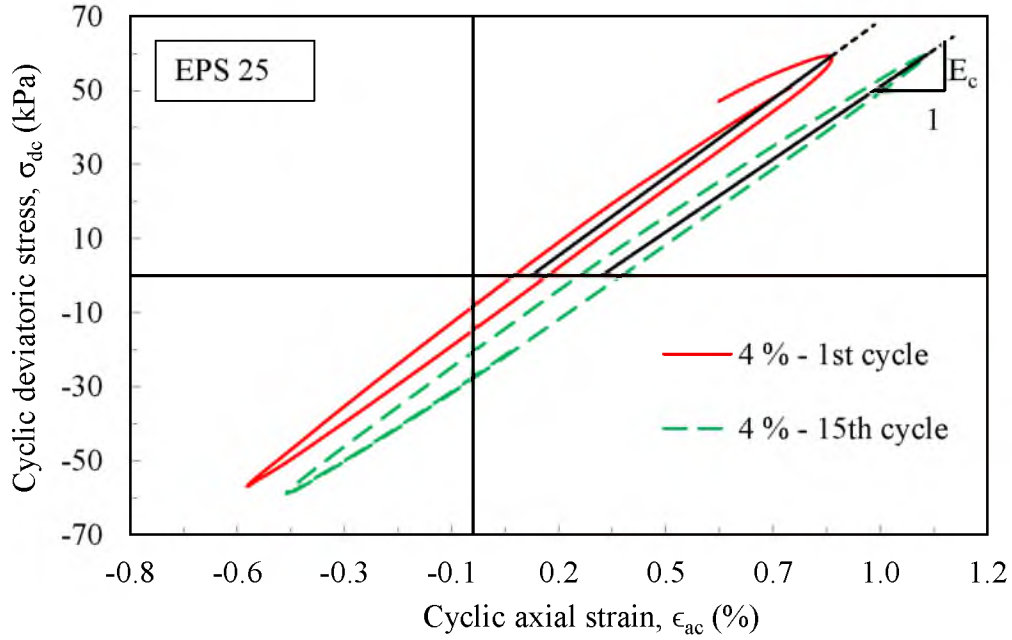

(a)

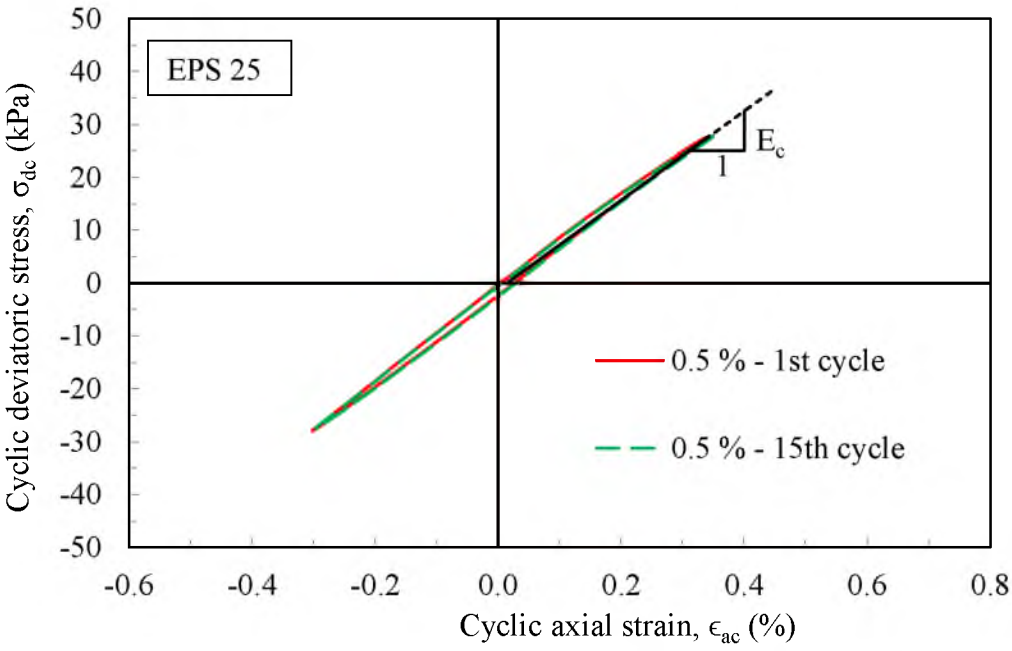

(b)

Figure 4.24. Repeated cyclic uniaxial tests at two different cyclic deviatoric stresses (a) Stress corresponds to 4 % strain (b) Stress corresponds to 0.5 % strain

Table 4.4. Young's modulus for repeated cyclic loads

EPS type	ρ	N	ϵ_a	$E_{c\ (mean)}$
----------	*(kg/m^3)*	----------	*(%)*	*(kPa)*
EPS 25	25.8	15	2	8959
			1.5	9350
	25.8		5	8159
			1.5	8419

The cyclic strain under the cyclic load is the cyclic plastic axial strain. The plots of cyclic plastic axial strain with number of cycles at various cyclic deviatoric stresses for EPS 25 is shown in Figure 4.25. The plastic axial strain increased with increase of cyclic deviatoric stresses for both 15 and 30 cycles.

4.4.3 Postcyclic Creep Tests

The postcyclic creep test provided the various data related to displacement and time. The plot of percentage of vertical strain versus time and logarithm of time were made for various conditions. The postcyclic creep strain for a 50-year design period was calculated in a similar manner to the precyclic creep strain. The postcyclic creep strain is shown in Table 4.5.

Figure 4.26 shows the result of postcyclic uniaxial tests with same cyclic deviatoric stresses but three different numbers of cycles. Figure 4.27 reveals the result of postcyclic uniaxial tests with three different cyclic deviatoric stresses and 5 numbers of cycles. Figure 4.28 reveals the result of postcyclic uniaxial tests with the same cyclic deviatoric stresses but 3 different numbers of cycles. Figure 4.29 shows the result of postcyclic uniaxial tests with 4 different cyclic deviatoric stresses and 15 numbers of cycles.

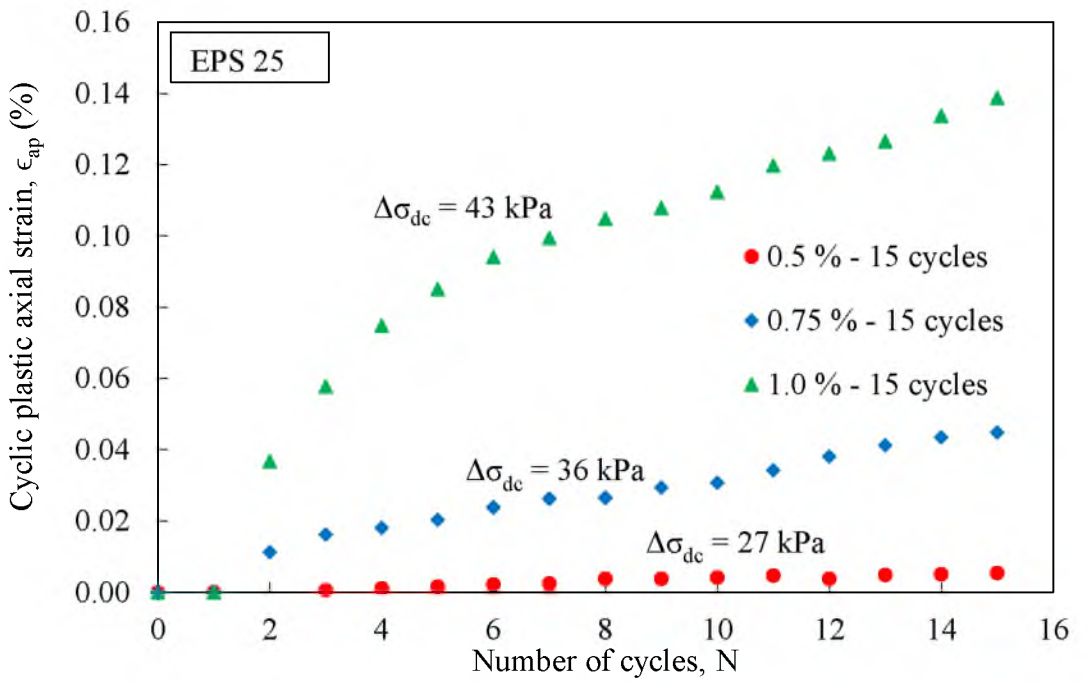

(a)

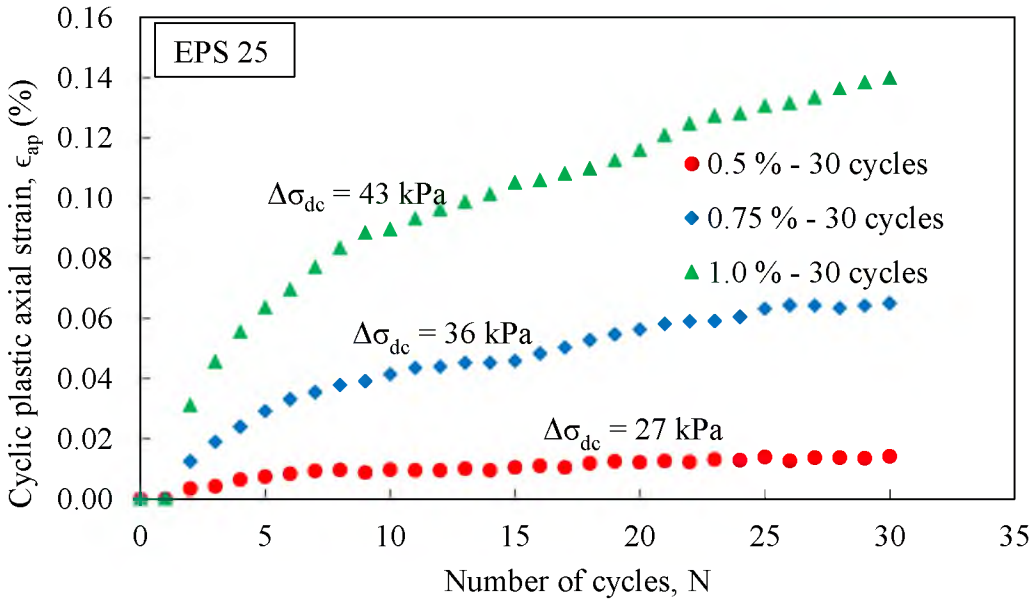

(b)

Figure 4.25. Cyclic plastic axial strain with number of cycles at different cyclic deviatoric stresses (a) 15 number of cycles (b) 30 number of cycles

Table 4.5. Postcyclic creep and total strain for design period

EPS type	Density	Axial strain	No. of cycles	Cyclic plastic axial strain	Post cyclic creep strain in 50 years	Total creep strain in 50 years
----------	*(kg/m3)*	*(%)*	*(N)*	*(%)*	*(%)*	*(%)*
	25.0	1.5	5	0.008	0.298	0.306
	25.4	1.5	15	0.014	0.252	0.266
	25.5	1.5	30	0.028	0.283	0.311
	24.7	1.75	5	0.030	0.207	0.237
	25.6	1.75	15	0.045	0.262	0.307
	24.6	1.75	30	0.065	0.330	0.395
EPS 25	24.9	2	5	0.048	0.286	0.334
	24.5	2	15	0.139	0.333	0.472
	25.8	2	30	0.140	0.351	0.491
	26.3	5	15	0.239	0.368	0.607
	24.5	1.5	5	0.029	14.834	14.863
	24.6	1.75	15	0.036	25.670	25.706
	24.8	2	30	0.067	41.260	41.327
	33.8	2	5	0.070	0.353	0.423
EPS 29	34.0	2	15	0.147	0.381	0.528
	33.2	2	30	0.179	0.430	0.609
	34.2	5	15	0.288	0.419	0.707
	40.0	2	5	0.032	0.393	0.425
EPS 39	41.1	2	15	0.060	0.425	0.485
	39.8	2	30	0.110	0.397	0.507

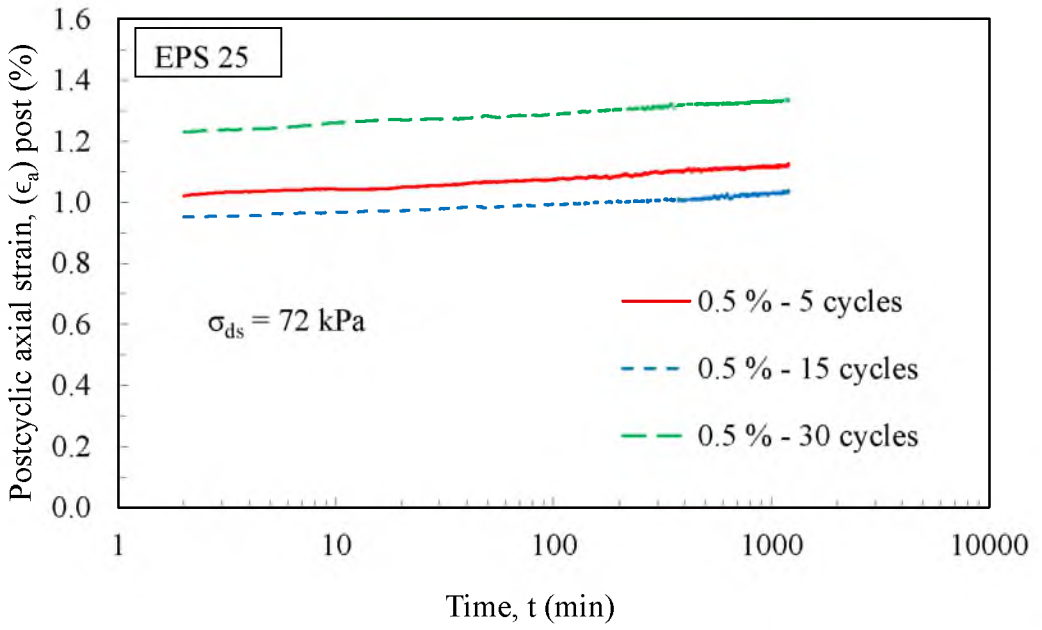

Figure 4.26. Results of postcyclic uniaxial test at same level of cyclic deviatoric stresses and at different number of cycles on EPS 25

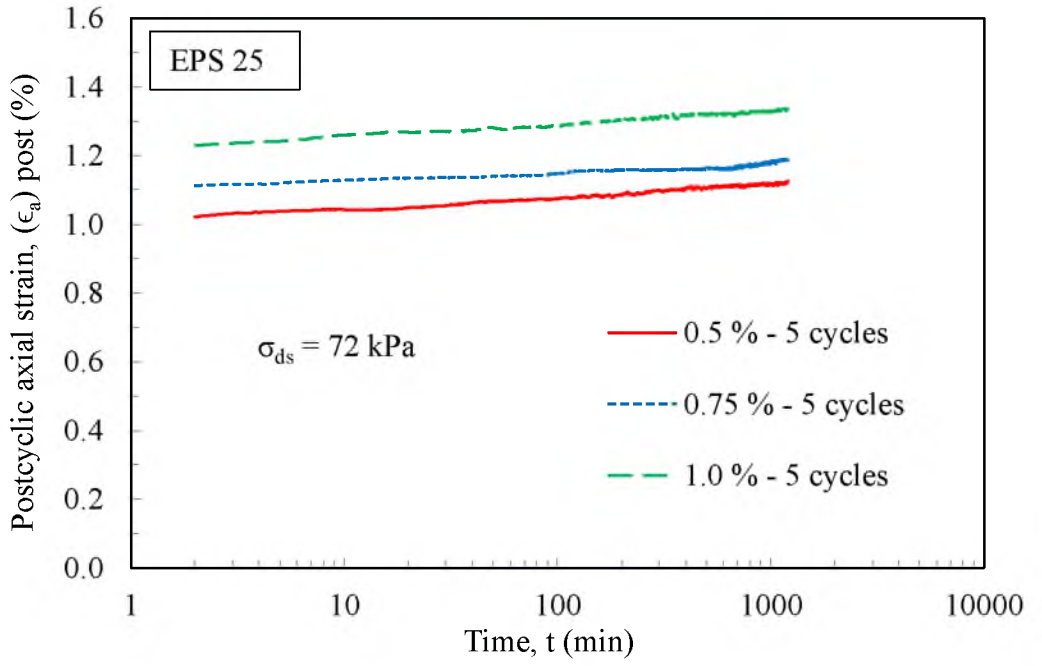

Figure 4.27. Results of postcyclic uniaxial tests on three samples at three different cyclic deviatoric stresses with same number of cycles on EPS 25

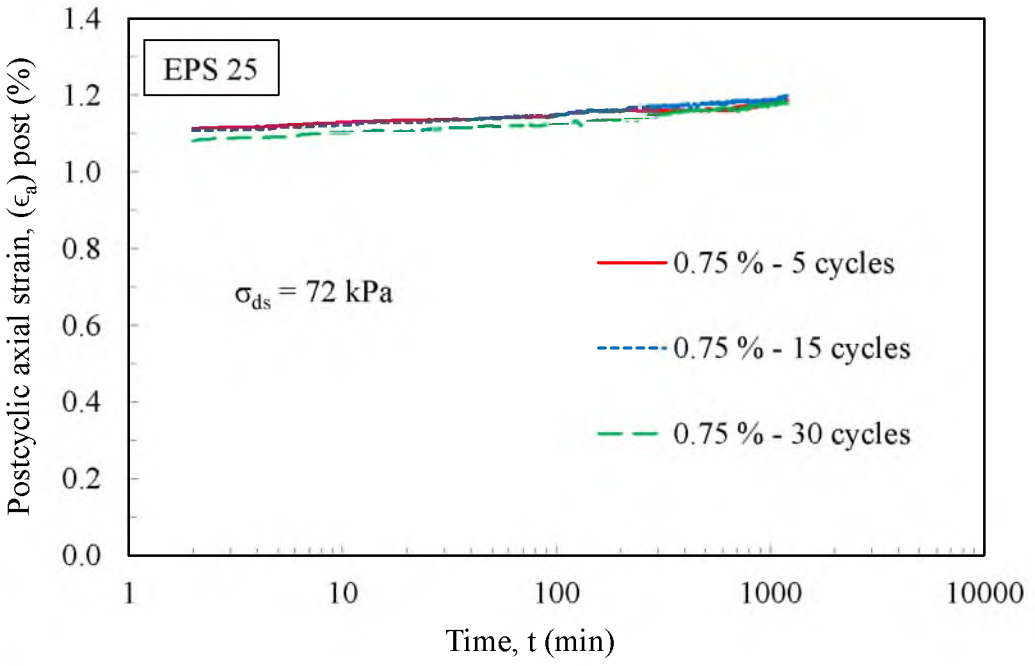

Figure 4.28. Results of postcyclic uniaxial tests on three samples at same cyclic deviatoric stresses with three different numbers of cycles on EPS 25

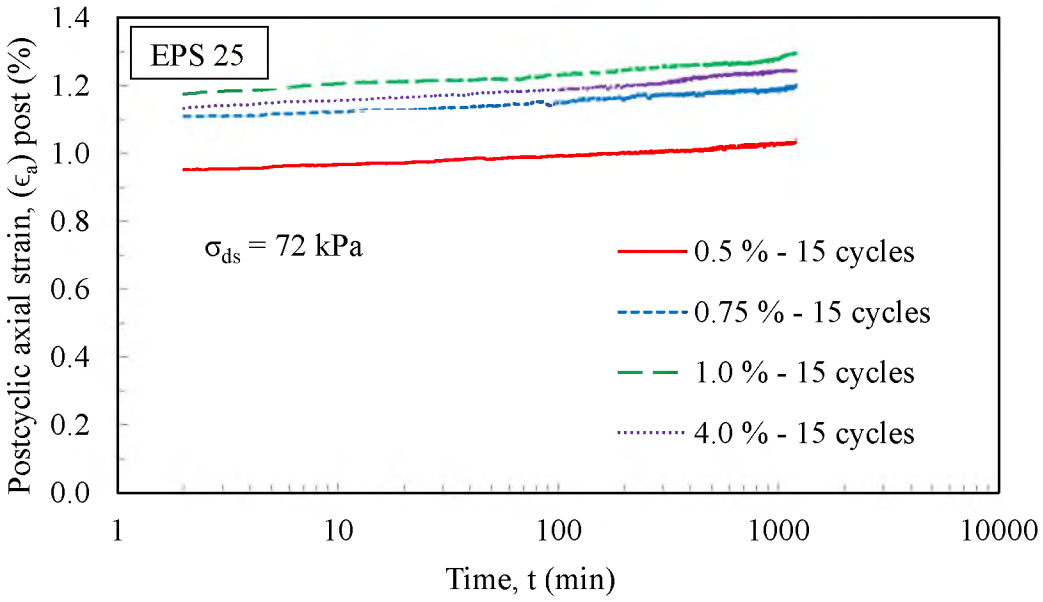

Figure 4.29. Results of postcyclic uniaxial tests on four samples at 15 numbers of cycles with four different cyclic deviatoric stresses on EPS 25

Figures 4.30 and 4.31 reveal the results of the postcyclic uniaxial test for the same level of cyclic deviatoric stresses at three different numbers of cycles and three different levels of cyclic deviatoric stresses at 30 numbers of cycles on EPS 25.

Figures 4.32 and 4.33 reveal the test results of postcyclic uniaxial test for two different levels of cyclic deviatoric stresses at three different number of cycles and the same cyclic deviatoric stresses at three different numbers of cycles on EPS 29 and 39, respectively.

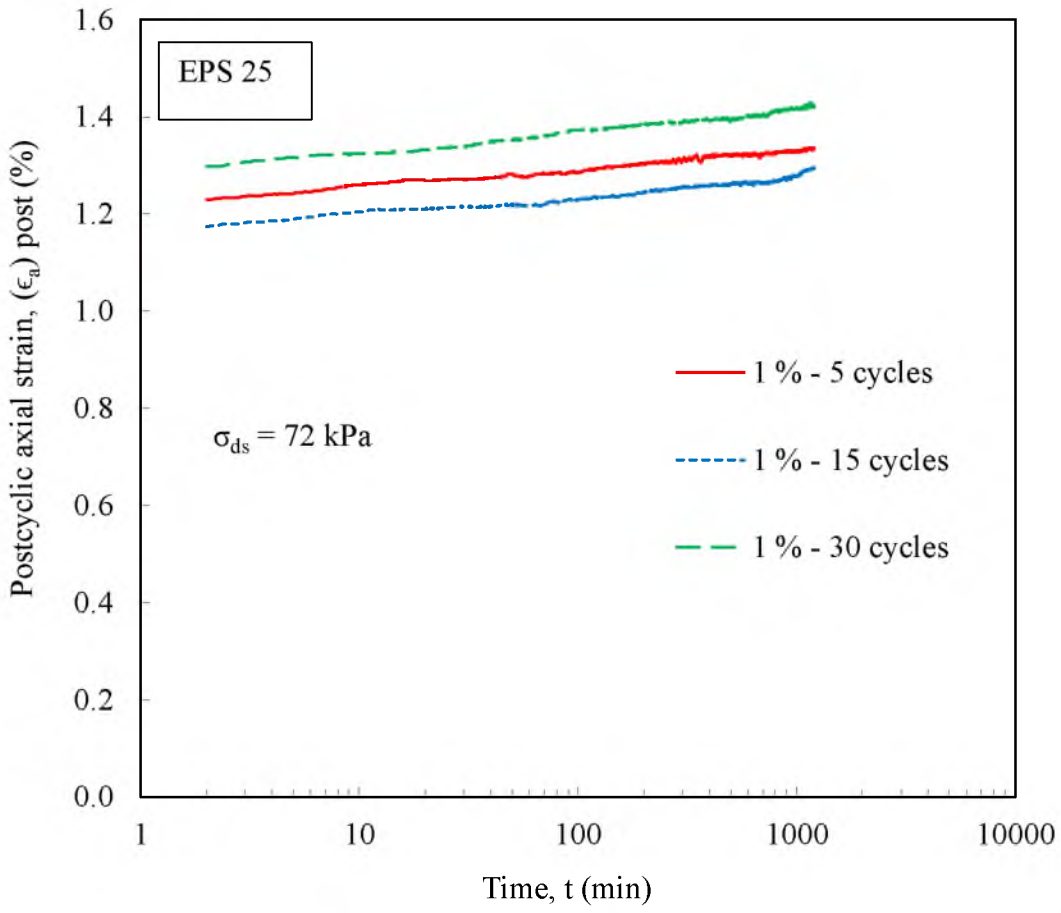

Figure 4.30. Results of postcyclic uniaxial tests on three samples at the same cyclic deviatoric stresses (corresponds to 1% strain) with three different numbers of cycles on EPS 25

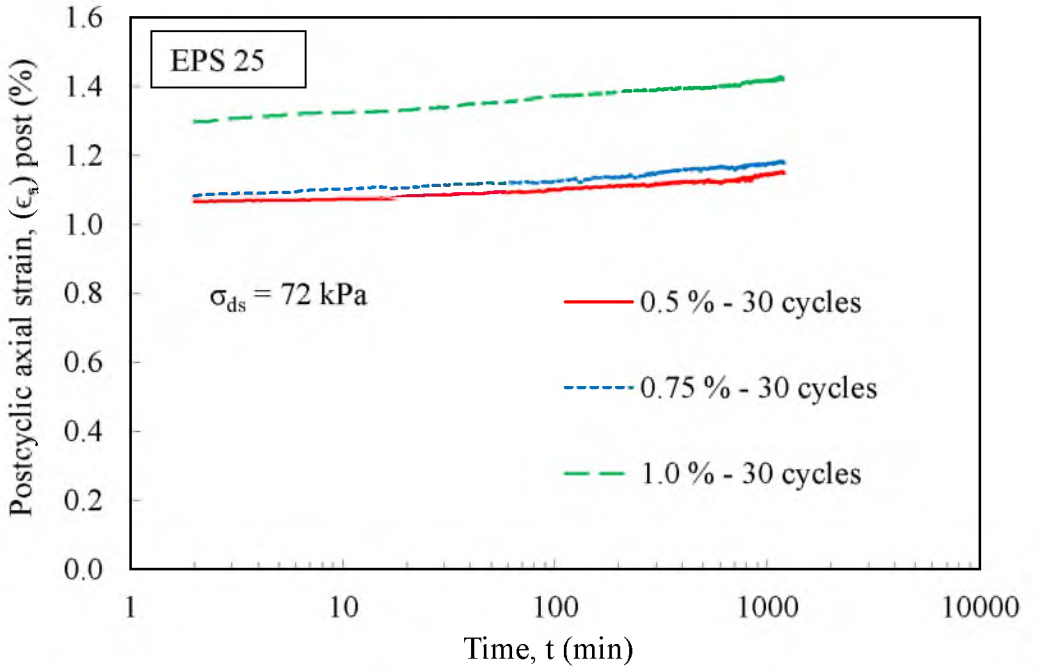

Figure 4.31. Results of postcyclic uniaxial tests on three samples at 30 numbers of cycles with three different cyclic deviatoric stresses on EPS 25

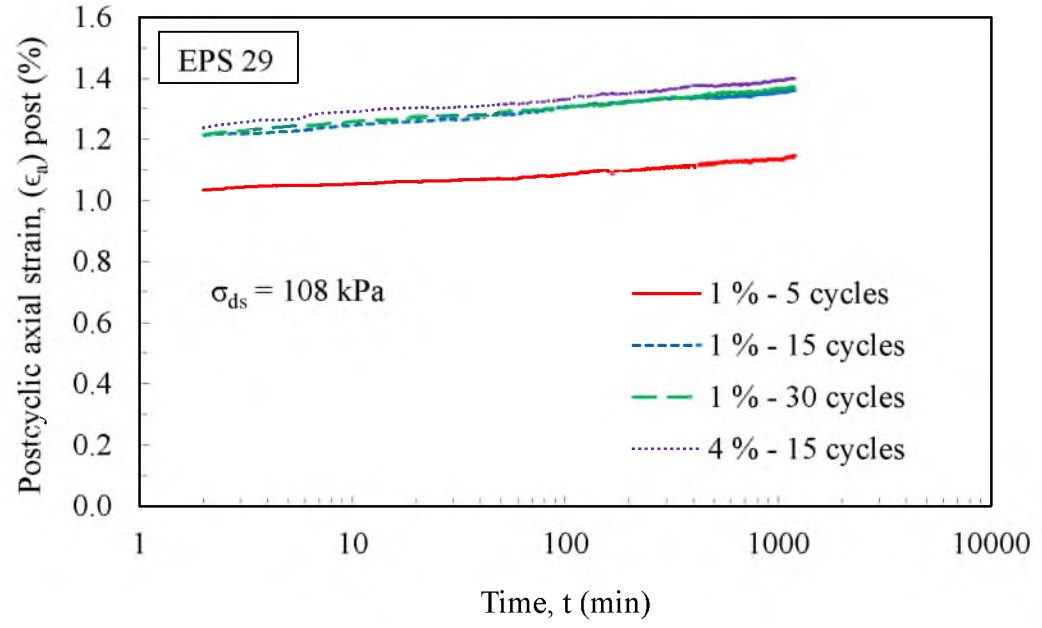

Figure 4.32. Results of postcyclic uniaxial tests on four samples at two different levels of cyclic deviatoric stresses with three different numbers of cycles on EPS 29

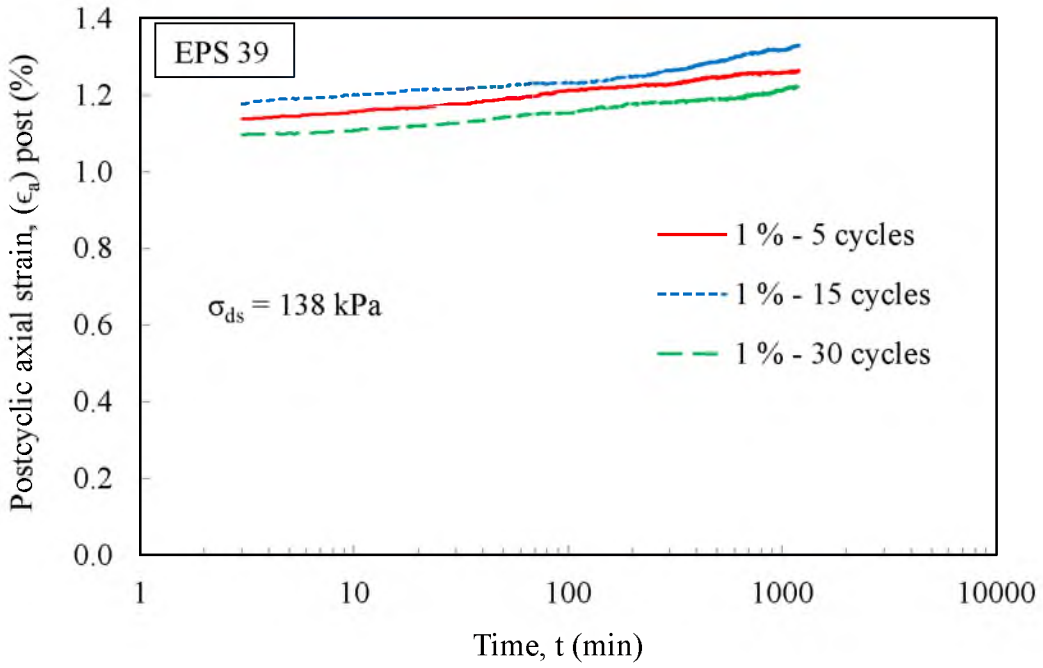

Figure 4.33. Results of postcyclic uniaxial tests on three samples at the same level of cyclic deviatoric stresses with three different numbers of cycles on EPS 39

From the results of postcyclic uniaxial tests and Table 4.5, in most of the cases, it is seen that the postcyclic creep strain increased with an increase of number of cycles at the same deviatoric stress. This might be due to softening of EPS geofoam under the larger number of cycles. The results obtained from postcyclic uniaxial tests depict the amount of postcyclic creep strain obtained after constant dead load (stress corresponding to 1 per cent strain) applied for 20 hours to the specimens which were subjected to a different number of cycles at different levels of axial strain. The postcyclic creep strain value for a 50-year postconstruction period was then calculated by linear extrapolation of the rate of creep strain obtained from the 20-hour creep tests.

Figure 4.34 shows a plot of postcyclic axial strain versus time under a "peak load." The peak load is defined as a case where the postcyclic load was equivalent to the magnitude of total stress applied on the specimen during the cyclic phase. For example, if

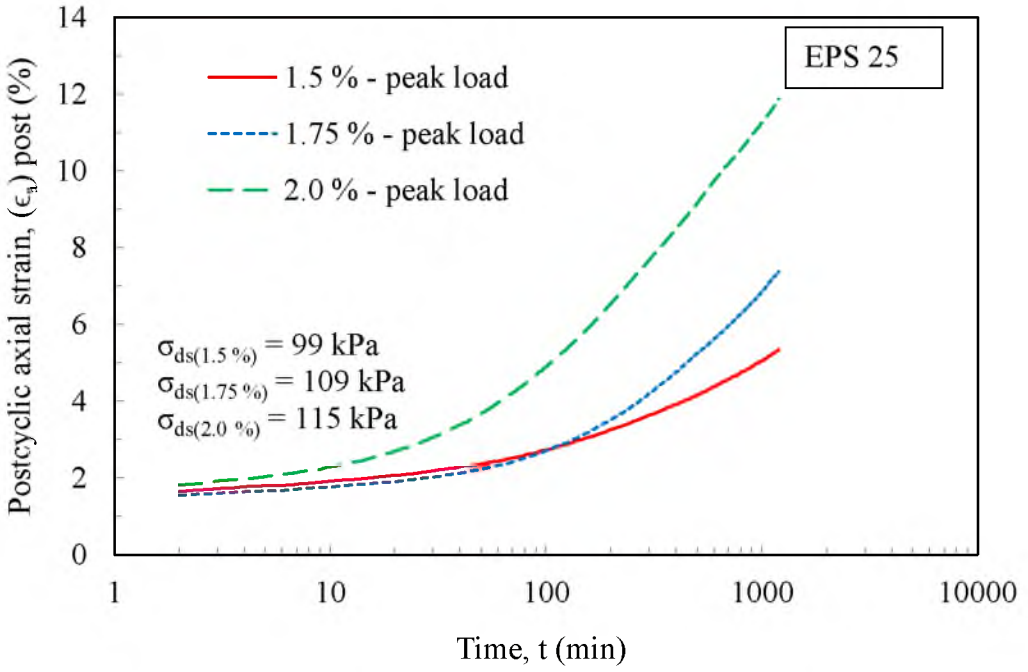

Figure 4.34. Postcyclic axial strain with time for EPS 25 under the peak load (stress same as the total stress during cyclic phase)

the stress during the cyclic phase was equivalent to the 1.5 percent strain level, then the same stress level was applied for the postcyclic phase and the corresponding creep was measured. For this case, the postcyclic creep strain was found to be very high as seen in Figure 4.34 and Table 4.5 for these cases.

4.5 Total Axial Strain

The total axial strain is the sum of the permanent axial strain incurred under cyclic loading and the postcyclic creep project for a postconstruction time period of 50 years. The total axial strain was calculated for all specimens for the various test conditions shown in Table 4.5. In this table, it is seen that projected total axial strain is less than 2 percent for a 50-year postconstruction period except for cases where the postcyclic stress level was

higher than the compressive resistance of the EPS at 1 percent strain. Therefore, it was concluded that the postcyclic dead load cannot be higher than this stress level. However, the combined dead load and cyclic loads can temporarily reach stress levels corresponding to the compressive resistance at 2 percent strain without incurring deleterious creep.

From these test results, it is clear that cycling the EPS to cyclic deviatoric stress levels corresponding to 1 percent axial strain did not have a significant impact on the postcyclic creep behavior, even when the specimen had to continue to resist the preapplied monotonic stress at a stress level corresponding to 1 percent axial strain. In fact, the cycling and its associated strain appears to have conditioned (stiffened) the EPS so that the rate of postcyclic creep strain diminished when compared with uncycled EPS.

Therefore, from a design perspective it seems reasonable to limit the allowable dead load in the EPS to a compressive resistance associated with 1 percent axial strain, and if earthquake loadings are to be considered, then the load combination of dead plus dynamic loading should attempt to limit the monotonic + cyclic load deviatoric stresses to a compressive resistance associated with 2 percent axial strain (i.e., 1 percent vertical allowed for the dead load and an additional 1 percent cyclic strain allowed for the short-term cyclic loading condition). This finding can be considered as a basic design guideline while using EPS in the embankment for bridge support system.

4.6 Conclusions

Monotonic uniaxial tests on EPS 15, EPS 19, EPS 25, EPS 29 and EPS 39 were conducted to determine the deviatoric stress at various strain levels (e.g., 1 percent, 1.75 percent, 2 percent, 5 percent and 10 percent.) The plots of monotonic deviatoric stress

versus axial strain were normalized to 10 percent strain values for interpretation. These plots suggest that the upper bound of the linear range (i.e., point where nonlinearity first begins in monotonic loading) is generally at axial strain values of 1.5 percent, or higher, for EPS geofoam densities commonly used in civil engineering applications.

The relationships developed for Young's modulus and shear modulus from the test data revealed that these moduli can be estimated as a function of EPS density using a second-order polynomial.

Subsequently, stress-controlled, cyclic uniaxial tests were carried out on specimens of EPS 25, EPS 29 and EPS 39 using various levels of cyclic deviatoric stress and number of stress cycles. All of the cyclic tests were initiated with a consolidation phase where an axial stress corresponding to 1 percent axial strain was applied. During this phase, the specimens were allowed to undergo elastic and creep strain for 30 minutes. This monotonic loading was maintained and an additional cyclic deviatoric stress was applied for 5, 15 or 30 stress cycles. The results revealed that higher levels of cyclic deviatoric stresses produced higher amounts of permanent plastic axial strain. Similarly, greater numbers of applied stress cycles also produced higher amounts of permanent plastic strain.

Postcyclic creep tests were also performed to explore the influence of cycling on the long-term postcyclic creep behavior. In general, the cycling of the EPS produced a beneficial effect in that the postcyclic creep rate was less for cycled specimens when compared with the creep rate for uncycled specimens. Hence, it appears for modest levels of cycling, EPS geofoam has a lower rate of creep strain when compared to uncycled material. This might be due to the compression that might occur in the material without damaging of EPS geofoam.

Based on the results of the monotonic, cyclic and creep testing, it is recommended that the dead load (i.e., static deviatoric stress) should not be higher than the stress level corresponding to about 1 percent axial strain. Based on the cyclic loading and postcyclic loading creep tests, it is also recommended that the load combination of static plus dynamic loading should limit the monotonic plus cyclic deviatoric stresses to a compressive resistance associated with 2 percent axial strain (i.e., 1 percent strain allowed for the dead load and an additional 1 percent strain allowed for the cyclic loading). If done in this manner, the testing indicates that the permanent cyclic strains and postconstruction creep strain will be less than 2 percent vertical in 50 years, which is deemed an acceptable value. This provides the basic guideline while using EPS geofoam in the embankment to support bridge system.

4.7 References

Aaboe, R. (1987). "13 Years of experience with expanded polystyrene as a lightweight fill material in road embankments." Norwegian Road Research Laboratory, Oslo, Norway, 21-27.

Aaboe, R., and Frydenlund, T. E. (2011). "40 years of experience with the use of EPS geofoam blocks in road construction." *Proc., 4th Intl. Conf on Geofoam Blocks in Construction Applications,* Lillestrom, Norway.

Athanasopoulos, G., Pelekis, P., and Xenaki, V. (1999). "Dynamic properties of EPS geofoam: an experimental investigation." *Geosynthetics International*, 6(3), 171-194.

Beinbrech, G., and Hillmann, R. (1997). "EPS in road construction current situation in Germany." *Geotextiles and Geomembranes*, 15(1), 39-57.

Duškov, M. (1997). "Materials research on EPS20 and EPS15 under representative conditions in pavement structures." *Geotextiles and Geomembranes*, 15(1), 147-181.

Elragi, A. F. (2000). "Selected engineering properties and application of EPS geofoam." Ph.D. thesis, State University of New York, Syracuse, USA.

Geocomp (2006). "Triaxial cyclic user's manual."Boxborough, MA, USA, 71p.

Holtz, R. D., Kovacs, W. D., and Sheahan, T. C. (2010). *An introduction to geotechnical engineering*, Pearson, New Jersey, USA.

Horvath, J. S. (1995). *Geofoam geosynthetic*, Horvath Engr., P.C., Scarsdale, New York, USA.

Lingwall, B. N. (2011). "Development of an expanded polystyrene geofoam cover system for pipelines at fault crossings." Ph.D. Thesis, The University of Utah, Utah, USA.

Newman, M. P., Bartlett, S., and Lawton, E. (2009). "Numerical modeling of geofoam embankments." *Journal of Geotechnical and Geoenvironmental Engineering*, 136(2), 290-298.

Refsdal, G. (1985). "Plastic foam in road embankments: future trends for EPS use." Internal Report, Norwegian Road Research Laboratory, Oslo, Norway

Seed, H. B., and Idriss, I. (1982). *Ground motions and soil liquefaction during earthquakes*, Earthquake Engineering Research Institute, Oakland, California, USA.

Snow, C. L., and Nickerson, C. R. (2004). "Case study of EPS geofoam lightweight fill for settlement control at bridge approach embankment." *Proc., Geotechnical Engineering for Transportation Projects*, ASCE, Los Angeles, California, USA, 580-589.

Stuedlein, A. W., and Negussey, D. (2013). "Use of EPS geofoam for support of a bridge." *Sound Geotechnical Research to Practice: Honoring Robert D. Holtz, Geotechnical Special Publication*(230), 334-345.

Trandafir, A. C., Bartlett, S. F., and Lingwall, B. N. (2010). "Behavior of EPS geofoam in stress-controlled cyclic uniaxial tests." *Geotextiles and Geomembranes*, 28(6), 514-524.

Zou, Y., Leo, C., and Small, J. (2000). "Behaviour of EPS geofoam as flexible pavement subgrade material in model tests." *Geosynthetics International*, 7(1), 1-22.

CHAPTER 5

SIZING OF BRIDGE, FUNDAMENTAL PERIOD OF STRUCTURE AND SLIDING MODE OF EPS EMABANKMENT

5.1 Introduction

Construction of an embankment to support bridge system on soft soil is challenging. Settlement is the major issue in such case. The settlement can be minimized by decreasing the loading, by altering the foundation conditions with some ground improvement techniques or by constructing deep foundations (e.g., piles, shaft etc.). Construction of a deep foundation is rather a general solution and is not an appropriate solution for speeding up the construction process as preconsolidation takes longer. Thus the construction could turn out to be expensive in terms of time and labor.

Light weight fill material like EPS can be a good option thereby reducing the construction time with tolerable settlement in structures. The EPS geofoam in embankment for the direct support of the bridge has been used in very few instances. The Norwegian Public Roads Administration (NPRA) pioneered this technique where the bridge structures rest solely on EPS blocks. In their designs, only static loading condition was considered. This study emphasized dynamic analysis of such support system without overstressing the EPS.

In bridge support systems, embankments can be overstressed from three different loading conditions: type of loads (dead and live), seismic excitation, and duration of loadings (shot term and long term). While considering extreme events like earthquakes in design, the embankment should be able to restrain against the associated forces like sliding, sway and rocking. This study mainly focused on restraint against sliding.

Type of EPS and size of foundation for bridge play important roles for deciding the length of bridge to be constructed. The length of bridge can be increased with the use of higher density EPS. If we assume width of the bridge being equal to the width of embankment then it is easier to analyze the system. The area of embankment at top is the same as the area of bridge foundation. The shape of embankment affects the vertical stress distribution.

The vertical stress distribution on the EPS embankment to support the bridge or pavement system was reported by some researchers (Tefera et al., 2011; Tsukamoto, 2011). Tefera et al. (2011) reported the Finite Element Method (FEM) simulation results of vertical stress distribution using PLAXIS for the EPS embankment to support bridge. Laboratory and field tests were conducted to study the stress distribution within the blocks and fills of EPS and the FEM model was also prepared for the same blocks and fills. The FEM results showed the vertical stress distribution zone inside the EPS embankment was around 60^0 with horizontal surface. In the study of Tsukamoto (2011), the vertical stress distribution inside the EPS embankment was 70^0 with horizontal surface.

The geofoam embankment performance in terms of settlement and rapid construction with time consideration had been studied by Farnsworth et al. (2008). In the study, one

stage mechanically stabilized earth (MSE) wall supported by lime columns; EPS geofoam embankment with tilt up panel facia and two-stage MSE wall with prefabricated vertical drain were compared. The study revealed EPS geofoam embankment had the best performance.

Use of EPS geofoam to support bridge system has been studied by some researchers (McDonald and Brown, 1993; Snow and Nickerson, 2004; Aaboe and Frydenlund, 2011; Stuedlein and Negussey, 2013). McDonald and Brown (1993) studied the use of EPS geofoam for bridge approach fill. The differential settlement between approach fills and bridge abutment structures was greatly reduced by using EPS geofoam. Snow and Nickerson (2004) did a case study of EPS geofoam as lightweight fill for settlement control in bridge approach embankment. According to the study, the results from three different alternatives for settlement mitigation (no mitigation measure; wick drains with surcharge; and EPS geofoam lightweight fill) were compared. EPS geofoam lightweight fill alternative was better over other two alternatives because it overcame the time constraint.

Aaboe and Frydenlund (2011) reported 40 years of experience with the use of EPS geofoam block in road construction in Norway. The paper describes use of trapezoidal EPS embankment in three bridges, namely, Lokkeberg bridge, Hjelmungen bridge and Grimsoyvegen bridge, without the use of deep foundations. Stuedlein and Negussey (2013) studied the EPS geofoam embankment to support the single span Buffalo Road Bridge crossing of Oatka Creek, USA. The subsurface investigation showed the soil on the project site was too weak to support a shallow foundation and EPS was used for the foundation system.

In general design, EPS embankments are mostly rectangular and trapezoidal. The shape of structures plays a vital role in calculation of fundamental period. For the seismic design, a fundamental period of structures is paramount because the embankment systems generate the maximum displacement when excited at fundamental period (Makdisi and Seed, 1978): this is the time at which the embankment moves one cycle back and forth under free vibration. The fundamental period is used for the determination of spectral acceleration from the response spectra for site specific design but the spectral acceleration needs to be assumed in general design. The inertial force is calculated by using Newton's second law of motion as the product of mass (above the embankment) and spectral acceleration. Once the force at the top of the embankment is known, the safety factor of the bridge support system can be calculated.

The fundamental period calculation of EPS embankment to support pavement structure was reported by researches like Horvath (2004) and Amini (2014). Both of the researchers treated the EPS embankment as two-dimensional (2D) with an assumption that one side is infinitely large. In this research, the fundamental period was derived based on the assumption that EPS embankment was fixed at the base and the load was applied at the top which is similar to the cantilever beam with load at free end. In this case, the embankment was modeled with a single degree of freedom (SDOF) system.

The flexural stiffness, shear stiffness and axial stiffness were calculated based on the direction of seismic excitation. Fast Lagrangian Analysis of Continua (Itasca, 2005) based on finite difference technique was used by Amini (2014) to compare the analytical results. In the study, the Japanese equation, an equation published in National Cooperative Highway Research Program (NCHRP) by Stark et al. (2000) and an equation

by Horvath (2004) were used. The conclusion was based on base to height aspect ratios. The FLAC results were close to the Japanese equation for aspect ratio higher than 2 and close to the Stark et al. (2000) equation for aspect ratio less than 1.5.

The dynamic response of EPS embankment is very complex at high level of seismic excitation. The EPS material is flexible. The possible modes after excitation mentioned in Riad and Horvath (2004) are: (1) rigid-body translation (sliding), (2) horizontal flexibility and deformation (lateral sway), and (3) rigid-body rotation (seismic rocking). The seismic stability and performance of freestanding geofoam embankment was studied by Bartlett and Lawton (2008). In the study, it was mentioned that the interlayer sliding can be addressed easily during construction. The construction of shear key is one of the important techniques to stop the possible interlayer sliding. The shear key will disrupt horizontal planes. Amini (2014) also mentioned the use of shear keys and proper adhesive for preventing interlayer sliding.

These studies considered the use of EPS to support pavement system but it is unknown how an EPS embankment supporting bridge system would perform during a seismic excitation. The load exerted on EPS embankment by the bridge is higher than the load exerted by the pavement. In the case of the bridge, the length of footing of bridge has finite dimensions. So, the use of FLAC 2D analysis does not represent the real system. It is necessary to study the dynamics of the system with consideration of three dimensions and the possible restraint system against sliding at a higher level of excitations.

The main objectives of this study were to: (1) determine the size of bridge (2) calculate the fundamental period of structure (3) calculate the critical acceleration against

sliding and (4) analyze the possible restraint system against sliding for higher level of excitations.

The size of bridge was determined based on EPS type and size of footing. Steel and concrete bridges were analyzed with varying lengths of footing to determine the choice of type of bridge. Two bridge support systems were developed separately considering rectangular prismatic and symmetrical trapezoidal prismatic shape of embankments supporting the bridge. These two types of embankments were used for the calculation of fundamental period and determination of critical acceleration. Critical acceleration is the acceleration at which factor of safety is equal to unity. Fundamental period was calculated considering excitation along the direction of bridge, across the bridge and the plane outward. These excitations were denoted by longitudinal, transverse and vertical directions hereafter. The derivation for fundamental period was done for three-dimensional (3D) embankment and the results were compared with FLAC 3D (Itasca, 2006). The critical acceleration was calculated and restraint systems against sliding for higher level of excitations were determined.

5.2 Method of Sizing of Bridge

EPS 22 and EPS 29 were selected for sizing of bridge. The minimum design values of compressive resistance of EPS 22 and EPS 29 at 1 percent strain level was selected from ASTM (2007) given in Table 5.1 The total width of bridges for single and double lanes with one-sided sidewalk was 5.25 m and 9 m, respectively. A footing was placed at the top of an embankment. The width of footing was assumed to be same as the width of the bridge. The height of embankment was assumed to be 6 m. Sizing of bridge was done

Table 5.1. Compressive resistance of EPS geofoam at various levels of strain (ASTM, 2007)

Type	EPS12	EPS15	EPS19	EPS22	EPS29	EPS39	EPS46
Density, min., kg/m^3(lb/ft^3)	11.2 (0.70)	14.4 (0.90)	18.4 (1.15)	21.6 (1.35)	28.8 (1.80)	38.4 (2.40)	45.7 (2.85)
Compressive Resistance, min., kPa (psi) at 1 %	15 (2.2)	25 (3.6)	40 (5.8)	50 (7.3)	75 (10.9)	103 (15.0)	128 (18.6)
Compressive Resistance, min., kPa (psi) at 5 %	35 (5.1)	55 (8.0)	90 (13.1)	115 (16.7)	170 (24.7)	241 (35.0)	300 (43.5)
Compressive Resistance, min., kPa (psi) at 10 %[A]	40 (5.8)	70 (10.2)	110 (16.0)	135 (19.6)	200 (29.0)	276(40.0)	345 (50)
Flexural Strength, min., kPa (psi)	69 (10.0)	172 (25.0)	207 (30.0)	276 (40.0)	345 (50.0)	414 (60.0)	517 (75.0)
Oxygen index, min., volume %	24.0	24.0	24.0	24.0	24.0	24.0	24.0

with consideration of rectangular prismatic embankment. The allowable load of embankment was the ratio of compressive strength to plan area of footing. The calculated load was the maximum load that a single abutment can bear. The maximum load two abutments could support was obtained by doubling the load taken by single abutment.

Dead load for steel and concrete bridge was calculated. For the steel bridges, Acrow and Mabey bridges were chosen for analysis. The weight per meter of Acrow bridges was based on (Needham, Randy, personal communication, Jan 14, 2014) and for Mabey bridges was calculated from the data given in the website (Maybehire, 2012).The weight per meter of Acrow bridges was higher than for Mabey bridges and therefore the values obtained from Acrow bridges were used. For the concrete bridges, the calculation was based on Modjeski-Masters-Inc (2003).

Live load was calculated based on the characteristic of the design truck given in AASHTO (2012) as shown in Figure 5.1. For a consideration of critical load, the spacing of middle and rear axle was taken as 14 feet and the spacing between the two vehicles was 5 feet. Live load per meter was calculated for the single lane and double lane by dividing the axle load by length of loading.

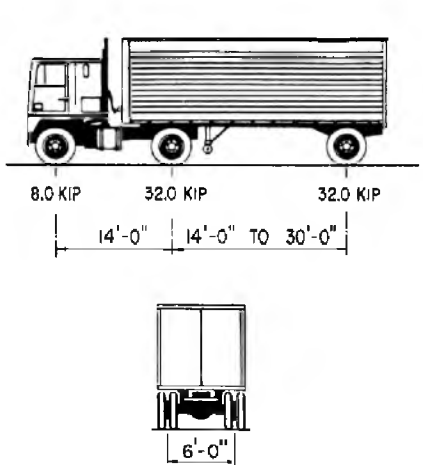

Figure 5.1. Characteristic of the design truck (AASHTO, 2012)

The thickness of footing and unit weight of concrete were assumed to be 0.5 m and 23.56 kN/m^3, respectively, and dead load was calculated. Total weight exerted by dead load and live load was determined. The length of bridge is the ratio of total load to the load per meter with safety factor of 1.2.

The lengths of steel and concrete bridges for single and double lane by using EPS 22 and 29 were calculated for footing length of 2 m, 3 m, 4 m, 5 m and 6 m. The 4 m length of footing was used for further analysis because a 4 m length of footing is more practical from a construction point of view. The detailed calculation of length of bridge for footing length 4 m for steel and concrete bridges is shown in Appendix B.

5.3 Bridge Support Systems

This study focused on bridge structures supported directly by EPS geofoam atop soft ground conditions without the support of deep foundations or soil improvement. Central to this application is the capacity of the EPS geofoam to support the associated dead loads and live loads without being overstressed. The live loads consist of cyclic and

impact vehicular loads, and extreme event loadings, such as those from earthquake events. For extreme events, the embankment design must address forces associated with sliding, sway and rocking of the bridge/embankment system. The lateral restraint systems with two shape of embankments (rectangular and trapezoidal) shown in Figure 5.2 and Figure 5.3 were considered. Figure 5.2 is the system at which high density EPS was used below the footing of bridge and low density EPS was used below the load distribution slab of rod pavement. The rectangular prismatic embankment was used to support the bridge.

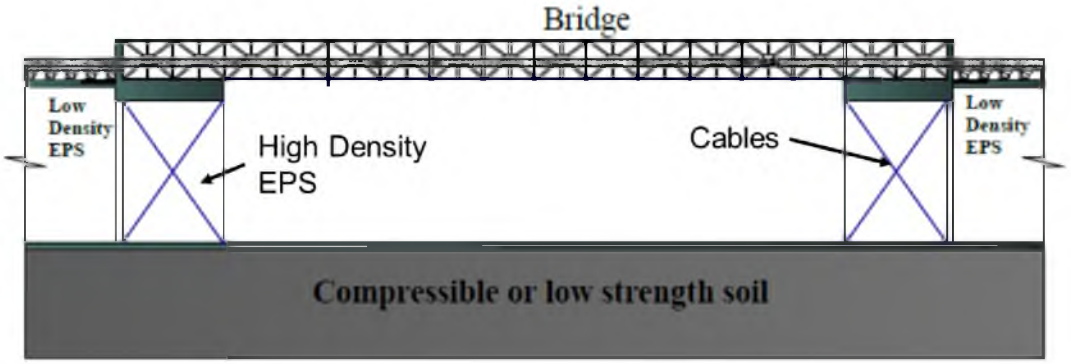

Figure 5.2. Bridge support system with rectangular prismatic shape EPS embankment

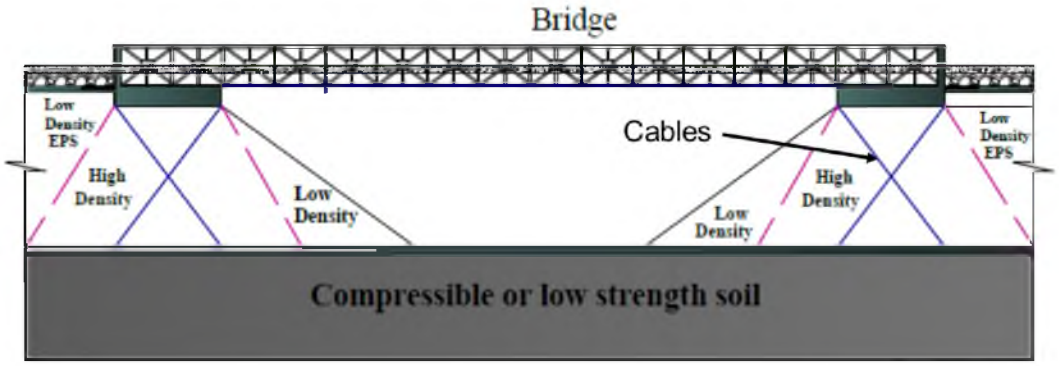

Figure 5.3. Bridge support system with trapezoidal prismatic shape EPS embankment

Two different densities of EPS were used because the load from the bridge is much higher than load from the pavement. At the interface of two systems a joint was placed in order to reduce the stress.

Due to the difference in loadings, a floating slab was placed in between the footing of the bridge and load distribution slab of pavement in order to overcome the effect of possible differential settlement. Cables/thread bars were used in lateral restraint system in case of high seismic excitation. Cables/thread bars were placed externally in a criss-cross pattern between footing and bottom load distribution slab. In the case of highly compressible soil, ground improvement or pinned connection to the soil is required.

Figure 5.3 is the system at which trapezoidal prismatic embankment was used to support the bridge. Higher density EPS was used in the trapezoidal section and lower density EPS was used at the remaining part of embankment. The side slope of embankment was made 1V:2H similar to the embankments mentioned in Aaboe and Frydenlund (2011). The vertical stress distribution inside the EPS embankment was considered to be 2V:1H which falls in between the value used in Tsukamoto (2011) and Tefera et al. (2011). In this analysis, the major focus was on the embankment beneath the foundation of bridge. So, rectangular and trapezoidal shape embankments (Figures 5.4 and 5.5) were considered.

5.4 Fundamental Period of EPS Embankment

The mass density of EPS geofoam is almost 100 times lighter than other conventional geotechnical materials like soil and rock, so the majority of the mass is located at the top of the embankment. EPS embankment is flexible and has no confinement.

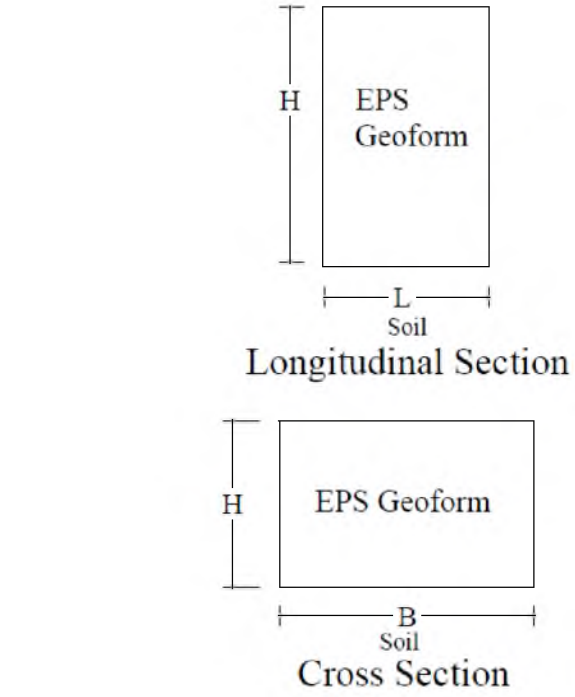

Figure 5.4. Longitudinal and cross section of rectangular prismatic shape EPS Embankment

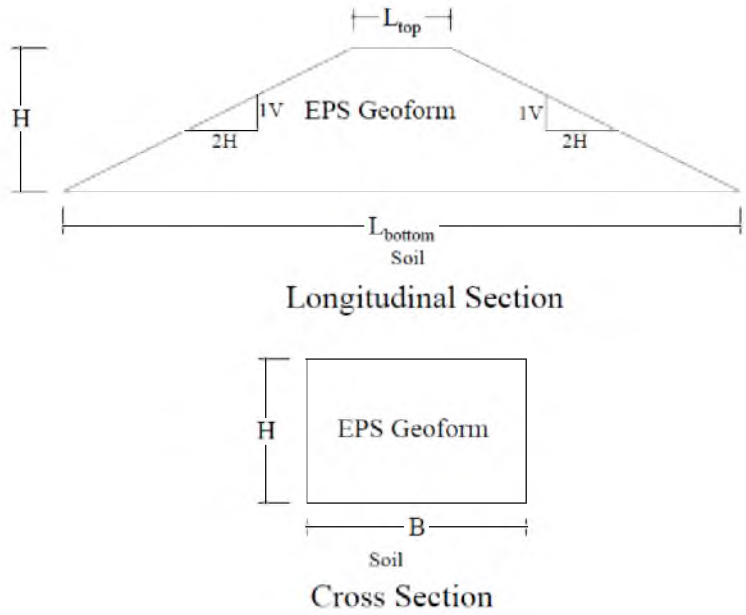

Figure 5.5. Longitudinal and cross section of trapezoidal prismatic shape EPS Embankment

When a seismic excitation was applied at the base of the embankment then a large displacement would occur at the top. Horvath (1995) mentioned that EPS fill can be modeled as single degree of freedom (SDOF). In this approach, EPS embankment is modeled as fixed-end cantilever beam. Two embankments were considered for fundamental period calculation. Even though the embankments were three-dimensional, the Horvath (1995) approach was considered for analytical solutions. In this study, both analytical and numerical approaches were employed for fundamental period calculation.

5.4.1 Analytical Approach

For the fundamental period calculation equation (3D), the concept of flexural, shear and axial stiffness based on Timoshenko and Gere (1972) were used.

5.4.1.1 Derivation Based on Flexural and Shear Stiffness

The method of derivation of fundamental period with consideration of flexural and shear stiffness is denoted as "Method I" hereafter.

Fundamental period of any SDOF system is,

$$T_0 = 2\pi \left[m \left(\frac{1}{k} \right) \right]^{0.5} \tag{5.1}$$

where m and k represents the mass and spring stiffness of the SDOF system. Equation (5.1) in terms of weight is,

$$T_0 = 2\pi \left[\left(\frac{W}{g}\right)\left(\frac{1}{k}\right)\right]^{0.5} \tag{5.2}$$

For the fixed-end cantilever beam with transverse concentrated force (P) at free end and the maximum transverse displacement (Δ), the stiffness is defined by:

$$k = \frac{P}{\Delta} \tag{5.3}$$

Timoshinko's beam theory considered two components of spring stiffness which are: flexural stiffness (k_F) and shear stiffness (k_S). In such cases, two springs are in series with the applied force P. The equivalent spring constant for two stiffness in series is:

$$k = \frac{1}{\frac{1}{k_F} + \frac{1}{k_S}} \tag{5.4}$$

$$\frac{1}{k} = \frac{1}{\frac{1}{\frac{1}{k_F} + \frac{1}{k_F}}} = \frac{1}{k_F} + \frac{1}{k_S} \tag{5.5}$$

Substituting the value of k in Eq. (5.2),

$$T_0 = 2\pi \left[\left(\frac{W}{g}\right)\left(\frac{1}{k_F} + \frac{1}{k_S}\right)\right]^{0.5} \tag{5.6}$$

The maximum flexural transverse displacement Δ_F is:

$$\Delta_F = \frac{PL^3}{3EI} \tag{5.7}$$

where E is Young's modulus of the beam material, I is moment of inertia of the beam, L is beam length. For the EPS geofoam embankment, E equals to E_{ti} is initial tangent Young's modulus of EPS. L equals to H and I depends upon the direction of seismic excitation.

Excitation along the longitudinal direction,

$$I = \frac{BL^3}{12} \tag{5.8}$$

where B is width of embankment. Equation (5.7) becomes,

$$\Delta_F = \frac{12PH^3}{3E_{ti}BL^3} = \frac{4PH^3}{E_{ti}BL^3} \tag{5.9}$$

Combining Eqs (5.3) and (5.9),

$$k_F = \frac{P}{\Delta_F} = \frac{PE_{ti}BL^3}{4PH^3} = \frac{E_{ti}BL^3}{4H^3} \tag{5.10}$$

$$\frac{1}{k_F} = \frac{4H^3}{E_{ti}BL^3} \tag{5.11}$$

The shear deflection at free end is,

$$\Delta_S = \alpha_S \frac{PL}{GA} \tag{5.12}$$

where α_s is shear coefficient used to get shear stress at centroid, G is shear modulus of the beam material and A is beam cross-sectional area. According to Cowper (1966), the shear coefficient for solid rectangular section is:

$$\alpha_S = \frac{12 + 11\nu}{10(1+\nu)} \tag{5.13}$$

$$k_S = \frac{P}{\Delta_S} = \frac{GA}{\alpha_S L} = \frac{10(1+\nu)GA}{(12+11\nu)L} \tag{5.14}$$

$$\frac{1}{k_S} = \frac{(12+11\nu)L}{10(1+\nu)GA} \tag{5.15}$$

For the linear elastic material,

$$G = \frac{E}{2(1+\nu)} \tag{5.16}$$

where E is Young's modulus of the material and v is Poisson's ratio of the material. Replacing L by H, E by E_{ti} and G by relation with E in Eq. (5.15),

$$\frac{1}{k_S} = \frac{(12+11v)2H(1+v)}{10(1+v)E_{ti}A} = \frac{H(12+11v)}{5E_{ti}LB} \tag{5.17}$$

Combining Eqs (5.6), (5.11) and (5.17),

$$T_0 = 2\pi\left[\left(\frac{W}{g}\right)\left(\frac{4H^3}{E_{ti}BL^3} + \frac{H(12+11v)}{5E_{ti}LB}\right)\right]^{0.5} \tag{5.18}$$

$$T_0 = 2\pi\left\{\left[\frac{WH}{gE_{ti}LB}\right]\left[4\left(\frac{H}{B}\right)^2 + \frac{(12+11v)}{5E_{ti}LB}\right]\right\}^{0.5} \tag{5.19}$$

$$T_0 = 2\pi\left\{\left[\frac{\sigma'_{v0}H}{E_{ti}g}\right]\left[4\left(\frac{H}{B}\right)^2 + \frac{(12+11v)}{5}\right]\right\}^{0.5} \tag{5.20}$$

where σ'_{v0} is vertical effective stress at the top acting on the top of the EPS.

Excitation along the transverse direction,

$$I = \frac{LB^3}{12} \tag{5.21}$$

Similar to derivation of excitation along the longitudinal direction, the fundamental period is:

$$T_0 = 2\pi \left\{ \left[\frac{\sigma'_{v0} H}{E_{ti} g} \right] \left[4 \left(\frac{H}{L} \right)^2 + \frac{(12 + 11\nu)}{5} \right] \right\}^{0.5} \tag{5.22}$$

5.4.1.2 Derivation Based on Stark et al. (2000)

The shear coefficient reported in Stark et al. (2000) is,

$$\alpha_S = \frac{5}{6} \tag{5.23}$$

By substituting α_S in Eq. (5.14), the final result for excitation along the longitudinal direction and transverse direction are:

Excitation along the longitudinal direction,

$$T_0 = 2\pi \left\{ \left[\frac{\sigma'_{v0} H}{E_{ti} g} \right] \left[4 \left(\frac{H}{B} \right)^2 + \frac{(12 + 12\nu)}{5} \right] \right\}^{0.5} \tag{5.24}$$

Excitation along the transverse direction,

$$T_0 = 2\pi \left\{ \left[\frac{\sigma'_{v0} H}{E_{ti} g} \right] \left[4 \left(\frac{H}{L} \right)^2 + \frac{(12 + 12\nu)}{5} \right] \right\}^{0.5} \tag{5.25}$$

5.4.1.3 Derivation Based on Flexural, Shear and Axial Stiffness

The derivation with consideration of all three stiffnesses (flexural, shear and axial) is denoted as "Method II" hereafter. As mentioned in Horvath (2004), the Japanese equation is obtained by adding one additional spring stiffness in the flexural and shear stiffness as in Stark et al. (2000) criteria. Amini (2014) mentioned that the additional stiffness is the axial stiffness for EPS embankment. The axial displacement of beam is,

$$\Delta_A = \frac{PL}{AE} \tag{5.26}$$

Replacing L and E by H and E_{ti},

$$\Delta_A = \frac{PH}{AE_{ti}} \tag{5.27}$$

$$k_A = \frac{P}{\Delta_A} = \frac{H}{AE_{ti}} \tag{5.28}$$

$$\frac{1}{k_A} = \frac{AE_{ti}}{H} \tag{5.29}$$

Eq. (5.5) can be written as,

$$\frac{1}{k} = \frac{1}{k_F} + \frac{1}{k_S} + \frac{1}{k_A} \tag{5.30}$$

Eq. (5.6) can be rewritten as,

$$T_0 = 2\pi \left[\left(\frac{W}{g}\right)\left(\frac{1}{k_F} + \frac{1}{k_S} + \frac{1}{k_A}\right)\right]^{0.5} \tag{5.31}$$

Excitation along the longitudinal direction,

By substituting the values from Eq. (5.11), Eq. (5.17) and Eq. (5.29) in Eq. (5.31),

$$T_0 = 2\pi \left\{\left[\frac{\sigma'_{v0}H}{E_{ti}g}\right]\left[4\left(\frac{H}{B}\right)^2 + \frac{(12+11\nu)}{5} + 1\right]\right\}^{0.5} \tag{5.32}$$

Excitation along the transverse direction,

$$T_0 = 2\pi \left\{\left[\frac{\sigma'_{v0}H}{E_{ti}g}\right]\left[4\left(\frac{H}{L}\right)^2 + \frac{(12+11\nu)}{5} + 1\right]\right\}^{0.5} \tag{5.33}$$

5.4.1.4 Derivation for Excitation Along the Vertical Direction

This is the case at which force is perpendicular to the cross section of the cantilever beam. The beam is in compression in this case. The stiffness is equivalent to the axial stiffness only.

$$k = \frac{AE}{L} \tag{5.34}$$

Replacing L by H and E by E_{ti} in Eq. (5.34) and substituting the value of k in Eq. (5.2),

$$T_0 = 2\pi\left[\left(\frac{W}{g}\right)\left(\frac{H}{AE_{ti}}\right)\right]^{0.5} = 2\pi\left[\left(\frac{W}{g}\right)\left(\frac{H}{LBE_{ti}}\right)\right]^{0.5} \quad (5.35)$$

$$T_0 = 2\pi\left[\frac{\sigma'_{v0}H}{E_{ti}g}\right]^{0.5} \quad (5.36)$$

The excitation along the vertical direction from the analytical method is denoted as "Analytical" hereafter. In the above equations, W is the total weight at the top of an embankment. AASHTO (2012) describes the combination of loads and load factors. The load factor of live load should be determined on a project-specific basis for the extreme event like earthquake. It indicates that there is a possibility of partial live load and taking a load factor of 0.5 on such extreme event would be reasonable. In this study, the load factor of 0.5 is taken for live load. Therefore, W is the combination of dead load and 50 percent of live load during seismic excitation.

The trapezoidal prismatic embankment is a complex shape structure and therefore calculation of stiffness is difficult, so the trapezoidal shape was converted into equivalent rectangular shape by calculating the equivalent length without altering the height and width. A similar concept was used in Horvath (1995) for 2D.

The fundamental periods were calculated for single and double lane with footing length 2 m, 3 m, 4 m, 5 m and 6 m. The detailed calculation for two different types of embankments using 4 m length of embankment employing analytical method is shown in Appendix C.

5.4.2 Numerical Approach

Rectangular and trapezoidal prismatic shaped EPS geofoam embankments were modeled in FLAC 3D to compare the result with analytical methods. In the model, 2 m, 3 m, 4 m, 5 m, and 6 m length of footings were chosen. A typical model of 4 m length, 9 m width and 6 m height is shown in Figure 5.6. In Figure 5.6, blue and red colors represent the bridge foundation and EPS embankment, respectively.

For each model, excitation was made in longitudinal, transverse and vertical directions. Material properties were calculated. For example, calculation for 4 m length of bridge is given in Appendix D. The compressive strength of concrete was assumed to be 5000 psi (34474 kPa) (Concrete-Properties, 2014). MacGregor and Wight (2005) mentioned that the Poisson's ratio for most concrete falls in the range of 0.15 to 0.20. In this study, the Poisson's ratio of 0.18 was selected.

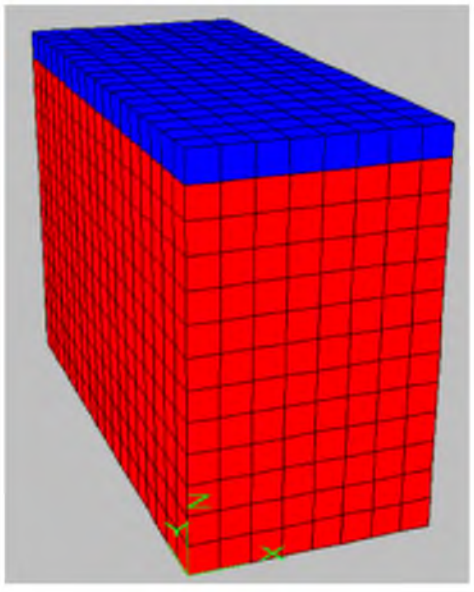

Figure 5.6. EPS geofoam embankment system

The modulus of elasticity of concrete was calculated from the Eq.(5.37) as given in MacGregor and Wight (2005):

$$E_C = 33(w^{1.5})\sqrt{f'_c}\, psi \tag{5.37}$$

where w is weight of the concrete in lb/ft^3 and f'_c is compressive strength of concrete in psi. The shear modulus and bulk modulus were calculated from the Eqs (5.16) and (5.38), respectively.

$$K = \frac{E_C}{3(1-2\nu)} \tag{5.38}$$

The precise density of EPS 29 was taken from the laboratory tests results given in Chapter 4. The density and modulus of elasticity of EPS geofoam were 34.02 kg/ m^3 and 12547 kPa respectively. The Poisson's ratio of EPS was calculated from the relation of Poisson's ratio and density as given in Eq. (5.39) by Horvath (1995).

$$\nu = 0.0056\rho + 0.0024 \tag{5.39}$$

The shear and bulk modulus of EPS material were calculated from the Eqs (5.16) and (5.38), respectively. The density of material used in footing was calculated by incorporating the dead load of bridge and half of live load. In this case, the volume of footing was calculated first and then the density was calculated from the simple ratio of total mass to the volume. The material properties are shown in Table 5.2. The density of

Table 5.2. Material properties of EPS geofoam embankment system

Material	ρ	E	ν	G	K
----------	kg/m^3	MPa	----------	MPa	MPa
EPS	34.02	12.55	0.19	5.26	6.81
Concrete	2400.00	29557.00	0.18	12523.00	15394.00

concrete used in the model was different from the usual density of concrete. The density varied with type of lanes and length of footing.

In the model, foundation of embankment was not considered because EPS is very light weight material and there is not much interaction between EPS and soil below. The assumption was based on the findings reported by Amini (2014). Amini studied soil-structure interaction by considering foundation soil below EPS embankment. In the study, the acceleration response was analyzed by applying the acceleration at the base of embankment and at the base of the soil. The acceleration response was found quite similar in both cases.

The EPS embankment was modeled as a single body with consideration of coherent mass which means there are no vertical and horizontal interfaces. The material properties given in Table 5.2 were used in the model.

The embankment had no confinement in reality. Thus, the sides of embankment were kept free. The fixed boundary conditions were applied at the base. The base was fixed to the direction other than the direction of excitation. For example, transverse and vertical directions were fixed to excite the model in the longitudinal direction. No material damping was provided into the model. The velocity was applied as forcing function at the base of the model. The waves were assigned either free vibration or force vibration. Both

methods were employed and the results were compared.

In the force vibration, a trial and error method was used. In this method, the period was changed in the wave equation and the displacement was monitored at the uppermost node of the footing. Since the damping was not provided in the model, the displacement increased until it reached the resonance condition. The displacement at the top node versus dynamic time for EPS embankment of 4 m length, 6 m height and 9 m width due to excitation along the longitudinal direction with period of 1.095 sec is shown in Figure 5.7.

The forced vibration method is more time consuming for calculating fundamental period. The free vibration was also employed for the same model. In this method, *sin* wave was used as input motion at which free vibration occurred with pulse loading.

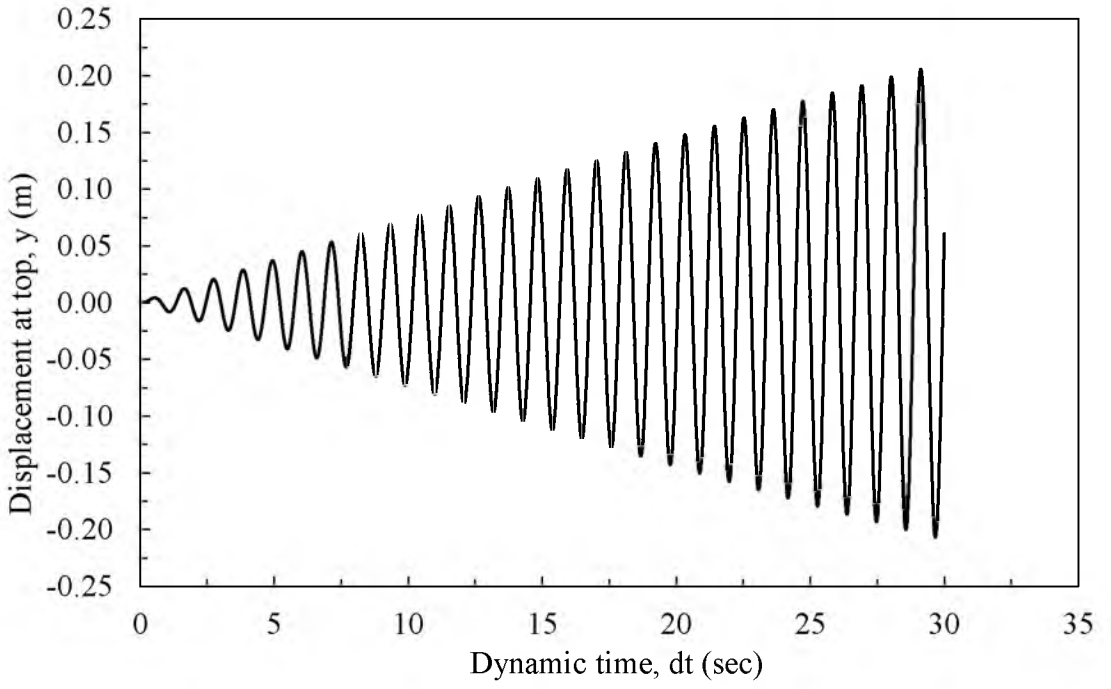

Figure 5.7. Displacement at top versus dynamic time under forced vibration

Figure 5.8 revealed the pulse loading at which the embankment starts to move back and forth freely once the pulse loading ceased. From Figure 5.8, it is seen clearly that free vibration starts after one cycle of pulse loading. The data were extracted to plot displacement versus dynamic time.

For verification, the same model was used for forced vibration. The displacement versus time plot is shown in Figure 5.9. The fundamental period was then calculated by measuring the time required for one complete cycle. In this case, the first cycle could not represent the fundamental period because of the application of pulse loading. The period of one cycle after the first cycle was considered the fundamental period. From the plot, the fundamental period was 1.095 sec. This revealed that free vibration is a more efficient way of calculating fundamental period and it was used in this study.

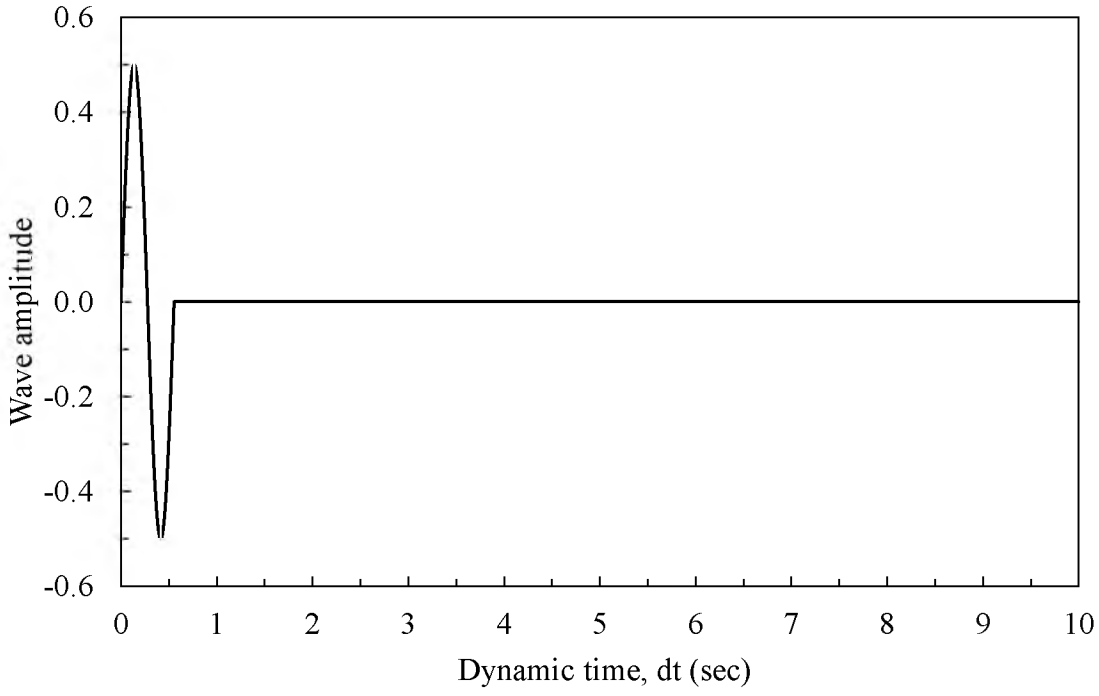

Figure 5.8. Relationship of wave and dynamic time as pulse loading condition

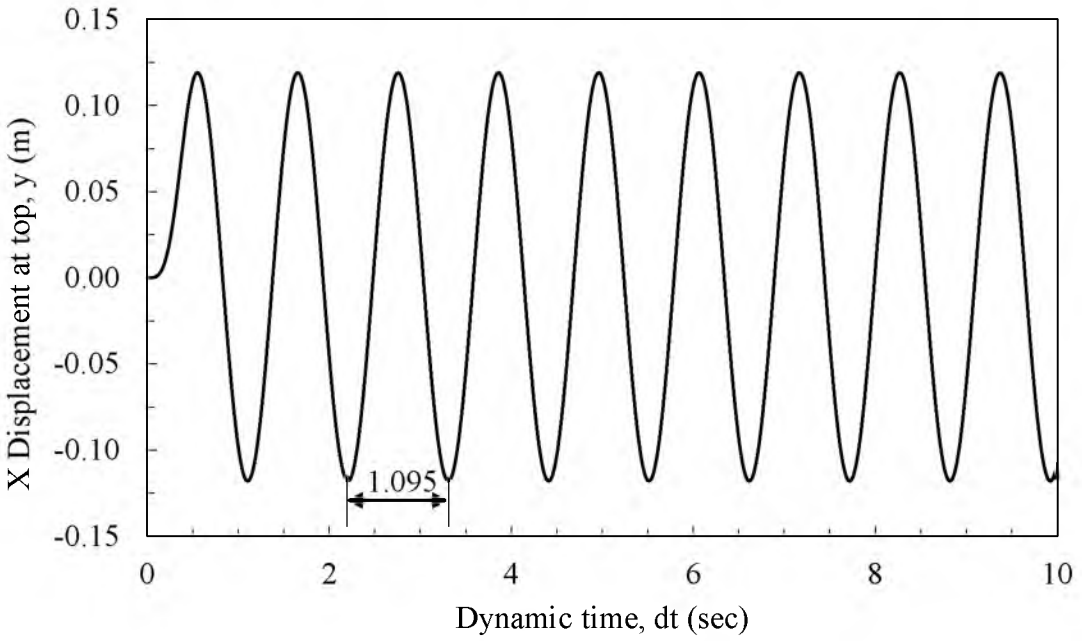

Figure 5.9. Displacement at top node versus time at fundamental period

The FLAC code for the calculation of fundamental period by using free vibration by providing excitation along the longitudinal direction for 4 m length of footing is given in Appendix E.

5.5 Factor of Safety Against Sliding and Preventive Measures

Since EPS geofoam is very light weight material, the weight of EPS was neglected in the calculation. AASHTO (2012) described the consideration of seismic vertical and horizontal acceleration for wall design. According to guideline, vertical accelerations are assumed to be zero because horizontal and vertical accelerations do not occur at the same time. The rigorous analysis of interlayer sliding and horizontal displacement was carried out by Bartlett and Lawton (2008) and Amini (2014). In this research, it was concluded that the maximum amount of sliding does not change at higher level of horizontal

acceleration while considering vertical accelerations. Hence, in this study only the horizontal acceleration was included for the calculation of factor of safety against sliding. For the calculation of interlayer and basal layer sliding, peak ground acceleration and spectral acceleration are required. The spectral acceleration is determined from the site specific response spectrum. In this study, the peak ground acceleration and spectral acceleration were assumed to be same for the matter of generalized concept of design. For the site specific analysis, the methods used in Bartlett and Lawton (2008) and Amini (2014) could be used.

The analytical method was used for the calculation of critical acceleration. The rectangular and trapezoidal prismatic shape embankments were analyzed in a similar manner. The inertial force was calculated by the product of mass and acceleration. The mass was the mass above the embankment and the acceleration was the assumed horizontal acceleration. The frictional resisting force was calculated from normal stress and internal friction between geofoam-geofoam and geofoam-soil interfaces. The geofoam-geofoam and geofoam-soil internal friction was calculated from the relationship of friction factor and normal stress developed by Sheeley and Negussey (2001) and Bartlett et al. (2000), respectively. In the trapezoidal prismatic shape embankment, the stress distribution was considered to be 2V:1H, so the stress concentration was different on each layer. The stress concentration was calculated from the following relationship:

$$\sigma_z = \frac{\sigma_v L_{top} B}{\left[L_{top} + (n-1)\Delta z\right] B} \tag{5.40}$$

where σ_z is stress at any depth, σ_v is stress at top of embankment, n is number of layers

measured from top, L_{top} is length of trapezoidal footing at top of embankment, Δz is thickness of each layer and B is width of embankment.

One of the methods to prevent interlayer sliding is the use of shear keys during construction. Shear keys are half-height EPS blocks which interrupt the formation of continuous horizontal slide planes during high excitation. The shear key is calculated as percentage shear coverage and is expressed in terms of percentage. The shear key provides the cohesive resisting force. The cohesive resisting force per unit area is the product of geofoam shear strength and shear coverage.

The geofoam shear strength is obtained from the laboratory tests. Direct shear test is the most common test for shear strength determination but it is more suitable for the evaluation of frictional interface shear resistance for rigid body. EPS is flexible material, so one of the appropriate methods for the determination of shear strength is direct simple shear. This is the most representative test for the determination of shear strength of EPS but is hardly used in practice because this test is relatively expensive and complex. In this study, the shear strength of EPS based on ASTM (2010) as mentioned in BenchmarkFoam (2009) was used. In this method, a punch type shear tool was used for determining the shear strength. The specimen was clamped during the test and the punching tool was pushed through the specimen. The shear strength was then calculated by dividing the load required to shear the specimen by the area of sheared edge.

Foundation embedment is one of the easiest techniques to prevent basal sliding However, the depth of embedment is limited to 1.5 m in most of cases. From the construction point of view, deep embedment is very expensive. In embedded foundation, the seismic passive force provides the resistant for sliding. When the seismic excitation

takes place, the embedment along the leading side of excitation yields the passive earth pressure and the trailing side yields the active earth pressure.

In this study, the embedment depth was assumed to be less than 1.5 m. According to AASHTO (2012) for such depth, passive pressure should be calculated using the static methods. The active earth pressure was also calculated from static methods using Coulomb's Theory. Active earth pressure coefficient (K_{AE}) can be calculated from the Eq. (5.41).

$$K_{AE} = \frac{cos^2(\varphi - \beta)}{cos^2\beta\cos(\delta + \beta)\left[1 + \sqrt{\frac{\sin(\varphi + \delta)\sin(\varphi - i)}{\cos(\delta + \beta)\cos(i - \beta)}}\right]^2} \tag{5.41}$$

where φ is the wall backfill friction angle, i is backfill slope angle, K_{AE} is seismic active earth pressure coefficient, δ is wall backfill interface friction angle and β is slope of wall to the vertical.

In this study, the seismic passive earth pressure was calculated using the static method mentioned in AASHTO (2012). The coefficient of passive pressure (K_P) was determined from the plot reported in AASHTO. In the plot, K_P was the relation between φ and angle of back face of wall to the horizontal (θ). The reduction factor (R) was calculated according to the ratio of δ to φ and φ. The corrected value was the simple product of K_P and R. The active and passive force was then calculated by using Eqs (5.42) and (5.43), respectively.

$$P_{AE} = \frac{1}{2} K_{AE} \gamma D^2 B \tag{5.42}$$

where γ is the unit weight of soil, D is depth of embedment, B is width of embankment.

$$P_{PE} = \frac{1}{2} K_{PE} \gamma D^2 B \tag{5.43}$$

where K_{PE} is seismic passive earth pressure coefficient.

Once the seismic active and passive earth pressure were calculated, the seismic horizontal and vertical components were also determined. Similarly, the resisting and driving forces were obtained. The resistant force was the combination of horizontal component of passive force and frictional force. The frictional force is the product of normal force and tangent of friction angle of soil. The driving force is the sum of the inertial force and horizontal component of active force. The factor of safety against sliding is the ratio of resisting force to the driving force. The factor safety due to excitation along both directions was determined.

5.6 Results and Discussion

5.6.1 Sizing of Bridge

The results of calculating length of bridge using steel and concrete and EPS 22 and 29 embankment materials for footing of length 4 m are summarized in Table 5.3. Even if steel was used for bridge, the maximum length of bridge using EPS 22 was 20 m. Figure 5.10 showed the relationship of length of footing with length of bridge for both steel and

Table 5.3. Length of concrete and steel bridge for embankments with EPS 22 and 29 for 4 m length of footing

Material	Lane	Width of bridge	Type of EPS	Length of bridge
---	---	*m*	---	*m*
Steel	Single	5.25	22	20
Steel	Double	9	22	18
Steel	Single	5.25	29	34
Steel	Double	9	29	31
Concrete	Single	5.25	22	12
Concrete	Double	9	22	11
Concrete	Single	5.25	29	21
Concrete	Double	9	29	18

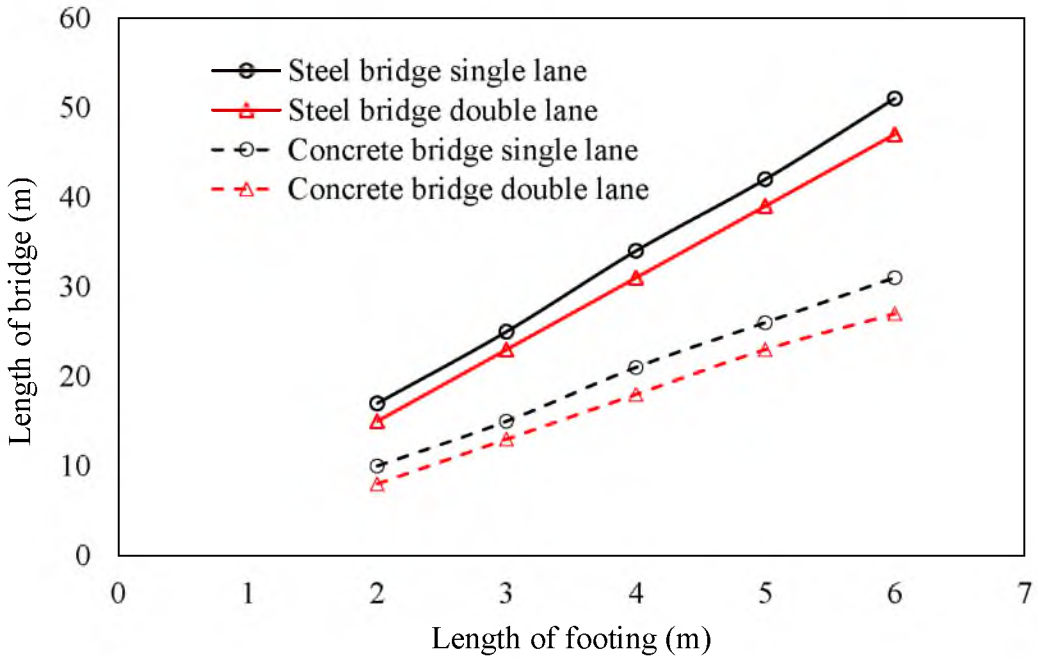

Figure 5.10. Relationship of length of bridge with length of footing for single and double lane bridges

concrete bridges. The expected length of bridge was around 30 m. It could also be achieved by using concrete material but this required 6 m of footing. A steel bridge with EPS 29 of length 4 m seemed to be more reasonable. In this study, EPS 29 of length 4 m was considered for detailed analysis. The length of bridge was increased linearly with increase of length of footing. For the same length of footing, length of bridge for a single lane was slightly longer than for a double lane because the load was doubled for double lane but the width of bridge was not exactly doubled.

5.6.2 Fundamental Period

The fundamental period for rectangular prism when it was excited in three directions for single and double lane is shown in Figure 5.11 and Figure 5.12. The figures reveal that fundamental period decreased with increased in length of footing when the seismic excitation was introduced along that direction. Fundamental period mainly depends on the mass and stiffness of material. It is directly proportional to the mass and inversely proportional to the stiffness.

Mass above the embankment and embankment itself was constant for all cases, so the stiffness of embankment depended on the dimensions of embankment. Since width and height remained constant, stiffness increased with increased in length and the fundamental period decreased. The fundamental period along transverse and vertical directions was almost constant because of the constant width and height. For the single lane, the fundamental period along the longitudinal direction was higher than the transverse direction for the length less than width. Once the length exceeded the width, the period along the longitudinal direction decreased.

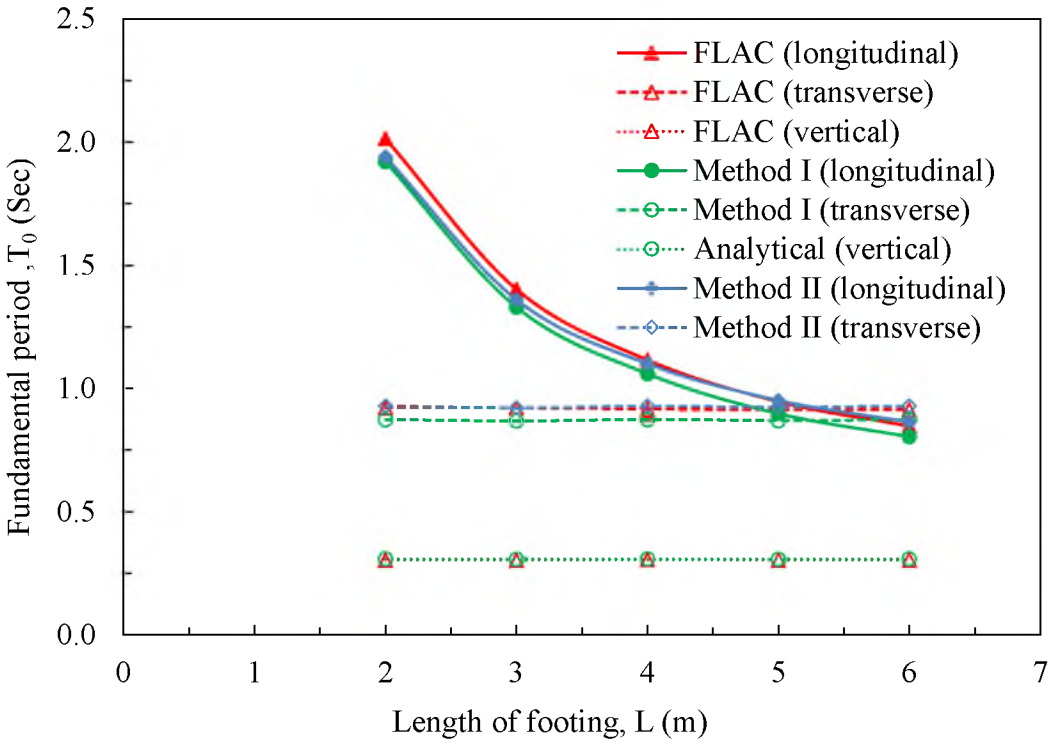

Figure 5.11. Fundamental period of rectangular prismatic shape embankment from numerical and analytical methods at various length of footing for single lane

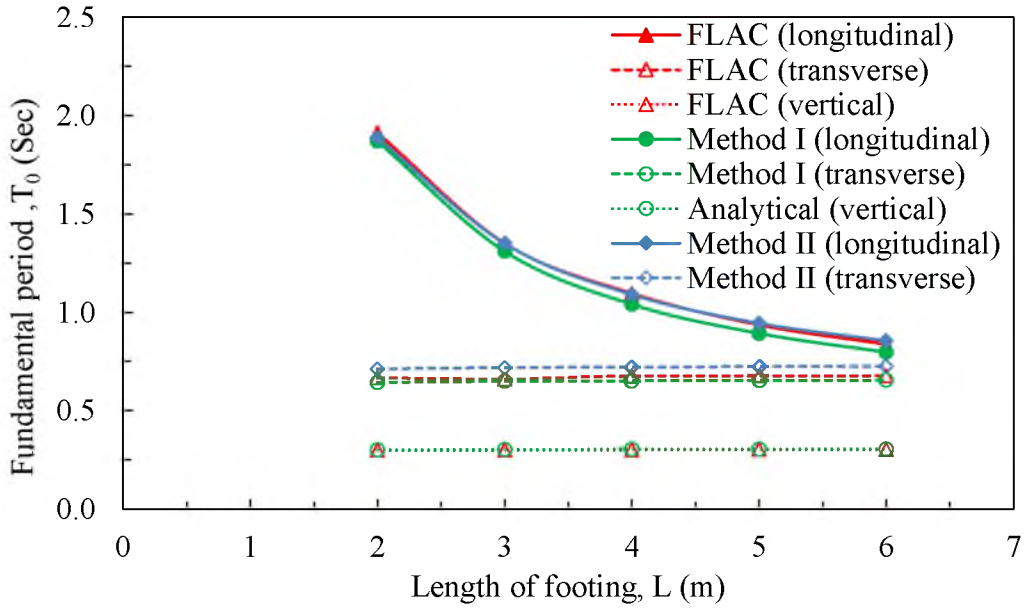

Figure 5.12. Fundamental period of rectangular prismatic shape embankment from numerical and analytical methods at various length of footing for double lane

Similar results were obtained for the double lanes. In the double lane, the width exceeded length in all cases and the fundamental period was higher in the longitudinal direction for all values of length. The fundamental period for the excitation along the longitudinal direction was in the range of 0.8 to 2.0 sec. Value was smaller for higher length and vice versa. The fundamental periods were around 0.9 sec and 0.3 sec for excitation along transverse and vertical directions, respectively.

The percentage errors for different geometries are presented in Table 5.4. FLAC results were used as baseline to find the percentage errors because FLAC 3D analysis included all stiffness such as flexural, shear and axial stiffness. The following relation was used for the calculation of percentage errors:

$$Percentage\ error = \frac{T_{0(Analytical)} - T_{0(FLAC)}}{T_{0(FLAC)}} 100 \tag{5.44}$$

There was no definite relationship of percentage error with length of footing. In most of the cases, percentage error was smaller for higher length of embankment. Method II results were very close to the FLAC results for a single lane whereas Method I results were close to FLAC results for a double lane with excitation along the transverse direction. The percentage error was less than 10 percent, meaning that the analytical method can be used in designing for simple types of embankments. In most cases, Method II results were close to FLAC results. This means that the consideration of flexural, shear and axial stiffness is a better representation for fundamental period calculation. Numerical techniques are required for complex geometrical embankments.

Table 5.4. Percentage error of FLAC with Method I and Method II for single lane and double lane with various lengths of footing for rectangular prismatic shape embankment

	Percentage Error									
	Single Lane					Double Lane				
	Method I and FLAC			Method II and FLAC		Method I and FLAC			Method II and FLAC	
Length of Footing	Longitudinal	Transverse	Vertical	Longitudinal	Transverse	Longitudinal	Transverse	Vertical	Longitudinal	Transverse
m	%	%	%	%	%	%	%	%	%	%
2	-4.667	-5.212	1.650	-3.674	0.760	-2.197	-3.598	-1.151	-1.151	6.747
3	-5.203	-5.863	0.990	-3.065	0.000	-2.963	-1.667	1.003	0.000	8.788
4	-5.018	-4.694	0.984	-1.434	1.310	-5.023	-3.840	1.333	-0.457	6.499
5	-5.174	-4.819	0.658	0.422	1.205	-4.599	-3.259	0.662	0.963	7.111
6	-5.077	-4.381	1.316	1.889	1.643	-4.785	-3.540	1.329	2.273	6.785

The fundamental period of trapezoidal prismatic shape embankment for single and double lanes under excitation along three directions for various lengths is shown in Figure 5.13 and Figure 5.14. For the single and double lane, fundamental period increased with increase in length. Fundamental period along the transverse direction was larger than for the longitudinal direction. The average length of trapezoidal section was larger than the width for both single and double lane. As the distance of excitation increased, the stiffness of embankment increased and the corresponding fundamental period decreased. The percentage error for single lane and double lane with various lengths of embankment is shown in Table 5.5. The results revealed that percentage error decreased with increase in length of footing.

The relationship of percentage errors with length is shown in Figures 5.15, 5.16, 5.17 and 5.18. In these figures, the maximum percentage error was 40. The larger percentage in error might be due to the assumption of equivalent rectangular prism in analytical analysis. In FLAC, models were prepared with real geometry, so the corrections were made according to FLAC results. Errors in longitudinal directions were smaller than in transverse directions. Moreover, the percentage errors were slightly lower for Method II in comparison to Method I for most of the cases. From the analysis of two different methods, it seemed more reasonable to consider the flexural, shear and axial stiffness for the calculation of fundamental period. The linear regression of percentage error with length of footing due to excitation along three directions is shown in Figures 5.15, 5.16, 5.17 and 5.18.

In the design, these errors need to be adjusted. In this study, the adjustment of error was done by using following relation:

Table 5.5. Percentage error of FLAC with Method I and Method II for single lane and double lane with various length of footing for trapezoidal prismatic shape embankment

	Percentage Error									
	Single Lane					Double Lane				
	Method I and FLAC			Method II and FLAC		Method I and FLAC			Method II and FLAC	
Length of Footing	Longitudinal	Tranverse	Vertical	Longitudinal	Transverse	Longitudinal	Transverse	Vertical	Longitudinal	Transverse
m	%	%	%	%	%	%	%	%	%	%
2	-23.9	-29.5	-40.2	-13.8	-25.0	-25.17	-31.9	-33.7	-15.03	-24.6
3	-19.9	-27.1	-37.7	-8.5	-22.6	-20.75	-31.0	-33.8	-9.75	-23.6
4	-17.5	-26.6	-34.7	-5.5	-20.8	-17.46	-26.7	-33.9	-5.62	-18.9
5	-14.4	-23.4	-32.1	-2.0	-18.7	-13.26	-25.0	-31.1	-0.58	-16.9
6	-12.8	-20.9	-29.1	0.3	-15.9	-12.15	-23.9	-28.2	0.83	-15.9

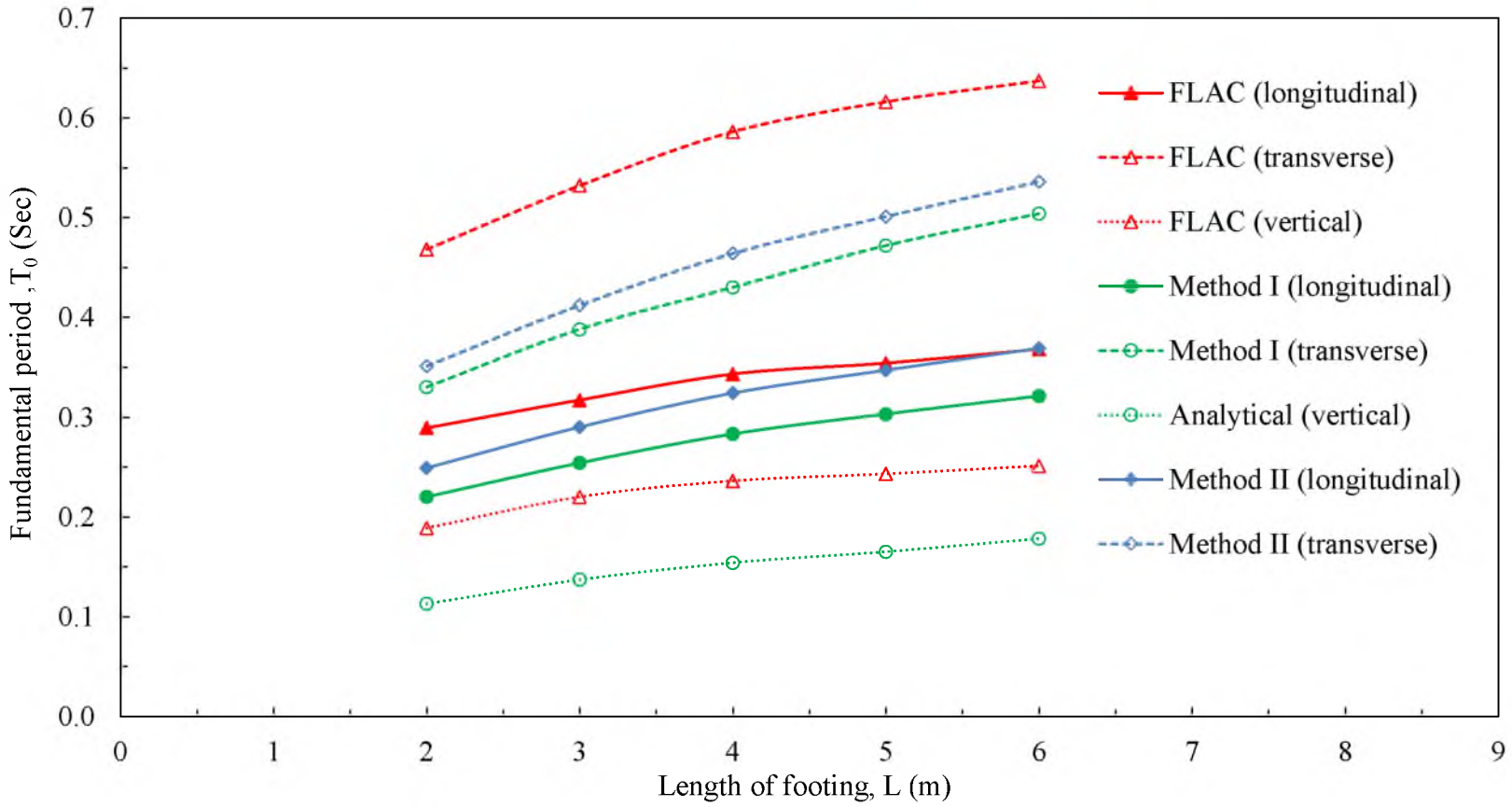

Figure 5.13. Fundamental period of trapezoidal prismatic shape embankment for single lane obtained from numerical and analytical methods for various lengths of footing

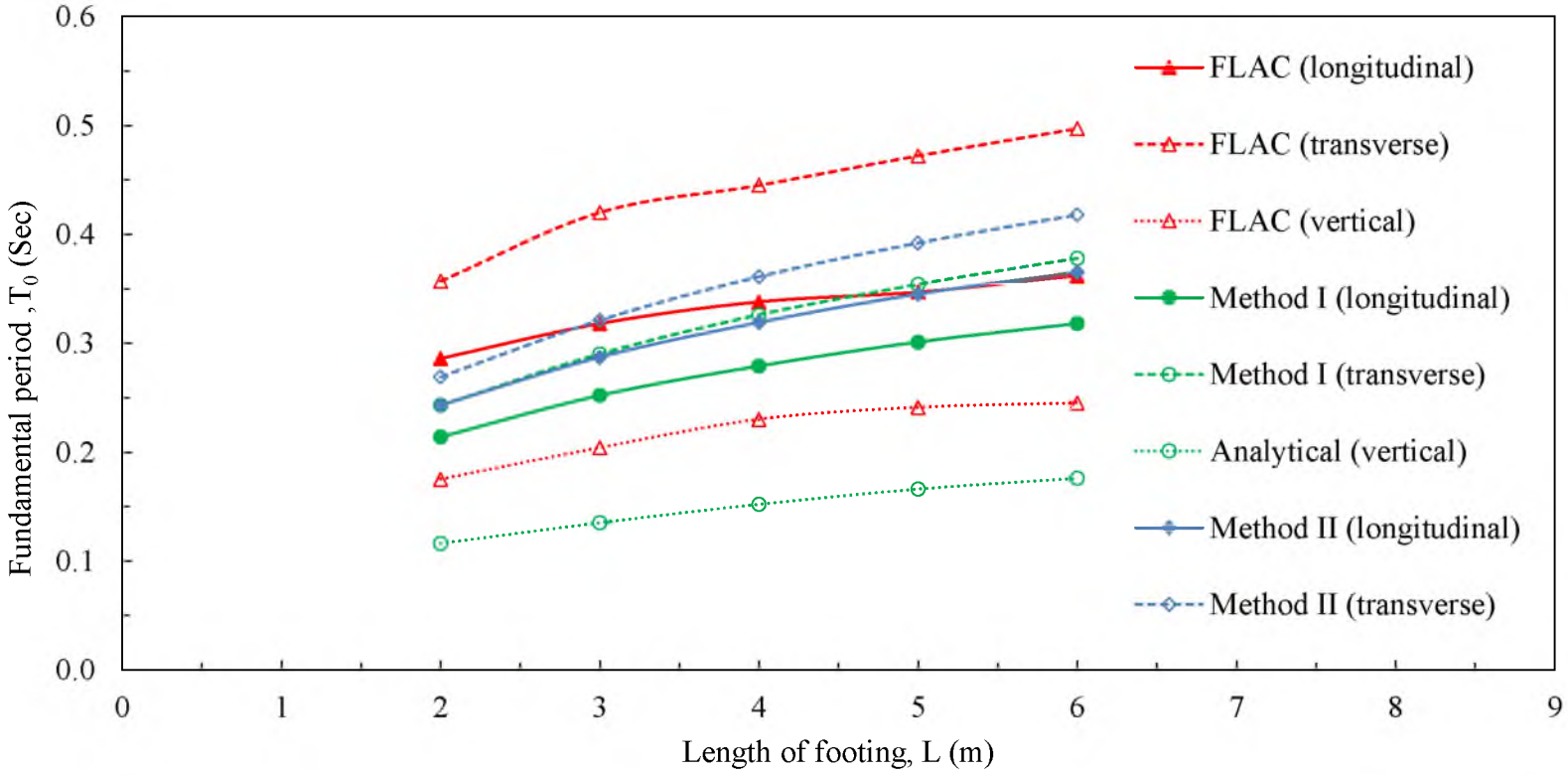

Figure 5.14. Fundamental period of trapezoidal prismatic shape embankment for double lane obtained from numerical and analytical methods for various lengths of footing

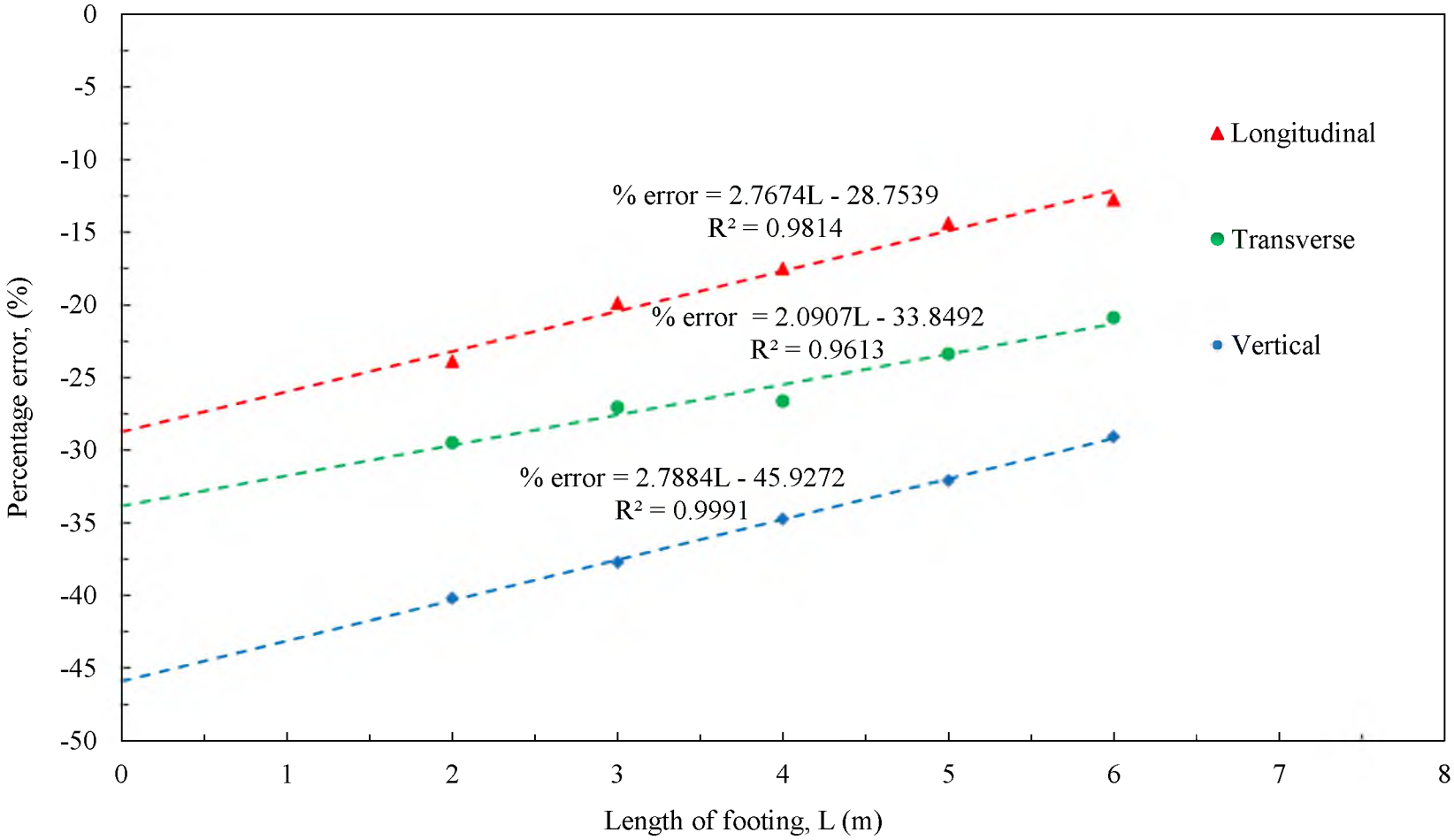

Figure 5.15. Percentage error with length of footing for single lane between FLAC and Method I

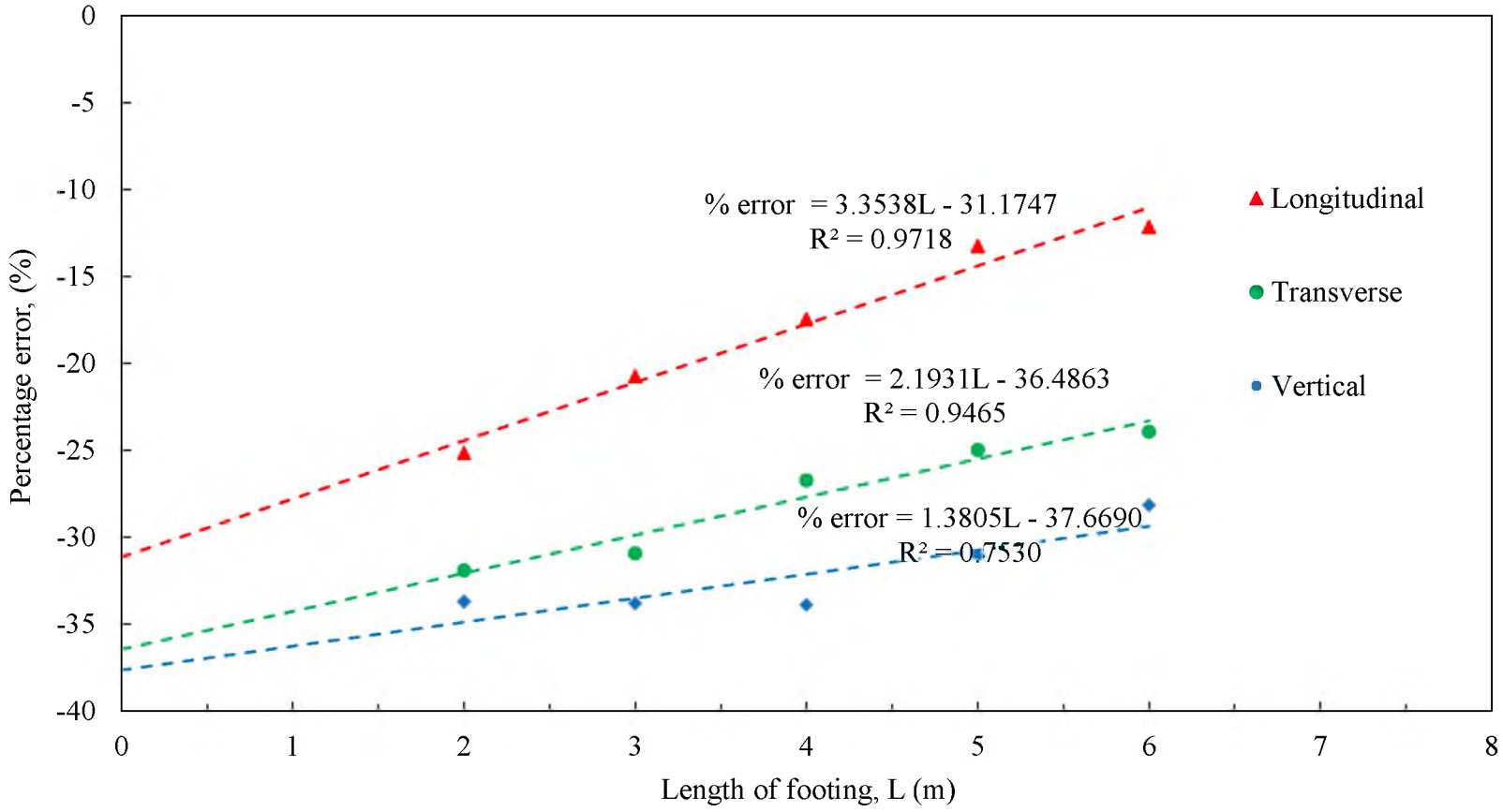

Figure 5.16. Percentage error with length of footing for double lane between FLAC and Method I

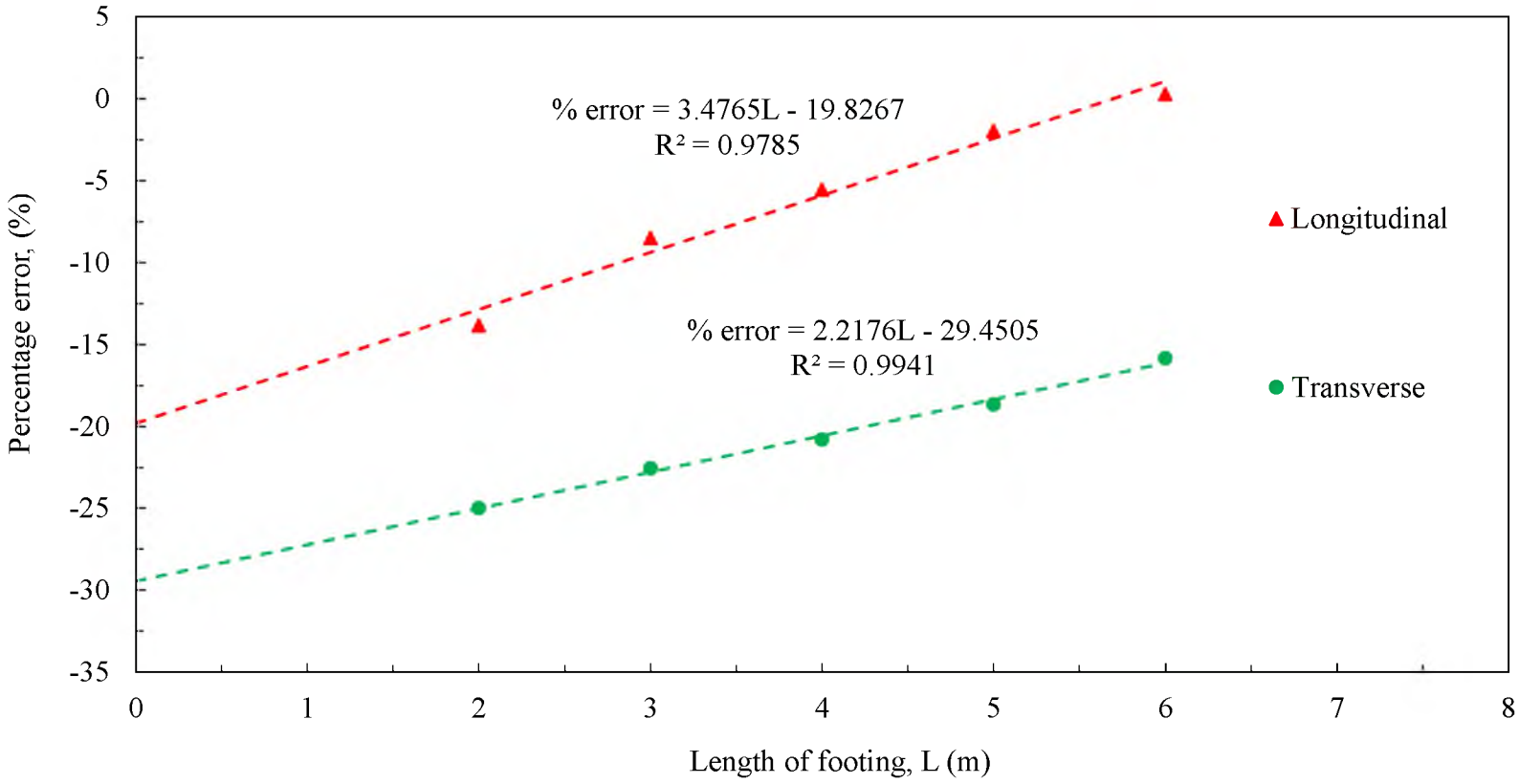

Figure 5.17. Percentage error with length of footing for single lane between FLAC and Method II

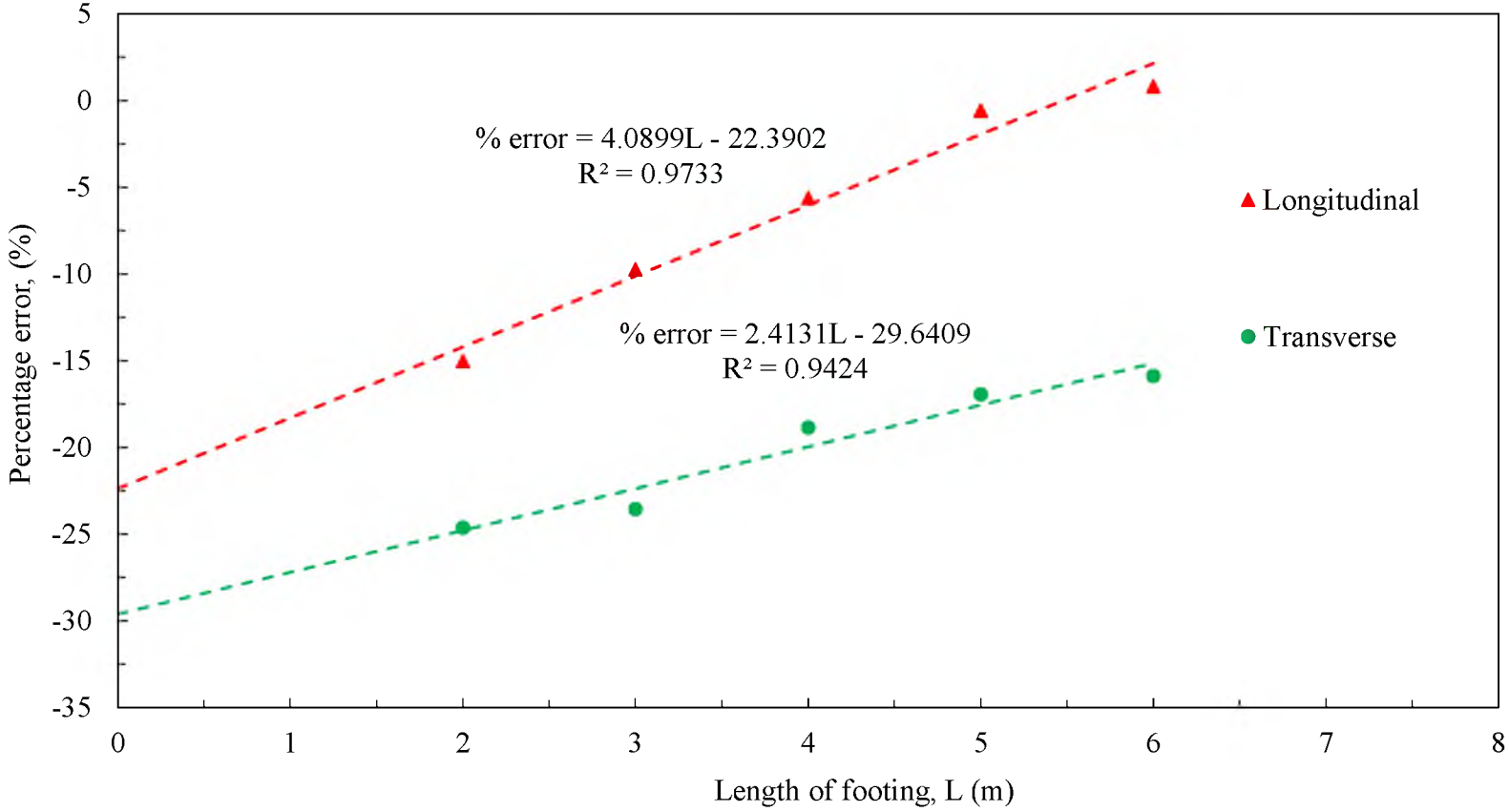

Figure 5.18. Percentage error with length of footing for double lane between FLAC and Method II

Adjusted value = Calculated value – Calculated value x (Linear regression equation)/100

The adjusted and calculated values were denoted by AV and CV hereafter. The adjusted value in terms of length of footing for single lane and double lane for Methods I and II are given below.

5.6.2.1 Method I and Single Lane

Excitation along the longitudinal direction,

$$AV = CV - (2.7674L - 28.7539)\frac{CV}{100} \tag{5.45}$$

Excitation along the transverse direction,

$$AV = CV - (2.0907L - 33.8492)\frac{CV}{100} \tag{5.46}$$

Excitation along the vertical direction,

$$AV = CV - (2.7884L - 45.9272)\frac{CV}{100} \tag{5.47}$$

5.6.2.2 Method I and Double Lane

Excitation along the longitudinal direction,

$$AV = CV - (3.3580L - 31.1747)\frac{CV}{100} \tag{5.48}$$

Excitation along the transverse direction,

$$AV = CV - (2.1931L - 36.4863)\frac{CV}{100} \tag{5.49}$$

Excitation along the vertical direction,

$$AV = CV - (1.3850L - 37.6690)\frac{CV}{100} \tag{5.50}$$

5.6.2.3 Method II and Single Lane

Excitation along the longitudinal direction,

$$AV = CV - (3.4765L - 19.8267)\frac{CV}{100} \tag{5.51}$$

Excitation along the transverse direction,

$$AV = CV - (2.2176L - 29.4505)\frac{CV}{100} \tag{5.52}$$

5.6.2.4 Method II and Double Lane

Excitation along the longitudinal direction,

$$AV = CV - (4.0899L - 22.3902)\frac{CV}{100} \tag{5.53}$$

Excitation along the transverse direction,

$$AV = CV - (4.0899L - 22.3902)\frac{CV}{100} \tag{5.54}$$

In the above adjusted value relations, L is denoted as the length of footing. During design, the derived relation of adjusted value can be used to calculate fundamental period of trapezoidal prismatic shape without using numerical methods. The values obtained from the above relations after adjustment should be within 10 percent of the value obtained from numerical methods with exact geometry difference except for the excitation along the vertical direction. The adjusted value in the vertical direction should be within 20 percent of the value obtained from numerical methods. However the error should decrease with increase of length of footing. Hence, the trapezoidal prismatic shape can be converted into equivalent rectangular prismatic shape and the adjusted value can be used in design for the calculation of fundamental period.

5.6.3 Sliding and Preventive Measures

The critical acceleration for single lane and double lane bridge with various lengths of footing for rectangular and trapezoidal prismatic shape embankment was calculated. The calculated value is shown in Table 5.6.

In this study, simplified analytical techniques like shear keys and embedment at the base were employed to prevent sliding. The shear keys were used in between the interlayers where the factor of safety against sliding was less than 1.1. In dynamics, the structure is considered safe if the factor of safety against sliding is in the range of 1.1 to

Table 5.6. Summary of critical acceleration for rectangular and trapezoidal prismatic shape embankments

Footing length	Critical acceleration for single lane		Critical acceleration for double lane	
	Rectangular	Trapezoidal	Rectangular	Trapezoidal
m	*g*	*g*	*g*	*g*
2	0.6	0.6	0.6	0.6
4	0.6	0.6	0.6	0.6
6	0.6	0.6	0.6	0.6

1.2. The interlayer sliding was prevented by using proper percentage of shear key coverage in the layer where the factor of safety was less than minimum required value. The embankment was embedded where the factor of safety was less than 1.1. In the embedded embankment, the passive earth pressure provides extra resistance against sliding and thus the factor of safety is increased.

The depth of embedment and shear key coverage varied according to the embankment size. The use of shear key and embedment of embankment for double lane bridge with 4 m length of footing for both types of embankments with excitation along longitudinal and transverse directions is given in Appendix F. In these calculations, it was shown that shear key is not required for the horizontal acceleration of less than or equal to 0.7 g whereas embedment is required to stop basal layer sliding. For the acceleration equal to or higher than 0.8 g, shear key is required. The calculation for shear key coverage and factor of safety against sliding for 1.0 g is shown in Appendix F. The shear key coverage was 8 percent for the acceleration of 1.0 g.

The depths of embedment for trapezoidal and rectangular prismatic shape embankments for the acceleration of 1.0 g were 1.0 m and 1.4 m, respectively. The detailed calculation is shown in Appendix F. In general, 1.0 g acceleration would occur in extreme cases. In the trapezoidal prismatic shape, the factor of safety was higher when the system was excited along the transverse direction. As the dimension of embankment got larger, the factor of safety became higher. For the rectangular prismatic shape, the factor of safety against sliding was higher when it was excited along the longitudinal direction because the size of the resisting side was higher, since 1.0 g is the extreme value of excitation and in most cases excitation is quite below 1.0 g. Hence, 1 m depth of embedment might be enough for most cases.

5.7 Conclusions

The size of bridge, fundamental period of structure, critical acceleration and preventive measure of sliding were studied. EPS 22 and 29 were selected for the analysis. The bridge was designed on the basis of EPS density used in the embankment. The length of bridge was determined for various lengths of footing, and steel and concrete materials. The length of bridge increased with increase in length of footing. The desirable length of bridge was around 30 m. The most appropriate combination for acquiring such length was 4 m length of footing with EPS 29 and steel bridge.

The fundamental period of structure was calculated for bridge support systems by considering rectangular and trapezoidal prismatic shapes using analytical and numerical methods. In analytical methods, the concept of Timoshenko and Gere (1972) was used for the calculation of flexural, shear and axial stiffness. The stiffness calculation of

trapezoidal prismatic shape was difficult and therefore it was converted into equivalent rectangular prismatic shape in analytical methods. The results of analytical method were compared with FLAC results. The results from analytical methods for rectangular prisms were very close to FLAC results. The values were within 10 percent difference of each other. The fundamental period was in the range of 0.8 - 2.0 sec, around 0.9 sec and 0.3 sec for excitation along longitudinal, transverse and vertical directions, respectively.

The percentage difference between the two methods was higher for the trapezoidal prism because the equivalent rectangular prism was used instead of real geometry. The fundamental periods were in the range of 0.2-0.4 sec, 0.2-0.5 sec and 0.1-0.3 sec for excitation along longitudinal, transverse and vertical directions, respectively. The errors were adjusted and equations were developed for various conditions. The consideration of flexural and shear stiffness seemed to be more appropriate in analytical methods. Numerical methods were required only for complex geometry. For designing purposes, these analytically developed equations are useful.

The critical acceleration for both of the embankments were found to be 0.6 g. The interlayer sliding did not occur for the acceleration of less than or equal to 0.8 g whereas basal sliding occurred beyond 0.6 g. The shear keys were used to stop the interlayer sliding. The basal layer sliding was stopped by embedding the embankment. For the excitation of 1.0 g, the required depth of embedment was 1.4 m for critical case. The critical acceleration and restraint against sliding can be calculated by using analytical methods. This concept can be used in design for simple geometrical shape embankments without the need of numerical techniques.

5.8 References

Aaboe, R., and Frydenlund, T. E. (2011). "40 years of experience with the use of EPS geofoam blocks in road construction." *Proc., 4th Intl. Conf on Geofoam Blocks in Construction Applications,* Lillestrom, Norway.

AASHTO (2012). *AASHTO LRFD bridge design specifications*, Washington DC 20001.

Amini, Z. A. (2014). "Dynamic characteristics and seismic stability of expanded polystyrene geofoam embankments." Ph.D. thesis, The University of Utah, Utah, USA.

ASTM D6817 (2007). *Standard specification for rigid cellular polystyrene geofoam*, American Society for Testing and Materials, West Conshohocken, PA, USA.

ASTM D732 (2010). *Standard test method for shear strength of plastics by punch tool*, American Society for Testing and Materials, West Conshohocken, PA, USA.

Bartlett, S., Negussey, D., Kimble, M., and Sheeley, M. "Use of geofoam as super-lightweight fill for I-15 reconstruction." *Proc., Transportation Research Board 79th Annual Meeting*, Transportation Research Board Washington, DC.

Bartlett, S. F., and Lawton, E. C. "Evaluating the seismic stability and performance of freestanding geofoam embankment." *Proc., 6th National Seismic Conf on Bridges and Highways*, Federal Highways Administration (FHA) and Multidisciplinary Center for Earthquake Engineering Resarch (MCEER) Charleston, SC, 17.

BenchmarkFoam (2009). "Physical properties of EPS." *Strength properties*, <http://benchmarkfoam.com/wpcontent/uploads/2009/09/physicalepsproperties_rev040510.pdf>. (November 15, 2014).

Concrete-Properties (2014). "The engineering tool box." *Properties of normal strength Portland cement concrete*, <http://www.engineeringtoolbox.com/concrete-properties-d_1223.html>. (October 16, 2014).

Cowper, G. (1966). "The shear coefficient in Timoshenko's beam theory." *Journal of Applied Mechanics*, 33(2), 335-340.

Farnsworth, C., Bartlett, S. F., Negussey, D., and Stuedlein, A. (2008). "Rapid construction and settlement behavior of embankment systems on soft foundation soils." *Journal of Geotechnical and Geoenvironmental Engineering*, 134(3), 289-301.

Horvath, J. S. (1995). *Geofoam geosynthetic*, Horvath Engr., P.C., Scarsdale, New York, USA.

Horvath, J. S. (2004). "A tenchical note re calculating the fundamental period of an EPS-block-geofoam embankment." *Rpt. No. CGT-2004*, Manhattan College, School of Engineering, Bronx, New York, USA.

Itasca (2005). "FLAC: Fast Lagrangian Analysis of Continua: structural elements, version 5." Minneapolis, MN.

Itasca (2006). "FLAC: Fast Lagrangian Analysis of Continua: structural elements, version 3.1." Minneapolis, MN.

MacGregor, J. G., and Wight, J. K. (2005). *Reinforced concrete design*, Prentice Hall, Upper Saddle River, NJ.

Makdisi, F. I., and Seed, H. B. (1978). "Simplified procedure for estimating dam and embankment earthquake-induced deformations." *Journal of Geotechnical Engineering* 104(7), 849-867.

Maybehire (2012). "Quickbridge." *Specifications*, <http://www.mabeyhire.co.uk/temporary-bridging/quickbridge/>. (November 16, 2014).

McDonald, P., and Brown, P. (1993). "Ultra lightweight polystyrene for bridge approach fill." *Proc., 11th Southeast Asian Geotechnical Conference,* Singapore, 664-668.

Modjeski-Masters-Inc (2003). "Comprehensive design example for prestressed concrete girdger superstructure bridge with commentry."REPORT FHWA NHI -04-043, Pennsylvania, USA.

Riad, H. L., and Horvath, J. S. (2004). "Analysis and design of EPS-geofoam embankments for seismic loading." *Proc., Geotechnical Engineering for Transportation Projects*, ASCE, Los Angeles, CA, USA, 2028-2037.

Sheeley, M., and Negussey, D. (2001). "An investigation of geofoam interface strength behavior." *Geotechnical Special Publication*, 292-303.

Snow, C. L., and Nickerson, C. R. (2004). "Case study of EPS geofoam lightweight fill for settlement control at bridge approach embankment." *Proc., Geotechnical Engineering for Transportation Projects*, ASCE, Los Angeles, CA, USA, 580-589.

Stark, T., Arellano, D., Horvath, J., and Leshchinsky, D. (2000). "Guidelines for geofoam applications in embankment projects." *by National Cooperative Highway Research Program, Project*(24-11).

Stuedlein, A. W., and Negussey, D. (2013). "Use of EPS geofoam for support of a bridge." *Sound Geotechnical Research to Practice: Honoring Robert D. Holtz, Geotechnical Special Publication*(230), 334-345.

Tefera, T. H., Aaboe, R., Bruum, H., and Aunaas, K. (2011). "FEM simulation of full scale and laboratory model tests of EPS." The Norwegian Public Roads Administration, Norway.

Timoshenko, S., and Gere, J. M. (1972). *Mechanics of materials*, Van Nostrand Reinhold Co., New York, USA.

Tsukamoto, H. (2011). "History of R&D and design code for EDO-EPS method in Japan." Oslo, Norway.

CHAPTER 6

SWAY AND ROCKING ON EPS EMBANKMENT TO SUPPORT BRIDGE SYSTEM

6.1 Introduction

Soft soil is more compressible and the construction of embankment in such soil is always challenging. Bridges are usually supported by deep foundations (e.g., piles, shafts etc.) to transfer the load into a relatively strong layer of soil. Deep foundations are not a perfect solution in all cases considering time and cost. In these cases, use of Expanded Polystyrene (EPS) material might be a good alternative. By using EPS, the construction can be done at a rapid rate and the load on the soil can be reduced a significant amount. The Norwegian Public Roads Administration (NPRA) used EPS embankments to support bridges. The construction of bridge support systems considered static loads but not dynamic loads (exerted by earthquake).

During extreme events like earthquake, the free standing EPS embankment may undergo various modes such as horizontal translation (sliding), horizontal sway and rigid body rocking (Riad and Horvath, 2004). The EPS may be unstable and overstressed from the seismic internal forces associated with these modes.

The inertial force is calculated from the spectral acceleration. The spectral acceleration is the acceleration corresponding to the fundamental period. In the study, an emphasis was

made on general design rather than site specific design, so the spectral acceleration was assumed for the calculation of fundamental period of EPS embankment.

There is some research done on EPS embankment to support road pavement (Riad and Horvath, 2004; Stark et al., 2004; Bartlett and Lawton, 2008; Amini, 2014). Amini (2014) mentioned that the system experienced sway and rocking after the sliding was stopped during seismic excitation. The horizontal sway occurred from the flexibility of structural mass movement in the horizontal direction and the rocking resulted from the two-dimensional (2D) rigid body rotation (Riad and Horvath, 2004). When a structure attempted horizontal sway, it produced shear stresses and strains. During rocking, it produced alternate tensile and compressive stresses and their corresponding strains. The uplift at the corner of the basal zone occurred during rocking (Bartlett and Lawton, 2008).

Some researchers (McDonald and Brown, 1993; Snow and Nickerson, 2004; Aaboe and Frydenlund, 2011; Stuedlein and Negussey, 2013) studied the use of EPS geofoam to support a bridge system. These studies mainly focused on static loading conditions. So far, there is no study on the dynamics of EPS embankment to support a bridge system. The detailed study of sliding for rectangular prismatic shaped EPS embankment is given in Chapter 5. It is also necessary to study the dynamics of the system once the sliding has stopped. It is not known how the bridge support system would response to different level of excitations and if it shows similar behavior to the pavement support system. The system may enter into sway and rocking modes after stoppage of sliding. Higher rocking may lead to uplift. Therefore, it is important to determine the critical accelerations against these modes.

The main objectives of this study were to: (1) calculate the fundamental period of

structures for sway and rocking modes and (2) determine the critical accelerations against sway, rocking and uplift.

The analysis was done through the series of steps: fundamental period determination, excitation with various amplitudes of harmonic motion, calculation of normal stresses, shear stresses and relative displacements at interface The sway, rocking and uplift were explored by using FLAC 3D (Itasca, 2006).

6.2 Fundamental Period

The fundamental period of the structures changes once the structure enters into various modes. The fundamental period mainly depends on the mass and stiffness. The fundamental period of sway is related with shear stiffness whereas rocking is related to shear, flexural and axial stiffness. Fundamental period was calculated by using both numerical and analytical approach. Timoshinko's beam theory and FLAC 3D were used for analytical and numerical approaches.

6.2.1 Analytical Approach

For the sway mode, the fundamental period was calculated by considering only shear from the basic equation of SDOF system. Fundamental period of any SDOF system is,

$$T_0 = 2\pi \left[m \left(\frac{1}{k} \right) \right]^{0.5} \tag{6.1}$$

where k is spring stiffness of the SDOF system and m is mass of the SDOF system. Eq. (6.1) in terms of weight W is,

$$T_0 = 2\pi \left[\left(\frac{W}{g}\right)\left(\frac{1}{k}\right)\right]^{0.5} \tag{6.2}$$

where W is weight of the SDOF system. For the fixed-end cantilever beam with transverse concentrated force (P) at free end and the maximum transverse displacement (Δ), the stiffness is defined by,

$$k = \frac{P}{\Delta} \tag{6.3}$$

According to Timoshenko and Gere (1972), shear deflection at free end is,

$$\Delta_S = \alpha_S \frac{PL}{GA} \tag{6.4}$$

where α_s is shear coefficient used to get shear stress at centroid, G is shear modulus of the beam material, A is beam cross-sectional area and L is length of beam. According to Cowper (1966), the shear coefficient for solid rectangular section is,

$$\alpha_S = \frac{12 + 11\nu}{10(1+\nu)} \tag{6.5}$$

$$k_S = \frac{P}{\Delta_S} = \frac{GA}{\alpha_S L} = \frac{10(1+\nu)GA}{(12+11\nu)L} \tag{6.6}$$

$$\frac{1}{k_S} = \frac{(12 + 11\nu)L}{10(1 + \nu)GA} \tag{6.7}$$

For the linear elastic material,

$$G = \frac{E}{2(1 + \nu)} \tag{6.8}$$

where E is Young's modulus of the material, ν is Poisson's ratio of the material. Replacing L by H, E *by* E_{ti} and G by relation with E in Eq. (6.8),

$$\frac{1}{k_S} = \frac{(12 + 11\nu)2H(1 + \nu)}{10(1 + \nu)E_{ti}A} = \frac{H(12 + 11\nu)}{5E_{ti}LB} \tag{6.9}$$

For the EPS geofoam embankment, E equals to E_{ti} is initial tangent Young's modulus of EPS and L equal to H is the height of embankment. Substituting the reciprocal of k_s in Eq. (6.2) by replacing k with k_s,

$$T_0 = 2\pi \left[\left(\frac{W}{g} \right) \left(\frac{H(12 + 11\nu)}{5E_{ti}LB} \right) \right]^{0.5} \tag{6.10}$$

$$T_0 = 2\pi \left\{ \left[\frac{\sigma'_{v0}H}{E_{ti}g} \right] \left[\frac{(12 + 11\nu)}{5} \right] \right\}^{0.5} \tag{6.11}$$

where σ'_{v0} is vertical effective stress at the top acting on the top of the EPS. Eq. (6.11) reveals that the fundamental period depends on σ'_{v0}, H, ν, E_{ti} and these parameters are independent with direction of excitation. It means that fundamental period remains the same for excitation along longitudinal and transverse directions.

For the rocking mode, the fundamental period was calculated with consideration of flexural, shear and axial stiffness because the results with consideration of these stiffnesses provide more accurate results when compared with numerical results by using FLAC as mentioned in Chapter 5. The value depends on the direction of excitation because the moment of inertia is different in each direction.

Excitation along the longitudinal direction,

$$T_0 = 2\pi\left\{\left[\frac{\sigma'_{v0}H}{E_{ti}g}\right]\left[4\left(\frac{H}{B}\right)^2 + \frac{(12+11\nu)}{5} + 1\right]\right\}^{0.5} \tag{6.12}$$

Excitation along the transverse direction,

$$T_0 = 2\pi\left\{\left[\frac{\sigma'_{v0}H}{E_{ti}g}\right]\left[4\left(\frac{H}{L}\right)^2 + \frac{(12+11\nu)}{5} + 1\right]\right\}^{0.5} \tag{6.13}$$

where L is length of embankment, B is width of embankment.

Excitation along the vertical direction,

$$T_0 = 2\pi \left[\frac{\sigma'_{v0} H}{E_{ti} g}\right]^{0.5} \tag{6.14}$$

6.2.2 Numerical Approach

For sway condition, a model with length of footing 2 m, 3 m, 4 m, 5 m and 6 m for single and double lane bridge with height 6 m was chosen. A typical model for 4 m length and 6 m height is shown in Figure 6.1. In Figure 6.1, the dark red color represents the foundation for the bridge and the light red color is the EPS embankment. The material properties of EPS embankment are shown in Table 6.1.

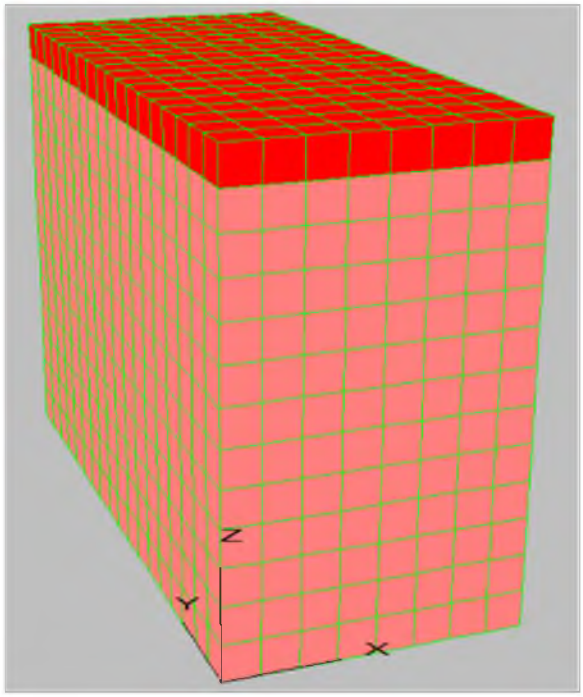

Figure 6.1. EPS geofoam embankment system

Table 6.1. Material properties of EPS geofoam embankment system for sway mode

Material	ρ	E	ν	G	K
----------	kg/m^3	MPa	----------	MPa	MPa
EPS	34.02	12.55	0.19	5.26	6.81
Concrete	2400.00	29557.00	0.18	12523.00	15394.00

The EPS embankment was modeled as coherent mass considering there is no interface between layers. The boundary at base was fixed along the perpendicular to the direction of applied excitation. The free-field boundary was used on the side of the model. In this case, the free field motion was enforced in such a way that boundaries retained their non-reflecting properties at which the outward waves originated from the structure were properly absorbed. The lateral boundaries of the main grid were coupled with free-field grid by using dashpots as used in Itasca (2006). The dynamic input was applied as a velocity history at the base. The velocity history was applied along both the longitudinal and the transverse direction and the excitation was applied along both directions one at a time. The resulting waves can be assigned in two ways, namely, free vibration and force vibration.

A trial and error method was used in case of force vibration. In the free vibration, a pulse loading was applied at the base and the displacement versus time was plotted for the top node. The period for the one cycle would be the fundamental period. The free vibration is the less time consuming and more appropriate method, so this method was applied for the calculation of fundamental period for sway. The fundamental period of embankment using both free and force vibration are shown in Figure 6.2 and Figure 6.3. The fundamental period of the structure was 0.472 sec.

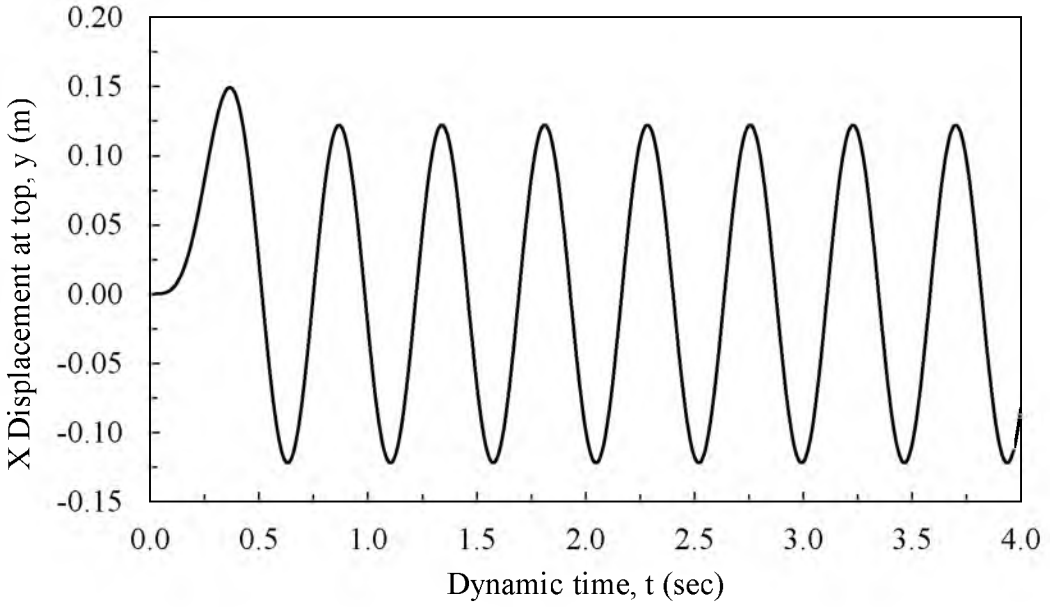

Figure 6.2. Displacement versus dynamic time at top node under free vibration for excitation along the longitudinal direction

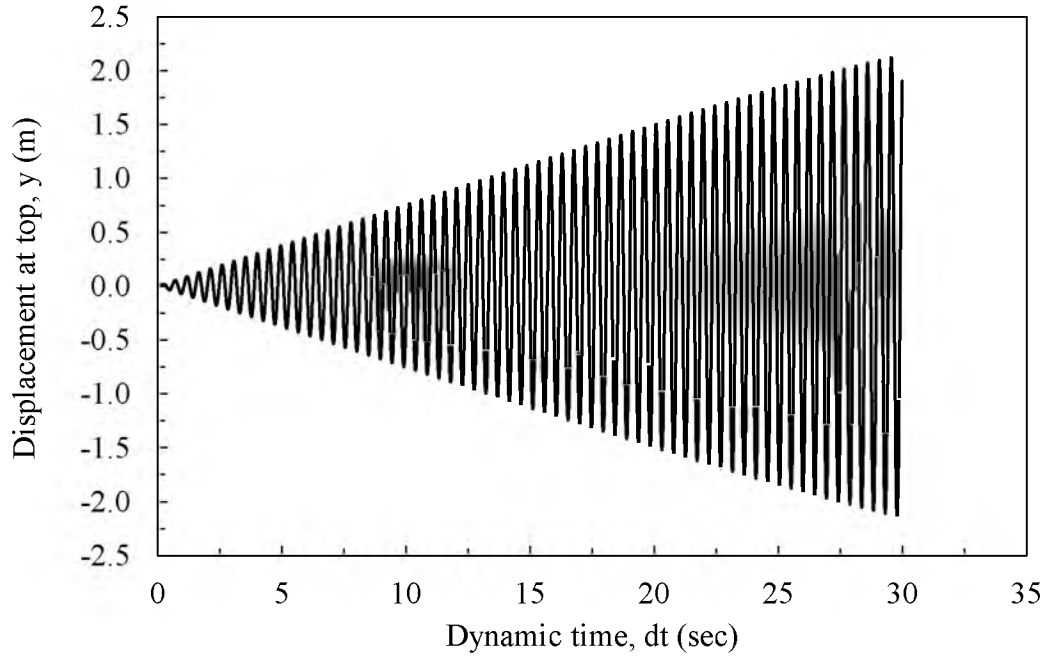

Figure 6.3. Displacement versus time at top node under force vibration for excitation along the longitudinal direction

For the rocking mode, the same model with free vibration was used for fundamental period calculation. However, the vertical sides of the EPS embankment system were different as no boundary condition was applied along this side. The velocity history was applied at the base of the model as dynamic input and the excitation was applied along longitudinal, transverse and vertical directions.

6.3 Sway, Rocking and Uplift

6.3.1 Model Development and Material Properties

For the analysis of sway mode, the model shown in Figure 6.1 was chosen. The material properties used in the model were the same as the properties shown in Table 6.1. The base was fixed in both directions for the static condition. The gravity was turned on and the static equilibrium was checked. Once the static equilibrium was achieved, the model's boundary conditions were changed for dynamic condition. The base of the model was changed into fixed on the sides other than the side at which dynamic input motion was applied. The free-field boundaries were applied on vertical sides. Athanasopoulos et al. (1999) conducted laboratory tests on EPS geofoam specimens under zero confining pressure in torsional resonant column tests and cyclic uniaxial tests. The test results showed the upper bound value of damping in resonant column and lower bound value of damping in cyclic uniaxial test to be 2 percent at the level of 2 percent shear strain. On this basis, 2 percent Rayleigh damping was used as the fundamental period of embankment. The horizontal harmonic motion of various amplitudes such as 0.2 g, 0.3 g, 0.4 g, 0.5 g, and 0.6 g were introduced at fundamental periods along the longitudinal and transverse direction separately. The shear and normal stresses were calculated at various zones of the model.

For the analysis of rocking and uplift, an interface was introduced in between EPS and soil. A model with soil at the base is shown in Figure 6.4. In Figure 6.4, red, green and blue color represents the foundation for bridge, EPS embankment and foundation soil respectively. The elastic material properties are shown in Table 6.2.

The coefficient of friction was assumed to be very high such that no sliding would occur (Housner, 1963). At the interface, the coefficient of friction needs to be very large to analyze the rocking mode. FLAC uses Mohr-Coulomb properties, and normal and shear stiffness at the interface. In this study, cohesion, dilation, friction, tension, normal stiffness (k_n) and shear stiffness (k_s) were assumed to be zero. The friction angle was assumed to be 89^0.

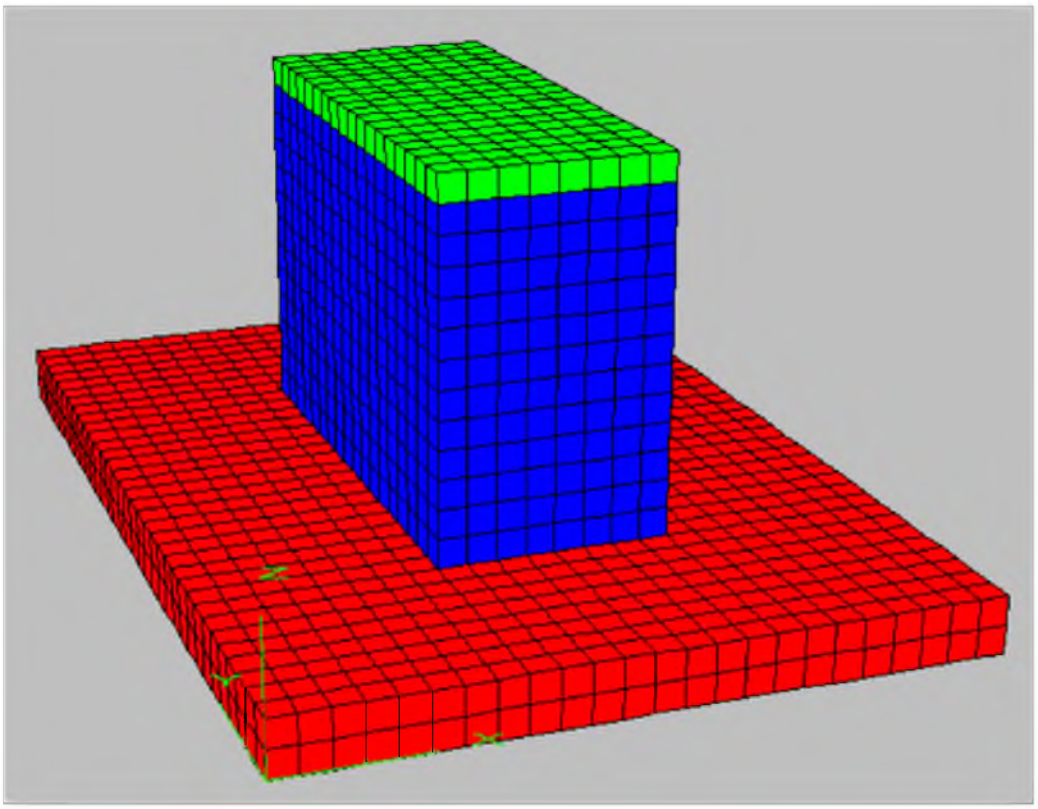

Figure 6.4. EPS embankment with soil and foundation of bridge

Table 6.2. EPS geofoam embankment system material properties for rocking mode

Material	ρ	E	ν	G	K
----------	kg/m^3	MPa	----------	MPa	MPa
EPS	34.2	12.55	0.19	5.26	6.81
Concrete	2400.00	29557.00	0.18	12523.00	15394.00
Soil	1900.00	20.00	0.40	7.14	33.33

According to the FLAC 3D manual (Itasca, 2006), k_n and k_s is set to be 10 times the stiffness of the neighboring zone.

$$k_n = k_s = 10\left[\left(\frac{K + \frac{4}{3}G}{\Delta z_{min}}\right)\right] \tag{6.15}$$

where K is bulk modulus, G is shear modulus, Δz_{min} is the smallest width of an adjoining zone in the normal direction.

Amini (2014) compared the acceleration response of embankment with no interface and with interfaces at which the stiffness values was set to be 50 times the stiffness of the neighboring zone. The dynamics of the system was not changed with consideration of higher stiffness. Considering stiffness to be 10 times that of neighboring zone still leads to loss of some energy in the system. Thus, the recommendation provided by Amini (2014) was used in this study. The final equation for k_n and k_s is given in Eq. (6.16).

$$k_n = k_s = 50\left[\left(\frac{K + \frac{4}{3}G}{\Delta z_{min}}\right)\right] \tag{6.16}$$

However, if the material on one side of the interface is much stiffer than the other, then Eq.(6.16) should be applied to the softer side. In this case, the deformability of the whole system is dominated by the soft side (Itasca, 2006). The geofoam properties were used to calculate the stiffness. The detailed calculation of stiffness is shown in Appendix D.

The fixed boundary was applied at the base of the model. The vertical side was kept free while solving for static condition. Once the static force equilibrium was reached, the bottom boundary was kept as same for dynamic condition. Two percent Rayleigh damping was applied for EPS material at the fundamental period of embankment. The horizontal harmonic motion of various amplitudes, namely, 0.2 g, 0.3 g, 0.4 g, 0.5 g and 0.6 g, were introduced at fundamental periods along the longitudinal direction, longitudinal and transverse directions and longitudinal, transverse and vertical directions at the top of the model. The shear stresses and normal stresses were calculated at basal corner zones. The relative vertical displacements were calculated at corner grid points. At amplitude 0.15 g, harmonic motion along the longitudinal direction was also applied to check the uplift behavior.

The horizontal amplitudes along longitudinal and transverse directions were the same whereas vertical harmonic motion amplitude was assumed as 70 percent of the horizontal motion amplitude according to ASCE (2005). According to ASCE (2005), the ratio of vertical to horizontal spectral ordinates can be taken as at least unity for frequencies higher than 5 Hz, 2/3 for frequencies below 3 Hz, and a transition from 2/3 to 1 for frequencies

between 3 Hz and 5 Hz. In this study, the frequency was chosen in between 3 Hz and 5 Hz and the vertical motion amplitude was taken as 70 percent of horizontal.

6.4 Results and Discussion

6.4.1 Fundamental Period

6.4.1.1 Sway Mode

The fundamental period results of sway mode from analytical and FLAC for single and double lane of rectangular prism embankment for various lengths are shown in Figures 6.5 and 6.6, respectively. The results revealed that values are quite similar in the two methods.

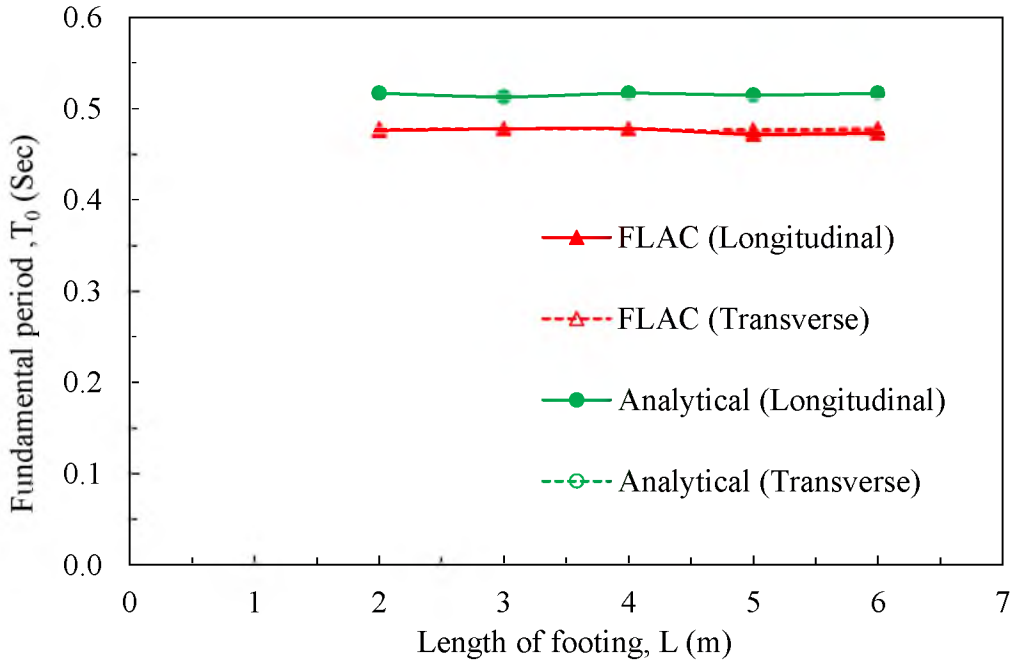

Figure 6.5. Fundamental period of analytical and FLAC for single lane rectangular prism embankment

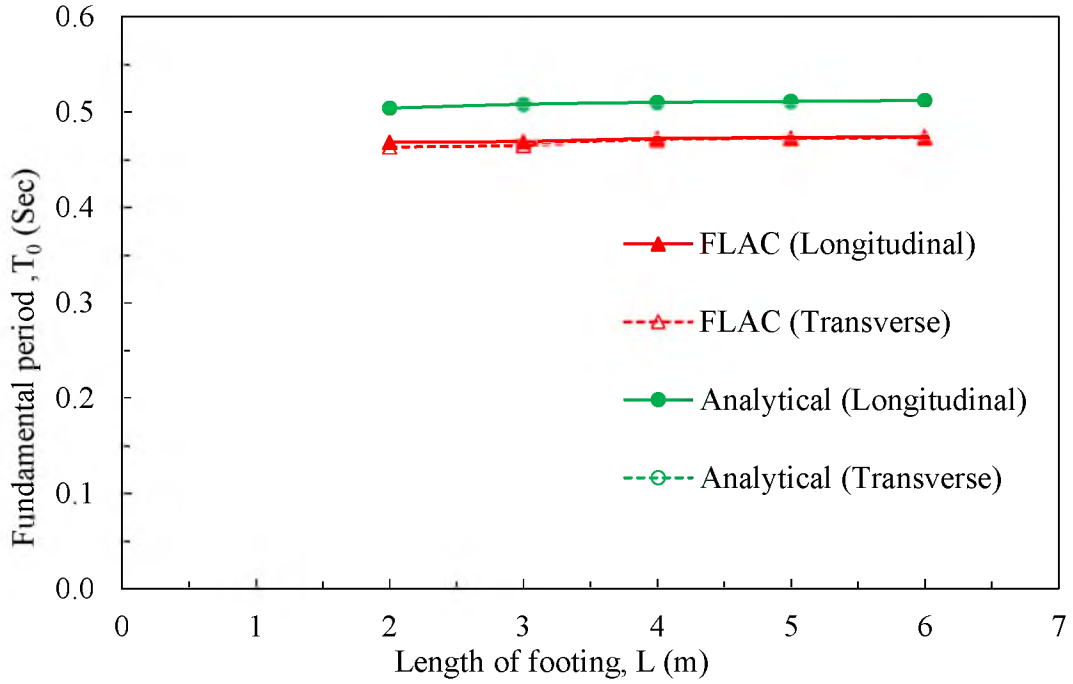

Figure 6.6. Fundamental period of analytical and FLAC for double lane rectangular prism embankment

The percentage error of different geometries is shown in Table 6.3. The percentage error was calculated on the basis of FLAC 3D results. Equation (6.17) was used for the calculation of percentage errors.

$$Percentage\ error = \frac{T_{0(Analytical)} - T_{0(FLAC)}}{T_{0(FLAC)}} 100 \tag{6.17}$$

The fact that the percentage error was less than 10 percent means that the analytical method can be used in designing for simple geometry of embankments. Numerical methods are required only for embankments with complex geometry.

Table 6.3. Percentage error of analytical method with FLAC for single and double lane with various lengths of footing for rectangular prism

Percentage Error				
	Single Lane Analytical and FLAC		Double Lane Analytical and FLAC	
Length of Footing *m*	Longitudinal %	Transverse %	Longitudinal %	Transverse %
2	8.61	8.16	7.69	8.86
3	7.32	7.32	8.32	9.25
4	8.16	8.16	8.05	8.28
5	9.11	7.97	8.03	8.26
6	9.30	8.16	8.02	8.25

6.4.1.2 Rocking Mode

The fundamental period of analytical method and FLAC for rectangular prism with consideration of flexural, shear and axial stiffness is shown in Figures 6.7 and 6.8. Since "Method II" results are close to FLAC results, Method II was chosen for analysis. The detailed explanation is given in Chapter 5. The results revealed that fundamental period decreases with increase of length for both single and double lane for the excitation along the longitudinal direction. The periods were almost constant for excitations along the transverse direction and vertical direction. The geometry was constant in these directions and therefore fundamental periods remained constant. The percentage error of analytical method and FLAC is given in Table 6.4.

The percentage error was calculated by using the relationship given in Eq. (6.17). The fact that the percentage error was less than 10 percent means that the analytical method can be used in the case of a simple geometrical shape of embankment. Numerical methods are required only for complex geometrical shape of embankment.

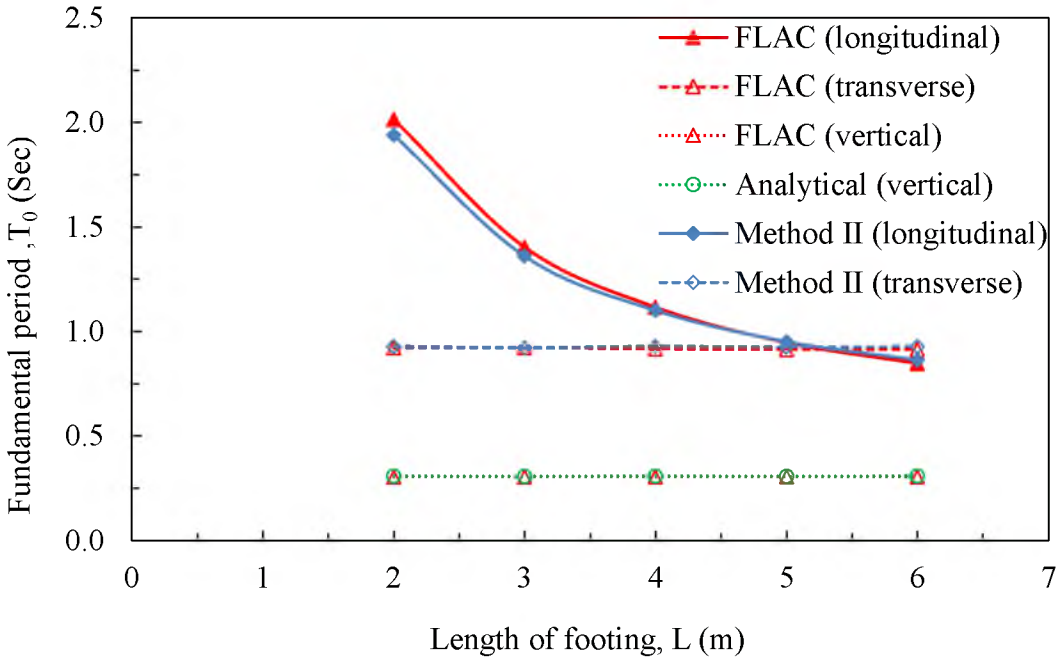

Figure 6.7. Fundamental period of rectangular prism embankment for single lane from analytical and FLAC

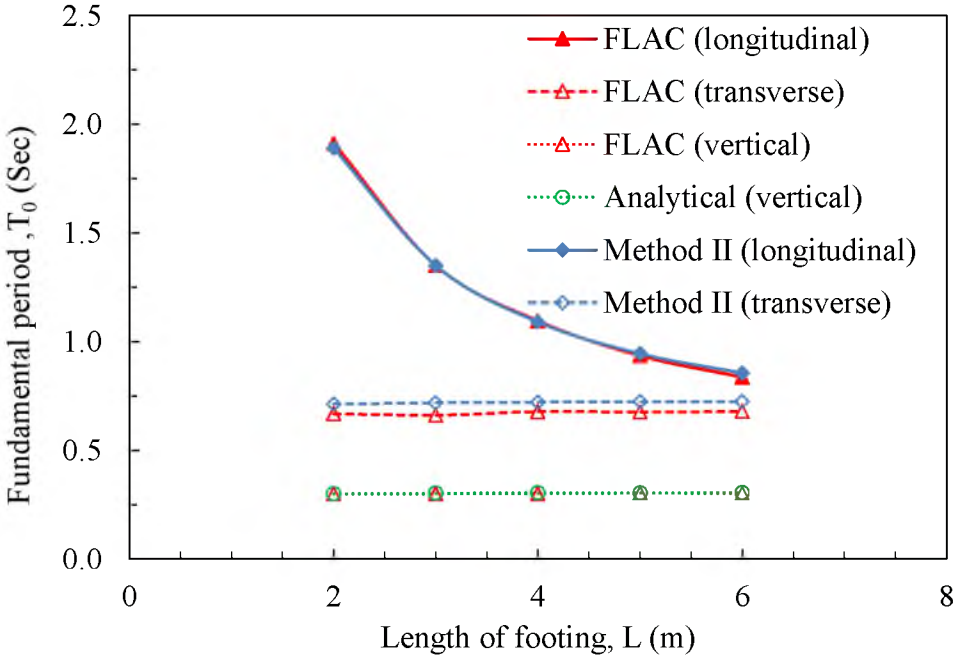

Figure 6.8. Fundamental period of rectangular prism embankment for double lane from analytical and FLAC

Table 6.4. Percentage error of analytical and FLAC for single and double lane with various lengths of footing for rectangular prism

Length of Footing *m*	Percentage Error			
	Single Lane Analytical and FLAC		Double Lane Analytical and FLAC	
	Longitudinal %	Transverse %	Longitudinal %	Transverse %
2	8.61	8.16	7.69	8.86
3	7.32	7.32	8.32	9.25
4	8.16	8.16	8.05	8.28
5	9.11	7.97	8.03	8.26
6	9.30	8.16	8.02	8.25

6.4.2 Sway, Rocking and Uplift

6.4.2.1 Sway Modes

The relationship of normal and shear stresses within the elastic limit was explained by Athanasopoulos et al. (1999) by using Eq.(6.18).

$$\tau = \frac{1}{2}\sigma \tag{6.18}$$

where τ and σ are the shear and normal stresses, respectively. The cyclic triaxial test results of EPS 29 described in Chapter 4 revealed that EPS was in elastic range for the axial strain up to 2 percent. At 2 percent strain level, the allowable normal stress was 182 kPa. From Eq. (6.18), the allowable shear stress turned out to be 91 kPa. Stresses obtained at the basal corner zones from sway and rocking were compared with allowable normal and shear

stresses.

The maximum shear and normal stresses at corners of basal layers due to 0.2 g, 0.3 g, 0.4 g, 0.5 g and 0.6 g accelerations at fundamental period of excitations were calculated. The direction vectors in the embankment model during excitation along the longitudinal direction at sway mode is shown in Figure 6.9. The number of zones is shown in Figure 6.10 at which 1 and 8 represent the left and right corner zones, respectively.

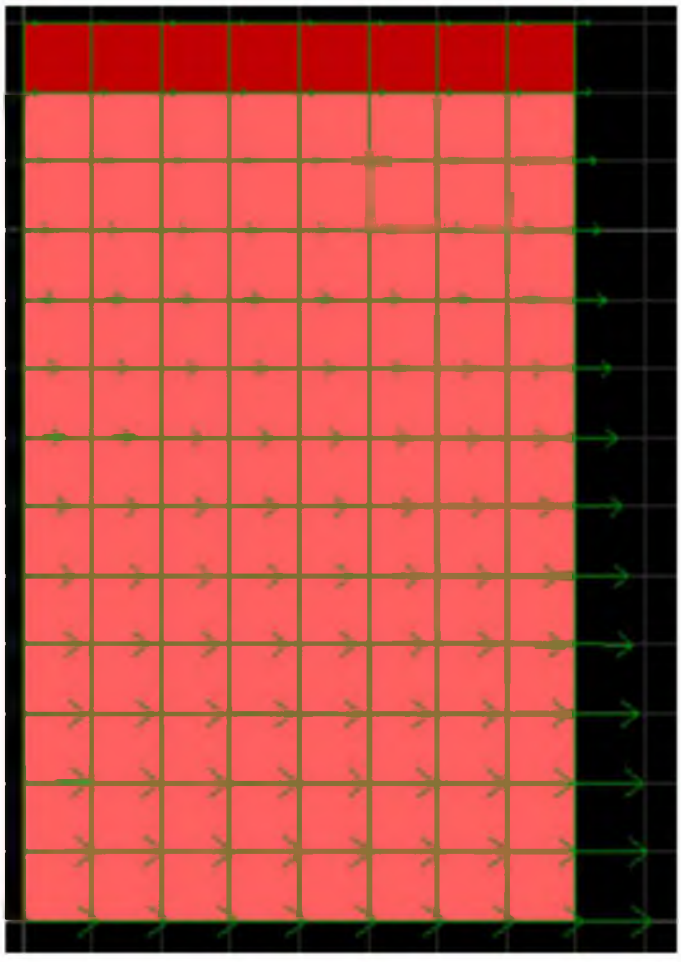

Figure 6.9. EPS geofoam embankment model under sway mode during excitation along the longitudinal direction

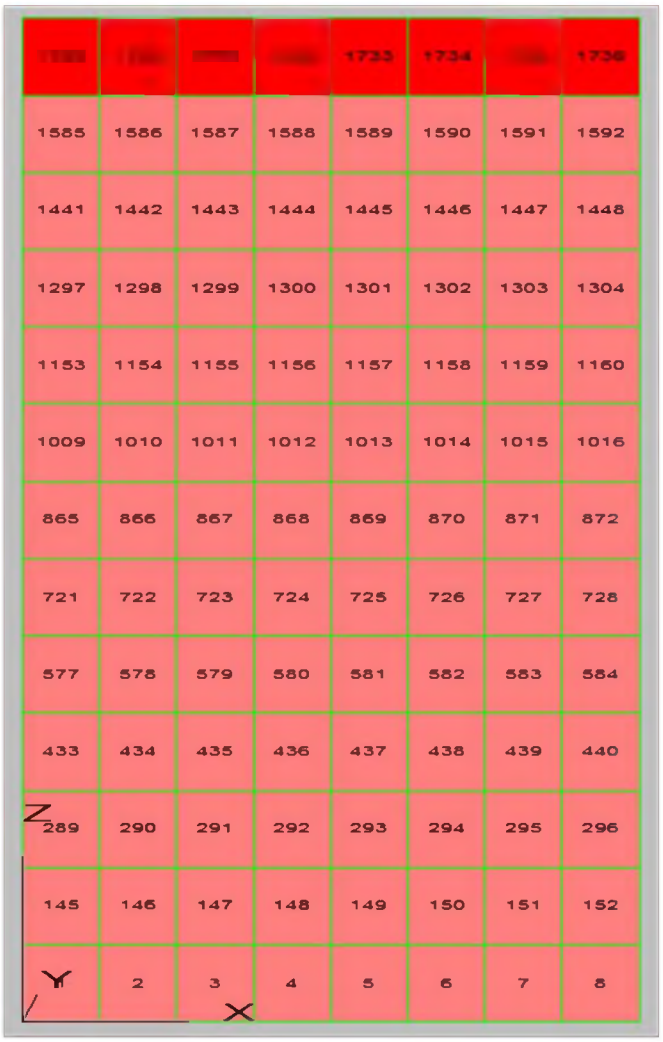

Figure 6.10. Number of zones on EPS embankment model under sway condition

The shear stresses were found to be higher along the direction of excitations whereas normal stresses were found to be higher along the vertical direction. For the excitation along the longitudinal direction, the maximum shear and normal stresses were τ_{xz} and σ_{zz}. Similarly, τ_{yz} and σ_{zz} were the maximum shear and normal stresses for the excitation along the transverse direction. Figures 6.11 and 6.12 revealed the relationship of shear and normal stresses with dynamic time taken for the excitations along the longitudinal directions.

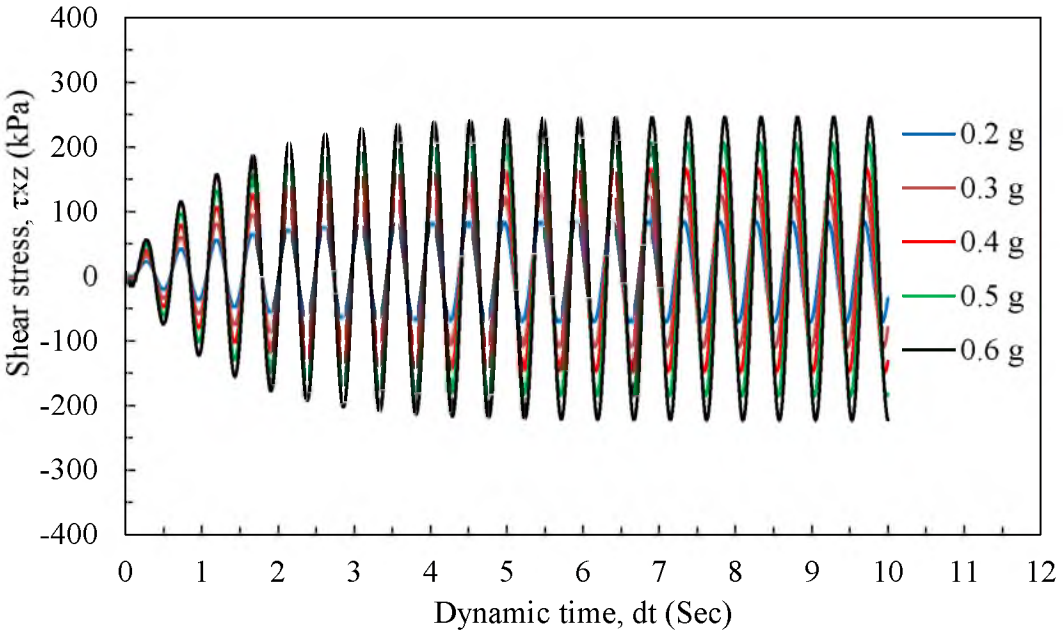

Figure 6.11. Relationship of shear stresses with dynamic time at different levels of excitations during fundamental period for sway along the longitudinal direction

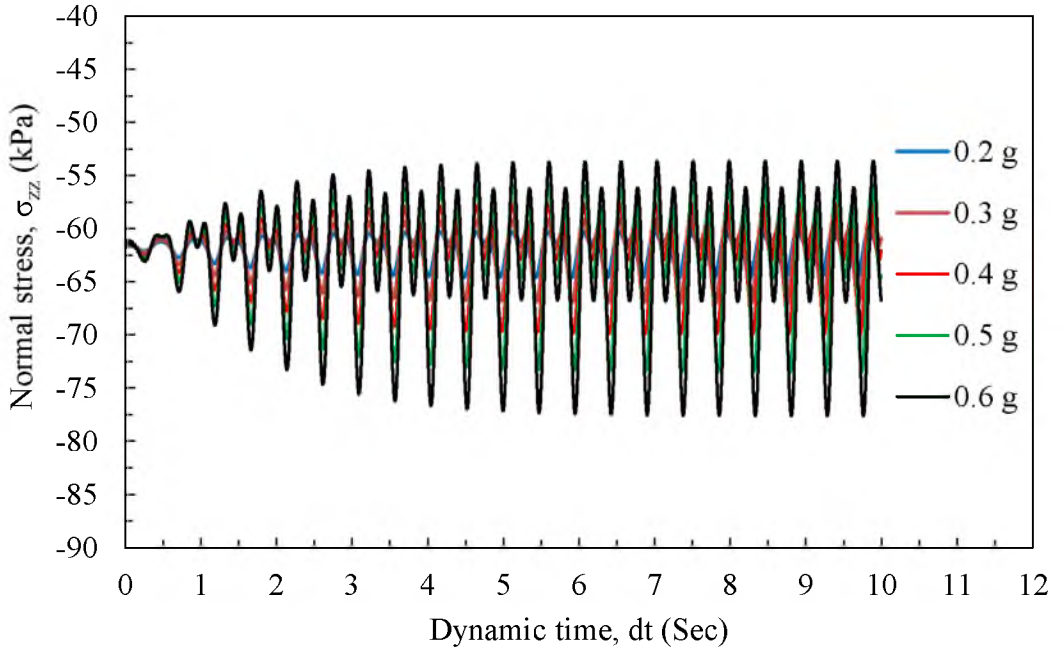

Figure 6.12. Relationship of normal stresses with dynamic time at different levels of excitations during fundamental period for sway along the longitudinal direction

Similarly, Figures 6.13 and 6.14 show the relationship between shear and normal stresses with dynamic time taken for the excitations along the transverse directions.

Figures 6.11, 6.12, 6.13 and 6.14 reveal maximum value of shear stresses and normal stresses increased with increase of degree of excitations. The relations of acceleration with shear and normal stresses were developed from these figures. The relationship of acceleration with shear stress and normal stress for sway along the longitudinal direction is shown in Figures 6.15 and 6.16. The critical acceleration is the acceleration that corresponds to the permissible values of shear and normal stresses of EPS specimen. Figure 6.15 revealed that critical acceleration with respect to permissible shear stresses for the excitation along the longitudinal direction was 0.215 g. Figure 6.16 shows that critical acceleration with respect to permissible normal stresses for the excitation along the longitudinal direction was 3.78 g.

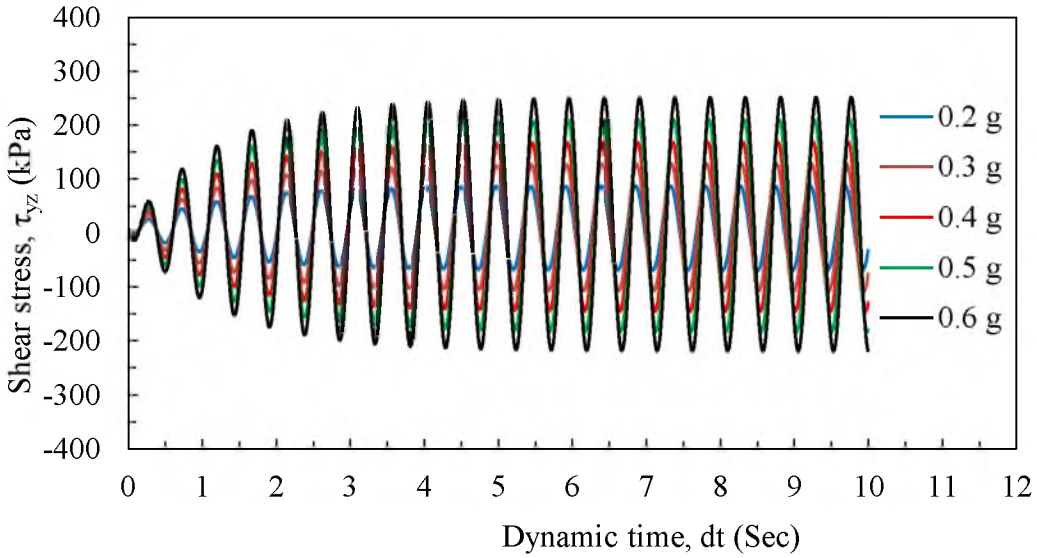

Figure 6.13. Relationship of shear stresses with dynamic time at different levels of excitations during fundamental period for sway along the transverse direction

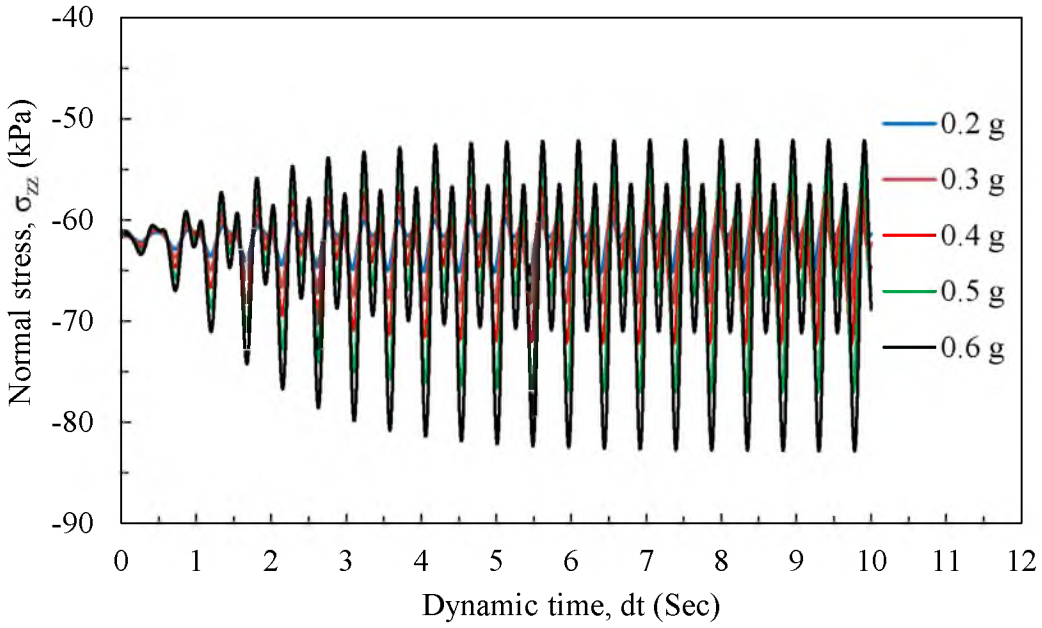

Figure 6.14. Relationship of normal stresses with dynamic time at different levels of excitations during fundamental period for sway along the transverse direction

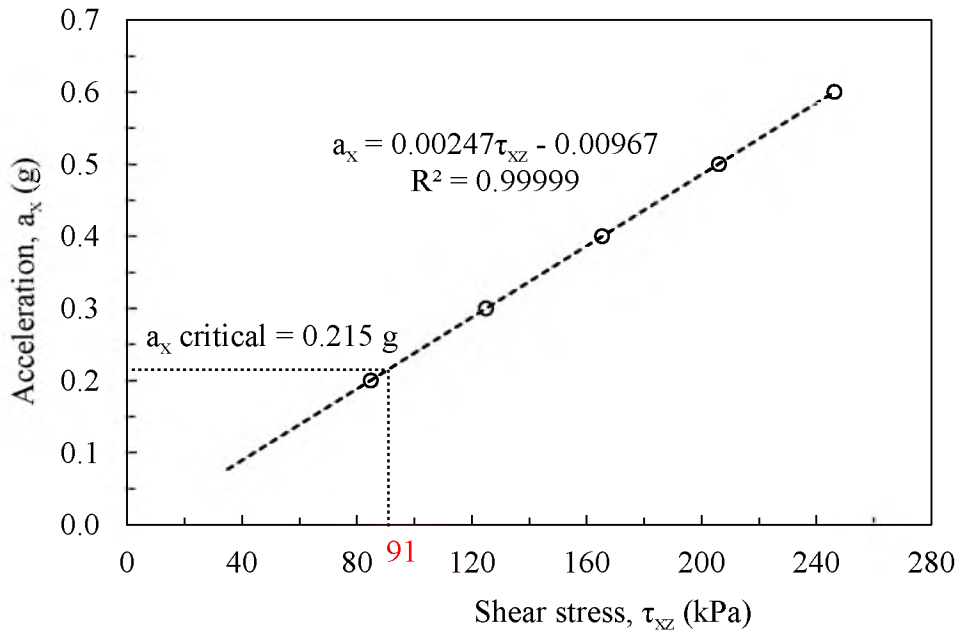

Figure 6.15. Relationship of acceleration and shear stress for sway along the longitudinal direction

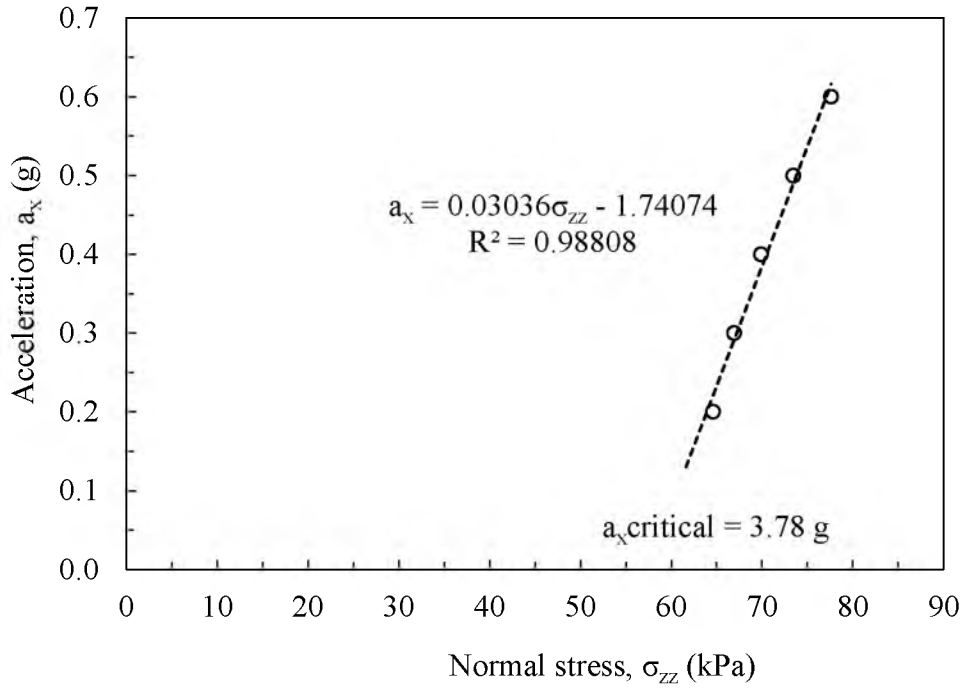

Figure 6.16. Relationship of acceleration and normal stress for sway along the longitudinal direction

From Figures 6.15 and 6.16, it can be concluded that EPS starts to get overstressed in shear after the excitation of 0.22 g whereas there is no overstressing in compression until the excitation exceeded 3.78 g.

Figures 6.17 and 6.18 revealed the relation of acceleration with shear and normal stresses for the excitation along the transverse direction. The relation revealed that EPS started to get overstressed in shear once the excitation exceeded 0.210 g whereas the overstressing did not occur in compression until the excitation reached 2.84 g. From the results of excitation along the longitudinal and transverse directions at fundamental periods, it can be concluded that use of EPS geofoam in embankments to support bridges does not get overstressed in shear up to around 0.2 g.

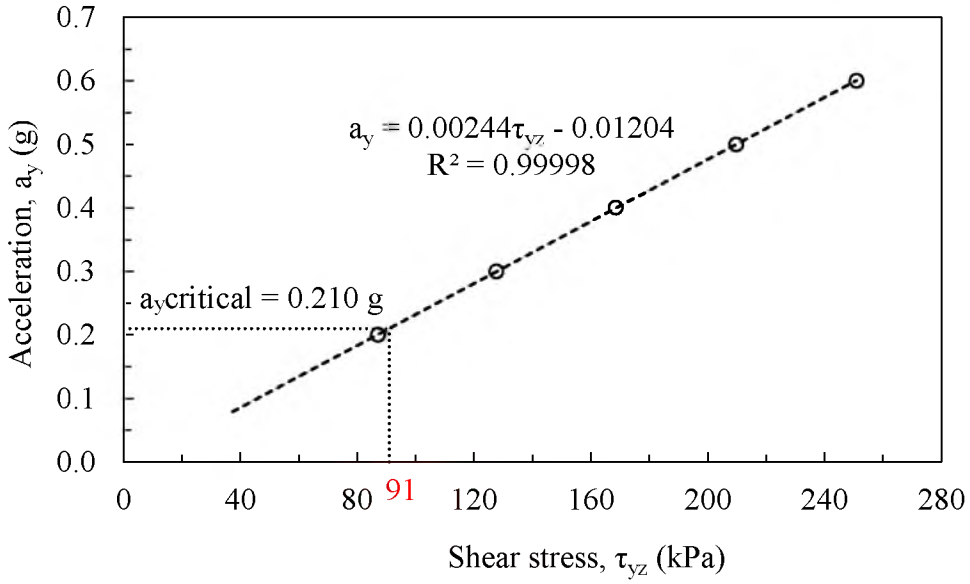

Figure 6.17. Relationship of acceleration and shear stress for sway along the transverse direction

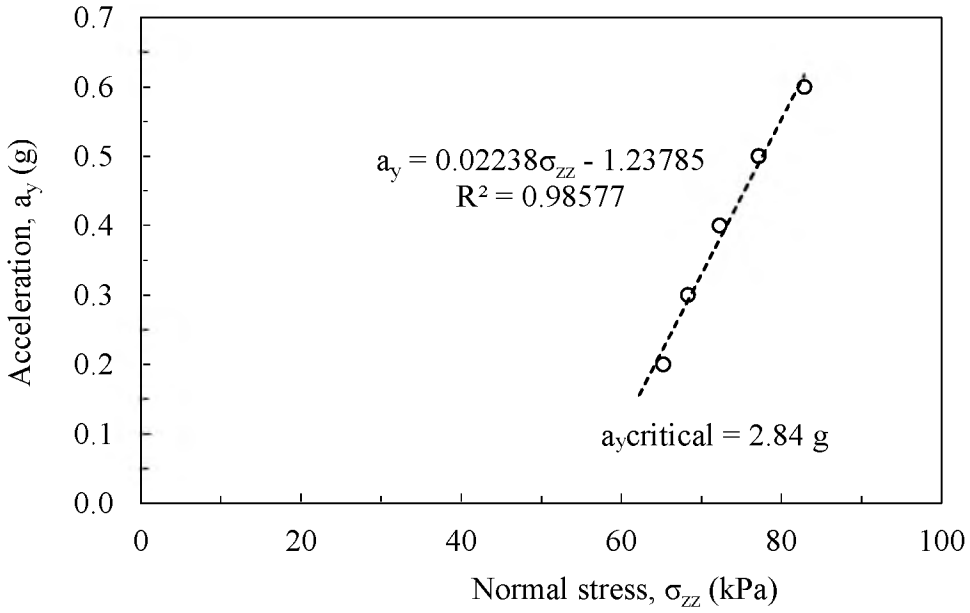

Figure 6.18. Relationship of acceleration and normal stress for sway along the transverse direction

The critical acceleration for sliding was explained in Chapter 5. The critical acceleration for sliding was 0.6 g. This means that critical acceleration for sliding is greater than critical acceleration for overstressing of EPS. The critical acceleration can be increased by using higher density EPS geofoam at the corners and by using seismic lateral restraint system. The use of higher density geofoam can increase the acceleration to some extent and the system might work for a moderate level of acceleration. However the lateral restraint system is required for higher level of excitations.

6.4.2.2 Rocking Modes

The maximum normal and shear stresses were observed at corner of the basal layer of EPS embankment. The maximum stresses were determined from normal stresses and shear stress plots with dynamic time for different level of excitations such as 0.2 g, 0.3 g, 0.4 g, 0.5 g and 0.6 g at fundamental periods along the longitudinal, longitudinal transverse and longitudinal transverse vertical directions. Significant rocking occurs in the transverse direction. However the rocking in the longitudinal direction is not likely to occur due to the presence of bridge deck. In reality, it is not possible that excitations occur in all three directions at the same time. However in the study, excitations were applied along above-mentioned directions to understand the behavior at the most critical condition. The embankment in rocking mode with direction vectors is shown in Figure 6.19. The number of zones is shown in Figure 6.20. For example, 1633 and 1640 are the left and right corner zones. The normal and shear stress plots with dynamic time for the excitation of 0.2 g along the longitudinal direction are shown in Figures 6.21 and 6.22.

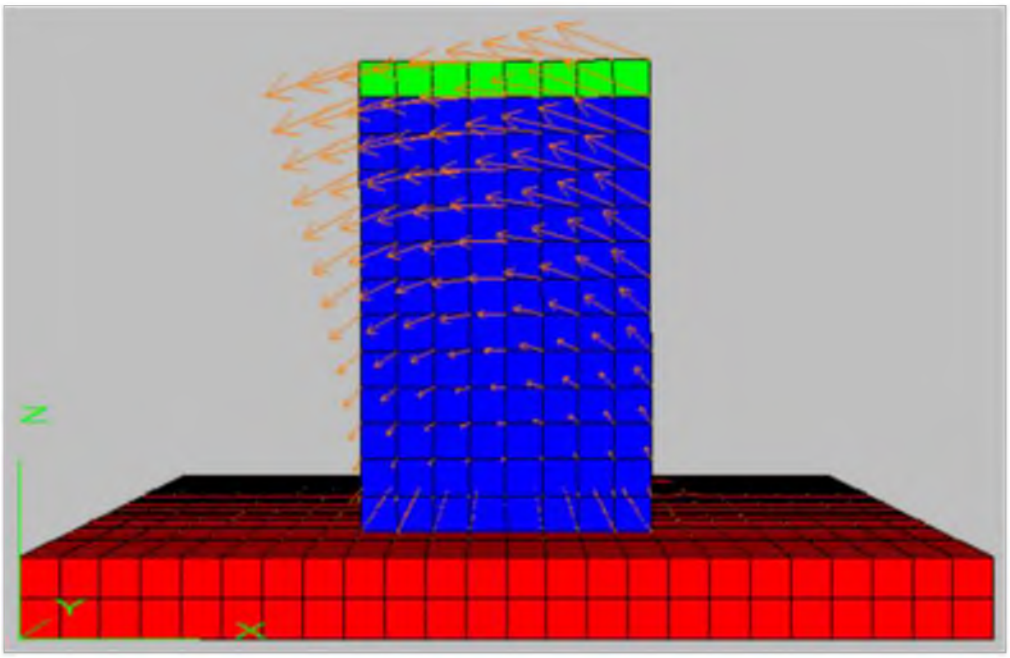

Figure 6.19. EPS geofoam embankment model under rocking along the transverse direction due to excitation along the longitudinal direction

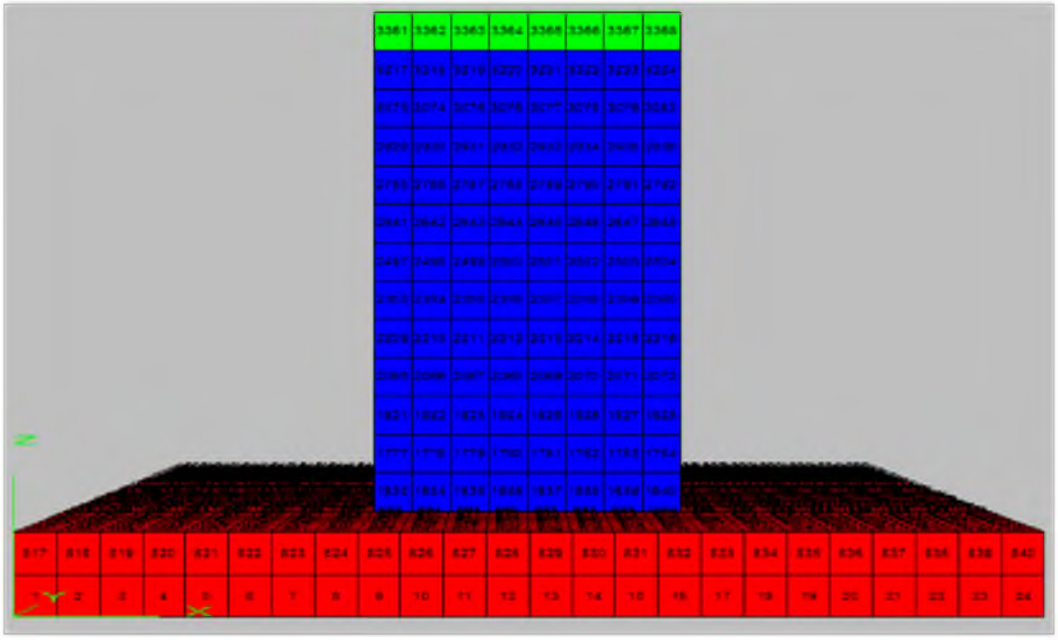

Figure 6.20. Number of zones on EPS embankment model under rocking condition

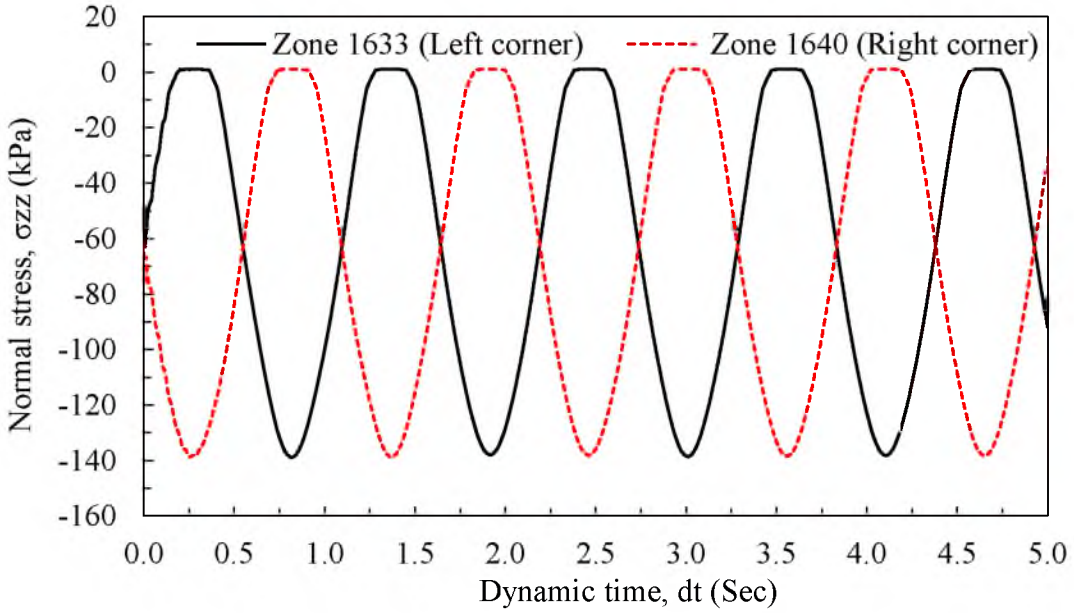

Figure 6.21. Relationship of normal stress with dynamic time at left and right corner zones under rocking along the transverse direction due to the excitation along the longitudinal direction at 0.2 g acceleration

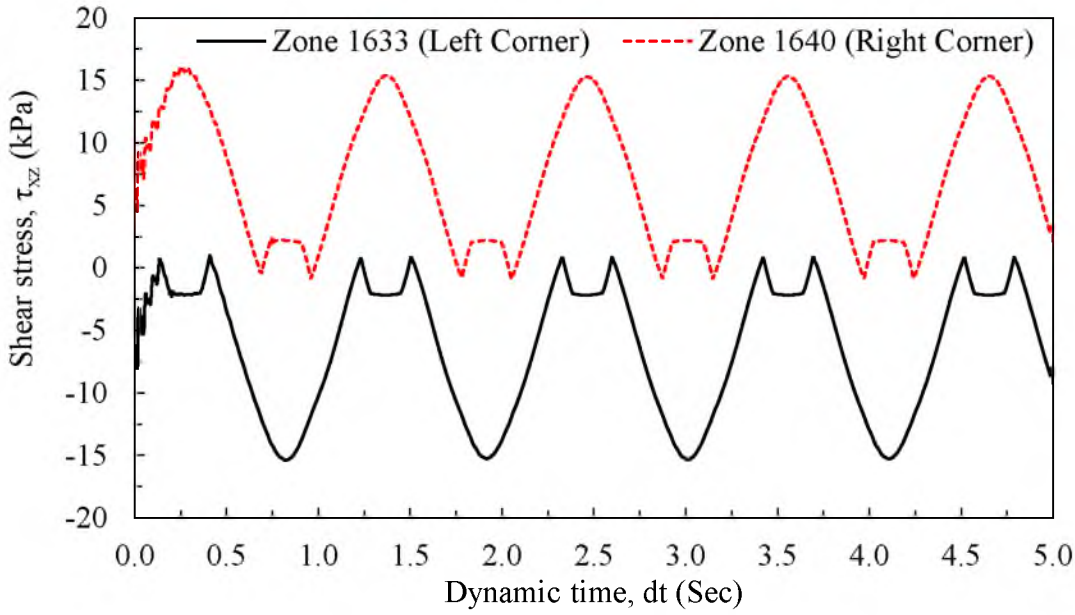

Figure 6.22. Relationship of shear stress with dynamic time at left and right corner zones under rocking along the transverse direction due to the excitation along the longitudinal direction at 0.2 g acceleration

Figure 6.21 reveals the relationship of normal stress with dynamic time at level of excitation of 0.2 g along the longitudinal direction at left and right corner zones. It showed that alternative compression and tension had occurred at the corner zones due to rocking. The figure also revealed that normal stress remain constant for a small interval of time even if the dynamic time was increased. The reason for constant stress might be the separation of nodes at the interface during rocking. Figure 6.22 reveals the relationship of shear stress with dynamic time at 0.2 g acceleration. In this figure, the shear stress also remained constant for a small interval of time which reinforces the idea that separation occurs at interface during rocking.

The relationship of acceleration with normal stresses for the excitation along the longitudinal direction is shown in Figure 6.23. The critical acceleration was 0.332 g.

The relationship of acceleration and shear stresses for the excitation along the longitudinal and transverse directions is shown Figure 6.24. The critical accelerations was 1.32 g for the excitation along the longitudinal direction in terms of shear.

The relationship of acceleration with normal and shear stresses along longitudinal and transverse directions are shown in Figures 6.25 and 6.26. Figure 6.25 revealed the critical acceleration to be 0.189 g in terms of normal stresses when the excitation took place along longitudinal and transverse directions at the same time. The critical acceleration was reduced by around 60 percent with the critical acceleration of excitation along the longitudinal direction only. Figure 6.26 showed the critical acceleration of 0.868 g for the excitation along both directions in terms of shear along the longitudinal direction. The relationship of acceleration and normal stresses for the excitation along longitudinal, transverse and vertical directions is shown in Figure 6.27.

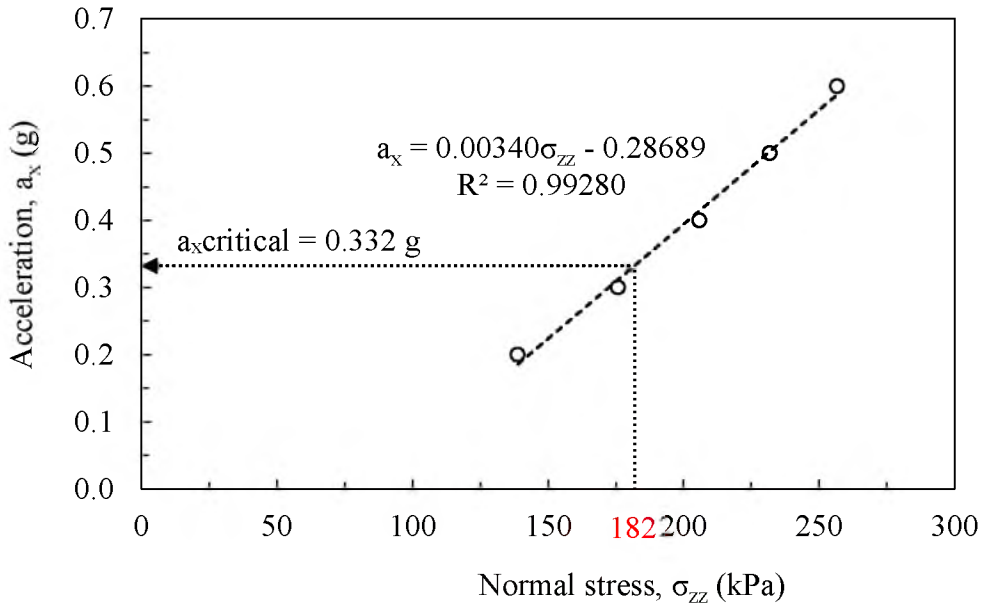

Figure 6.23. Relationship of acceleration with normal stress for rocking along the transverse direction due to the excitation along the longitudinal direction

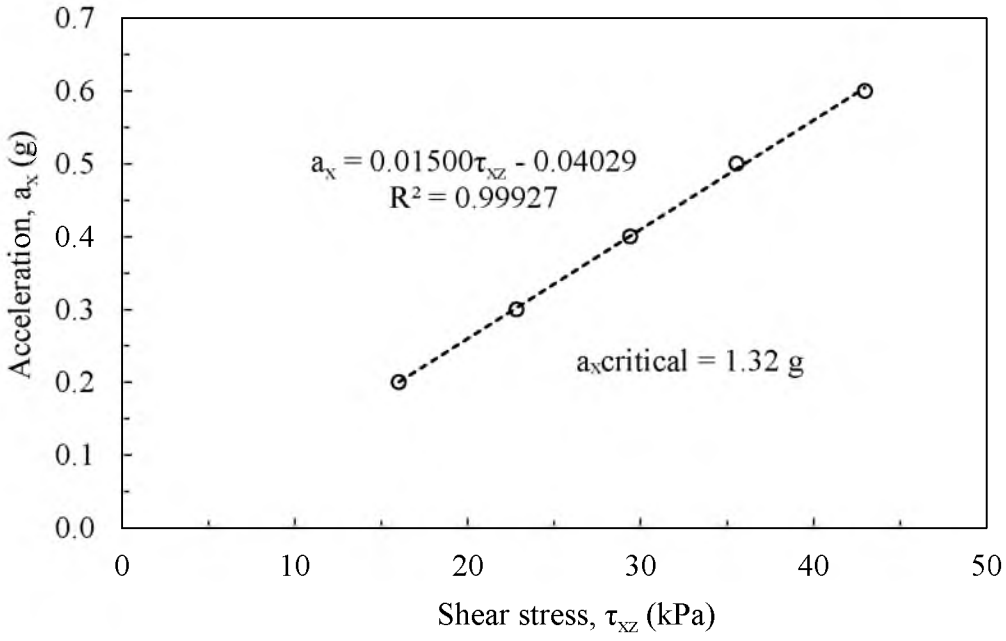

Figure 6.24. Relationship of acceleration with shear stress for rocking along the transverse direction due to excitation along the longitudinal direction

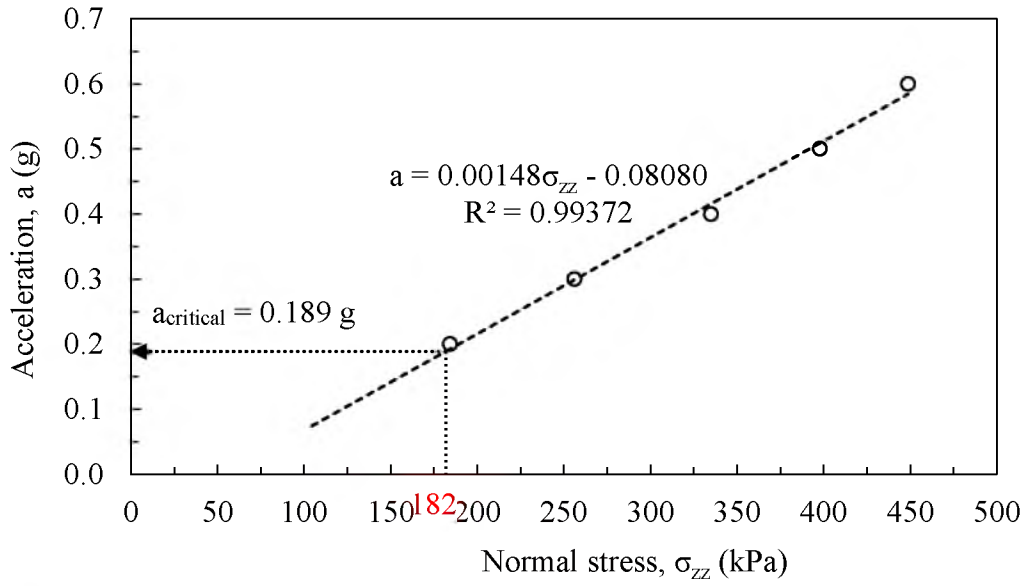

Figure 6.25. Relationship of acceleration with normal stress for rocking along the transverse direction due to excitation along the longitudinal direction

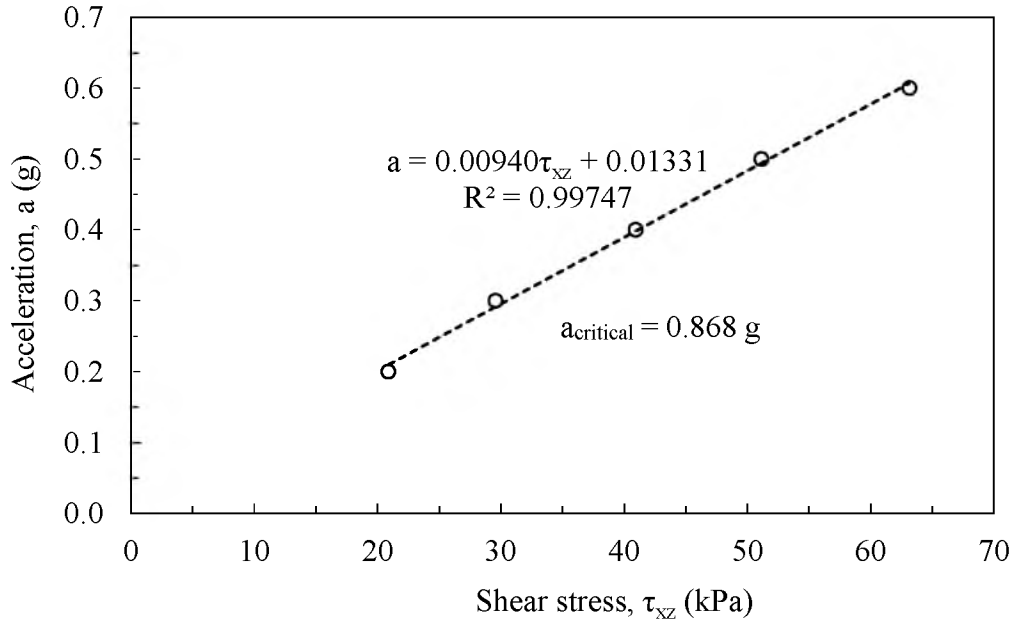

Figure 6.26. Relationship of acceleration with shear stress for rocking along the transverse direction due to excitation along longitudinal and transverse directions

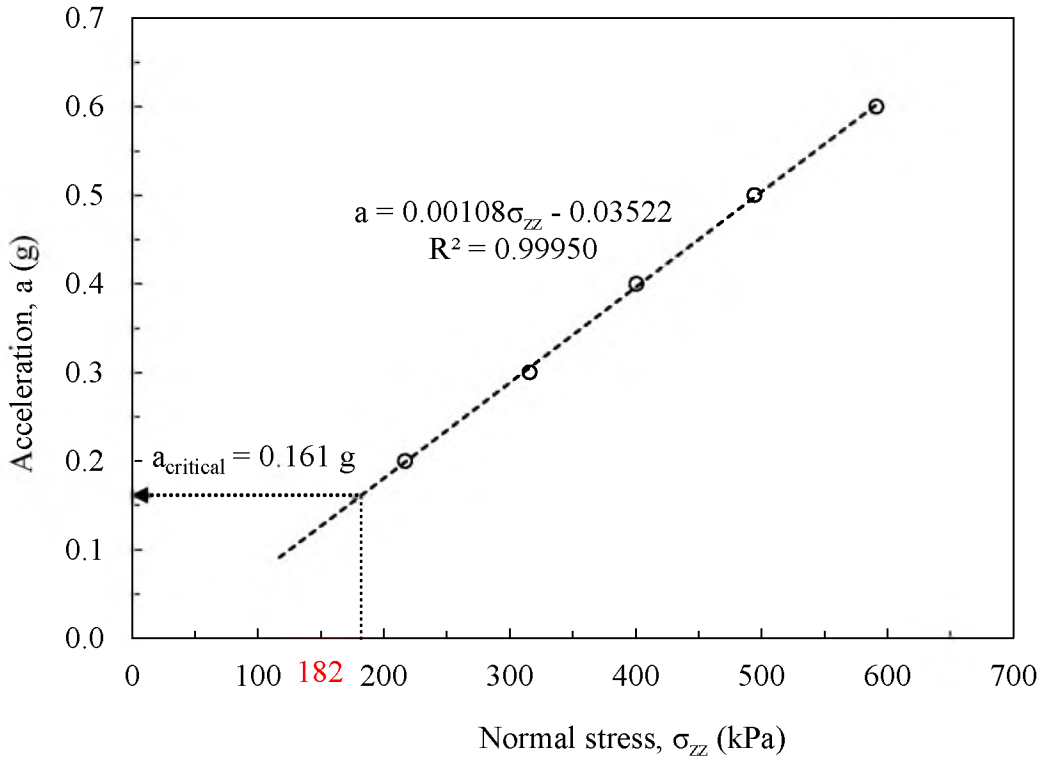

Figure 6.27. Relationship of acceleration with normal stress for rocking along the transverse direction for the excitation along longitudinal, transverse and vertical directions at the same time

The critical acceleration in terms of compression is 0.161 g. Figure 6.28 shows the critical acceleration of 0.373 g in terms of shear.

Even though the analysis was carried out for the possible excitations along three directions at the same time, this condition rarely happens in practice. From the analysis, the critical acceleration for excitation along the longitudinal direction was found to be more critical for rocking along the transverse direction. The system works perfectly for a low level of excitation. However the seismic lateral restraint system is required for moderate to higher level of excitation.

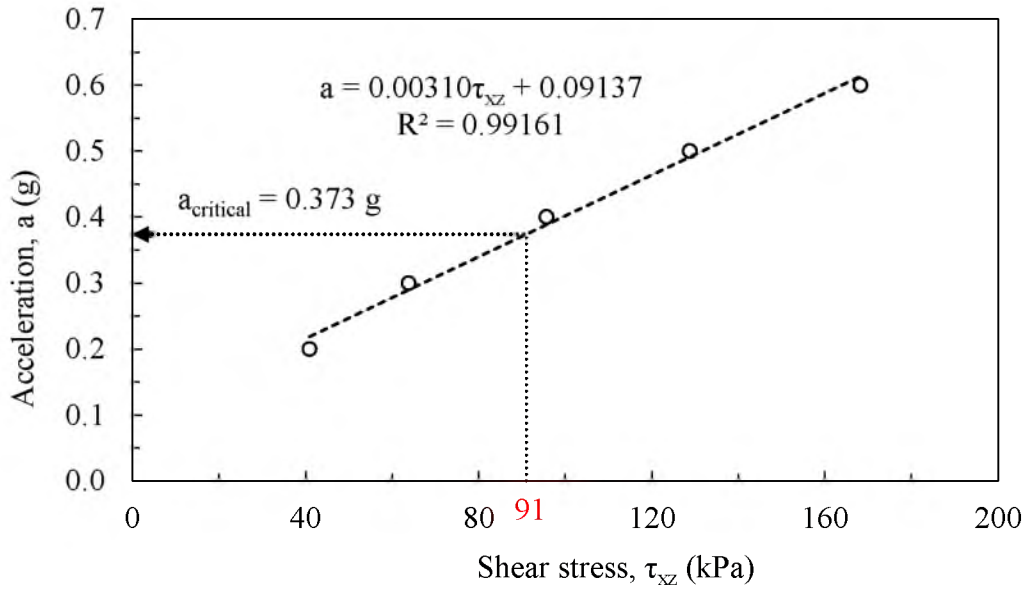

Figure 6.28. Relationship of acceleration with shear stress for rocking along the transverse direction due to the excitation along longitudinal, transverse and vertical directions at the same time

6.4.2.3 Uplift

The uplift occurred during excitation under rocking mode. A small amount of uplift is advantageous because it is the mechanism of dissipation of energy in the system without any disturbance. Uplift is the separation between the two adjacent nodes at interface during excitation. The uplift at the right side of model due to excitation of 0.5 g acceleration along the longitudinal direction is shown in Figure 6.29. The uplift was calculated from the relative displacement of the nodes at interface. Even if the elastic displacement occurs at each node, the relative displacement between the two consecutive nodes represents the actual displacement.

Figure 6.30 showed the relationship of normal stresses with dynamic time for the excitation along the longitudinal direction due to acceleration of 0.15 g and 0.2 g. In the

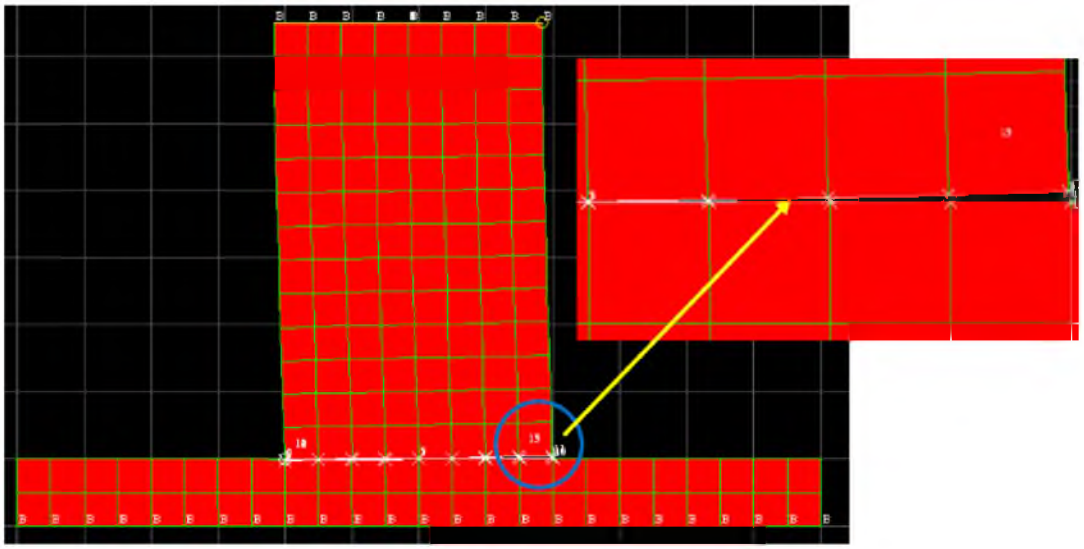

Figure 6.29. Uplift at right side of the model due to excitation of 0.5 g acceleration along the longitudinal direction for rocking along the transverse direction

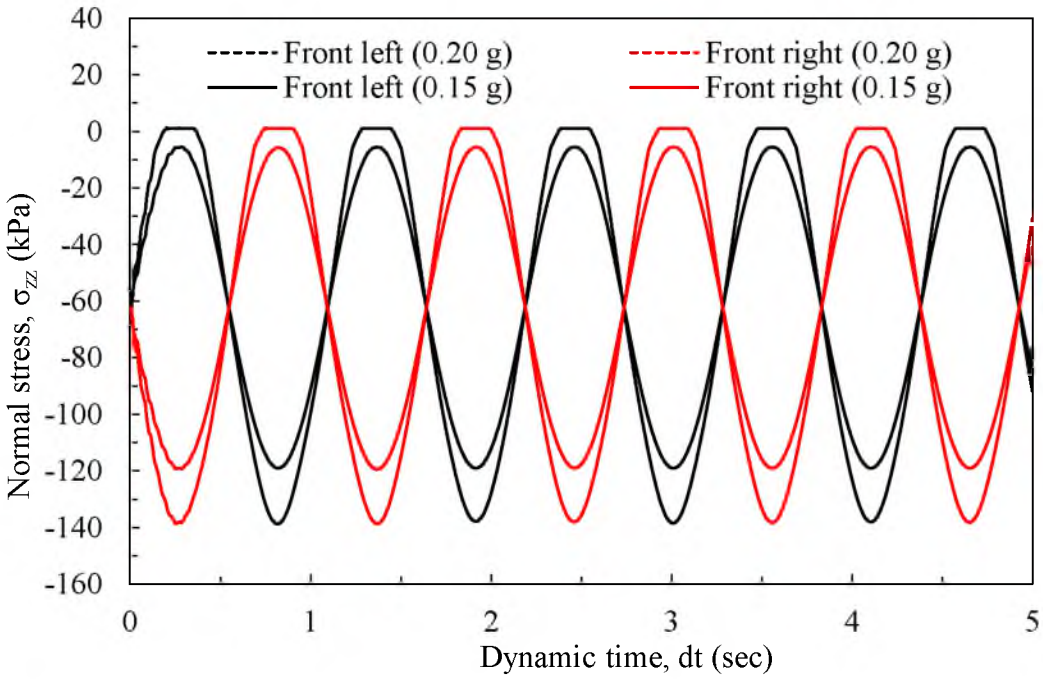

Figure 6.30. Relationship of normal stress and dynamic time at two levels of acceleration shows the initiation of uplift for the excitation along the longitudinal direction

figure, it is seen that at the level of acceleration of 0.2 g, normal stress remained constant for a small period of time even if the dynamic time was increased. This is the time at which separation took place at interface. In the same figure, it is seen that there is no separation for the excitation at acceleration 0.15 g. This means that uplifting initiated in the model for the acceleration in between 0.15 g and 0.2 g.

According to Brinch (1953), the allowable eccentricity for the swallow foundation in case of dynamic load at which uplift initiated was $B/4$ where B represents the width of footing. The forces acting on EPS embankment are depicted in Figure 6.31. At equilibrium, resisting moment should be equal to overturning moment.

$$F_i H = R_v e \tag{6.19}$$

where F_i is the inertial force acting at the top of embankment, H is the height of embankment, e is the eccentricity and R_v is the resultant of vertical forces. In Figure 6.31, q_{max} and q_{min} are the maximum and minimum bearing pressures on soil. W is the total weight at the top of the embankment. Back calculation of acceleration was made by considering the eccentricity equal to $B/4$.

$$F_i H = W\frac{B}{4} \tag{6.20}$$

$$F_i = \frac{Wa}{4g} = \frac{WB}{4H} \tag{6.21}$$

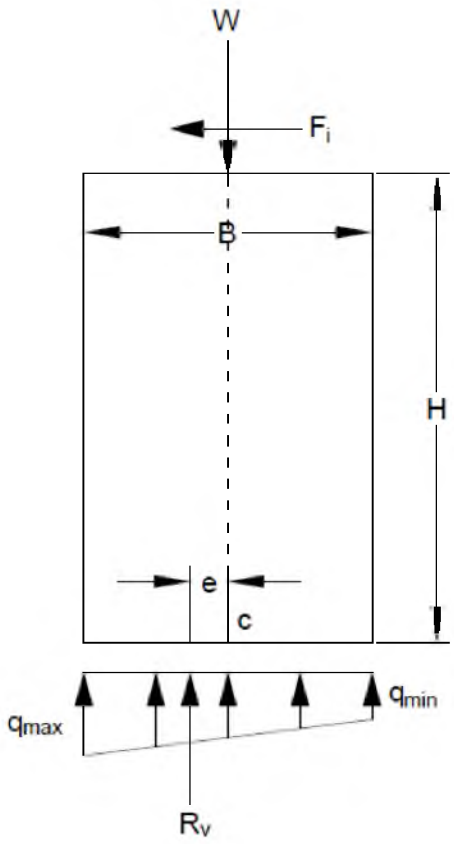

Figure 6.31. Cross-section of EPS embankment with forces acting on it

$$a = \frac{gB}{4H} \tag{6.22}$$

By substituting *B* equals to 4 and *H* equal to 6, the acceleration is given in Eq. (6.23).

$$a = \frac{1}{6}g \tag{6.23}$$

The acceleration value for the initiation of uplift from analytical method fell in the range of acceleration obtained from numerical technique. The uplift was calculated from

the relationship of relative displacement with dynamic time. The plot of relative displacement with time at acceleration level of 0.2 g for the excitation along the longitudinal direction is shown in Figure 6.32. The peak value on the plot was taken as the point where uplift occurred for such level of excitation.

The relationship of acceleration with uplift at different levels of excitations is shown in Figures 6.33, 6.34 and 6.35. Figure 6.33 is the relationship of acceleration with uplift for the excitation along the longitudinal direction. Figure 6.33 shows the maximum uplift for acceleration of 0.6 g to be around 0.06 m. Figures 6.34 and 6.35 reveals the relationship of acceleration with uplift for the excitation along longitudinal-transverse and longitudinal-transverse-vertical directions.

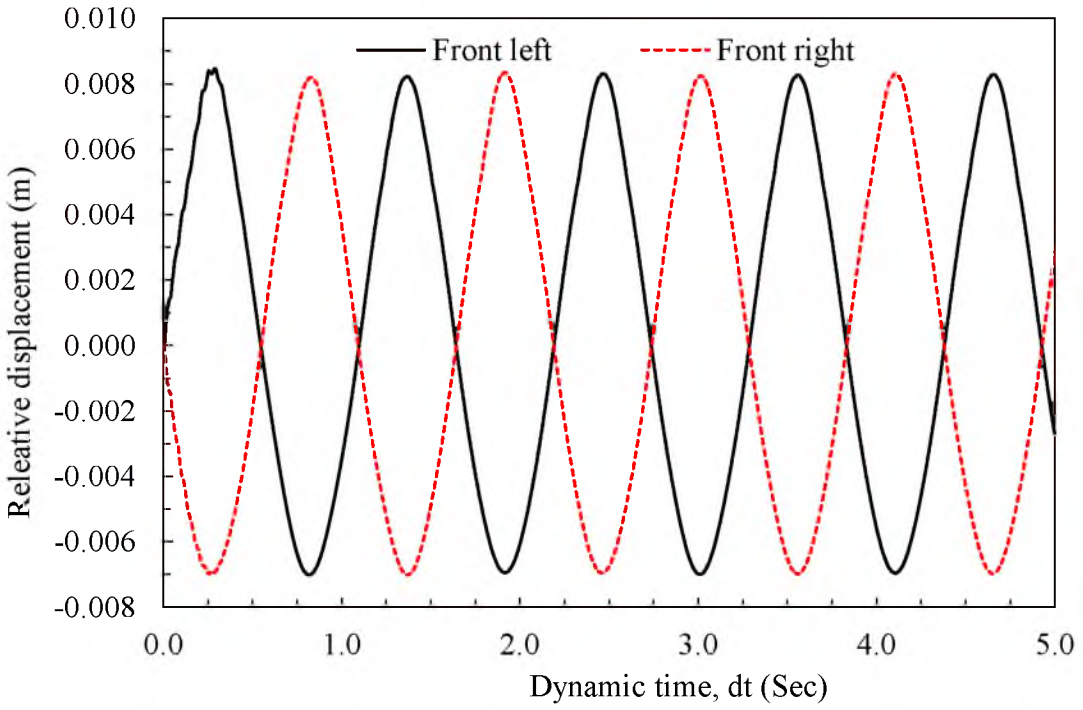

Figure 6.32. Relative displacement with dynamic time at level of acceleration of 0.2 g for the excitation along the longitudinal direction

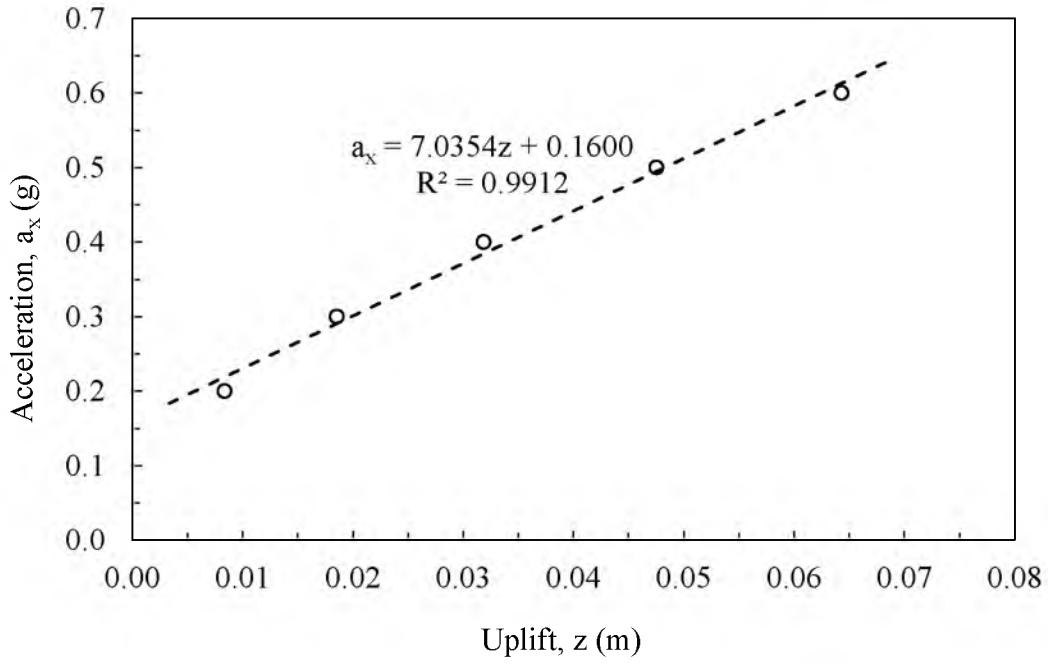

Figure 6.33. Relationship of acceleration and uplift for the excitation along the longitudinal direction

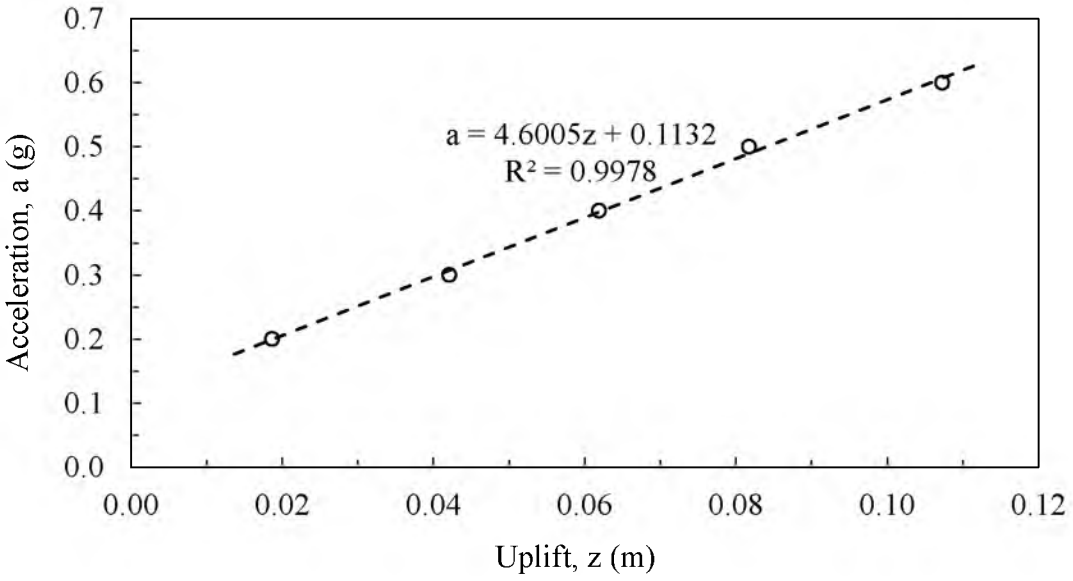

Figure 6.34. Relationship of acceleration and uplift for the excitation along longitudinal and transverse directions

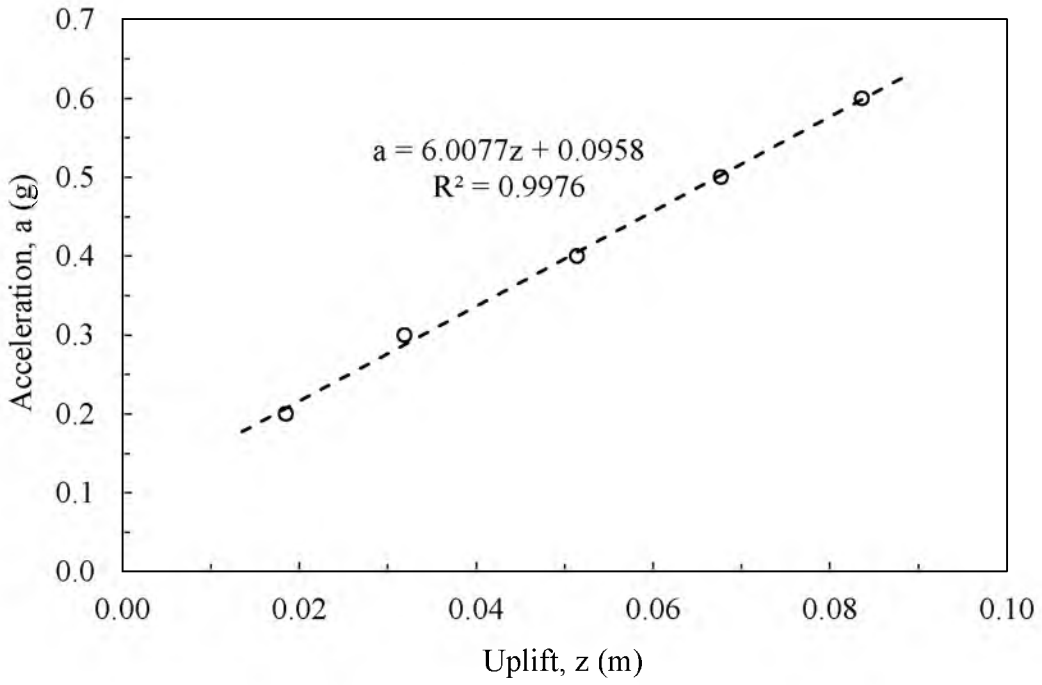

Figure 6.35. Relationship of acceleration and uplift for the excitation along longitudinal transverse and vertical directions

Uplift is one of the energy dissipation phenomena in the system. Higher levels of uplift are undesirable because they increase the instability of the system. There is no design guideline about the allowable value of uplift during earthquake. However, in this study it was found that the system still worked without being overstressed. Hence, 10 mm of uplift was considered a threshold value.

6.5 Conclusions

The fundamental period of EPS geofoam embankment system for sway and rocking modes was calculated by using both analytical and numerical methods. In the analytical methods, only shear stiffness was considered in sway mode whereas shear and flexural

stiffness were considered in rocking mode. The analytical results were compared with FLAC results and the results showed the percentage difference between the two methods being within about 10 percent. This indicates that analytical methods can be used when simple geometrical shapes, such as a rectangular prism, of embankments are considered in design.

The normal and shear stresses were determined under sway and rocking modes at various levels of excitation along different directions in FLAC. The results revealed that the critical acceleration for sway and rocking mode without overstressing EPS blocks at the bottom corners of the embankment were 0.2 g and 0.3 g, respectively. The critical acceleration for rocking and sway modes were smaller than the critical acceleration for interblock sliding (0.6 g). Uplift was initiated during rocking at the level of excitation in between 0. 15 g to 0.2 g. This range of acceleration for initiation of uplift resembled the analytically calculated acceleration based on Brinch (1953). The dynamic study of bridge support system was carried out and the critical accelerations against sway and rocking modes were calculated. The system works well for low levels of seismic excitations; however at higher levels, a seismic lateral restraint system may be required to prevent possible overstressing of the embankment in the basal. This will be explored in the next chapter of this dissertation.

6.6 References

Aaboe, R., and Frydenlund, T. E. (2011). "40 years of experience with the use of EPS geofoam blocks in road construction." *Proc., 4th Intl. Conf on Geofoam Blocks in Construction Applications,* Lillestrom, Norway.

Amini, Z. A. (2014). "Dynamic characteristics and seismic stability of expanded polystyrene geofoam embankments." Ph.D. thesis, The University of Utah, Utah, USA.

ASCE (2005). *Seismic design criteria for structures, systems, and components in nuclear facilities*, ASCE Standard 43-05, Reston, VA, USA.

Athanasopoulos, G., Pelekis, P., and Xenaki, V. (1999). "Dynamic properties of EPS geofoam: an experimental investigation." *Geosynthetics International*, 6(3), 171-194.

Bartlett, S. F., and Lawton, E. C. "Evaluating the seismic stability and performance of freestanding geofoam embankment." *Proc., 6th National Seismic Conf on Bridges and Highways*, Federal Highways Administration (FHA) and Multidisciplinary Center for Earthquake Engineering Resarch (MCEER) Charleston, SC, 17.

Brinch, H. (1953). *Earth pressure calculations*, Teknisk Forlag, Copenhagen.

Cowper, G. (1966). "The shear coefficient in Timoshenko's beam theory." *Journal of Applied Mechanics*, 33(2), 335-340.

Housner, G. W. (1963). "The behavior of inverted pendulum structures during earthquakes." *Bulletin of the Seismological Society of America*, 53(2), 403-417.

Itasca (2006). "FLAC: Fast Lagrangian Analysis of Continua: structural elements, version 3.1." Minneapolis, MN.

McDonald, P., and Brown, P. (1993). "Ultra lightweight polystyrene for bridge approach fill." *Proc., of the 11th Southeast Asian Geotechnical Conference, Singapore*, 664-668.

Riad, H. L., and Horvath, J. S. (2004). "Analysis and design of EPS-geofoam embankments for seismic loading." *Proc., Geotechnical Engineering for Transportation Projects*, ASCE, Los Angeles, CA, USA, 2028-2037.

Snow, C., and Nickerson, C. (2004). "Case study of EPS geofoam lightweight fill for settlement control at bridge approach embankment." *Geotechnical Engineering for Transportation Projects*, 580-589.

Stark, T., Arellano, D., Horvath, J., and Leshchinsky, D. (2004). "Guideline and recommended standard for geofoam applications in highway embankments."NCHRP Report 529, Transportation Research Board, Washington, D.C.

Stuedlein, A. W., and Negussey, D. (2013). "Use of EPS geofoam for support of a bridge." *Sound Geotechnical Research to Practice: Honoring Robert D. Holtz, Geotechnical Special Publication*(230), 334-345.

Timoshenko, S., and Gere, J. M. (1972). *Mechanics of materials*, Van Nostrand Reinhold Co., New York, USA.

CHAPTER 7

SEISMIC LATERAL RESTRAINT SYSTEM

7.1 Introduction

Soft soil is often compressible, has low shear strength and poor bearing capacity; therefore construction of large embankments in such conditions is always challenging. Highway bridges at soft soil sites are typically supported by deep foundations (e.g., piles, drilled shafts, etc.). This is done to transfer the gravity and other live loads to deeper and often more competent layers of soil. For rapid construction at soft soil sites, EPS geofoam embankment offers an alternative to pile-supported bridges due to its extreme light weight and ability to support light weight structures. For example, the Norwegian Public Roads Administration (NPRA) has used EPS embankments to support single span bridges on quick clays without using deep foundations. The design of bridge support system for these Norwegian cases considered only gravity loads from the bridge and live traffic loadings. Nonetheless, performance monitoring by NPRA has shown that these EPS bridge support systems are performing well (Aaboe and Frydenlund, 2011).

This research attempts to learn from the Norwegian practice and extend the application of bridges supported on EPS blocks to other areas of the world. In the previous chapters, it has explored the deformation behavior of EPS specimens under cyclic loading, focusing on the potential magnitude of the cyclic strain and postcyclic creep strain. In addition, it

has defined potential modes of seismic excitation and explored analytical and numerical methods to evaluate these modes to ensure that a failure state or overstressing of the EPS does not occur. The modes of excitation are: translation (i.e., interblock and basal sliding), horizontal sway and rocking (Riad and Horvath, 2004). These behaviors will impart additional loadings to the bridge and EPS support system that must be considered in the design and construction of the EPS embankment. Research presented in this dissertation has shown that if overloaded under gravity loads or overstressed under cyclic loading, the EPS support system has the potential to deform excessively and potentially reduce the service life, or in the extreme case compromise the function of the bridge system.

Bartlett and Lawton (2008) and Amini (2014) have previously explored the potential behavior of free-standing EPS embankment under seismic loading. Countermeasures were introduced by these studies to provide adequate counter-measures against interblock and basal sliding. For example, these studies have shown the potential failure mechanism can be remediated by using: (1) shear keys placed in strategic between the blocks, (2) adhesion of the block using glue, and (3) increasing the depth of embedment of the embankment system to prevent basal sliding. Although mechanical means were also suggested by these studies, no strategies were put forward by these researchers.

Because EPS embankment systems will experience sway, rocking and potential uplift modes during strong earthquake motion, these must be addressed, especially when EPS bridge support systems are being considered. Such vibrational modes will introduce alternating compressional and tensile forces in the EPS blocks that may lead to overstressing, especially at or near the basal corners where compressive stresses appear to reach a maximum (Bartlett and Lawton, 2008). In addition, because the EPS block are not

capable of resisting tensile and uplift forces due to the interfaces created at each layer, there need to be additional countermeasures applied to resist the forces created by these vibration modes for large earthquakes.

To improve the performance, resistance and seismic robustness of EPS bridge support systems in high seismicity area, a cable lateral restraint system will be explored in this chapter. Introduction of such a system has the goal to prevent separation and uplift at the layer interfaces without introducing potential overstressing of the EPS blocks undergoing the sway and rocking modes. High strength steel cabling offers a means to introduce a mechanical lateral restraint system that will add significant tensile capacity to the system which will prevent interblock and basal separation between the block and concrete interfaces. In addition, cabling will also help limit the amount of horizontal sway because the horizontal shear stiffness of the EPS embankment will be also governed by the diagonal cable elements placed in the system. The criss-cross or diagonal cabling will be constructed so that it connects the reinforced concrete bridge foundation with the basal reinforced concrete slab embedded in the soil. This will provide the capacity to transfer rocking and uplift forces from the bridge system to the foundation system and ultimately into the foundation soils.

The primary objective of this chapter is to perform a conceptual exploration of a cable lateral restraint system to resist sway, rocking and uplift forces for EPS embankment undergoing moderate to high levels of seismic excitation. The performance goals upon which to judge the success of the system are: (1) limiting the tensile stress that develops in the cables to the allowable elastic limit, (2) limiting the cyclic shear strain that develops in the EPS block to about 1 percent based on the testing performed in Chapter 4, (3)

preventing separation between the EPS block at their horizontal interfaces, and (4) limiting the amount of uplift of the basal concrete slab due to rocking to an acceptable value. This performance of the EPS bridge support system will be evaluated according to these goals using analytical and numerical methods.

7.2 Evaluation Methods

EPS bridge support system consists of (from top to bottom) bridge structure, bridge foundation (spread footing), reinforced concrete load distribution slab (LDS), layers of EPS block and reinforced concrete foundation slab. The details of the EPS bridge support system using two geometries (i.e., rectangular prismatic and trapezoidal prismatic shapes) were presented in Chapter 5. Because of its relatively slender nature, the rectangular prismatic embankment was considered the critical or controlling case for potential sway and rocking modes during seismic excitation. For this evaluation, the fundamental period of the support embankment was calculated and evaluated for various modes of excitation in terms of the critical acceleration as discussed in Chapter 6. The critical acceleration for sway and rocking were 0.2 g and 0.3 g. This means that accelerations above this value may begin to overstress the EPS in shear, particularly at the corners of the embankment.

The cable system evaluated consisted of a diagonal or criss-cross pattern placed external to the EPS embankment (Figure 7.1). In its final construction configuration, it is recommended that these cables be protected by a concrete fascia wall. Because of the high tensile capacity and modulus of the cables, the tensile forces generated from rocking and sway will distribute into the cable system. In addition, the shear forces will be reduced due to the diagonal cables providing significant horizontal resistances.

Figure 7.1. Cables in criss-cross pattern against rocking and sway

For these preliminary evaluations, the number of cables and diameter of cable were chosen in such a way that the performance goals previously stated will be met. In addition, the cables are anchored to the concrete bridge foundation and the basal concrete slab. The details of this anchorage system have not been explored. In addition, during construction, it is recommended that the cables be slightly tensioned once all dead load has been applied; however, such tensioning should not be large. In addition, some slack that develops in the cabling with time, mainly due to postconstruction creep, should not be of great concern, because slight movement of the system will improve the damping characteristics of the embankment system.

After cabling, there is no possibility of uplift at the interblock interfaces of the EPS and load distribution slab. However, there remains a possibility of uplift or separation at the bottom of foundation - top of soil interface. The potential for uplift at this interface was studied by using FLAC 3D and creating an interface at this location. An interface thus created in FLAC 3D allows for separation and slippage along the interface. The material and interface properties were calculated in similar manner to the calculation described in

Chapter 6. At the interface, soil is much softer than load distribution slab. So, soil properties were used to calculate the interface stiffness properties according to the recommendations of Itasca (2006). The uplift at corners of basal layer was calculated at different levels of excitation, as presented later.

7.3 Evaluation of Cabling System

This evaluation mainly focused on the sway mode. The involvement of the cable would reduce the overstressing on EPS blocks. There will be a time lag between when the EPS block and the cable will begin to provide resistance to the applied cyclic loading. The EPS block would start to provide compressive and shear resistance from the initiation of the cyclic loading; however, the cable, due to potential slack from creep strain of the EPS blocks, will be engaged somewhat later. For these evaluations, the creep strain corresponding to a 50-year design life (Chapter 4) was used to estimate when the cable would be engaged and begin receiving load. The vertical creep strain for this post-construction period is about 0.6 percent. The horizontal displacement resulting from sway required to engage the cabling system for this amount of vertical strain is about 0.053 m (Figure 7.2).

The results of experimental study on EPS 29 in Chapter 4 revealed that an acceptable value of axial strain ($\epsilon_{allowable}$) from the combined dead and earthquake load was about 2 percent to keep the creep strain in acceptable limits. The acceptable shear strain ($\gamma_{allowable}$) in the EPS block can correspondingly be estimated from elastic theory. The Possion's ratio of EPS 29 is 0.193; hence for the elastic range, the shear strain can be obtained from the

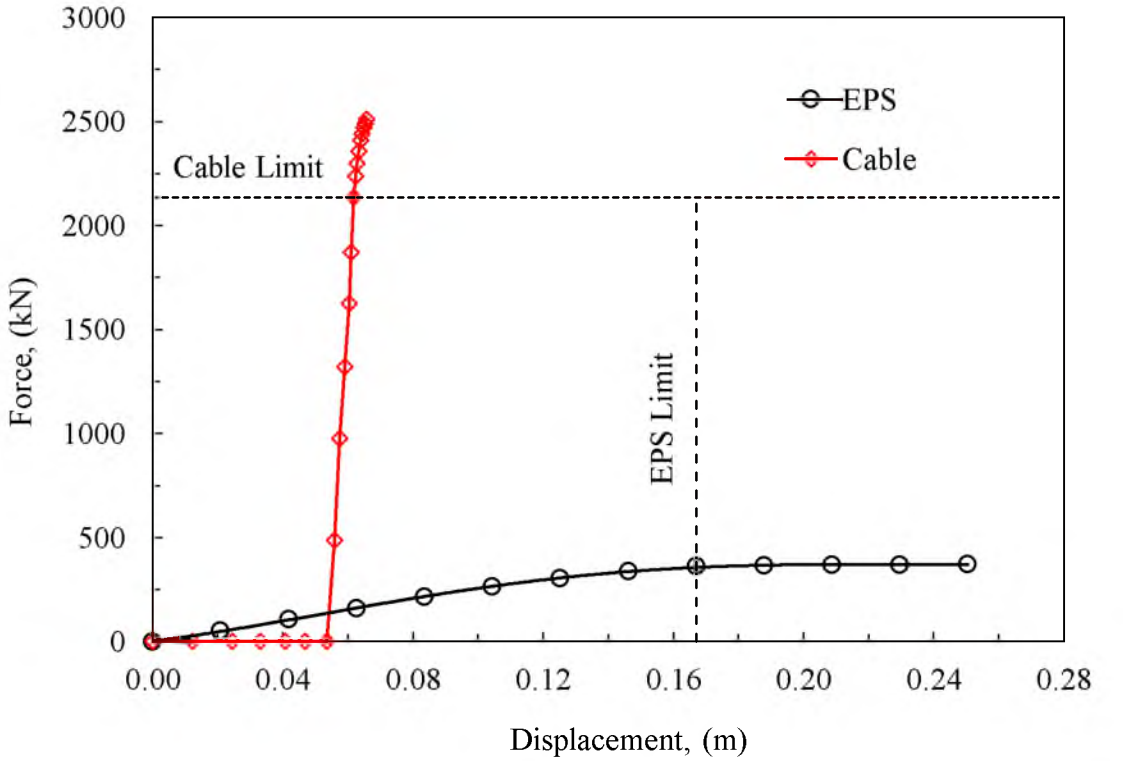

Figure 7.2. Force displacement relationship of EPS and cable

relation given in Eq. (7.1). Hence the acceptable shear strain that develops in EPS under seismic excitation based on the work presented in Chapter 4 would be about 2.4 percent. Thus, it is recommended that the maximum shear strain in the system should not be greater than this value during seismic excitation.

$$\Upsilon_{allowable} = \epsilon_{allowable}(1 + \nu) \tag{7.1}$$

The force displacement resistance relationships for the cable and EPS were determined. Because of strain incompatibility, the resistance in the cable is mobilized at a much higher rate than that of the EPS (Figure 7.2). A force and displacement resistance relation for EPS

placed in pure shear was calculated based on the stress-strain relationship obtained from uniaxial monotonic test results and application of elastic theory. The horizontal displacement was calculated as the product of shear strain and height of the embankment. Similarly, horizontal force was calculated as the product of shear stress and length along the longitudinal direction. In the case of cable, the stress-strain relation of Grade 270 strand given in Nawy (2006) was used for the calculation of axial force and displacement. The axial force along the cable was calculated as the product of stress and area of strand. The displacement (elongation) was calculated based on the force displacement relationship given in Eq. (7.2). In Eq. (7.2), P is the axial tensile force along the cable, L is the length of cable, A is the cross-sectional area of cable and E is the Young's modulus of elasticity of Grade 270 strand.

$$\Delta = \frac{PL}{AE} \tag{7.2}$$

In terms of the demand, the component of inertial force and its corresponding displacement in horizontal (i.e., sway) direction was calculated. The design horizontal force was simply calculated as the product of the total mass atop the EPS embankment (i.e., structural dead and live loads from the bridge and concrete foundations) times the level of excitation in terms of acceleration of gravity (g) in the horizontal direction. The number of strands and area of strand were varied in a trial-and-error method in order to achieve the desired resistance in the system within their allowable limits, or less. The cable limit is the maximum load that can sustain by the cable within linear range of stress-strain relationships. Similarly, the EPS limit was set as the acceptable shear strain for the EPS

based on the findings summarized in Chapter 4.

7.4 Results

The combined or total force displacement relationship of the composite EPS and cable system is shown in Figure 7.3. The details of the calculation of forces and displacements are given in Appendix G. The 1750 kN horizontal force shown in Figure 7.3 corresponds to 1 g horizontal acceleration which occurs at about 0.06 m of horizontal sway displacement. This design value remains below the "cable limit" and well below the "EPS" limit which represent the allowable and acceptable limits for the cable and EPS, respectively.

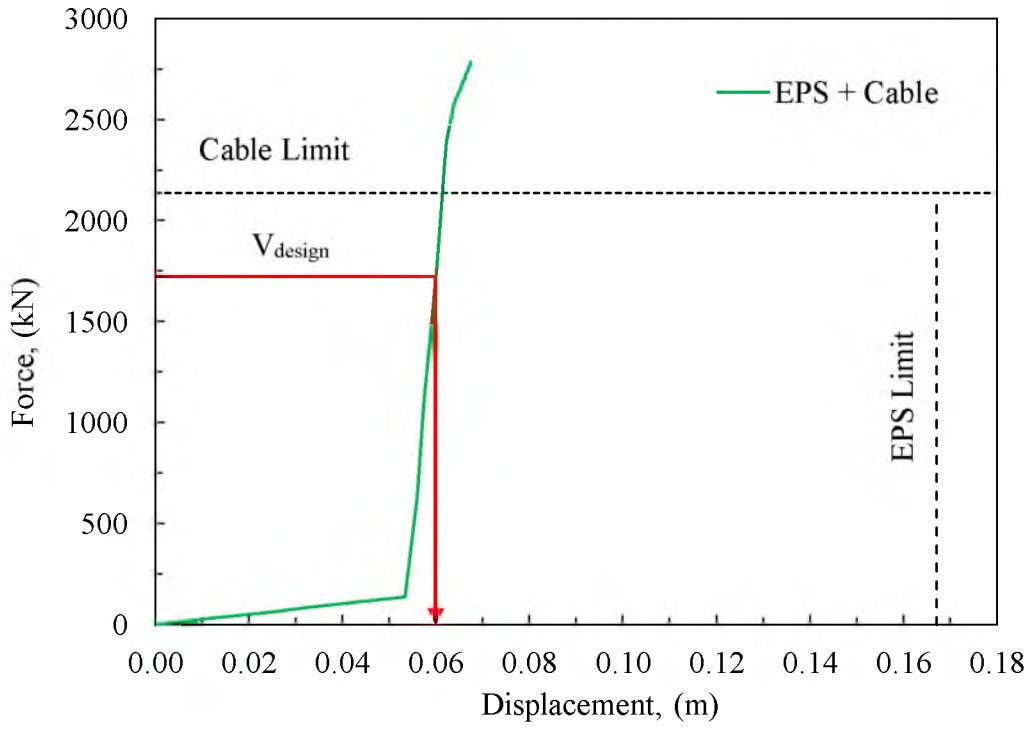

Figure 7.3. Force displacement relationship of combined EPS and cable

The uplift at corners of the foundation slab at different levels of excitation was studied using FLAC 3D. The relationship of horizontal acceleration (g) and vertical uplift at the corners (m) is shown in Figure 7.4. The relationship showed that uplift was found to be around 13 cm for the excitation level of 1 g. This modeling was done without the inclusion of the cabling system in the FLAC 3D model; hence it is a preliminary finding. The amount of uplift could be different for the case where cabling is included because such cabling will limit the amount of sway, which may in turn affect the rocking mode.

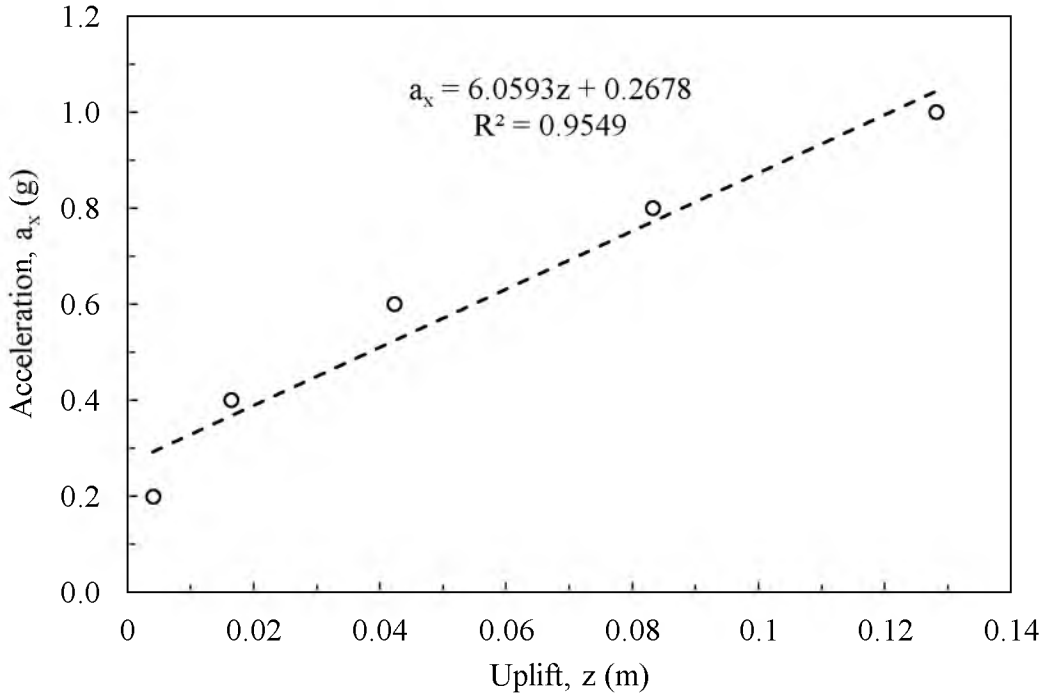

Figure 7.4. Relationship of acceleration and uplift at basal layer

7.5 Conclusions

The use of lateral restraint cabling system appears to be a viable counter-measure against sway and interblock uplift for EPS bridge support systems undergoing moderate to large levels of earthquake shaking. A prototype restraint system was proposed and analyzed in a preliminary fashion for the sway and rocking modes. It is clear that the use of cables can significantly reduce the potential for overstressing EPS blocks by limiting the amount of shear strain that can develop during sway. The numbers and diameter of the cables were determined for a 1 g acceleration. Six numbers of strands with diameter of 19 mm are recommended for this excitation level.

Even though the uplift at the inter-block interface of EPS and load distribution slab can be eliminated by cabling, uplift at the foundation-soil interface may still occur. An exhaustive study of rocking and uplift with cable restraints was not included in this study due to the complexity of the numerical analyses required. Further work on this topic is recommended.

7.6 References

Aaboe, R., and Frydenlund, T. E. (2011). "40 years of experience with the use of EPS geofoam blocks in road construction." *Proc., 4th Intl. Conf. on Geofoam Blocks in Construction Applications,* Lillestrom, Norway.

Amini, Z. A. (2014). "Dynamic characteristics and seismic stability of expanded polystyrene geofoam embankments." Ph.D. thesis, The University of Utah, Utah, USA.

Bartlett, S. F., and Lawton, E. C. "Evaluating the seismic stability and performance of freestanding geofoam embankment." *Proc., 6th National Seismic Conf. on Bridges and Highways*, Federal Highways Administration (FHA) and Multidisciplinary Center for Earthquake Engineering Resarch (MCEER) Charleston, SC, 17.

Itasca (2005). "FLAC: Fast Lagrangian Analysis of Continua: structural elements, version 5." Minneapolis, MN.

Itasca (2006). "FLAC: Fast Lagrangian Analysis of Continua: structural elements, version 3.1." Minneapolis, MN.

Nawy, E. G. (2006). *Prestressed concrete*, Prentice Hall, Upper Saddle River, NJ, USA.

Riad, H. L., and Horvath, J. S. (2004). "Analysis and design of EPS-geofoam embankments for seismic loading." *Proc., Geotechnical Engineering for Transportation Projects*, ASCE, Los Angeles, USA, CA, 2028-2037.

CHAPTER 8

CONCLUSIONS

This dissertation has investigated the use of EPS geofoam embankment to support rail and bridge systems.

Regarding the first topic, limiting the amount of vertical deflections of rail systems is important to the safety and performance of such systems. Vertical rail deflection measurements of a commuter and a light rail system, both supported by EPS geofoam, were obtained and evaluated using field methods. An accelerometer array with a high speed data acquisition system was ultimately used to measure the vertical rail deflections for the commuter and light rail systems constructed atop EPS embankment in the Salt Lake Valley, Utah. For comparative purposes, the amount of commuter rail deflections was also measured on an adjacent earthen embankment. For all locations, three accelerometers were glued on the concrete rail tie (i.e., sleeper) to record the acceleration time history during the passage of the trains. The acceleration time histories were converted into corresponding displacement time histories using a signal processing software. The maximum and average deflections of the commuter rail support on EPS embankment were about 6 mm and 2 mm, respectively, and were about 22 mm and 7.5 mm, respectively, for the adjacent earthen embankment. Therefore, it was found that the measured vertical deflections of the EPS

embankment were about 25 percent of those measured on the adjacent earthen embankment. The maximum vertical displacement of the light rail system atop EPS embankment was about around 0.6 mm. This value is much smaller than the commuter rail system due to the relatively light weight trains used in this system. Overall, the measurements indicate that the EPS embankment is performing well and provides acceptable deflection performance.

In addition to the accelerometer array, a low cost optical technique was developed to measure the vertical deflection of rail systems. The technique was used to measure deflections in a laboratory setting and the results were compared with LVDT results obtained from a MTS system. The difference in results of the two methods was about 2 percent. However, the optical technique was not used in the field because the equipment setup was sensitive to wind, vibration and other environmental factors. Nonetheless, this method may still be applicable for field conditions that are more favorable. Lastly, a large-scale monotonic and cyclic triaxial, and large chamber cyclic tests were conducted in the laboratory to determine Young's modulus and the cyclic nonlinear modulus of the rail ballast material. The cyclic nonlinear secant modulus at low amplitude strain was found to be 24000 kPa in the large chamber tests. Ultimately, it was concluded that the stress-strain relation obtained from the large chamber was more representative of the behavior of the ballast material subjected to cyclic loading produced by passing trains; hence it is recommend for future modeling and design assessments. The large chamber test was also found to be less time consuming and cost effective in comparison to the cyclic triaxial test.

Regarding the second topic, the conceptual development of EPS bridge support system was evaluated using laboratory, analytical and numerical techniques. From these, the size

(i.e., length and width) of possible bridge was determined, and the EPS support system was evaluated for potential seismic behavior in terms of interblock and basal sliding, sway and rocking modes. A mechanical restraint system was added to the EPS support system and evaluated to explore the viability of using cabling as a method to improve the seismic performance of the EPS bridge support system for earthquake prone regions. The bridges considered were 18 to 34 m single-span steel and concrete structures with 1 or 2 traffic lanes supported primarily on EPS with a density of 29 kg/m^3. Two types of embankment geometries were introduced: (1) rectangular and (2) trapezoidal. The rectangular prismatic shape embankment with exterior diagonal cable restraints was also analyzed for the sway and rocking modes. For the case without cable restraints, the critical acceleration for initiation of interlayer sliding within the EPS mass, or at its base, was 0.6 g for both geometrical cases. The potential use of shear keys within the EPS embankment was explored to resist interblock sliding. In addition, the potential reduction of basal layer sliding was explored by embedding the EPS embankment in the foundation soil. With these countermeasures, and for horizontal excitation levels of 1.0 g at the fundamental period of the embankment, it was found that the required depth of embedment for trapezoidal and rectangular prismatic embankments was 1.0 m and 1.4 m, respectively, to guard against basal sliding.

Furthermore, the potential for overstressing of the EPS during earthquake loading was studied by monotonic and cyclic triaxial testing in the laboratory and by numerical evaluations of the proposed embankment geometries. The potential for overstressing was checked in terms of allowable shear and normal stresses. The recommended allowable stresses were determined from monotonic uniaxial testing for various densities of EPS. For

EPS 29, which was selected for the bridge support evaluations herein, the recommended allowable values of shear and normal stresses are 91 and 182 kPa, respectively. The cyclic uniaxial test results revealed that EPS geofoam when cycled to stress levels below about 5 percent axial strain had stiffened when a monotonic load was applied following the cycling. This stiffening reduced the amount of postcyclic creep. Therefore for EPS 29, the total vertical strain from the combined static and cyclic deviator stresses was estimated to be below 2 percent for a projected 50-year bridge performance period. However it is recommended for any situation that the dead loads imposed on the embankment do not exceed the compressive resistance of the EPS measured at 1 percent value.

The numerical evaluations suggested that EPS might be overstressed during the sway and rocking modes at relatively low horizontal accelerations of 0.2 g and 0.3 g, respectively. In addition, the model suggested that minor uplift was initiated during rocking once the horizontal excitation reached about 0.15 g to 0.2 g; however, this amount of uplift was relatively small and may not have any consequence.

Ultimately, it was concluded that a lateral restraint system using diagonal cabling may be required for horizontal accelerations that exceed about 0.2 g. The cabling was a mechanical restraint employed to limit sway and uplift and reduce the potential overstressing of the EPS in compression and shear. It was found that six strands with 19-mm diameter cable were required to resist the forces associated with sway for the excitation level of 1 g placed in the transverse direction of the embankment.

Further research may be required to more fully describe the dynamic behavior of the EPS embankment behavior with cabling attached. The evaluations in this study were done at the conceptual level using simple models and a combination of analytical and numerical

methods. However, more detailed numerical modeling of the structural and embankment response may be warranted in order to more rigorously understand and evaluate the complex dynamic behavior of these systems. These appear to be especially warranted when a cabling is employed as a lateral restraint system for the EPS support embankment. In addition, it may be of interest to explore the postcyclic creep behavior of EPS specimens subjected to various levels of cyclic direct simple shear testing. Such results could be compared with the results obtained in the study, which were cyclic uniaxial (compressive) tests. It is possible that the postcyclic creep behavior may be different for specimens subject to different modes of cyclic loading.

APPENDIX A

ALOGORITHM FOR IMAGE PROCESSING IN OPTICAL TECHNIQUE

```
%% Load all data
[filename,pathname]=uigetfile('*.jpg','open image from camera');
n=380; % number of frames
Input=[pathname filename];
for i=1:9
   path=[Input(1:50),num2str(i),'.jpg'];
   temp=imread(path);
   Data(:,:,i)=temp(:,:,1);
end
for i=10:99
   path=[Input(1:49),num2str(i),'.jpg'];
   temp=imread(path);
   Data(:,:,i)=temp(:,:,1);
end
for i=100:n
   path=[Input(1:48),num2str(i),'.jpg'];
   temp=imread(path);
   Data(:,:,i)=temp(:,:,1);
end
%% Finding region of interest
pin=40;% choose frame for reference(base image) at which no disturbance
figure;image(Data(:,:,pin));
pause;
```

```
v=round(axis);
a=double(Data(:,:,pin));
figure;image(a)
b=zeros(size(a,1),size(a,2));
b(v(3):v(4),v(1):v(2))=a(v(3):v(4),v(1):v(2)); temp=a(v(3):v(4),v(1):v(2));
figure;image(b);
temp1=double(temp(1:size(temp,1)*size(temp,2)));
x=linspace(min(temp1),max(temp1),20);
figure;plot(x,hist(temp1,x)); [thx,thy]=ginput(1);
b(b>thx)=0;
figure;image(b);
b(b>0)=1;
clm=sum(b,2);
total_pixels=sum(clm);
test=find(clm>0);
centery=round(test(1)+length(test)/2);
figure;plot(1:size(b,1),clm);
[centery,sizeofROI] = findcenter(Data,v,thx);
n_centery=centery(51:252);
figure;plot(n_centery)
%% Finding center
function [centery,sizeofROI] = findcenter(Data,v,thx)
for i=1:size(Data,3)
```

```
    a=double(Data(:,:,i));
    b=zeros(size(a,1),size(a,2));
    b(v(3):v(4),v(1):v(2))=a(v(3):v(4),v(1):v(2));
    b(b>thx)=0;
    b(b>0)=1;
    sizeofROI(i)=sum(sum(b));
    clm=sum(b,2);
    test=find(clm>0);
    centery(i)=round(test(1)+length(test)/2);
end
figure;plot(centery)
figure;plot(sizeofROI)
end
%% Finding pixel to length
pin = 40;
Test_im=double(Data(:,:,pin));
figure;image(Test_im);
yvalue = 275;
figure;plot(Test_im(yvalue,:))
```

APPENDIX B

SIZING OF BRIDGE

B.1 Steel Bridge

B.1.1 Selection of Type of Steel Bridge

B.1.1.1 Acrow Bridge

From the personal communication with Acrow bridges regional office in Colorado (Needham, Randy), the maximum dead load including all elements of bridge for single lane road with one-sided sidewalk is 5.25 m.

Width of sidewalk,

$B_{sidewalk} := 1.5;$ = 1.50 m

$B_{single-lane} := 3.75;$ = 3.75 m

$B_{total-single} := B_{sidewalk} + B_{single-lane};$ = 5.25 m

$DL := 1.04;$ = 1.04 tons/ft

Dead load in terms of SI unit is,

$DL_{Acrow} := \frac{1.04 \cdot 2 \cdot 1000}{68.52177};$ = 30.35532 kN/m

B.1.1.2 Mabey Bridge

The Mabey bridge website provides the information on quick bridges and their dimensions. From the information, the longest length of flat top type bridges was considered for the calculation.

Modular width,

$B_m := 1.725;$ = 1.725 m

Unit weight excluding parapet,

$M_{without\ parapet} := 14250;$ = 14250.0 kg

Parapet and kerb weight (one side),

$M_{parapet-kerb(one\ side)} := 1960;$ $= 1960.0\ kg$

Parapet and kerb weight on both sides,

$M_{parapet-kerb(one\ side)} := 2 \cdot M_{parapet-kerb(one\ side)};$ $= 3920.0\ kg$

Total weight for single unit,

$M_{total} := M_{without\ parapet} + M_{parapet-kerb(one\ side)};$ $= 18170.0\ kg$

$DL_{Mabey} := M_{total} \cdot \frac{9.81}{1000} \cdot \frac{1}{B_m} \cdot B_{total-single} \cdot \frac{1}{20};$ $= 27.125\ kN/m$

From the calculation of dead load of two bridges, it was found that weight per linear meter of Acrow bridges is slightly higher, so weight per linear meter of Acrow bridge is considered for sizing of steel bridge.

$DL_{bridge} := \max(DL_{Acrow}, DL_{Mabey});$ $= 30.35\ kN/m$

B.1.2 Load Calculation

B.1.2.1 Calculation of Dead Load

Width of pavement for double lane,

$B_{pavement} := 7.5;$ $= 7.50\ m$

Width of bridge,

$B_{bridge} := B_{pavement} + B_{sidewalk};$ $= 9.00\ m$

$DL_{bridge-double\ lane} := DL_{bridge} \cdot \frac{B_{bridge}}{B_{total-single}};$ $= 52.038\ kN/m$

Footing dimensions are,

$B_{footing} := 9;$ $= 9.00\ m$

$L_{footing} := 4;$ = 4.00 m

$\Upsilon_{concrete} := 23.56;$ = 23.56 kN/m^3

$h_{concrete} := 0.50;$ = 0.50 m

Dead load of footing,

$DL_{footing} := \Upsilon_{concrete} \cdot h_{concrete} \cdot B_{footing} \cdot L_{footing};$ = 424.08 kN

Total dead load from footing on both sides of abutment,

$DL_{footing-total} := 2 \cdot DL_{footing};$ = 848.16 kN

B.1.2.2 Calculation of Allowable Load

The compressive strength based on ASTM D6817 at 1 percent strain,

$\sigma_c := 75;$ = 75.00 kPa

Axial strain,

$\varepsilon_a := 0.01;$ = 0.01

$A_{footing} := L_{footing} \cdot B_{footing};$ = 36.00 m

Allowable load,

$Q := \sigma_c \cdot A_{footing};$ = 2700.00 kN

Maximum load that can support by abutment on both sides of bridge.

$Q_{allowable} := 2 \cdot Q;$ = 5400.00 kN

B.1.2.3 Calculation of Live Load

Live load of the truck was calculated from the loading configuration given in AASHTO 2012. The spacing between rear axle to driver axle and front vehicle to back vehicle is 14

feet and 5 feet, respectively.

Length of loading,

$$L_{loading} := \frac{(14 + 14 + 5)}{3.281}; \quad = 10.06\ m$$

Point load,

$$W_{point} := (32 + 32 + 8) \cdot 4.4482; \quad = 320.27\ kN$$

Load per meter run,

$$LL := \frac{W_{point}}{L_{loading}} \cdot 2; \quad = 63.68\ kN/m$$

B.1.3 Calculation of Length of Bridge

Length of bridge is obtained from trial and error method.

$$L_{bridge} := 31.6; \quad = 31.60\ m$$

Applied total load is,

$$Q_{applied} := DL_{bridge-double\ lane} \cdot L_{bridge} + DL_{footing-total} + LL \cdot L_{bridge}; \quad = 4505.01\ kN$$

Factor of safety,

$$FS := \frac{Q_{allowable}}{Q_{applied}}; \quad = 1.20$$

Length of bridge for design,

$$L_{bridge-design} := 31.0; \quad = 31.0\ m$$

B.2 Concrete Bridge

Width of pavement for double lane,

$B_{pavement} := 7.5;$ = 7.50 m $B_{sidewalk} := 1.5;$ = 1.50 m

Width of bridge,

$B_{bridge} := B_{pavement} + B_{sidewalk};$ = 9.00 m

B.2.1 Calculation of Dead Load

The calculation was made based on the comprehensive design example of concrete girder super structure bridge by Modjeski and Masters Inc. (2003),

Unit weight of concrete,

$\Upsilon_{concrete} := \frac{150}{6.366};$ = 23.56 kN/m

B.2.1.1 Design of Deck

Thickness,

$t := \frac{8}{12 \cdot 3.281};$ = 0.20 m

Deck weight per meter,

$W_{deck} := B_{pavement} \cdot \Upsilon_{concrete} \cdot t;$ = 35.91 kN/m

B.2.1.2 Design of Girder

Longitudinal girder,

Cross-sectional area of girder,

$A_{long-girder} := \frac{1085}{(12 \cdot 3.281)^2};$ = 0.70 m^2

Girder spacing,

$S_{long} := \frac{10}{3.281};$ = 3.05 m

Number of girders,

$N_{long} := 3;$ = 3

Girder weight per meter,

$W_{long-girder} := \Upsilon_{concrete} \cdot A_{long-girder} \cdot N_{long};$ = 49.48 kN/m

Cross Girder,

Cross-sectional area of girder,

$A_{cross-girder} := \frac{1085}{(12 \cdot 3.281)^2};$ = 0.70 m^2 $S_{cross} := \frac{25}{3.281};$ = 7.62 m

Number of girders,

$N_{cross} := 3;$ = 3

Girder weight per meter per width,

$W_{cross-girder} := \Upsilon_{concrete} \cdot A_{cross-girder} \cdot N_{cross};$ = 49.48 kN/m

B.2.1.3 Design of Parapet Wall

Cross-sectional area of parapet,

$A_{cross-parapet} := \frac{4.33}{3.281^2};$ = 0.402 m^2

Parapet weight per meter,

$W_{parapet} := \Upsilon_{concrete} \cdot A_{cross-parapet};$ = 9.48 kN/m

Number of parapets,

$N_{parapets} := 2;$ = 2

Total weight of parapets,

$W_{total-parapets} := N_{parapets} \cdot W_{parapet};$ = 18.95 kN/m

B.2.1.4Design of Wearing Surface

Weight per meter square,

$W_{per-m2-wearing} := 0.03 \cdot 47.8802;$

$W_{per-meter-wearing} := W_{per-m2-wearing} \cdot B_{pavement};$ = 10.77 kN/m

Dead load per meter of bridge,

$DL_{per-meter} := W_{deck} + W_{long-girder} + W_{total-parapets} + W_{per-meter-wearing};$ = 115.11 kN/m

Footing dimensions,

$B_{footing} := 9;$ = 9.00 m

$L_{footing} := 4;$ = 4.00 m

$h_{concrete} := 0.50;$ = 0.50 m

Dead load from footing,

$DL_{footing} := \Upsilon_{concrete} \cdot h_{concrete} \cdot B_{footing} \cdot L_{footing};$ = 424.13 kN

Total dead load from footing on both sides of abutment,

$DL_{footing-total} := 2 \cdot DL_{footing};$ = 848.26 kN

B.2.2 Calculation of Allowable Load

Compressive strength based on ASTM D6817 at 1 percent strain is,

$\sigma_c := 75;$ = 75.00 kPa

Axial strain,

$\varepsilon_a := 0.01;$ $= 0.01$ $A_{footing} := L_{footing} \cdot B_{footing};$ $= 36.00\ m$

Allowable load,

$Q := \sigma_c \cdot A_{footing};$ $= 2700.00\ kN$

Maximum load that can be supported by abutment on both sides of bridge,

$Q_{allowable} := 2 \cdot Q;$ $= 5400.00\ kN$

B.2.3 Calculation of Live Load

Live load from the truck,

According to AASHTO 2012, the spacing between rear axle to driver axle and front vehicle to back vehicle is 14 feet and 5 feet, respectively.

Length of loading,

$$L_{loading} := \frac{(14 + 14 + 5)}{3.281}; \quad = 10.06\ m$$

Point load,

$W_{point} := (32 + 32 + 8) \cdot 4.4482;$ $= 320.27\ kN$

Load per meter run,

$$LL := \frac{W_{point}}{L_{loading}} \cdot 2; \quad = 63.68\ kN/m$$

Length of bridge was obtained from trial and error method.

$L_{bridge} := 17.9;$ $= 17.90\ m$

B.2.4 Calculation of Length of Bridge

Applied total load,

$$Q_{applied} := DL_{per-meter} \cdot L_{bridge} + DL_{footing-total} + LL \cdot L_{bridge} + W_{cross-girder} \cdot B_{bridge}; \quad = 4494.03 \text{ kN/m}$$

Factor of safety,

$$FS := \frac{Q_{allowable}}{Q_{applied}}; \quad = 1.20$$

Length of bridge for design,

$$L_{bridge-design} := 18.0; \quad = 18.0 \text{ m}$$

APPENDIX C

ANALTYTICAL METHOD FOR FUNDAMENTAL PERIOD CALCULATION

C.1 Rectangular Prism

Density of EPS,

$\rho := 34.02;$ = 34.02 kg/m^3

Height of embankment,

$H := 6;$ = 6 m

Width of embankment,

$B := 9;$ = 9.00 m

Length of embankment,

$L := 4;$ = 4 m

Young's modulus of elasticity,

$E_c := 12547;$ = 12547 kPa

Poisson's ratio from Horvath (1995),

$\nu := 0.0056 \cdot \rho + 0.0024;$ = 0.192912

Shear modulus,

$$G := \frac{E_c}{2 \cdot (1 + \nu)};$$ = 5259 Pa

$g := 9.81;$ = 9.81 m/sec^2

Dead load from bridge,

$DL_{bridge} := 806.58;$ = 806.58 kN

Live load is taken as half of the live load from truck,

$LL_{truck} := 987.13;$ = 987.13 kN

Dead load from foundation,

$DL_{foundation} := 424.08;$ = 424.08 kN

Total load,

$$W := \left(DL_{bridge} + 0.5 \cdot LL_{truck} + DL_{foundation}\right); \quad = 1724.22\ kN$$

Vertical effective stress at top of foundation,

$$\sigma_{v(prime)} := \frac{W}{L \cdot B}; \quad = 47.89513889$$

C.1.1 Method I

Excitation along the longitudinal direction,

$$T_0 := evalf\left(2 \cdot \pi \cdot \left(\frac{\sigma_{v(prime)} \cdot H}{E_c \cdot g}\left(4 \cdot \left(\frac{H}{L}\right)^2 + \left(\frac{12 + 11 \cdot \nu}{5}\right)\right)\right)^{0.5}\right); \quad = 1.0440\ sec$$

Excitation along the transverse direction,

$$T_0 := evalf\left(2 \cdot \pi \cdot \left(\frac{\sigma_{v(prime)} \cdot H}{E_c \cdot g}\left(4 \cdot \left(\frac{H}{B}\right)^2 + \left(\frac{12 + 11 \cdot \nu}{5}\right)\right)\right)^{0.5}\right); \quad = 0.6513\ sec$$

C.1.2 Method II

Excitation along the longitudinal direction,

$$T_0 := evalf\left(2 \cdot \pi \cdot \left(\frac{\sigma_{v(prime)} \cdot H}{E_c \cdot g}\left(4 \cdot \left(\frac{H}{L}\right)^2 + 1 + \left(\frac{12 + 12 \cdot \nu}{5}\right)\right)\right)^{0.5}\right); \quad = 1.0888\ sec$$

Excitation along the transverse direction,

$$T_0 := evalf\left(2 \cdot \pi \cdot \left(\frac{\sigma_{v(prime)} \cdot H}{E_c \cdot g}\left(4 \cdot \left(\frac{H}{B}\right)^2 + 1 + \left(\frac{12 + 12 \cdot \nu}{5}\right)\right)\right)^{0.5}\right); \quad = 0.7210\ sec$$

C.1.3 Analytical Method

Excitation along the vertical direction,

$$T_0 := \text{evalf}\left(2\cdot\pi\cdot\left(\frac{\sigma_{v(prime)}\cdot H}{E_c\cdot g}\right)^{0.5}\right); \quad = 0.3036 \text{ sec}$$

C.2 Trapezoidal Prism

Density of EPS,

$\rho := 34.02;$ = 34.02 kg/m^3

Height of embankment,

$H := 6;$ = 6 m

Width of embankment,

$B := 9;$ = 9.00 m

Length of embankment at top,

$L_{top} := 4;$ = 4 m

Slope of an embankment is 2H: 1V.

Length of embankment at bottom,

$L_{bottom} := L_{top} + 2\cdot 2\cdot H;$ = 28.00 m

Volume of trapezoidal section,

$$V_{trapezoidal-section} := B\cdot\frac{L_{top}+L_{bottom}}{2}\cdot H; \quad = 864.00 \text{ m^3}$$

According to Horvath (1995),

The equivalent length of prismatic section,

$$L := \frac{V_{trapezoidal-section}}{B\cdot H}; \quad = 16.00 \text{ m}$$

Young's modulus of elasticity,

$E_c := 12547;$ = 12547 Kpa

Poisson's ratio from Horvath (1995),

$\nu := 0.0056 \cdot \rho + 0.0024;$ = 0.192912

Shear modulus,

$G := \frac{E_c}{2 \cdot (1 + \nu)};$ = 5259 Pa $g := 9.81;$ = 9.81 m/sec^2

Dead load from bridge,

$DL_{bridge} := 806.58;$ = 806.58 kN

Live load is taken as half of the live load from truck,

$LL_{truck} := 987.13;$ = 987.13 kN

Dead load from foundation,

$DL_{foundation} := 424.08;$ = 424.08 kN

Total load,

$W := (DL_{bridge} + 0.5 \cdot LL_{truck} + DL_{foundation});$ = 1724.22 kN

Vertical effective stress at top of foundation,

$\sigma_{v(prime)} := \frac{W}{L \cdot B};$ = 11.97378472

C.2.1 Method I

Excitation along the longitudinal direction,

$$T_0 := evalf\left(2 \cdot \pi \cdot \left(\frac{\sigma_{v(prime)} \cdot H}{E_c \cdot g}\left(4 \cdot \left(\frac{H}{L}\right)^2 + \left(\frac{12 + 11 \cdot \nu}{5}\right)\right)\right)^{0.5}\right); \quad = 0.2794 \text{ sec}$$

Excitation along the transverse direction,

$$T_0 := \text{evalf}\left(2\cdot\pi\cdot\left(\frac{\sigma_{v(prime)}\cdot H}{E_c\cdot g}\left(4\cdot\left(\frac{H}{B}\right)^2+\left(\frac{12+11\cdot\nu}{5}\right)\right)\right)^{0.5}\right); = 0.3256 \text{ sec}$$

C.2.2 Method II

Excitation along the longitudinal direction,

$$T_0 := \text{evalf}\left(2\cdot\pi\cdot\left(\frac{\sigma_{v(prime)}\cdot H}{E_c\cdot g}\left(4\cdot\left(\frac{H}{L}\right)^2+1+\left(\frac{12+12\cdot\nu}{5}\right)\right)\right)^{0.5}\right); = 0.3193 \text{ sec}$$

Excitation along the transverse direction,

$$T_0 := \text{evalf}\left(2\cdot\pi\cdot\left(\frac{\sigma_{v(prime)}\cdot H}{E_c\cdot g}\left(4\cdot\left(\frac{H}{B}\right)^2+1+\left(\frac{12+12\cdot\nu}{5}\right)\right)\right)^{0.5}\right); = 0.3605 \text{ sec}$$

C.2.3 Analytical Method

Excitation along the vertical direction,

$$T_0 := \text{evalf}\left(2\cdot\pi\cdot\left(\frac{\sigma_{v(prime)}\cdot H}{E_c\cdot g}\right)^{0.5}\right); = 0.1518 \text{ sec}$$

APPENDIX D

MODEL PARAMETERS

D.1 Foundation Material

$t1 := 0.50;$ $= 0.50\ m$

$w := 9;$ $= 9.00\ m$

$l1 := 4;$ $= 4.00\ m$

$A := w \cdot l1;$ $= 36.00\ m^2$

Assumptions,

$f_{prime(c)} := 5000;$ $= 5000.00\ psi$

$\rho := 2400;$ $= 2400.00\ kg/m^3$

From Reinforced Concrete Mechanics and Design Book (James G. MacGregor and James K. Wight), Poisson's ratio is in the range of 0.15 to 0.20.

$\nu := 0.18;$ $= 0.18$

$\Upsilon := 150;$ $= 150.00\ pcf$

$W := \Upsilon;$ $= 150.00\ pcf$

$Ec := 33 \cdot (W^{1.5}) \cdot (f_{prime(c)})^{0.5} \cdot 6.89475729 \cdot 1e3;$ $= 2.955662309\,10^{10}\ Pa$

$G := \frac{Ec}{2 \cdot (1 + \nu)};$ $= 12.52399283 \times 10^{09}\ Pa$

$K := \frac{Ec}{3 \cdot (1 - 2 \cdot \nu)};$ $= 15.3940745 \times 10^{09}\ Pa$

D.2 Density of Foundation Material

From AASHTO 2012,

For extreme event, the live load factor is 0.5.

$DL_{foundation} := 23.56 \cdot t1 \cdot w \cdot l1;$ $= 424.0800\ kN$

$Volume := t1 \cdot w \cdot l1;$ $= 18.00\ m^3$

$$Mass := \frac{(DL1 + 0.5 \cdot LL + DL_{foundation})}{9.81} \cdot 1000; \quad = 1.75761977610^5 \text{ kg}$$

$$\rho := \frac{Mass}{Volume}; \quad = 9764.554311 \text{ kg/m^3}$$

D.3 EPS Embankment

$h := 6.0; \quad = 6.00 \text{ m}$

$w := 9; \quad = 9.00 \text{ m}$

$l := 4; \quad = 4.00 \text{ m}$

$Ec := 12547 \cdot 1e3; \quad = 12.5470000 \times 10^6 \text{ Pa}$

$\rho := 34.02; \quad = 34.02 \text{ kg/m^3}$

$\nu := 0.193; \quad = 0.193$

$$G := \frac{Ec}{2 \cdot (1 + \nu)}; \quad = 5.2585918 \times 10^{06} \text{ Pa}$$

$$K := \frac{Ec}{3 \cdot (1 - 2 \cdot \nu)}; \quad = 6.8116178 \times 10^{06} \text{ Pa}$$

Load from Bridge,

$DL1 := 806.58; \quad = 806.58 \text{ kN}$

$LL := 987.13; \quad = 987.13 \text{ kN}$

D.4 Base Soil

$E := 2e7; \quad = 20.0000000 \times 10^6 \text{ Pa}$

$\rho := 1900; \quad = 1900.00 \text{ kg/m^3}$

$\nu := 0.4; \quad = 0.4$

$$G_{soil} := \frac{E}{2\cdot(1+\nu)}; \quad = 7.1428571 \times 10^{06} \text{ Pa}$$

$$K_{soil} := \frac{E}{3\cdot(1-2\cdot\nu)}; \quad = 3.3333333 \times 10^{07} \text{ Pa}$$

D.5 Stiffness at Interface

From FLAC 3D manual the stiffness at interface is,

$$k_n := \left(\frac{K_{geofoam} + \frac{4}{3}\cdot G_{geofoam}}{\Delta z} \right);$$

where, K and G are the bulk and shear moduli, respectively. k_n and k_s are the normal and shear stiffness which are equal and Δz_{min} is the smallest width of an adjoining zone in the normal direction.

$$\Delta z := 0.5; \quad = 0.5$$

$$k_n := \left(\frac{K_{geofoam} + \frac{4}{3}\cdot G_{geofoam}}{\Delta z} \right); \quad = 2.764614704\,10^{7} \text{ Pa}$$

$$k_s := k_n; \quad = 2.764614704\,10^{7} \text{ Pa}$$

According to Amini (2014),

$$k_{n1} := 50\cdot k_n; \quad = 1.382307352\,10^{9} \text{ Pa}$$

$$k_{s1} := 50\cdot k_s; \quad = 1.382307352\,10^{9} \text{ Pa}$$

APPENDIX E

FLAC FUNDAMENTAL PERIOD CALCULATION

E.1 Fundamental Period

E.1.1 Free Vibration

The FLAC code for the calculation of fundamental period under free vibration for 4 m long and double lane wide rectangular prism for the excitation along the longitudinal direction is given below.

```
;  Fundamental Time Period Calculation
;   Excitation along the longitudinal direction
;  Free standing embankment with foundation for bridge at top
;  Length is equal to length of footing
;  Double lane with width of 9 m
new
;
;set mechanical ratio 1e-3
;
config dyn
set large
;----------GENERATE THE MODEL----------------------------
;Generate the EPS embankment below foundation
gen zone brick p0(0,0,0) p1(4,0,0) p2(0,9,0) &
p3(0,0,6)&
                    size 8,18,12 group E1
;
;Generate the foundation
```

```
gen zone brick p0(0,0,6) p1(4,0,6) p2(0,9,6) &
p3(0,0,6.5) &
                size 8,18,1 group F1
;
;---------Assign material properties-----------------
model elas range group E1
prop bulk 6.8116e6 shear 5.2586e6 range group E1
;
model elas range group F1
prop bulk 15.3941e9 shear 12.524e9 range group F1
;
ini dens 34.02 range group E1
;
ini dens 9764.55 range group F1
;
;-------COLOR OF THE GROUP------------
group 1 Red range group E1
group 2 blue range group F1
;
;---BOUNDARY CONDITIONS FOR DYNAMIC CASE------------
fix y z range z -0.1,0.1
;----------SET DAMPING--------------------
;set dyn damp rayleigh 0.02 2
```

```
;
;------ Sin, Cos WAVE AS INPUT MOTION-----------------
def setup
 omega=2*pi*freq
 period=1/freq
end
 set freq=1.8
setup
;Free Vibration(Pulse Loading)
def wave
if dytime>period
 wave=0
else
 wave=amp*sin(omega*dytime)
  endif
end
set amp=0.5
;
;Forced Vibration
;wave=amp*cos(2*pi/period*dytime)
;end
;
;---------FORCING FUNCTION-------------
```

```
apply xvel=1 hist wave range z -0.1,0.1
;apply yvel=1 hist wave range z -0.1,0.1
;apply zvel=1 hist wave range z -0.1,0.1
;
;--------HISTORIES----------------------
his id 2 gp xdisp 0,0,0
his id 3 gp xdisp 0,0,6.5
his id 4 gp xvel 0,0,0
his id 5 gp xvel 0,0,6.5
his id 6 gp xacc 0,0,0
his id 7 gp xacc 0,0,6.5
;his id 8 gp ydisp 0,0,0
;his id 9 gp ydisp 0,0,6.5
;his id 10 gp yvel 0,0,0
;his id 11 gp yvel 0,0,6.5
;his id 12 gp yacc 0,0,0
;his id 13 gp yacc 0,0,6.5
his id 14 dytime
his id 15 wave
;
;-------------SOLVE FOR DYNAMIC----------
solve age 10
;
```

```
save fund1.sav
;
rest fund1
;
plot set title text
X displacement at top of embankment for 4 m length of footing
plot hist 3 vs 14
plot show
;----------HISTORY OUTPUT IN TEXT FILE----------
his write 3 vs 14 file Xforce.his
```

APPENDIX F

SLIDING MODE OF EPS EMBANKMENT

F.1 Rectangular Prism

F.1.1 Critical Acceleration

Bridge load,

$DL_{bridge} := 806.58;$ = 806.58 kN

$LL_{bridge} := 987.13;$ = 987.13 kN

Foundation load,

$DL_{foundation} := 424.08;$ = 424.08 kN

Geofoam embankment geometry,

$B := 9;$ = 9.00 m

$H := 6;$ = 6.00 m

$L := 4;$ = 4.00 m

Assumptions:

Soil below the embankment is sand. The vertical acceleration is negligible. The accelerations along longitudinal and transverse directions of the bridge are same. The spectral and peak ground acceleration is same. The block height is assumed to be 1m.

$g := 9.81;$ = 9.81 m/sec^2

Calculations:

The calculation of basal layer at zero interface is shown in Table F.1.

$$\sigma_{v0} := \frac{DL_{bridge} + 0.5 \cdot LL_{bridge} + DL_{foundation}}{(L \cdot B)};$$ = 47.8951 kPa

From the relation given by Sheeley and Negussey (2000), friction factor for geofoam-geofoam interface is:

$\tan\delta$ = 0.81

Table F.1. Calculation of critical acceleration for rectangular prism

Interface	Horizontal acceleration (g)	Mass/unit area (kg/m2)	Inertial force (N/m2)	Frictional resisting force (W/K) (N/m2)	Frictional resisting force (WO/K) (N/m2)	Shear key coverage (%)	Cohesive resisting force (N/m2)	FS sliding (without key)	FS sliding (with key)
6	0.599	5020	29519	39886	39886	0	0	1.35	1.35
5	0.599	5020	29519	39886	39886	0	0	1.35	1.35
4	0.599	5020	29519	39886	39886	0	0	1.35	1.35
3	0.599	5020	29519	39886	39886	0	0	1.35	1.35
2	0.599	5020	29519	39886	39886	0	0	1.35	1.35
1	0.599	5020	29519	39886	39886	0	0	1.35	1.35
0	0.599	5020	29519	29545	29545	0	0	1.00	1.00

The relation given by Bartlett et al. (2000), the friction factor for geofoam-soil interface is:

$\tan\delta = 0.6$

Geofoam shear strength from Benchmark Foam (2009) is:

$$\tau := \frac{33 \cdot 144 \cdot 95}{2000}; \quad = 225.7200 \text{ kPa}$$

The critical acceleration was obtained from the goal seek in spreadsheet. The calculation for 6 layers is shown in Table F.1.

$a_{critical} := 0.5995; \quad = 0.5995 \text{ g}$

Sample calculation for basal layer,

Mass per unit area,

$$m := \frac{\sigma_{v0} \cdot 1000}{9.81}; \quad = 4882.277 \text{ kg/m^2}$$

Inertial force,

$F_{inertial} := m \cdot a_{critical} \cdot g; \quad = 28713.136 \text{ N/m^2}$

Frictional resisting force,

$F_{resisting} := \sigma_{v0} \cdot 0.6 \cdot 1000; \quad = 28737.083 \text{ N/m^2}$

Factor of safety against sliding,

$$FS_{sliding} := \frac{F_{resisting}}{F_{inertial}}; \quad = 1.00$$

F.1.2 Shear Key Coverage

Bridge load,

$DL_{bridge} := 806.58; \quad = 806.58 \text{ kN}$

$LL_{bridge} := 987.13; \quad = 987.13 \text{ kN}$

Foundation load,

$DL_{foundation} := 424.08;$ = 424.08 kN

Ground soil properties,

$\Upsilon_{soil} := \frac{1900 \cdot 9.81}{1000};$ = 18.64 kN/m^2

$\phi_{soil} := evalf\left(\frac{\pi}{180} \cdot 35\right);$ = 0.6108652381

$\delta_{soil} := evalf\left(\frac{\pi}{180} \cdot 31\right);$ = 0.5410520681

$c := 0;$ = 0

Geofoam embankment geometry,

$B := 9;$ = 9.00 m

$H := 6;$ = 6.00 m

$L := 4;$ = 4.00 m

Assumptions:

Soil below the embankment is sand. The vertical acceleration is negligible. The acceleration along longitudinal and transverse directions of the bridge is same. The spectral and peak ground acceleration is the same. The block height is assumed to be 1m.

$g := 9.81;$ = 9.81 m/sec^2

Calculations:

The calculation for the top layer is shown in Table F.2.

$\sigma_{v0} := \frac{DL_{bridge} + 0.5 \cdot LL_{bridge} + DL_{foundation}}{(L \cdot B)};$ = 47.8951 kPa

From the relation given by Sheeley and Negussey (2000), the friction factor for geofoam-geofoam interface is: $\tan\delta$ = 0.81

Table F.2. Calculation of shear key coverage for rectangular prism

Interface	Horizontal acceleration (g)	Mass/unit area (kg/m^2)	Inertial force (N/m^2)	Frictional resisting force (W/K) (N/m^2)	Frictional resisting force (WO/K) (N/m^2)	Shear key coverage (%)	Cohesive resisting force (N/m^2)	FS sliding (without key)	FS sliding (with key)
6	1.000	5020	49242	36695	39886	8	18058	0.81	1.11
5	1.000	5020	49242	36695	39886	8	18058	0.81	1.11
4	1.000	5020	49242	36695	39886	8	18058	0.81	1.11
3	1.000	5020	49242	36695	39886	8	18058	0.81	1.11
2	1.000	5020	49242	36695	39886	8	18058	0.81	1.11
1	1.000	5020	49242	36695	39886	8	18058	0.81	1.11
0	1.000	5020	49242	29545	29545	0	0	0.60	0.60

The friction factor for geofoam-soil according to Bartlett et al. (2000) is:

$\tan\delta = 0.6$

Geofoam shear strength from Benchmark Foam (2009),

$$\tau := \frac{33 \cdot 144 \cdot 95}{2000}; \quad = 225.7200 \text{ kPa}$$

For the acceleration of 1 g,

$a_x := 1; \quad = 1 \text{ g}$

$a_y := 1; \quad = 1 \text{ g}$

$a_z := 0; \quad = 0$

Mass per unit area,

$$m := \frac{\sigma_{v0} \cdot 1000}{9.81}; \quad = 4882.277 \text{ kg/m}^2$$

Inertial force,

$F_i := m \cdot a_x \cdot g; \quad = 47895.139 \text{ N/m}^2$

Frictional resisting force,

$F_r := \sigma_{v0} \cdot 0.81 \cdot 1000; \quad = 38795.062 \text{ N/m}^2$

Factor of safety against sliding,

$$FS_{sliding} := \frac{F_r}{F_i}; \quad = 0.81$$

The factor of safety against sliding is 0.81. The following is the calculation for the first layer. Similar calculations were made for other layers. The factor of safety should be in the range of 1.1 to 1.2 to make the structure safe against sliding. The shear key coverage was assumed to increase the factor of safety.

Shear key coverage = 8 percent

$S_c := \frac{8}{100};$ = 0.08

Frictional resisting force,

$F_r := \sigma_{v0} \cdot 0.81 \cdot 1000 \cdot (1 - S_c);$ = 35691.46 N/m^2

Cohesive resisting force,

$C_r := \tau \cdot 1000 \cdot S_c;$ = 18057.60 N/m^2

Factor of safety against sliding,

$FS_{sliding} := \frac{F_r + C_r}{F_i};$ = 1.12

F.1.3 Embedment Depth for Excitation Along the Longitudinal Direction

Bridge load,

$DL_{bridge} := 806.58;$ = 806.58 kN

$LL_{bridge} := 987.13;$ = 987.13 kN

Foundation load,

$DL_{foundation} := 424.08;$ = 424.08 kN

Ground soil properties,

$\Upsilon_{soil} := \frac{1900 \cdot 9.81}{1000};$ = 18.64 kN/m^2

$\phi_{soil} := evalf\left(\frac{\pi}{180} \cdot 35\right);$ = 0.6108652381

$\delta_{soil} := evalf\left(\frac{\pi}{180} \cdot 31\right);$ = 0.5410520681

$c := 0;$ = 0

Geofoam embankment geometry,

$B := 9;$ = 9.00 m

$H := 6;$ = 6.00 m

$L := 4;$ = 4.00 m

Assumptions:

Soil below the embankment is sand. The vertical acceleration is negligible. The accelerations along longitudinal and transverse directions of the bridge are the same. The spectral and peak ground acceleration is the same. The block height is assumed to be 1m.

$g := 9.81;$ = 9.81 m/sec^2

Calculations:

For the acceleration of 1 g,

$a_x := 1;$ = 1 g

$a_y := 1;$ = 1 g

$a_z := 0;$ = 0

The basal layer sliding requires embedment to stop sliding. The calculation of active earth pressure for seismic case is the same as static. Coulomb's equation was used.

$$\beta := \text{evalf}\left(\frac{\pi}{180}\cdot 0\right);$$ = 0.0000

The backfill slope angle,

$i := 0;$ = 0

$$K_A := \text{evalf}\left(\left(\cos^2\left(\phi_{soil}-\beta\right)\right) \Big/ \left(\cos^2(\beta)\cdot\cos\left(\delta_{soil}+\beta\right)\cdot\left(1 + \sqrt{\frac{\sin\left(\delta_{soil}+\phi_{soil}\right)\cdot\sin\left(\phi_{soil}-i\right)}{\cos\left(\delta_{soil}+\beta\right)\cdot\cos(i-\beta)}}\right)^2\right)\right);$$ = 0.2465569320

$D1 := 1.4;$ = 1.40 m

$P_A := 0.5 \cdot K_A \cdot \Upsilon_{soil} \cdot D1^2 \cdot B;$ $= 40.5330\ kN$

$P_{AE} := P_A;$ $= 40.5330\ kN$

$P_{AEH} := P_{AE} \cdot \cos(\delta_{soil});$ $= 34.7435\ kN$

$P_{AEV} := P_{AE} \cdot \sin(\delta_{soil});$ $= 20.8760\ kN$

$\Delta P_{AE} := P_{AE} - P_A;$ $= 0.0000\ kN$

For the embedment less than 5 feet, the seismic passive earth pressure can be estimated using the static methods. The reduction factor (*R*) is from AASHTO (2012),

$R := 0.836;$ $= 0.836$ for $\phi_{soil} = 35^0$, and $\delta/\phi_{soil} = 0.886$

From Fig.3.11.5.4-1 in AASHTO (2012),

For $\theta = 90^0$ and $\phi_{soil} = 35^0$,

$k_p := 10.1;$ $= 10.1$

Since the reduction factor is 0.836,

$K_P := R \cdot k_p;$ $= 8.4436$

$P_{PE} := 0.5 \cdot K_P \cdot \Upsilon_{soil} \cdot D1^2 \cdot B;$ $= 1388.0939\ kN$

$P_{PEH} := P_{PE} \cdot \cos(\delta_{soil});$ $= 1189.8287\ kN$

$P_{PEV} := P_{PE} \cdot \sin(\delta_{soil});$ $= 714.9212\ kN$

$W := DL_{bridge} + 0.5 \cdot LL_{bridge} + DL_{foundation};$ $= 1724.22\ kN$

$m := \frac{W \cdot 1000}{g};$ $= 175761.9776\ kg$

Inertial force,

$F_i := \frac{m \cdot a_x \cdot g}{1000};$ $= 1724.2250\ kN$

$R1 := P_{AEV} + W + P_{PEV};$ = 2460.0222 kN

$F_r := R1 \cdot \tan(\phi_{soil});$ = 1722.5261 kN

Factor of safety against sliding

$F_{Resisting} := F_r + P_{PEH};$ = 2912.3548 kN

$F_{Driving} := F_i + P_{AEH};$ =1758.9685 kN

$FS_{sliding} := \frac{F_{Resisting}}{F_{Driving}};$ = 1.655717399

F.1.4 Embedment Depth for Excitation Along the Transverse Direction

Bridge load,

$DL_{bridge} := 806.58;$ = 806.58 kN

$LL_{bridge} := 987.13;$ = 987.13 kN

Foundation load,

$DL_{foundation} := 424.08;$ = 424.08 kN

Ground soil properties,

$\Upsilon_{soil} := \frac{1900 \cdot 9.81}{1000};$ = 18.64 kN/m^2

$\phi_{soil} := evalf\left(\frac{\pi}{180} \cdot 35\right);$ = 0.6108652381

$\delta_{soil} := evalf\left(\frac{\pi}{180} \cdot 31\right);$ = 0.5410520681

$c := 0;$ = 0

Geofoam embankment geometry,

$B := 9;$ = 9.00 m

$H := 6;$ = 6.00 m

$L := 4;$ = 4.00 m

Assumptions:

Soil below the embankment is sand. The vertical acceleration is negligible. The acceleration along longitudinal and transverse directions of the bridge are same. The spectral and peak ground acceleration is same. The block height is assumed to be 1m.

$g := 9.81;$ = 9.81 m/sec^2

Calculations:

For the acceleration of 1 g,

$a_x := 1;$ = 1 g

$a_y := 1;$ = 1 g

$a_z := 0;$ = 0

The basal layer sliding requires embedment to stop sliding. The calculation of active earth pressure for dynamic is the same as static. The Coulomb's equation was used.

$$\beta := \text{evalf}\left(\frac{\pi}{180}\cdot 0\right);$$ = 0.0000

The backfill slope angle,

$i := 0;$ = 0

$$K_A := \text{evalf}\left(\left(\cos^2(\phi_{soil}-\beta)\right) \Big/ \left(\cos^2(\beta)\cdot\cos(\delta_{soil}+\beta)\cdot\left(1 + \sqrt{\frac{\sin(\delta_{soil}+\phi_{soil})\cdot\sin(\phi_{soil}-i)}{\cos(\delta_{soil}+\beta)\cdot\cos(i-\beta)}}\right)^2\right)\right);$$ = 0.2465569320

$D1 := 1.4;$ = 1.40 m

$P_A := 0.5 \cdot K_A \cdot \Upsilon_{soil} \cdot D1^2 \cdot L;$ $= 18.0146\ kN$

$P_{AE} := P_A;$ $= 18.0146\ kN$

$P_{AEH} := P_{AE} \cdot \cos(\delta_{soil});$ $= 15.4416\ kN$

$P_{AEV} := P_{AE} \cdot \sin(\delta_{soil});$ $= 9.2782\ kN$

$\Delta P_{AE} := P_{AE} - P_A;$ $= 0.0000\ kN$

For the embedment less than 5 ft, the seismic passive earth pressure can be estimated using the static methods. The reduction factor (R) according to AASHTO (2012) is,

$R := 0.836;$ $= 0.836$ for $\phi_{soil} = 35^0$, and $\delta/\phi_{soil} = 0.886$

From Fig.3.11.5.4-1 in AASHTO (2012),

For $\theta = 90^0$ and $\phi_{soil} = 35^0$,

$k_p := 10.1;$ $= 10.1$

Since the reduction factor is 0.836,

$K_P := R \cdot k_p;$ $= 8.4436$

$P_{PE} := 0.5 \cdot K_P \cdot \Upsilon_{soil} \cdot D1^2 \cdot L;$ $= 616.9306\ kN$

$P_{PEH} := P_{PE} \cdot \cos(\delta_{soil});$ $= 528.8127\ kN$

$P_{PEV} := P_{PE} \cdot \sin(\delta_{soil});$ $= 317.7428\ kN$

$W := DL_{bridge} + 0.5 \cdot LL_{bridge} + DL_{foundation};$ $= 1724.22\ kN$

$m := \frac{W \cdot 1000}{g};$ $= 175761.9776\ kg$

Inertial force,

$F_i := \frac{m \cdot a_x \cdot g}{1000};$ $= 1724.2250\ kN$

$R1 := P_{AEV} + W + P_{PEV}$; = 2051.2460 kN

$F_r := R1 \cdot \tan(\phi_{soil})$; = 1436.2979 kN

Factor of safety against sliding

$F_{Resisting} := F_r + P_{PEH}$; = 1965.1107 kN

$F_{Driving} := F_i + P_{AEH}$; = 1739.6666 kN

$FS_{sliding} := \frac{F_{Resisting}}{F_{Driving}}$; = 1.129590401

F.2 Trapezoidal Prism

F.2.1 Critical Acceleration

Bridge load,

$DL_{bridge} := 806.58$; = 806.58 kN

$LL_{bridge} := 987.13$; = 987.13 kN

Foundation load,

$DL_{foundation} := 424.08$; = 424.08 kN

Geofoam embankment geometry,

$B := 9$; = 9.00 m

$H := 6$; = 6.00 m

$L_{top} := 4$; = 4.00 m

$\Delta z := 1$; = 1.00 m

Stress distribution slope is 2V:1H.

Assumptions:

Soil below the embankment is sand. The vertical acceleration is negligible. The

acceleration along longitudinal and transverse directions of the bridge are the same. The spectral and peak ground acceleration is the same. The block height is assumed to be 1m.

$g := 9.81;$ = 9.81 m/sec^2

Calculations:

The calculation was made at the basal layer which is at zero interface shown in Table F.3.

$$\sigma_{v0} := \frac{DL_{bridge} + 0.5 \cdot LL_{bridge} + DL_{foundation}}{(L_{top} \cdot B)}; \quad = 47.8951 \text{ kPa}$$

From the relation given by Sheeley and Negussey (2000),

The friction factor for geofoam-soil interface is,

$\tan\delta$ = 0.81

The friction factor for geofoam-soil interface according to Bartlett et al. (2000) is,

$\tan\delta$ = 0.6

Geofoam shear strength from Benchmark Foam (2009) is,

$$\tau := \frac{33 \cdot 144 \cdot 95}{2000}; \quad = 225.7200 \text{ kPa}$$

The critical acceleration at the basal layer was calculated by using goal seek in spreadsheet.

$a_{critical} := 0.60055;$ = 0.60055 g

Sample calculation for first and basal layers,

First layer,

$\sigma_{v0(1)} := \sigma_{v0};$ = 47.8951 kPa

Mass per unit area,

Table F.3. Calculation of critical acceleration for trapezoidal prism

Interface	Horizontal acceleration (g)	Normal stress (kPa)	Mass/unit area (kg/m^2)	Inertial force (N/m^2)	Frictional resisting force (W/K) (N/m^2)	Frictional resisting force (WO/K) (N/m^2)	Shear key coverage (%)	Cohesive resisting force (N/m^2)	FS sliding (without key)	FS sliding (with key)
6	0.601	47.90	4882	28763	38795	38795	0	0	1.35	1.35
5	0.601	38.32	3906	23011	31036	31036	0	0	1.35	1.35
4	0.601	31.93	3255	19176	25863	25863	0	0	1.35	1.35
3	0.601	27.37	2790	16436	22169	22169	0	0	1.35	1.35
2	0.601	23.95	2441	14382	19398	19398	0	0	1.35	1.35
1	0.601	21.29	2170	12784	17242	17242	0	0	1.35	1.35
0	0.601	19.16	1953	11505	11495	11495	0	0	1.00	1.00

$$m := \frac{\sigma_{v0(1)} \cdot 1000}{9.81}; \quad = 4882.277 \text{ kg/m^2}$$

Inertial force,

$$F_{inertial} := m \cdot a_{critical} \cdot g; \quad = 28763.426 \text{ N/m^2}$$

Frictional resisting force,

$$F_{resisting} := \sigma_{v0(1)} \cdot 0.81 \cdot 1000; \quad = 38795.062 \text{ N/m^2}$$

Factor of safety against sliding,

$$FS_{sliding} := \frac{F_{resisting}}{F_{inertial}}; \quad = 1.35$$

Critical acceleration = 0.600 g

For the basal layer,

$$\sigma_{v0(0)} := \sigma_{v0} \cdot \left(\frac{L_{top} \cdot B}{\left(L_{top} + 6 \cdot \Delta z\right) \cdot B} \right); \quad = 19.158 \text{ kPa}$$

Mass per unit area,

$$m := \frac{\sigma_{v0(0)} \cdot 1000}{9.81}; \quad = 1952.911 \text{ kg/m^2}$$

Inertial force,

$$F_{inertial} := m \cdot a_{critical} \cdot g; \quad = 11505.370 \text{ N/m^2}$$

Frictional resisting force,

$$F_{resisting} := \sigma_{v0(0)} \cdot 0.6 \cdot 1000; \quad = 11494.833 \text{ N/m^2}$$

Factor of safety against sliding

$$FS_{sliding} := \frac{F_{resisting}}{F_{inertial}}; \quad = 1.00$$

F.2.2 Shear Key Coverage

Bridge load,

$DL_{bridge} := 806.58;$ = 806.58 kN

$LL_{bridge} := 987.13;$ = 987.13 kN

Foundation load,

$DL_{foundation} := 424.08;$ = 424.08 kN

Geofoam embankment geometry

$B := 9;$ = 9.00 m

$H := 6;$ = 6.00 m

$L_{top} := 4;$ = 4.00 m

$\Delta z := 1;$ = 1.00 m

Stress distribution slope is 2V:1H.

$L_{bottom(stress)} := L_{top} + 0.5 \cdot H;$ = 7.00 m

Ground soil properties,

$\Upsilon_{soil} := \frac{1900 \cdot 9.81}{1000};$ = 18.64 kN/m^2

$\phi_{soil} := evalf\left(\frac{\pi}{180} \cdot 35\right);$ = 0.6108652381

$\delta_{soil} := evalf\left(\frac{\pi}{180} \cdot 31\right);$ = 0.5410520681

$\beta := 0;$ = 0

$c := 0;$ = 0

Assumptions:

Soil below the embankment is sand. The vertical acceleration is negligible. The

acceleration along longitudinal and transverse directions of the bridge are the same. The spectral and peak ground acceleration is the same. The block height is assumed to be 1m.

$g := 9.81;$ = 9.81 m/sec^2

Calculations:

The detailed calculation is shown in Table F.4. The calculation of first layer is given below.

$$\sigma_{v0} := \frac{DL_{bridge} + 0.5 \cdot LL_{bridge} + DL_{foundation}}{(L_{top} \cdot B)}; \quad = 47.8951 \text{ kPa}$$

From the relation given by Sheeley and Negussey (2000), the friction factor for geofoam-geofoam interface is:

$\tan\delta$ = 0.81

The friction factor for geofoam-soil interface according to Bartlett et al. (2000) is:

$\tan\delta$ = 0.6

Geofoam shear strength from Benchmark Foam (2009) is,

$$\tau := \frac{33 \cdot 144 \cdot 95}{2000}; \quad = 225.7200 \text{ kPa}$$

From the spread sheet below,

For the acceleration of 1 g,

$a_x := 1;$ = 1 g

$a_y := 1;$ = 1 g

$a_z := 0;$ = 0

Sample calculation for fifth layer that is second from top,

$n := 2;$ = 2

Table F.4. Calculation of shear key coverage for trapezoidal prism

Interface	Horizontal acceleration (g)	Normal stress (kPa)	Mass/unit area (kg/m^2)	Inertial force (N/m^2)	Frictional resisting force (W/K) (N/m^2)	Frictional resisting force (WO/K) (N/m^2)	Shear key coverage (%)	Cohesive resisting force (N/m^2)	FS sliding (without key)	FS sliding (with key)
6	1.000	47.90	4882	47895	35691	38795	8	18058	0.81	1.12
5	1.000	38.32	3906	38316	29174	31036	6	13543	0.81	1.11
4	1.000	31.93	3255	31930	24570	25863	5	11286	0.81	1.12
3	1.000	27.37	2790	27369	21282	22169	4	9029	0.81	1.11
2	1.000	23.95	2441	23948	18622	19398	4	9029	0.81	1.15
1	1.000	21.29	2170	21287	16725	17242	3	6772	0.81	1.10
0	1.000	19.16	1953	19158	11495	11495	0	0	0.60	0.60

$$\sigma_{v0(0)} := \sigma_{v0} \cdot \left(\frac{L_{top} \cdot B}{\left(L_{top} + (n-1) \cdot \Delta z\right) \cdot B} \right}; \quad = 38.316 \text{ kPa}$$

Mass per unit area,

$$m := \frac{\sigma_{v0(0)} \cdot 1000}{9.81}; \quad = 3905.822 \text{ kg/m^2}$$

Inertial force,

$$F_i := m \cdot a_x \cdot g; \quad = 38316.111 \text{ N/m^2}$$

Frictional resisting force,

$$F_r := \sigma_{v0(0)} \cdot 0.81 \cdot 1000; \quad = 31036.050 \text{ N/m^2}$$

Factor of safety against sliding,

$$FS_{sliding} := \frac{F_r}{F_i}; \quad = 0.81$$

Using the shear key coverage of 6 percent,

$$S_c := \frac{6}{100}; \quad = 0.06$$

Frictional resisting force,

$$F_r := \sigma_{v0(0)} \cdot 0.81 \cdot 1000 \cdot \left(1 - S_c\right); \quad = 29173.89 \text{ N/m^2}$$

Cohesive resisting force,

$$C_r := \tau \cdot 1000 \cdot S_c; \quad = 13543.20 \text{ N/m^2}$$

Factor of safety against sliding,

$$FS_{sliding} := \frac{F_r + C_r}{F_i}; \quad = 1.11$$

F.2.3 Embedment Depth for Excitation Along the Longitudinal Direction

Bridge load,

$DL_{bridge} := 806.58;$ = 806.58 kN

$LL_{bridge} := 987.13;$ = 987.13 kN

Foundation load,

$DL_{foundation} := 424.08;$ = 424.08 kN

Geofoam embankment geometry,

$B := 9;$ = 9.00 m

$H := 6;$ = 6.00 m

$L_{top} := 4;$ = 4.00 m

$\Delta z := 1;$ = 1.00 m

Stress distribution slope is 2V:1H.

$L_{bottom(stress)} := L_{top} + 0.5 \cdot H;$ = 7.00 m

Ground soil properties,

$\Upsilon_{soil} := \frac{1900 \cdot 9.81}{1000};$ = 18.64 kN/m^2

$\phi_{soil} := evalf\left(\frac{\pi}{180} \cdot 35\right);$ = 0.6108652381

$\delta_{soil} := evalf\left(\frac{\pi}{180} \cdot 31\right);$ = 0.5410520681

$\beta := 0;$ = 0

$c := 0;$ = 0

Assumptions:

Soil below the embankment is sand. The vertical acceleration is negligible. The

acceleration along the longitudinal and transverse directions of the bridge are the same. The spectral and peak ground acceleration is the same. The block height is assumed to be 1m.

$g := 9.81;$ = 9.81 m/sec^2

Calculations:

$$\sigma_{v0} := \frac{DL_{bridge} + 0.5 \cdot LL_{bridge} + DL_{foundation}}{(L_{top} \cdot B)}; \quad = 47.8951 \text{ kPa}$$

$a_x := 1;$ = 1 g

$a_y := 1;$ = 1 g

Depth of embedment,

$D1 := 1.0;$ = 1.00 m

Exterior slope is 1V:2H.

$L_{top(EP)} := L_{top} + H \cdot 2 \cdot 2;$ = 28.00 m

$L_{bottom(EP)} := L_{top} + H \cdot 2 \cdot 2;$ = 28.00 m

$L_{bottom} := L_{top} + 2 \cdot 2 \cdot (H + D1);$ = 32.00 m

$$\beta := -\text{evalf}\left(\arctan\left(\frac{L_{bottom} - L_{top}}{2 \cdot (H + D1)}\right)\right); \quad = -1.1071$$

$i := 0;$ = 0

$$K_A := \text{evalf}\left(\left(\cos^2(\phi_{soil} - \beta)\right) \Big/ \left(\cos^2(\beta) \cdot \cos(\delta_{soil} + \beta) \cdot \left(1 + \sqrt{\frac{\sin(\delta_{soil} + \phi_{soil}) \cdot \sin(\phi_{soil} - i)}{\cos(\delta_{soil} + \beta) \cdot \cos(i - \beta)}}\right)^2\right)\right); \quad = 0.02686566866$$

$P_A := 0.5 \cdot K_A \cdot \Upsilon_{soil} \cdot D1^2 \cdot B;$ = 2.2534 kN

$P_{AE} := P_A;$ $= 2.2534\ kN$

$P_{AEH} := P_{AE} \cdot \cos(-\beta - \delta_{soil});$ $= 1.9018\ kN$

$P_{AEV} := P_{AE} \cdot \sin(-\beta - \delta_{soil});$ $= 1.2086\ kN$

$\Delta P_{AE} := P_{AE} - P_A;$ $= 0.0000\ kN$

For the embedment less than 5 feet, the seismic passive earth pressure can be estimated using the static methods. The reduction factor (R) is,

$R := 0.836;$ $= 0.836$ for $\phi_{soil} = 35^0$, and $\delta/\phi_{soil} = 0.886$

From Fig.3.11.5.4-1 in AASHTO (2012),

$\theta := \text{evalf}\left(\left(\frac{\pi}{2} - \beta\right) \cdot \frac{180}{\pi}\right);$ $= 153.4349488$

For $\theta = 153^0$ and $\phi_{soil} = 35^0$,

$k_p := 14;$ $= 14$

Since the reduction factor is 0.836,

$K_P := R \cdot k_p;$ $= 11.704$

$P_{PE} := 0.5 \cdot K_P \cdot \Upsilon_{soil} \cdot D1^2 \cdot B;$ $= 981.6788\ kN$

$P_{PEH} := P_{PE} \cdot \cos(-\beta - \delta_{soil});$ $= 828.5379\ kN$

$P_{PEV} := P_{PE} \cdot \sin(-\beta - \delta_{soil});$ $= 526.5153\ kN$

$n := 8;$ $= 8$

$\sigma_{v0(0)} := \sigma_{v0} \cdot \left(\frac{L_{top} \cdot B}{(L_{top} + (n-1) \cdot \Delta z) \cdot B}\right);$ $= 17.416\ kPa$

$W := \sigma_{v0(0)} \cdot (L_{top} + H + D1) \cdot B;$ $= 1724.225000$

$m := \frac{W \cdot 1000}{g};$ $= 175761.9776\ kg$

Inertial force,

$F_i := \frac{m \cdot a_x \cdot g}{1000};$ = 1724.2250 kN

$R1 := P_{AEV} + W + P_{PEV};$ = 2251.9489 kN

$F_r := R1 \cdot \tan(\phi_{soil});$ = 1576.8316 kN

Factor of safety against sliding

$F_{Resisting} := F_r + P_{PEH};$ = 2405.3694 kN

$F_{Driving} := F_i + P_{AEH};$ = 1726.1268 kN

$FS_{sliding} := \frac{F_{Resisting}}{F_{Driving}};$ = 1.393506773

F.2.4 Embedment Depth for Excitation the Along the Transverse Direction

Bridge load,

$DL_{bridge} := 806.58;$ = 806.58 kN

$LL_{bridge} := 987.13;$ = 987.13 kN

Foundation load,

$DL_{foundation} := 424.08;$ = 424.08 kN

Geofoam embankment geometry,

$B := 9;$ = 9.00 m

$H := 6;$ = 6.00 m

$L_{top} := 4;$ = 4.00 m

$\Delta z := 1;$ = 1.00 m

Stress distribution slope is 2V:1H.

$L_{bottom(stress)} := L_{top} + 0.5 \cdot H;$ $= 7.00$ m

Ground soil properties,

$\Upsilon_{soil} := \frac{1900 \cdot 9.81}{1000};$ $= 18.64$ kN/m^2

$\phi_{soil} := evalf\left(\frac{\pi}{180} \cdot 35\right);$ $= 0.6108652381$

$\delta_{soil} := evalf\left(\frac{\pi}{180} \cdot 31\right);$ $= 0.5410520681$

$\beta := 0;$ $= 0$

$c := 0;$ $= 0$

Assumptions:

Soil below the embankment is sand. The vertical acceleration is negligible. The acceleration along longitudinal and transverse directions of the bridge are the same. The spectral and peak ground acceleration is the same. The block height is assumed to be 1m.

$g := 9.81;$ $= 9.81$ m/sec^2

Calculations:

$\sigma_{v0} := \frac{DL_{bridge} + 0.5 \cdot LL_{bridge} + DL_{foundation}}{(L_{top} \cdot B)};$ $= 47.8951$ kPa

$a_x := 1;$ $= 1$ g

$a_y := 1;$ $= 1$ g

Depth of embedment,

$D1 := 1.0;$ $= 1.00$ m

Exterior slope is 1V:2H.

$L_{top(EP)} := L_{top} + H \cdot 2 \cdot 2;$ $= 28.00$ m

$L_{bottom(EP)} := L_{top} + H \cdot 2 \cdot 2;$ $= 28.00$ m

$L_{bottom} := L_{top} + 2 \cdot 2 \cdot (H + D1);$ $= 32.00\ m$

$\beta := -evalf\left(\arctan\left(\frac{L_{bottom} - L_{top}}{2 \cdot (H + D1)}\right)\right);$ $= -1.1071$

$i := 0;$ $= 0$

$K_A := evalf\left(\left(\cos^2(\phi_{soil} - \beta)\right) \Big/ \left(\cos^2(\beta) \cdot \cos(\delta_{soil} + \beta) \cdot \left(1 + \sqrt{\frac{\sin(\delta_{soil} + \phi_{soil}) \cdot \sin(\phi_{soil} - i)}{\cos(\delta_{soil} + \beta) \cdot \cos(i - \beta)}}\right)^2\right)\right);$ $= 0.02686566866$

$P_A := 0.5 \cdot K_A \cdot \Upsilon_{soil} \cdot D1^2 \cdot \left(\frac{(L_{bottom(EP)} + L_{bottom})}{2}\right);$ $= 7.5112\ kN$

$P_{AE} := P_A;$ $= 7.5112\ kN$

$P_{AEH} := P_{AE} \cdot \cos(-\beta - \delta_{soil});$ $= 6.3395\ kN$

$P_{AEV} := P_{AE} \cdot \sin(-\beta - \delta_{soil});$ $= 4.0286\ kN$

$\Delta P_{AE} := P_{AE} - P_A;$ $= 0.0000\ kN$

For the embedment less than 5 ft, the seismic passive earth pressure can be estimated using the static methods. The reduction factor (R) is,

$R := 0.836;$ $= 0.836$ for $\phi_{soil} = 35^0$, and $\delta/\phi_{soil} = 0.886$

From Fig.3.11.5.4-1 in AASHTO (2012),

$\theta := evalf\left(\left(\frac{\pi}{2} - \beta\right) \cdot \frac{180}{\pi}\right);$ $= 153.4349488$

For $\theta = 153^0$ and $\phi_{soil} = 35^0$,

$k_p := 14;$ $= 14$

Since the reduction factor is 0.836.

$K_P := R \cdot k_p;$ = 11.704

$P_{PE} := 0.5 \cdot K_P \cdot \Upsilon_{soil} \cdot D1^2 \cdot \left(\frac{(L_{bottom(EP)} + L_{bottom})}{2} \right);$ = 3272.2628 kN

$P_{PEH} := P_{PE} \cdot \cos(-\beta - \delta_{soil});$ = 2761.7929 kN

$P_{PEV} := P_{PE} \cdot \sin(-\beta - \delta_{soil});$ = 1755.0510 kN

$n := 8;$ = 8

$\sigma_{v0(0)} := \sigma_{v0} \cdot \left(\frac{L_{top} \cdot B}{(L_{top} + (n-1) \cdot \Delta z) \cdot B} \right);$ = 17.416 kPa

$W := \sigma_{v0(0)} \cdot (L_{top} + H + D1) \cdot B;$ = 1724.225000

$m := \frac{W \cdot 1000}{g};$ = 175761.9776 kg

Inertial force,

$F_i := \frac{m \cdot a_x \cdot g}{1000};$ = 1724.2250 kN

$R1 := P_{AEV} + W + P_{PEV};$ = 3483.3046 kN

$F_r := R1 \cdot \tan(\phi_{soil});$ = 2439.0362 kN

Factor of safety against sliding

$F_{Resisting} := F_r + P_{PEH};$ = 5200.8290 kN

$F_{Driving} := F_i + P_{AEH};$ = 1730.5645 kN

$FS_{sliding} := \frac{F_{Resisting}}{F_{Driving}};$ = 3.005278954

APPENDIX G

DESIGN OF CABLES

G.1 Sway Mode

G.1.1 Excitation Along the Longitudinal Direction for 1 g

Geofoam embankment geometry,

$B := 9; \quad = 9.00$ m

$H := 7; \quad = 7.00$ m

$L1 := 4; \quad = 4.00$ m

Allowable axial strain due to the combined dead and cyclic load is,

$\varepsilon_{allowable} := 2; \quad = 2$ %

$\nu := 0.193; \quad = 0.193$

The sway mode with placement of cables is shown in Figure G.1.

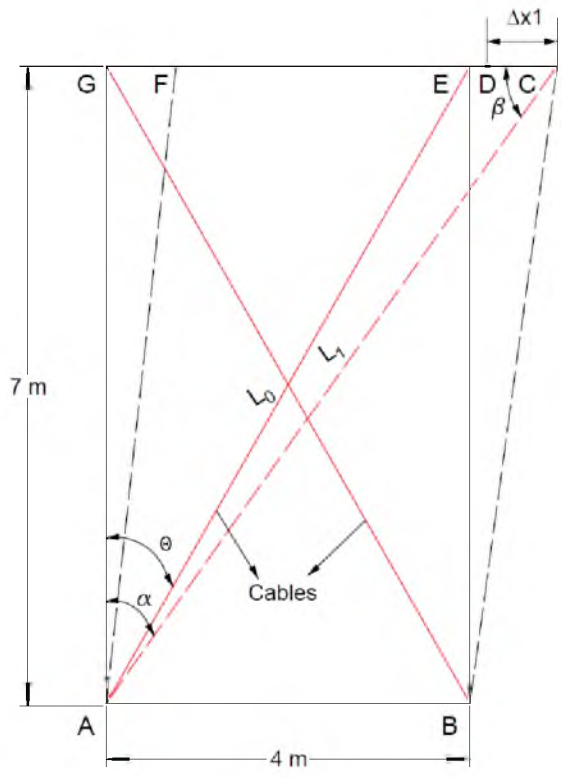

Figure G.1 Sway mode with placement of cables

During elastic limit,

$$\Upsilon_{allowable} := \varepsilon_{allowable} \cdot (1 + \nu); \quad = 2.386\ \%$$

In Figure G.1, AE and BG are two cables. D is the position after which the cable started to take load. Δx1 is the displacement of the system after cable started to take load. EC is the total displacement of system.

From Figure G.1,

$$Tangent_{theta} := \frac{L}{H}; \quad = \frac{4}{7}$$

$$\theta := evalf\left(\left(\arctan\left(Tangent_{theta} \right) \right) \cdot \frac{180}{\pi} \right); \quad = 29.74488129$$

Table G.1 and G.2 show the calculation of force and displacement of both EPS and cable, respectively. In Table G.1, strain (ε) and stress (σ) were taken from the stress-strain relationship of EPS 29 obtained from monotonic uniaxial test.

Table G.1. Calculation of force and displacement of EPS

ϵ *(%)*	ϒ *(%)*	Δx *(m)*	σ *(kPa)*	τ *(kPa)*	V_{EPS} *(kN)*
0.00	0.000	0.000	0.00	0.00	0.00
0.25	0.298	0.021	25.93	12.97	51.86
0.50	0.597	0.042	53.53	26.77	107.06
0.75	0.895	0.063	79.45	39.73	158.9
1.00	1.193	0.084	107.78	53.89	215.56
1.25	1.491	0.104	131.93	65.97	263.86
1.50	1.790	0.125	152.28	76.14	304.56
1.75	2.088	0.146	169.29	84.65	338.58
2.00	2.386	0.167	181.68	90.84	363.36
2.25	2.684	0.188	182.68	91.34	365.36
2.50	2.983	0.209	183.68	91.84	367.36
2.75	3.281	0.230	184.68	92.34	369.36
3.00	3.579	0.251	185.68	92.84	371.36

Table G.2. Calculation of force and displacement of cable

ϵ (%)	σ (kPa)	P (kN)	Pcosθ (kN)	Δx (m)	$\Delta x\cos\theta$ (m)	V_{cable} (kN)
0.00	0	0.00	0.00	0.000	0.0000	----------
0.10	330960	93.66	81.32	0.014	0.0122	----------
0.20	661920	187.32	162.64	0.028	0.0244	----------
0.30	896350	253.67	220.24	0.038	0.0331	----------
0.40	1103200	312.21	271.07	0.047	0.0407	----------
0.50	1268680	359.04	311.73	0.054	0.0468	----------
0.60	1447950	409.77	355.78	0.062	0.0534	0
0.70	1516900	429.28	372.72	0.064	0.0560	488
0.80	1558270	440.99	382.89	0.066	0.0575	976
0.90	1599640	452.70	393.05	0.068	0.0590	1321
1.00	1634115	462.45	401.52	0.069	0.0603	1626
1.10	1654800	468.31	406.61	0.070	0.0611	1870
1.20	1675485	474.16	411.69	0.071	0.0618	2135
1.30	1689275	478.06	415.08	0.072	0.0624	2236
1.40	1703065	481.97	418.46	0.072	0.0629	2297
1.50	1716855	485.87	421.85	0.073	0.0634	2358
1.60	1730645	489.77	425.24	0.074	0.0639	2409
1.70	1744435	493.68	428.63	0.074	0.0644	2440
1.80	1758225	497.58	432.02	0.075	0.0649	2470
1.90	1772015	501.48	435.41	0.075	0.0654	2490
2.00	1778910	503.43	437.10	0.076	0.0657	2511
2.10	1792700	507.33	440.49	0.076	0.0662	2531
2.20	1799595	509.29	442.18	0.077	0.0664	2551
2.30	1809938	512.21	444.72	0.077	0.0668	2572
2.40	1820280	515.14	447.27	0.077	0.0672	2592
2.50	1827175	517.09	448.96	0.078	0.0674	2612

In the Table G.1, γ, Δx, τ and V are the shear strain, horizontal displacement, shear stress and horizontal force. The calculation of force and displacement for strain level of 0.25 % is shown below.

$\varepsilon := 0.25; \quad = 0.25 \ \%$

$\Upsilon := \varepsilon \cdot (1 + \nu); \quad = 0.29825 \ \%$

$\Delta x := \frac{\Upsilon \cdot H}{100};$ $= 0.021$

$\sigma := 25.93;$ $= 25.93$ kPa

$\tau := \frac{\sigma}{2};$ $= 12.96$ kPa

$V := \tau \cdot L;$ $= 51.86$ kN

In Table G.2, ε and σ are taken from the stress-strain relationship of the strand of Grade 270 based on Nawy (2006).

The design force for the acceleration of 1 g along the longitudinal direction is shown below.

$a := 1;$ $= 1$ g

Weight at top of embankment,

$W := 1724;$ $= 1724$ kN

$V_{design} := W \cdot a;$ $= 1724$ kN

The length of strand was obtained from Figure G.1.

$$L_{strand} := evalf\left(\frac{L}{\sin\left(\theta \cdot \frac{\pi}{180}\right)}\right); \quad = 8.062257748 \text{ m}$$

Area of strand and number of strands were varied to get the design value within the limit of force and strain in cable and EPS. The calculation of force and displacement for strain level of 0.1 % is given below.

Area of strand for 19 mm diameter,

$$A_{strand} := evalf\left(\frac{283}{1000^2}\right); \quad = 0.000283 \text{ m^2}$$

Numbers of strand,

$n := 6;$ $= 6$

$\varepsilon 1 := 0.1;$ $= 0.1$ %

$\sigma 1 := 330960;$ $= 330960$ kPa

Axial force,

$P1 := \sigma 1 \cdot A_{strand};$ $= 93.6617$ kN

Horizontal component force,

$P_{Horizontal} := evalf\left(P1 \cdot \cos\left(\theta \cdot \frac{\pi}{180}\right)\right);$ $= 81.3211$ kN

Young's modulus of elasticity,

$E_{strand} := \frac{27500000}{100000} \cdot 689.5 \cdot 1000;$ $= 1.896125000\,10^{8}$ kPa

Displacement (elongation),

$\Delta x1 := \frac{P1 \cdot L_{strand}}{A_{strand} \cdot E_{strand}};$ $= 0.0141$ m

Horizontal component of displacement,

$\Delta x1_{Horizontal} := evalf\left(\Delta x1 \cdot \cos\left(\theta \cdot \frac{\pi}{180}\right)\right);$ $= 0.01222$ m

Since the cable was engaged at strain level of 0.6 %, the force in the cable was set zero up to this position. The combined plot of EPS and cable was made from the force and displacement relationship. The calculation of force and displacement for combined EPS and cable is shown in Table G.3. The limiting value of force in the cable was based on the stress value in the linear range of stress-strain relationship.

The design value was found to be within the limiting values of force and strain for both cable and EPS. The resisting forces on EPS and cable for the excitation level of 1 g were 157 kN and 2135 kN. The resisting force was found to be higher than the design load.

Number of strands = 6

Diameter of strand = 19 mm

Table G.3. Calculation of force and displacement for combined EPS and cable

Δx *(m)*	V_{EPS} *(kN)*	V_{cable} *(kN)*	V *(kN)*
0.0000	0.00	----------	0.00
0.0122	30.35	----------	30.35
0.0244	61.26	----------	61.26
0.0331	84.14	----------	84.14
0.0407	104.33	----------	104.33
0.0468	119.66	----------	119.66
0.0534	136.09	0.00	136.09
0.0560	142.41	487.93	630.34
0.0575	146.20	975.85	1122.05
0.0590	149.99	1321.47	1471.46
0.0603	153.15	1626.42	1779.57
0.0611	155.05	1870.39	2025.43
0.0618	156.94	2134.68	2291.62
0.0624	158.21	2236.33	2394.54
0.0629	159.53	2297.32	2456.85
0.0634	160.91	2358.31	2519.22
0.0639	162.29	2409.14	2571.43
0.0644	163.67	2439.63	2603.30
0.0649	165.05	2470.13	2635.18
0.0654	166.43	2490.46	2656.89
0.0657	167.12	2510.79	2677.91
0.0662	168.50	2531.12	2699.62
0.0664	169.20	2551.45	2720.65
0.0668	170.23	2571.78	2742.01
0.0672	171.27	2592.11	2763.38
0.0674	171.96	2612.44	2784.40